ONR Award # N00014-06-1-0577

FINAL REPORT

DYNAMIC RESPONSE AND SIMULATIONS OF NANOPARTICLE-ENHANCED COMPOSITES

Submitted by:

P. Raju Mantena, Ahmed Al-Ostaz, Alexander H.D. Cheng
Composite Structures and Nano-Engineering Research
University of Mississippi, University, MS 38677

To:

Dr. Yapa D.S. Rajapakse
Program Manger, Solid Mechanics
Office of Naval Research (ONR 332)
One Liberty Center (Suite 1425)
875 North Randolp Street
Arlington, VA 22203-1995

November 15, 2007

REPORT DOCUMENTATION PAGE

Form Approved
OMB No. 0704-0188

1. REPORT DATE *(15-11-2007)*	2. REPORT TYPE	3. DATES COVERED *(From - To)*
	Final	01-APR-06 to 31-AUG-07

4. TITLE AND SUBTITLE

Dynamic Response and Simulations of Nanoparticle-enhanced Composites

5a. CONTRACT NUMBER

5b. GRANT NUMBER
N00014-06-1-0577

5c. PROGRAM ELEMENT NUMBER

6. AUTHOR(S)
Mantena, P. Raju
Cheng, Alexander
Al-Ostaz, Ahmed

5d. PROJECT NUMBER

5e. TASK NUMBER

5f. WORK UNIT NUMBER

7. PERFORMING ORGANIZATION NAME(S) AND ADDRESS(ES)
The University of Mississippi
Office of Research and
Sponsored Programs
100 Barr Hall
University, MS 38677-0907

8. PERFORMING ORGANIZATION REPORT NUMBER
Final

9. SPONSORING / MONITORING AGENCY NAME(S) AND ADDRESS(ES)
Office of Naval Research
Atlanta Regional Office
100 Alabama St. SW, Ste. 4R15
Atlanta, GA 30303-3104

10. SPONSOR/MONITOR'S ACRONYM(S)
ONR

11. SPONSOR/MONITOR'S REPORT NUMBER(S)
Final

12. DISTRIBUTION / AVAILABILITY STATEMENT
Approved for Public Release; distribution is Unlimited.

13. SUPPLEMENTARY NOTES

14. ABSTRACT

Objectives of this research are to characterize the: (a) vibration and acoustic response; (b) low-velocity impact and high-strain energy absorption; (c) effects of freeze-thaw cycling; and (d) molecular dynamic simulations of nanoparticle-enhanced composites and fly-ash based foams that are being considered for the future generation naval structures or retrofitting of existing ones.

In this study, the flexural/extensional dynamic modulus, damping, low-velocity impact and high-strain (Hopkinson bar) response of nylon 6,6 thermoplastic reinforced with multi-wall carbon nano tubes (MWCNT) were characterized. Preliminary investigations were also conducted on Derakane 411-350 vinyl ester thermoset, reinforced with Cloisite 30B nanoclay and exfoliated graphite nanoplatelets (xGnP). Molecular Dynamic (MD) simulations are used for obtaining the elastic constants (C_{ij}) of SWCNT, MWCNT and nylon 6,6 nanocomposites.

15. SUBJECT TERMS: Vibration response, damping, nanoparticle-enhanced composites, MWCNT, nylon 6,6, nanoclay, graphite platelets, fly-ash foams, low-velocity impact, Hopkinson high-strain response, acoustic absorption, freeze-thaw, Molecular Dynamic Simulations

16. SECURITY CLASSIFICATION OF:			17. LIMITATION OF ABSTRACT	18. NUMBER OF PAGES	19a. NAME OF RESPONSIBLE PERSON
a. REPORT	b. ABSTRACT	c. THIS PAGE			Dr. P. Raju Mantena
U	U	U	UU	239	19b. TELEPHONE NUMBER *(include area code)* (662) 915-5990

ONR Award # N00014-06-1-0577

DYNAMIC RESPONSE AND SIMULATIONS OF NANOPARTICLE-ENHANCED COMPOSITES

P. Raju Mantena, Ahmed Al-Ostaz, Alexander H.D. Cheng
Composite Structures and Nano-Engineering Research
University of Mississippi, University, MS 38677

PROJECT SUMMARY

Fiber-reinforced polymer (FRP) composites are increasingly being used in naval platforms for improving stealth and reducing topside weight, corrosion mitigation, fatigue, maintenance and operational costs. FRP composites are presently being used in US Navy Ships such as the Osprey class mine hunter, and for topside structures on large warships such as the Advanced Enclosed Mast System (AEMS). The navy also has plans to integrate more composites into the new generation CV(X) and DD(X) ship class designs. Structures in these applications are often subjected to high strain rates due to impact by hard objects, mine blasts, projectile penetration and collisions. ONR sponsored research currently underway is focused on developing hybrid composite systems with nanoparticles such as clay nanomers and carbon nanotube dispersions for enhancing their multi-functionality. Vibration response, damping, acoustic impedance and the performance of these nanoparticle-enhanced composites and foams in cold regions under freeze-thaw conditions are some important factors which need to be addressed. Ultimate goal is the development of composite panels with low-cost fire resistant foams sandwiched in between nanoparticle-enhanced face sheets; forming structures that offer optimal flexural rigidity, vibration damping and impact energy absorption along with reduced weight.

Main objectives of this research are to characterize: (a) the vibration and acoustic response; (b) low-velocity impact and high-strain energy absorption; (c) effects of freeze-thaw cycling; and (d) molecular dynamic simulations of nanoparticle-enhanced composites and fly-ash based foams that are being considered for future generation naval structures or the retrofitting of existing ones. In this study, the flexural/extensional dynamic modulus, damping, low-velocity impact and high-strain (Hopkinson bar) response of nylon 6,6 thermoplastic reinforced with multi-wall carbon nano tubes (MWCNT) were characterized. Preliminary investigations were also conducted on Derakane 411-350 vinyl ester thermoset reinforced with Cloisite 30B nanoclay and exfoliated graphite nanoplatelets (xGnP). Molecular Dynamic (MD) simulations are used for obtaining the elastic constants (C_{ij}) of SWCNT, MWCNT and nylon 6,6 nanocomposites.

North Carolina A&T State University (NC AT) under a joint program with the Office of Naval Research has developed a process for producing low-cost syntactic foams Eco-Core® from fly ash, a waste product generated by the utility industry. In the event of a fire this foam material will generate little or no smoke and emit no toxic gases, a factor that would be of great importance for naval and other military applications as well as building constructions. Eco-Core foam samples supplied by NC AT were characterized for their vibration and acoustic response, and low-velocity impact energy absorption.

The project deliverables and their execution, in order of priority, are summarized here. Detailed descriptions of the work performed are given in following sections.

1) DYNAMIC MODULUS AND DAMPING: *Dynamic flexural/extensional modulus and damping of nylon 6,6 thermoplastic reinforced with multi-wall carbon nano tubes (MWCNT); Derakane 411-350 vinyl-ester thermoset reinforced with Cloisite 30-B nanoclay and exfoliated graphite platelets (xGnP); and fly ash based Eco-Core foams were characterized using the non-destructive impulse-frequency response vibration technique.*

2) IMPACT AND ENERGY ABSORPTION: *Low-velocity impact failure load and energy absorption of nylon 6,6 thermoplastic reinforced with multi-wall carbon nano tubes (MWCNT); Derakane 411-350 vinyl-ester thermoset reinforced with Cloisite 30-B nanoclay and exfoliated graphite platelets (xGnP); and fly ash based Eco-Core foams were characterized with a Dynatup Model 8250 instrumented impact test system for both notched and un-notched specimens.*

3) FREEZE-THAW EFFECTS: *EIS was used to examine the effects of freeze-thaw cycling and moisture ingression on nylon 6,6 thermoplastic reinforced with multi-wall carbon nano tubes (MWCNT) over a 45 and 90 day time period.*

4) MOLECULAR DYNAMICS OF NANOPARTICLE-ENHANCED PLASTICS: *Material Studio Software® has been used for performing molecular dynamic simulations of nylon 6,6 reinforced with single- and multi-wall carbon nano tubes; estimating mechanical properties of nano-composite constituents (i.e. matrix, reinforcements and interface) and studying the effects of varying type and weight-fraction of nano-reinforcement.*

5) ACOUSTIC IMPEDANCE OF NANOPARTICLE-ENHANCED PLASTICS AND FOAMS: *Sound absorption coefficients of nylon 6,6 thermoplastic reinforced with multi-wall carbon nano tubes (MWCNT), and fly ash based Eco-Core foams were characterized with a B&K Type 4002 Standing Wave Apparatus.*

COLLABORATION WITH UNIVERSITY OF NEW ORLEANS (UNO): *Small samples of nylon 6,6 thermoplastic reinforced with multi-wall carbon nano tubes (MWCNT) were subjected to high-strain rate compression testing using a Split-Hopkinson Pressure Bar (SHPB) apparatus.*

SIGNIFICANCE OF RESEARCH AND NAVY RELEVANCE: This research will aid in the development of nano-multifunctional materials and sandwich structures that offer optimal flexural rigidity, vibration damping and impact energy absorption along with reduced weight; contributing towards building lighter, stronger and faster ships for the US Navy. Research conducted in this project will also impact the development of composite materials technology in homeland security and civil-infrastructure areas. The research was conducted in close coordination with private industry and government agencies including Northrup Grumman Ship Systems (NGSS) and the Army Corps of Engineers Research and Development Center (ERDC). Both NGSS and ERDC are located in the State of Mississippi and have maintained strong connections with our research team at Ole Miss.

Preliminary work undertaken on this project has been beneficial for a larger one-million dollar congressional initiative on Blast/Shock/Impact Resistant Composites for Naval Structures; a collaborative effort between the University of Mississippi, Michigan State University and University of New Orleans. Results of this research have also been successfully leveraged for a 765K project on 'Nanoparticle Reinforced Composites for Critical Infrastructure Protection' from the Department of Homeland Security (DHS).

PUBLICATIONS (RESULTING FROM THIS RESEARCH):

1. Ghanshyam Pal, Ahmed Al-Ostaz, P. Raju Mantena and Alex Cheng, "Molecular Dynamics Simulation of SWCNT-Polymer Nanocomposite and its Constituents," *Proceedings of the 21st Annual Technical Conference of the American Society for Composites*, September 17-20, 2006, Dearborn, MI (CD-ROM)

2. Ahmed Al-Ostaz, Ghanshyam Pal, P. Raju Mantena and Alex Cheng, "Molecular Dynamics Simulation of SWCNT-Polymer Nanocomposite and its Constituents," *Journal of Materials Science* (accepted)

3. P. Raju Mantena, Ahmed Al-Ostaz and Alex Cheng, "Dynamic Response and Molecular Simulations of Nanocomposites," *Proceedings of the 16th International Conference on Composite Materials*, July 8-13, 2007, Kyoto, Japan (CD-ROM)

4. Ravi Zalani, P. Raju Mantena and Ahmed Al-Ostaz, "Dynamic Characterization of Nylon 6,6 / MWCNT Nanocomposites," *Proceedings of the 22nd Annual Technical Conference of the American Society for Composites*, September 17-19, 2007, Seattle, WA (CD-ROM)

ACKNOWLEDGEMENTS:

This research was supported by ONR Grant N00014-06-1-0577, Office of Naval Research, Solid Mechanics Program (Dr. Yapa D.S. Rajapakse, Program Manager).

Nanoclay and graphite platelet vinyl ester composite plates were manufactured by Dr. Larry Drzal's group at Michigan State University - Composite Materials and Structures Center. Eco-Core foam samples were supplied by Dr. Kunigal Shivkumar at NC A&T State University and Hopkinson bar high-strain rate testing was performed by Dr. David Hui's group at University of New Orleans.

Graduate students Ravi Zalani, Swasti Gupta and Hunain Alkhateb worked on this project. Workshop Supervisor Lynn Stewart helped with sample preparation.

TABLE OF CONTENTS

INTRODUCTION:

For this research, several 12" x 12" x 0.375" thick nylon 6,6 thermoplastic plates reinforced with 1.25, 2.5, 5 and 10 wt. percent multi-wall carbon nano tubes (MWCNT-from Hyperion Catalysis) were prepared by Ensinger Inc. using a proprietary pressure extrusion process. A higher 20 wt. percent MWCNT resulted in fractured plates.

Derakane 411-350 vinyl ester thermoset plates reinforced with 1.25 and 2.5 wt. percent MWCNT were attempted by Dr. Larry Drzal's research group at Michigan State University Composite Materials and Structures Center, our collaborator on this project. The high viscosity of CNT-vinyl ester resin hampered removal of entrapped air, and plaques with acceptable quality were not produced. It was also concluded that the CNTs themselves may poison the vinyl ester reaction, leading to unacceptable material properties. 11"x11"x0.4" thick Derakane 411-350 vinyl ester thermoset plates reinforced with 1.25 and 2.5 wt. percent Cloisite 30B nanoclay and exfoliated graphite nanoplatelets (xGnP) were successfully fabricated at Michigan State University.

Eco-Core foam plates supplied by North Carolina A & T State University were designated as OM11, OM12, OM16, OM21, OM18 and OM19. Plates OM11 and OM12 consist of fly ash with phenolic resin (no added fibers) + 1 ply phenolic resin-coated glass fiber veil (on top/bottom surface). Plate OM16 consists of fly ash w/phenolic resin (0% wt. 0.125-in chopped glass fiber) and no covering. Plate OM21 consisted of fly ash with phenolic resin (+ 6% wt. 0.125-in chopped glass fibers) and no covering. Plates OM18 & OM19 consisted of fly ash with phenolic resin (+ 6% wt. 0.125-in chopped glass fibers) and 1-ply covering of phenolic resin-coated glass fiber veil (on top/bottom surface).

All the nylon 6,6 nanocomposite configurations have been subjected to environmental aging for 90 days. The specimens were subjected to freeze-thaw cycling from 10 to 50° F at 6 cycles per day according to ASTM standard C666-97 Procedure-A (Freezing in water and thawing in water). The specimens were tested after 45 and 90 days aging period.

For identifying the specimens, a uniform coding system was used. The codification for nanocomposites consists of 8 digits with each digit representing a specific purpose. The codification scheme for nanocomposites is explained in Figure 1. The Eco-Core foams plates were supplied with four digit identifications, a three digits extension is given to identify them as explained in Figure 2.

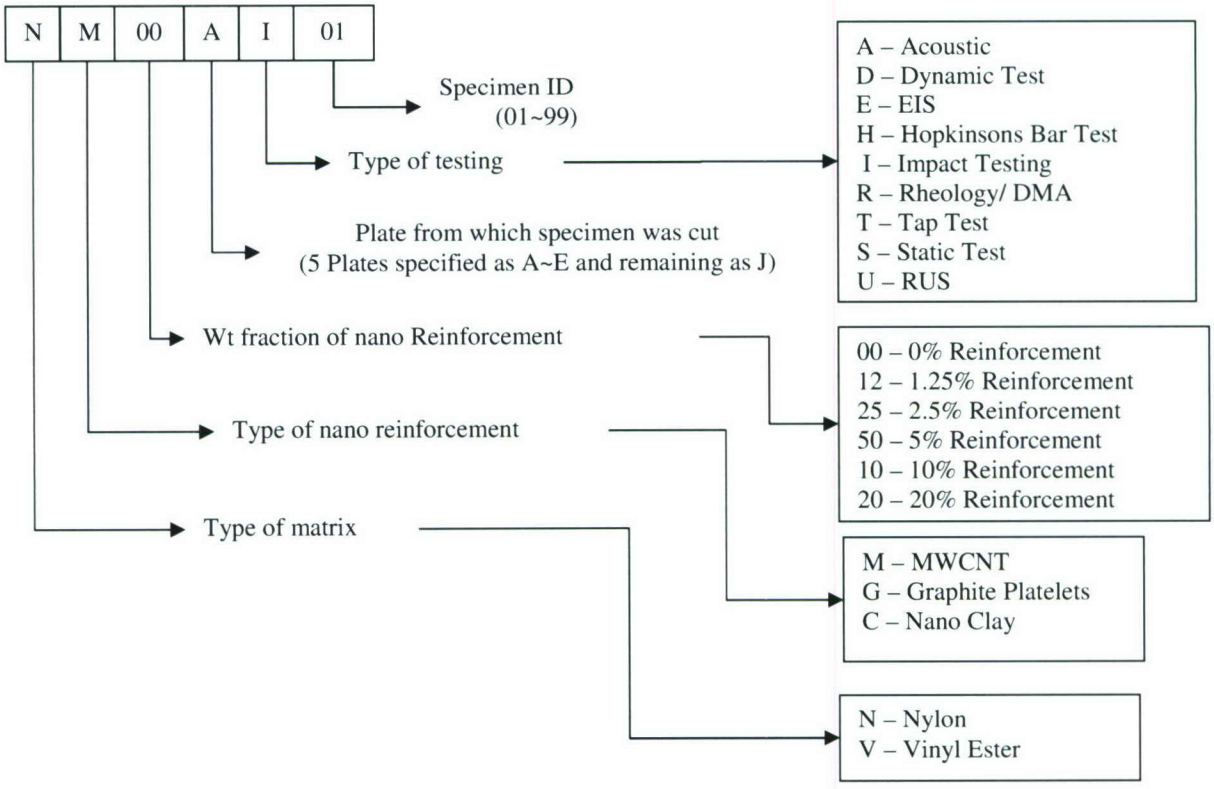

Figure 1: Codification of nanocomposite specimens

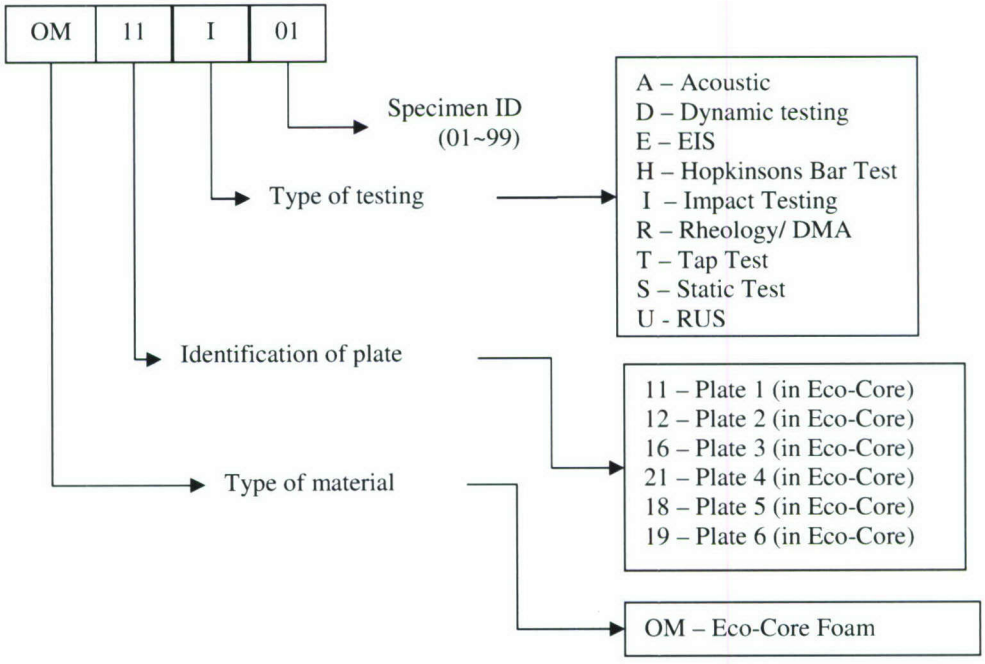

Figure 2: Codification of Eco-Core Foam specimens

Plate Vibration Signature Analysis:

A vibration signature analysis was initially performed to check the quality of the supplied nanoparticle enhanced plates of each configuration. The resonant frequencies for all the plates were recorded over a span of 0 to 800 Hz. The resonant frequencies of the plates are obtained with the Fast Fourier Transform (FFT) based on impulse-frequency response vibration technique [1.1-1.3]. The plates are tapped in a free-free condition achieved by hanging them with nylon wires on a steel frame. The experimental setup is shown in Figure 3. The hammer is of PCB Pizeotronics model 086BOI with an internal load cell. A steel tip is chosen as it gave clear resonant peaks. The output is measured with a PCB Pizeotronics 309A sn5406 accelerometer. The location of accelerometer is chosen at 32 mm from one of the plate corners after examining the node lines for free-free condition such that this point does not coincide with the nodal lines [1.4]. If the accelerometer is placed at one of the nodal lines then associated frequency of that nodal line will not appear in the response spectrum. The hammer and accelerometer are connected to a two channel HP36550A spectrum analyzer via PCB 482A04 amplifier. The driving point measurements are taken by tapping the hammer adjacent to the accelerometer. The resonant frequencies of the plate appear as peaks on the analyzer screen. A typical Frequency Response Function (FRF) output for a pure nylon plate is shown in Figure 4.

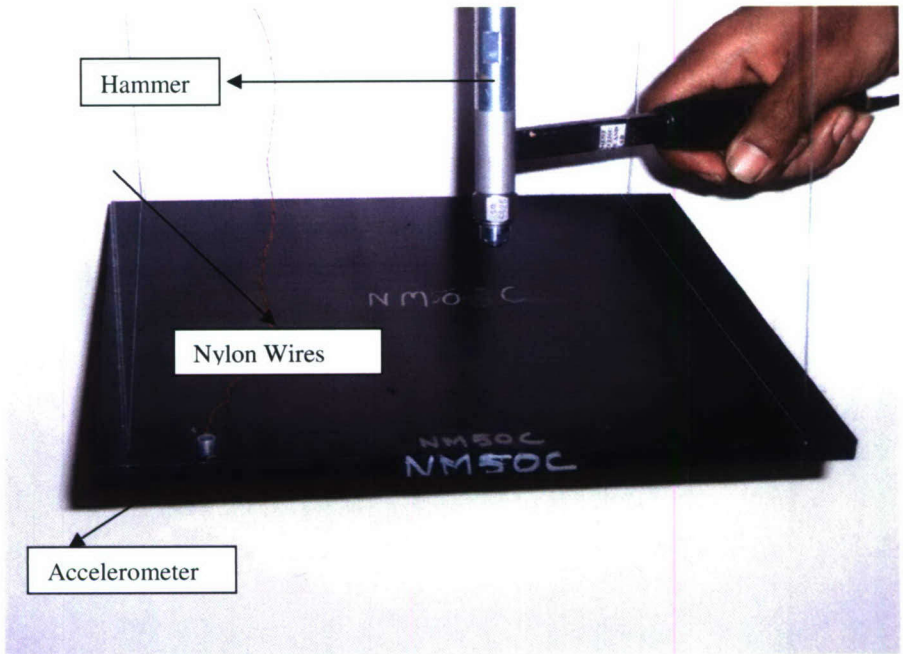

Figure 3: Free-free experimental setup for vibration tap test.

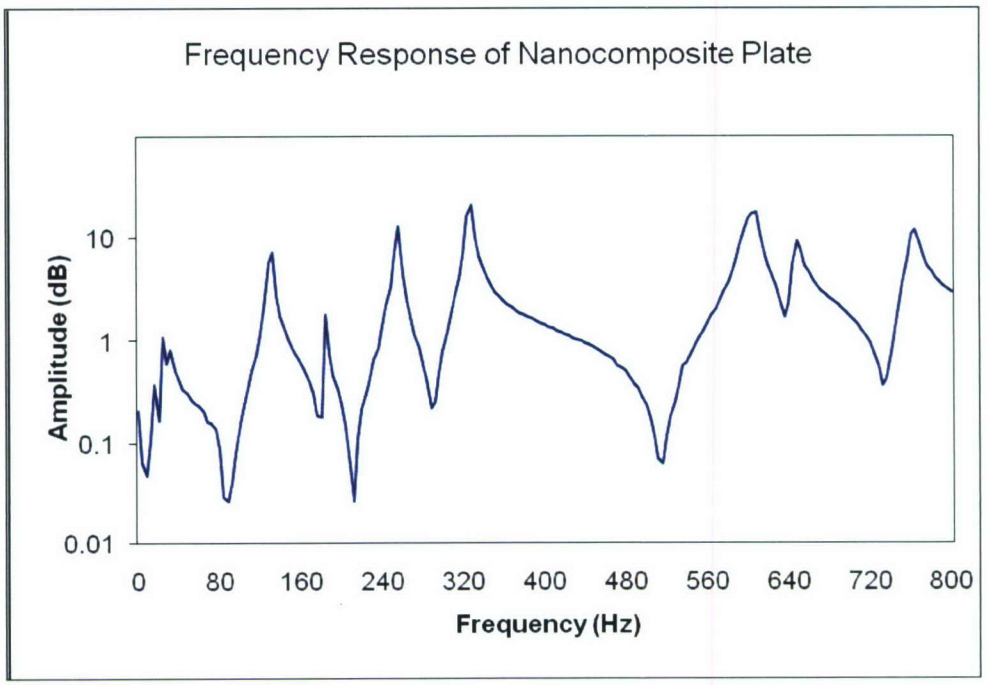

Figure 4: Typical frequency response of pure nylon 6,6 plates.

No significant variation was observed between different plates of each configuration indicating consistency in manufacturing process. An important point to note is that the frequencies for nylon 6,6 and vinyl ester nanocomposites shifted upward with reinforcement which could be attributed to the plates becoming stiffer with reinforcement (Figures 5 and 6). Also, the shift is more prominent at higher frequencies than the lower.

In the observed span eight peaks are observed for all the nylon nanocomposites except the 10 wt. percent reinforced plates which showed seven. The numerical values of the resonant frequencies are listed in Table 1. Note that the initial frequencies of 1.25 wt. percent plates are higher than the corresponding frequencies of 0 and 2.5 wt. percent. The 1.25 wt. percent plates are manufactured in a different batch than the others. Table 2 lists the detailed nylon 6,6 nanocomposites results for each plate.

Table 1: Resonant frequencies for nylon 6,6/ MWCNT nanocomposite plates.

Plate	1	2	3	4	5	6	7	8
0 %	22.00	126.80	182.00	250.00	322.80	596.40	639.20	750.80
1.25%	28.00	135.60	190.40	261.60	337.20	621.60	666.00	782.40
2.50%	22.00	132.40	190.80	261.20	339.20	626.80	671.60	785.60
5.00%	22.00	134.00	193.50	261.50	341.00	628.00	678.00	791.50
10.00%	23.50	139.00	200.50	267.00	352.00	642.00	699.50	

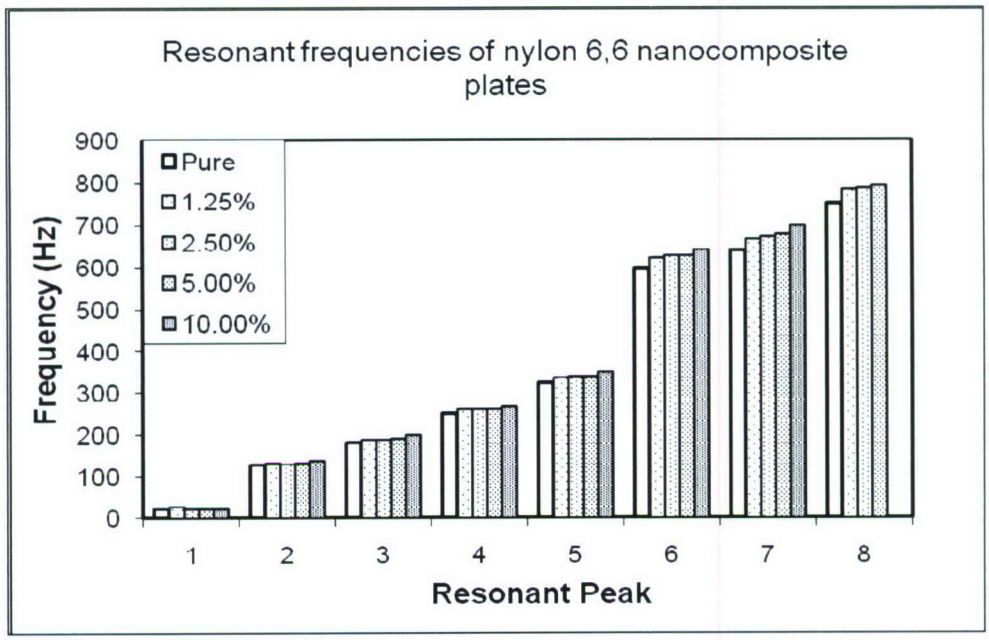

Figure 5: Resonant frequency shift for MWCNT reinforced nylon 6,6 nanocomposites.

Table 2: Resonant frequencies from Signature Analysis for Nylon6,6 nanocomposite plates.

Plate ID	1	2	3	4	5	6	7	8
NM00A	22	126	180	248	320	592	634	746
NM00B	22	126	182	250	322	600	638	750
NM00C	22	126	182	250	322	596	638	750
NM00D	22	128	182	252	324	602	642	754
NM00E	22	128	184	250	326	592	644	754
NM12A	28	136	190	262	336	620	666	782
NM12B	28	136	190	262	338	622	666	784
NM12C	28	136	192	262	338	624	670	786
NM12D	28	136	190	262	338	624	666	784
NM12E	28	134	190	260	336	618	662	776
NM25A	22	134	192	262	340	628	674	786
NM25B	22	132	190	262	340	626	672	786
NM25C	22	132	190	262	338	626	672	786
NM25D	22	132	192	260	338	628	672	784
NM25E	22	132	190	260	340	626	668	786
NM50A	22	134	194	262	342	628	678	792
NM50B	22	134	194	262	340	628	680	792
NM50C	22	134	194	260	342	628	678	792
NM50D	22	134	192	262	340	628	676	790
NM10A	22	138	200	266	352	638	698	
NM10B	22	138	200	266	350	640	696	
NM10C	22	138	200	268	352	648	698	
NM10D	28	142	202	268	354	642	706	

The resonant frequencies for vinyl ester nanocomposite plates reinforced with nanoclay and graphite platelets over the chosen span of 800 Hz are shown in Figure 6. The shift in the resonant frequency is observed more for graphite platelets reinforced plates as compared to nanoclay ones. Note these plates are 10 inch square which is shorter then the 11.5 inch sqaure nylon 6,6 composite plates. The values of the observed resonances are listed in Table 3. The values are an average data for two plates from each configuration. Table 4 lists the data from signature analysis of nanocomposites plates.

Table 3: Vinyl ester nanocomposite plates signature analysis results.

Plate ID	1	2	3	5	6	7
Pure Vinyl ester	24.00	160.00	234.00	310.00	412.00	750.00
VE+1.25%Clay	22.00	175.00	255.00	337.00	449.00	
VE+2.5%Clay	24.00	175.00	256.00	339.00	453.00	
VE+1.25%Graphite	22.00	178.00	261.00	339.00	460.00	
VE+2.5%Graphite	22.00	195.00	285.00	366.00	500.00	

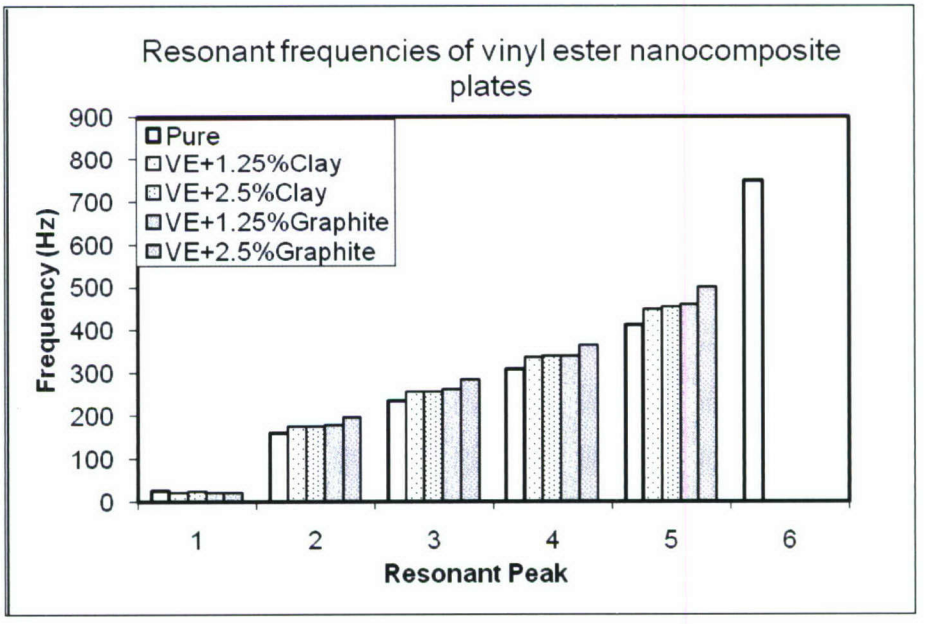

Figure 6: Resonant Frequency of vinyl ester reinforced with Graphite platelets and nano clay (Note: These plates are 10"x10"x0.4").

Table 4: Resonant frequencies for each vinyl ester nanocomposite plates.

Plate ID	1	2	3	4	5	6
VC00A	24	160	234	310	412	750
VC12A	22	176	256	338	450	
VC12B	22	174	254	336	448	
VC25A	24	176	256	340	454	
VC25B	24	174	256	338	452	
VG12A	22	178	260	338	458	
VG12B	22	178	262	340	462	
VG25A	22	194	284	364	498	
VG25B	22	196	286	368	502	

Among Eco-Core foams, OM12 showed the highest frequencies. Over the chosen span of 800 Hz OM16 and OM21 recorded 6 resonant frequenices while all the others showed only 5 resonances. Figure 7 shows the frequency pattern of Eco-Core foam plates signature analysis. Table 5 lists the results for each plate.

Table 5: Eco-Core foam signature analysis results.

Peak No.	1	2	3	4	5	6
OM11	34	214	302	352	522	
OM12	34	220	312	364	534	
OM21	28	180	256	290	446	760
OM18	30	204	290	340	504	
OM16	32	194	272	308	464	786
OM19	30	206	296	348	510	

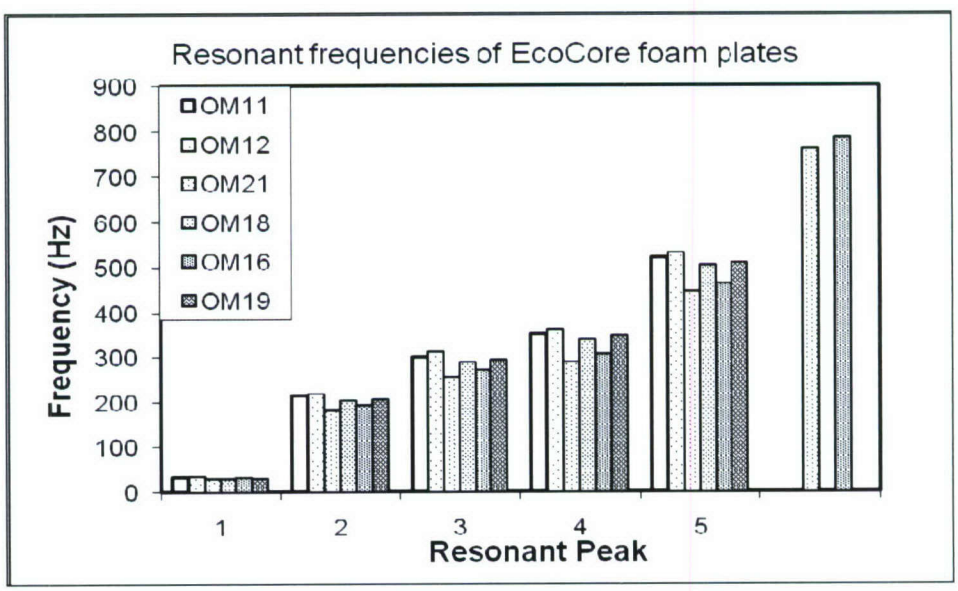

Figure 7: Resonant Frequency of Eco-Core foam plates.

1.0 DYNAMIC PROPERTY MEASUREMENTS

Long samples 254 mm x 25.4 mm x 9.5 mm (10"x1"x3/8") are cut from different plates of each configuration for flexural and extensional dynamic property characterization. Same samples are used for both the measurements as the experimentation technique involved is a non destructive technique and three specimens of each configuration are tested. Samples of 1"x1"x3/8" are cut for density measurements, with two samples from each configuration.

The experimental procedure used for measuring the dynamic storage modulus, dynamic loss modulus and damping of the nanocomposites used for this research is a non-destructive vibration response technique applied for the study of traditional composites dynamic properties in the past [1.1, 1.3]. This technique has an advantage of determining the dynamic properties without destroying the specimens being tested.

1.1 Density measurement

Densities of different materials are calculated based on the mass-volume relation: $D = M / V$ where D is density of material, M is the mass of the sample and V is the volume of the sample. A 1"x1"x3/8" sample was used for density measurements. The dimensions for each specimen are measured using vernier calipers with a least count of 0.01 mm. Dimensions of the prepared samples are taken along both ends and averaged. The wt of the specimen is measured using OHAUS precision scale. The density obtained is averaged for two samples from each configuration of nanocomposites. The density measured experimentally is entered as input for the modulus and damping computations.

Volume and density calculations for nylon 6,6 and vinyl ester nanocomposites are listed in Tables 1.1.1 and 1.1.3 with the averaged density values. For nanocomposites the addition of reinforcements showed a consistent increase in densities. Experimentally calculated densities compared with the theoretical prediction as per the rule of mixtures [1.5], are within 5% variation as shown in Figures 1.1.1 and 1.1.3.

$$\rho_c = \frac{1}{\frac{w_f}{\rho_f} + \frac{w_m}{\rho_m}}$$

Where

w_f weight fraction of fiber

ρ_f density of fiber

w_m weight fraction of matrix or polymer

ρ_m density of polymer

For Eco-Core foams the measured densities were similar to those supplied by the manufacturer. Thus these manufacturer supplied densities listed in Table 1.1.4 are used in dynamic measurements. For nanocomposites the experimentally measured densities are used. The densities for nylon 6,6 nanocomposites after 45 and 90 days aging are listed in Table 1.1.2. The variation of density with aging is shown in Figure 1.1.2. A consistent increase in density with aging is observed.

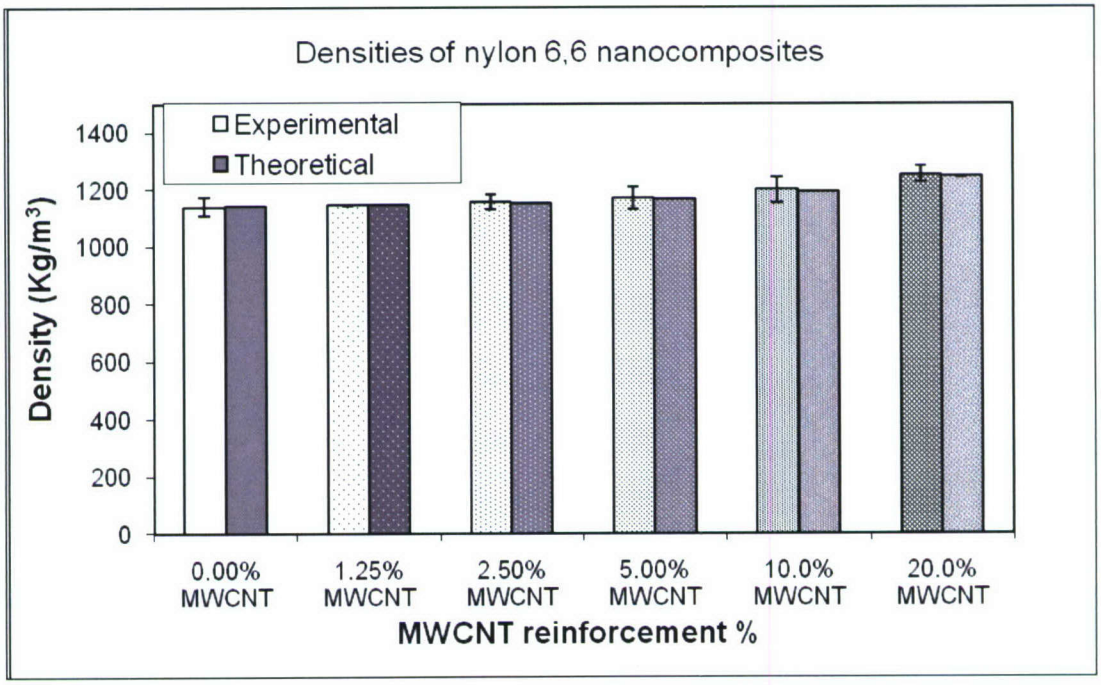

Figure 1.1.1: Densities of nylon 6,6 nanocomposites and theoretical predictions.

Table 1.1.1: Experimental density calculations for nylon 6,6/MWCNT nanocomposites.

Sample	Length	Width	Thick	Volume	Wt	Density	Avg density	Nano
	mm	mm	Mm	mm^3	g	kg/m^3	Kg/m^3	%
NM00CE01	25.44	25.39	10.05	6491.86	7.38	1172.89	**1139.34**	0.0%
NM00AE02	25.51	25.58	10.00	6525.74	7.45	1105.80		
NM12CE01	24.98	25.19	9.86	6204.37	7.12	1147.58	**1144.61**	1.25%
NM12CE01	25.05	25.10	9.92	6236.60	7.12	1141.65		
NM25CE01	25.54	25.54	9.96	6494.07	7.53	1180.48	**1153.77**	2.5%
NM25AE02	25.38	25.71	9.96	6497.81	7.32	1127.06		
NM50CE01	25.66	25.37	9.91	6449.83	7.60	1207.22	**1167.82**	5.0%
NM50AE02	25.56	25.43	9.91	6445.05	7.51	1128.42		
NM10CE01	25.36	25.59	9.80	6355.66	7.60	1241.89	**1197.14**	10.0%
NM10AE02	25.68	25.20	9.84	6367.48	7.57	1152.40		
NM20JE01	25.28	25.18	9.77	6216.07	7.86	1281.18	**1251.59**	20.0%
NM20JE02	25.40	25.02	9.85	6256.81	7.84	1222.00		

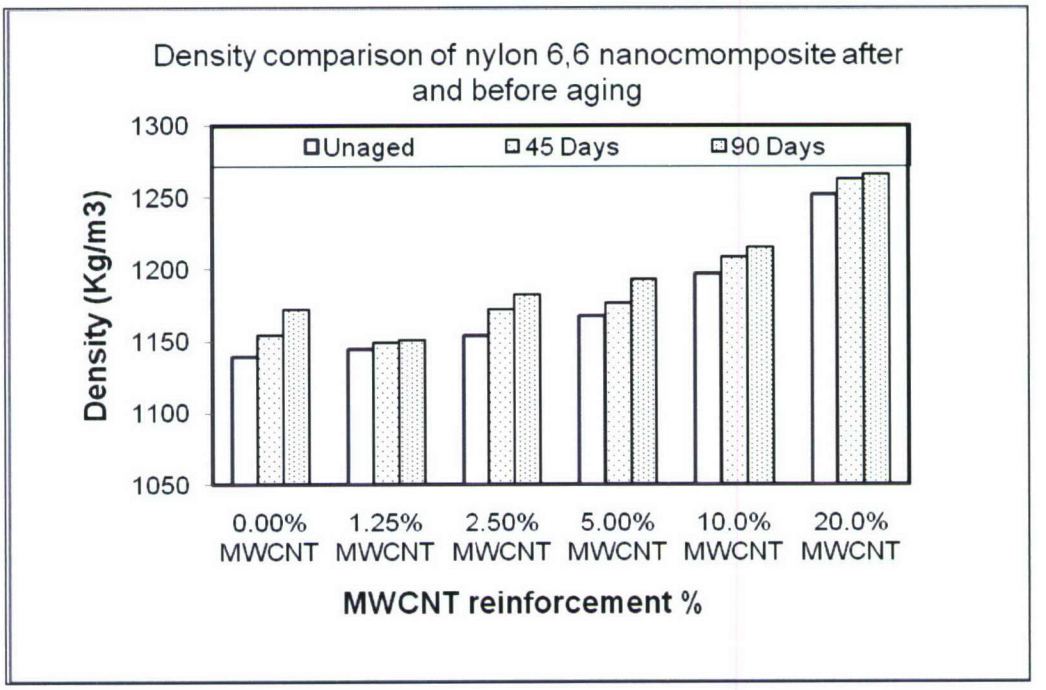

Figure 1.1.2: Density variations of nylon 6,6 nanocomposites with 45 and 90 days aging.

Table 1.1.2: Densities of nylon 6,6 nanocomposite configurations with environmental aging.

Configuration	Unaged	45 Days	90 Days
0.00% MWCNT	1139.34	1153.98	1171.95
1.25% MWCNT	1144.61	1149.25	1150.26
2.50% MWCNT	1153.77	1172.26	1182.30
5.00% MWCNT	1167.82	1176.29	1192.64
10.0% MWCNT	1197.14	1208.26	1215.19
20.0% MWCNT	1251.59	1261.91	1265.44

Table 1.1.3: Experimental density calculations for vinyl ester nanocomposites.

Sample	Length	Width	Thick	Volume	Wt	Density	Avg density	Nano %
	mm	mm	mm	mm^3	g	kg/m^3	kg/m^3	
VC00AE01	25.40	25.64	10.17	6623.27	7.35	1109.72	**1112.44**	0.00%
VC00AE02	25.63	25.54	10.11	6617.91	7.38	1115.16		
VC12AE01	25.66	25.78	10.14	6707.76	7.48	1115.13	**1132.99**	1.25% Clay
VC12BE02	25.60	24.84	10.18	6473.50	7.45	1150.85		
VC25AE01	25.46	25.72	10.17	6659.63	7.62	1144.21	**1139.65**	2.5% Clay
VC25BE02	25.55	25.59	10.20	6669.01	7.57	1135.10		
VG12AE01	25.37	25.55	10.26	6650.57	7.38	1109.68	**1117.29**	1.25% Graphite
VG12BE02	25.71	25.49	10.16	6658.33	7.49	1124.91		
VG25AE01	25.64	25.23	10.13	6553.07	7.46	1138.40	**1133.58**	2.5% Graphite
VG25BE02	25.65	25.68	10.02	6600.09	7.45	1128.77		

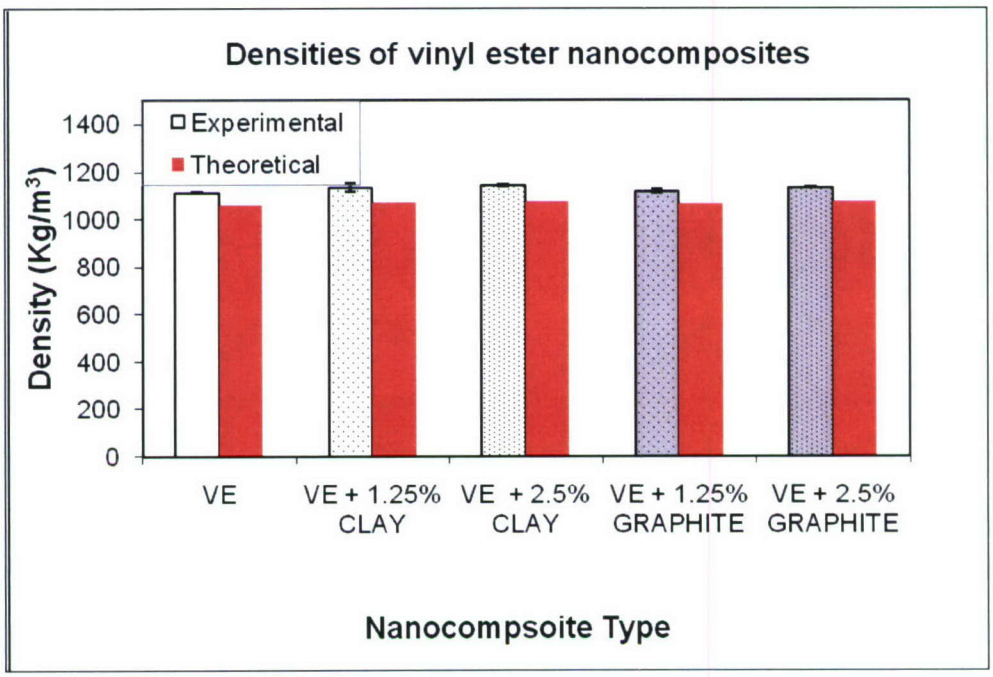

Figure 1.1.3: Densities of vinyl ester nanocomposites with theoretical predictions.

Table 1.1.4: Eco-Core foam densities provided by the supplier(NCAT University).

Foam ID	Density (Kg/m^3)
OM11	490
OM12	500
OM16	460
OM21	490
OM18	530
OM19	530

The densities of nylon 6,6 reinforced with MWCNT and vinyl ester reinforced with Cloisite nanoclay and graphite platelets are shown in Figure 1.1.4. As can be observed, the densities of vinyl ester reinforced with graphite platelets and nanoclay is lower than their counterpart nylon 6,6 reinforced with MWCNT.

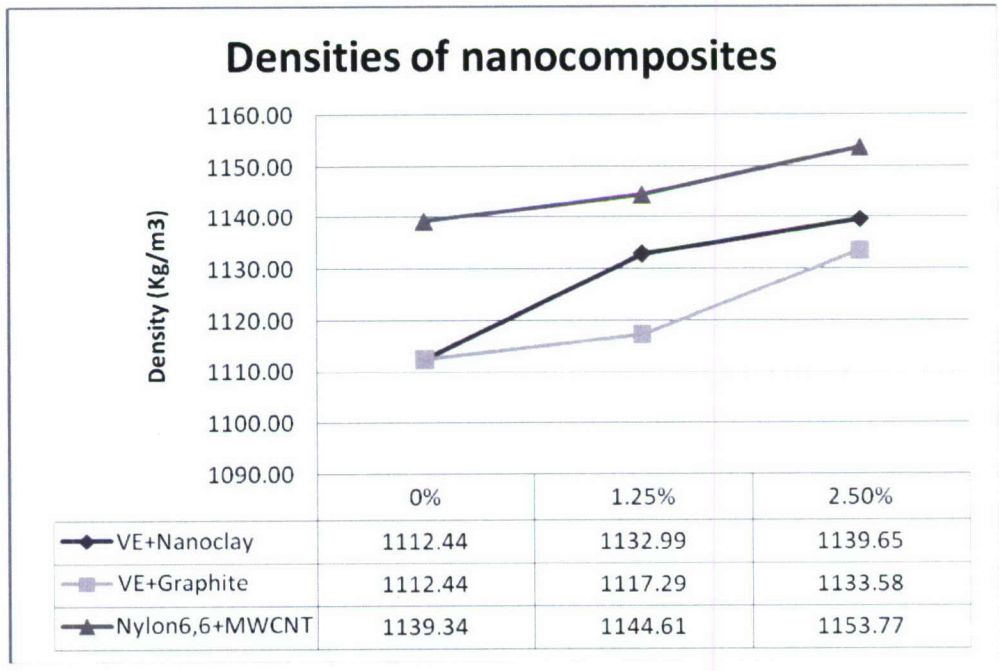

Figure 1.1.4: Comparison of densities of nanocomposites.

The experimental and theoretical densities of nylon 6,6 and vinyl ester nanocomposites along with their wt and corresponding volume fractions are listed in Tables 1.1.5 and 1.1.6.

Table 1.1.5: Comparison of theoretical and experimental densities of nylon 6,6 nanocomposites along with their corresponding wt and volume fractions.

Reinforcement wt. percent	Experimental Kg/m^3	Theoretical Kg/m^3	WT FRAC	VOL FRAC
0.0	1139.34	1140.00	0.000	0.000
1.25	1144.61	1145.94	0.0125	0.007
2.5	1153.77	1151.95	0.025	0.015
5.0	1167.82	1164.16	0.050	0.030
10.0	1197.14	1189.36	0.100	0.061
20.0	1251.59	1243.20	0.200	0.128

Table 1.1.6: Comparison of theoretical and experimental densities of vinyl ester nanocomposites along with their corresponding wt and volume fractions.

Reinforcement wt. percent	Experimental Kg/m^3	Theoretical Kg/m^3	WT FRAC	VOL FRAC
0	1112.44	1050.00	0	0.000
0.0125 clay	1132.99	1057.18	0.0125	0.006
0.025 clay	1139.65	1064.46	0.025	0.012
0.0125 graphite	1117.29	1055.90	0.0125	0.007
0.025 graphite	1133.58	1061.88	0.025	0.014

The volume fractions for all the configurations of nanocomposites under study are back calculated using the rule of mixtures of the densities [1.5]:

$$\rho_c = v_f . \rho_f + v_m . \rho_m$$

$$v_m = 1 - v_f .$$

Rearranging

$$v_f . = \frac{\rho_c - \rho_m}{\rho_f - \rho_m}$$

where

ρ_c density of composite

ρ_m density of polymer

ρ_f density of fiber

v_f volume fraction of fiber

v_m volume fraction of polymer

1.2 Dynamic Flexural Property Measurements:

Non-destructive vibration response technique has been used to measure the dynamic flexural modulus and damping of the nanocomposites under study. The sample is clamped at one end in a vise. The accelerometer is placed at the free-end and the specimen is excited by impacting with a hammer with a load cell. The hammer and accelerometer are connected to the spectrum analyzer via an amplifier. The experimental setup for dynamic flexural measurements is shown in Figure 1.2.1. Note that the resonant frequencies obtained by this setup are of flexural mode. The spectrum analyzer is hooked to a computer with in-house developed software "ICARUS" which calculates the dynamic modulus & loss factor based on the specimen dimensions and curve fitting the resonant peak data obtained from the spectrum analyzer [1.1, 1.2]. The specimens are first tapped and a frequency response function is obtained on a broad span of 1600 Hz. The first fundamental peak is then zoomed with 50 Hz span for the final calculations. Loss factor is calculated based on the 3 dB half-power bandwidth of the frequency peak and the dynamic modulus is calculated from the resonant frequency. The frequency spectrum is averaged three times on the analyzer before feeding it to "ICARUS". The software has provision for averaging the modulus and loss factor for two tests. Three samples from each configuration of nanocomposites are tested.

The storage modulus is computed using the natural frequency formulae:

$$f_n = \frac{\lambda_n^{\,2}}{2\pi L^2}\left(\frac{EI}{\rho A}\right)^{1/2}$$

where L is the length of beam, n the mode number, λ_n is the eigenvalue for nth mode and f_n is the nth mode frequency, E is the effective Young's modulus of beam material, I is the moment of inertia of beam cross-section about its neutral axis, A is the cross-sectional area of beam, ρ is mass density of beam material. The eigenvalues depend on the boundary conditions [1.2], which is a cantilever configuration in this case.

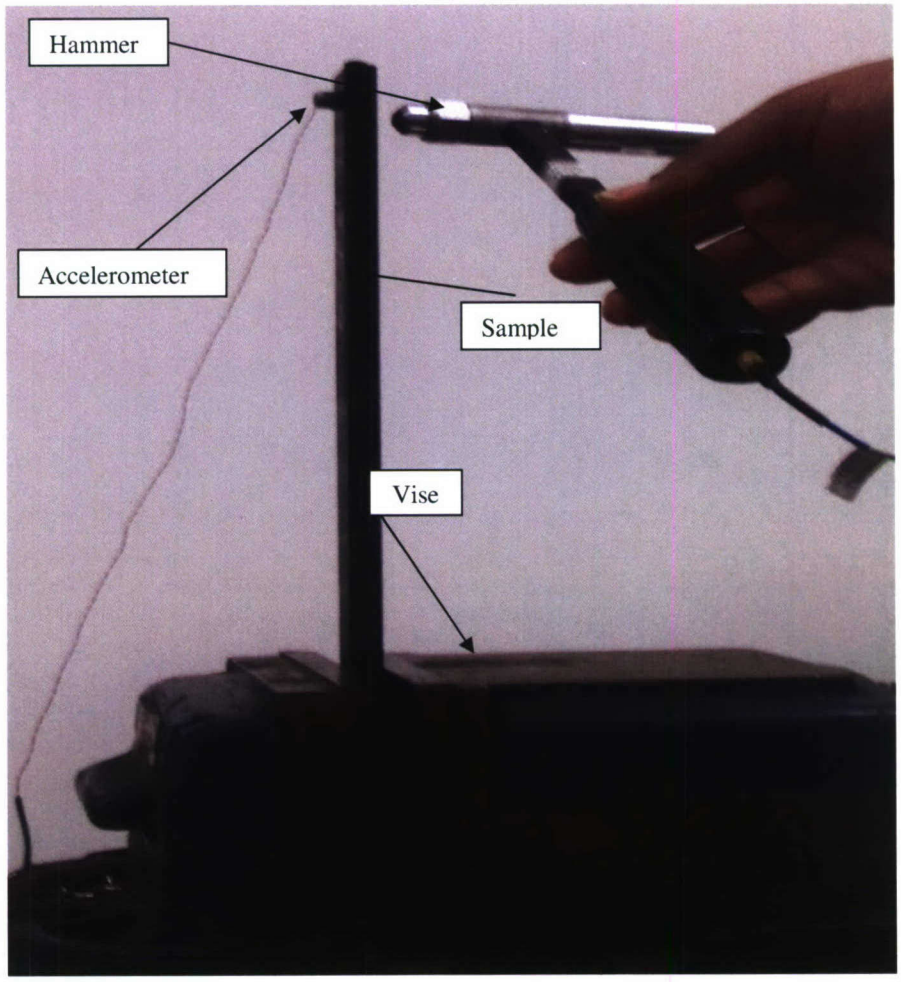

Figure 1.2.1: Experimental setup for dynamic flexural measurements

The nylon 6,6 showed a slight increase in resonant frequencies with increase in MWCNT reinforcement till 2.5 wt. percent after which it slightly dropped. The flexural dynamic modulus also follows the trend of the resonant frequency. The 20 wt. percent reinforced composites had the highest modulus but these plates had cracked during the extrusion process suggesting the increase in brittle nature at higher reinforcements, thus not practical. Also not much change in the resonant frequency is observed between 2.5 and 10 wt. percent composites. Thus the primary range of interest could be from 0 to 2.5 wt. percent loadings. Figure 1.2.2 shows the variation of resonant frequency with increase in reinforcements and Figure 1.2.3 shows the flexural dynamic modulus.

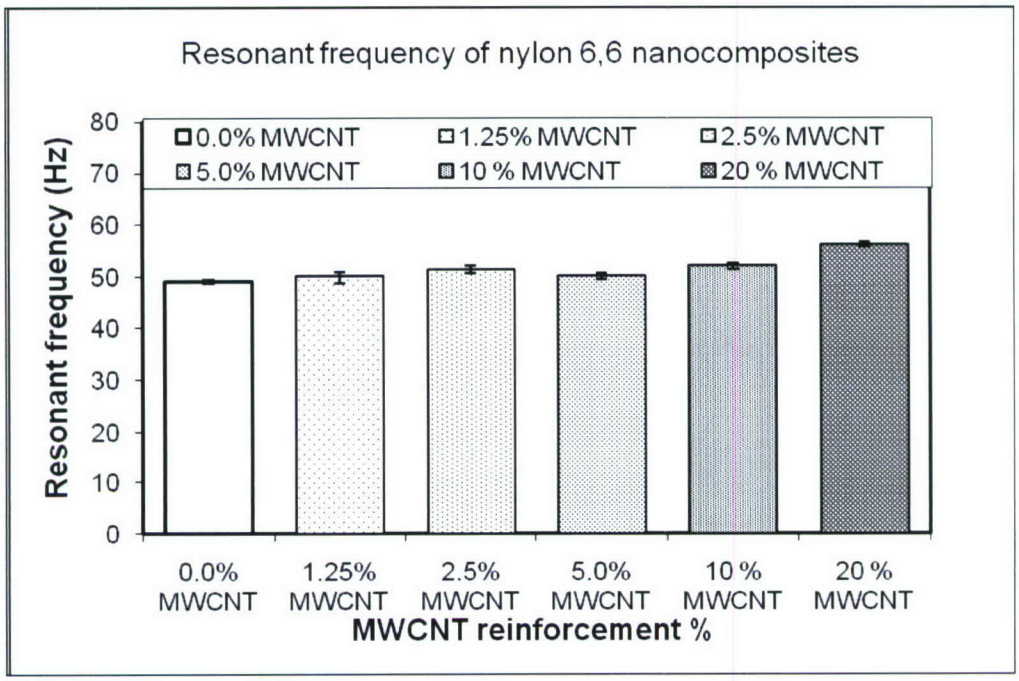

Figure 1.2.2: Resonant frequency of nylon 6,6/MWCNT nanocomposites.

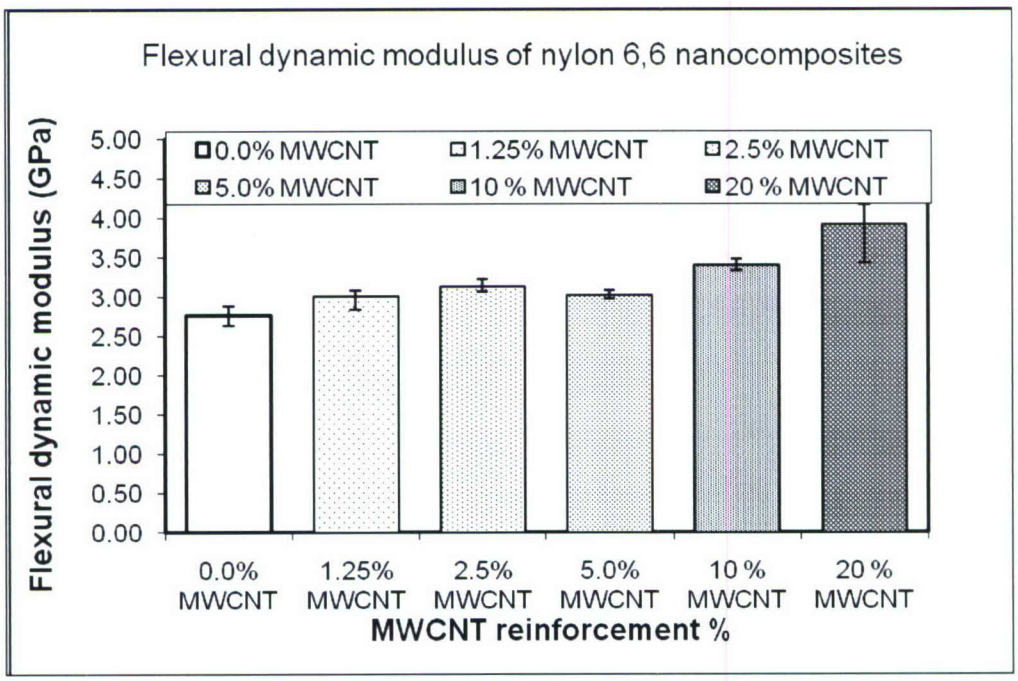

Figure 1.2.3: Flexural dynamic modulus of nylon 6,6/ MWCNT nanocomposites.

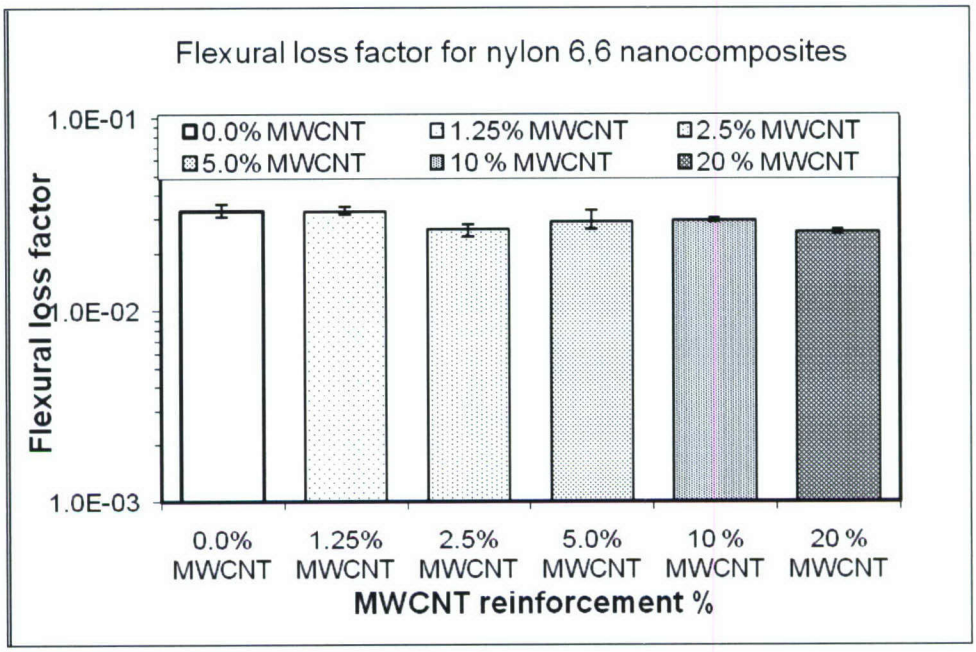

Figure 1.2.4: Loss factor (damping) for nylon 6,6 nanocomposites in flexural mode.

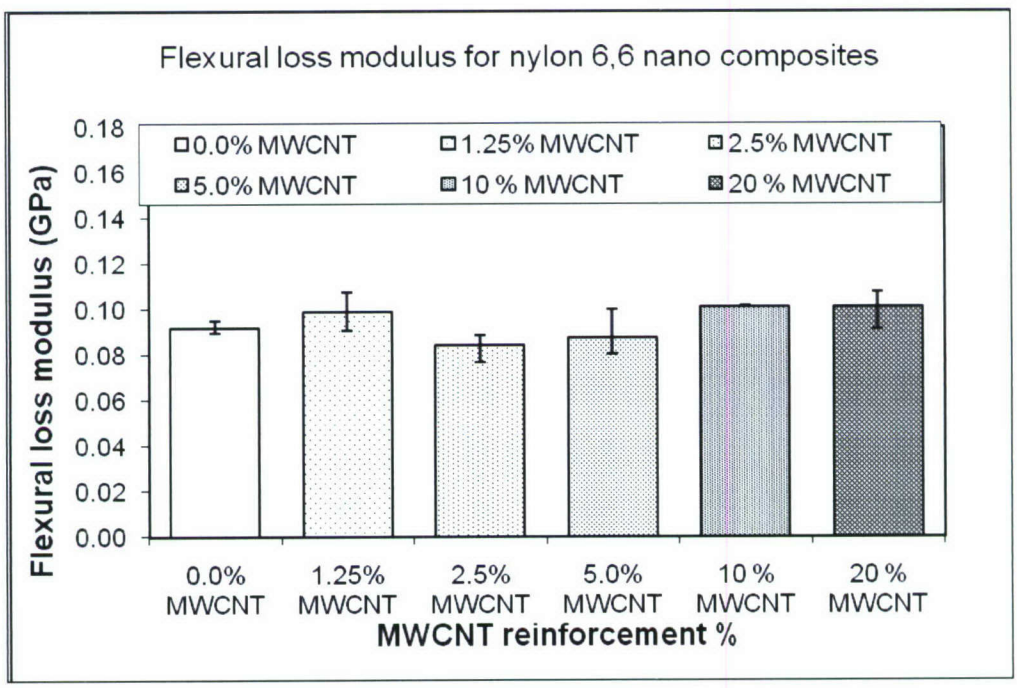

Figure 1.2.5: Flexural loss modulus of nylon 6,6 nanocomposites

For nylon 6,6 the damping first decreased till 2.5 wt. percent addition of MWCNT but then again increased with further additions of MWCNT as shown in Figure 1.2.4. The 20 wt. percent nanocomposite showed an abruptly low damping. The flexural loss modulus followed the trend of loss factor as shown in Figure 1.2.5. Table 1.2.1 lists the detailed results for nylon 6,6 nanocomposites flexural test results. All the data have been averaged for three samples from each configuration of composites.

Table 1.2.1: Flexural dynamic properties of nylon 6,6/MWCNT nanocomposites.

Sample ID	Resonant frequency (Hz)	Flexural loss factor	Flexural dynamic modulus (GPa)	Loss modulus (GPa)
NM00AD01	48.56	3.60E-02	2.64	0.10
NM00AD02	48.75	3.27E-02	2.76	0.09
NM00CD03	49.38	3.10E-02	2.88	0.09
0 % Average	**48.90**	**3.32E-02**	**2.76**	**0.09**
NM12AD01	48.63	3.19E-02	2.83	0.09
NM12AD02	50.75	3.48E-02	3.09	0.11
NM12AD03	50.75	3.23E-02	3.09	0.10
1.25 % Average	**50.04**	**3.30E-02**	**3.00**	**0.10**
NM25AD01	51.88	2.75E-02	3.22	0.09
NM25AD02	51.12	2.45E-02	3.13	0.08
NM25CD03	50.62	2.83E-02	3.07	0.09
2.5% Average	**51.21**	**2.68E-02**	**3.14**	**0.08**
NM50AD01	49.31	3.33E-02	3.00	0.10
NM50AD02	50.50	2.67E-02	3.08	0.08
NM50CD03	50.00	2.70E-02	2.98	0.08
5.0% Average	**49.94**	**2.90E-02**	**3.02**	**0.09**
NM10AD01	52.44	2.92E-02	3.47	0.10
NM10AD02	51.31	3.03E-02	3.33	0.10
NM10CD03	51.88	2.97E-02	3.40	0.10
10 % Average	**51.88**	**2.97E-02**	**3.40**	**0.10**
NM20JD01	56.37	2.51E-02	4.15	0.10
NM20JD02	56.50	2.59E-02	4.16	0.11
NM20JD03	55.56	2.65E-02	3.43	0.09
20 % Average	**56.14**	**2.58E-02**	**3.91**	**0.10**

A drop in resonant frequency and flexural dynamic modulus is observed after subjecting the nylon 6,6 nanocomposites to environmental aging for all the configurations. A further drop is observed after 90 days aging for pure nylon 6,6 and 1.25 wt. percent

nanocomposites while for all the other configurations a marginal increase is observed after 90 days aging as compared to 45 days aging as shown in Figures 1.2.6 and 1.2.7. The numerical values of these results are listed in Tables 1.2.2 and 1.2.3 for 45 days and 90 days aging respectively.

Loss factor consistently increased with aging for all the configurations as shown in Figure 1.2.8. Loss modulus (Figure 1.2.9) increased for 90 days aging as compared to non aged samples for all the configuration. For 45 days aging the loss modulus decreased for pure nylon 6,6 and 2.5 wt. percent while a slight increase is observed for all the other configurations.

Table 1.2.2: Nylon 6,6 nanocomposites 45 days environmental aging results for dynamic flexural tests.

Sample ID	Resonant Frequency (Hz)	Flexural loss factor	Flexural dynamic modulus (GPa)	Loss modulus (GPa)
NM00AD01	41.38	3.39E-02	1.93	0.07
NM00AD02	40.31	3.42E-02	1.83	0.06
NM00CD03	37.44	4.34E-02	1.58	0.07
0 % Average	**39.71**	**3.72E-02**	**1.78**	**0.07**
NM12AD01	42.31	5.57E-02	2.07	0.12
NM12AD02	41.19	5.97E-02	1.93	0.12
NM12AD03	38.44	6.05E-02	1.67	0.10
1.25 % Average	**40.65**	**5.86E-02**	**1.89**	**0.11**
NM25AD01	44.69	3.29E-02	2.34	0.08
NM25AD02	42.31	3.66E-02	2.13	0.08
NM25CD03	42.63	3.93E-02	2.12	0.08
2.5% Average	**43.21**	**3.63E-02**	**2.20**	**0.08**
NM50AD01	43.00	4.65E-02	2.26	0.11
NM50AD02	44.63	3.77E-02	2.43	0.09
NM50CD03	43.44	3.77E-02	2.35	0.09
5.0% Average	**43.69**	**4.06E-02**	**2.35**	**0.09**
NM10AD01	43.63	4.23E-02	2.43	0.10
NM10AD02	41.69	4.88E-02	2.17	0.11
NM10CD03	44.94	3.97E-02	2.48	0.10
10 % Average	**43.42**	**4.36E-02**	**2.36**	**0.10**
NM20JD01	50.44	3.89E-02	3.39	0.13
NM20JD02	49.88	2.96E-02	3.38	0.10
NM20JD03	50.75	3.54E-02	3.32	0.12
20 % Average	**50.36**	**3.46E-02**	**3.36**	**0.12**

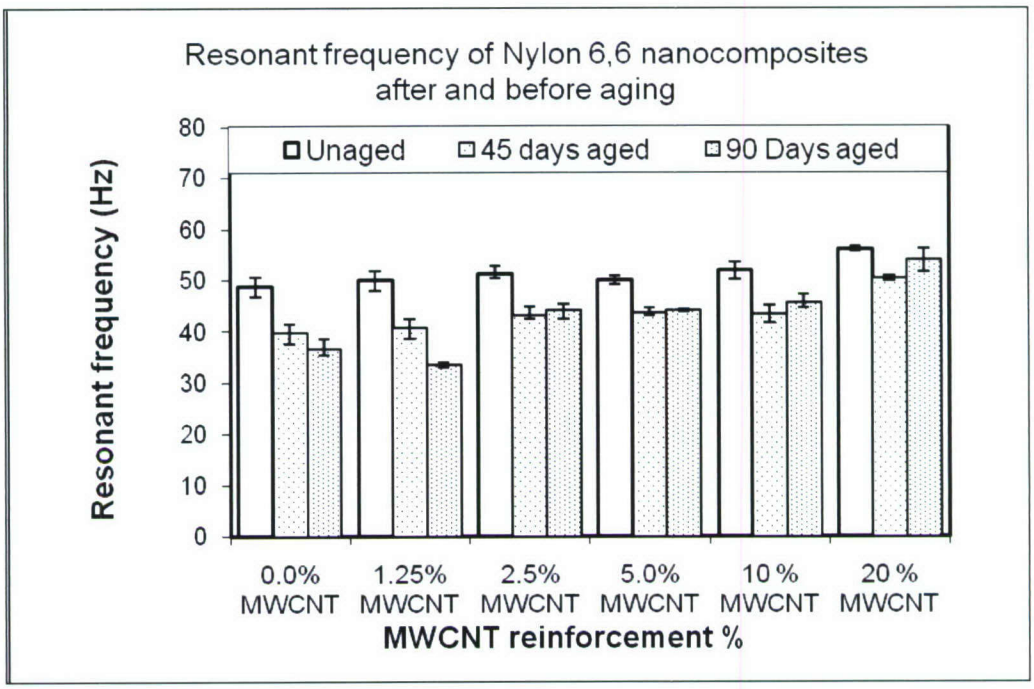

Figure 1.2.6: Resonant frequencies comparison for nylon 6,6 nanocomposites for 45 and 90 days environmental aging.

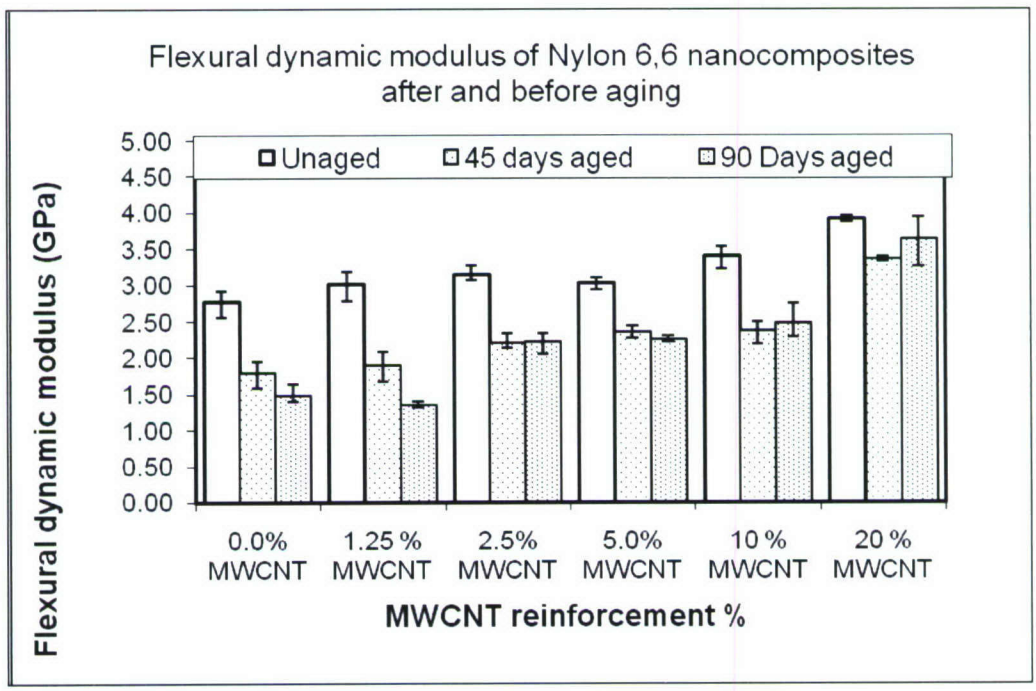

Figure 1.2.7: Flexural dynamic modulus comparison for nylon 6,6 nanocomposites for 45 and 90 days environmental aging.

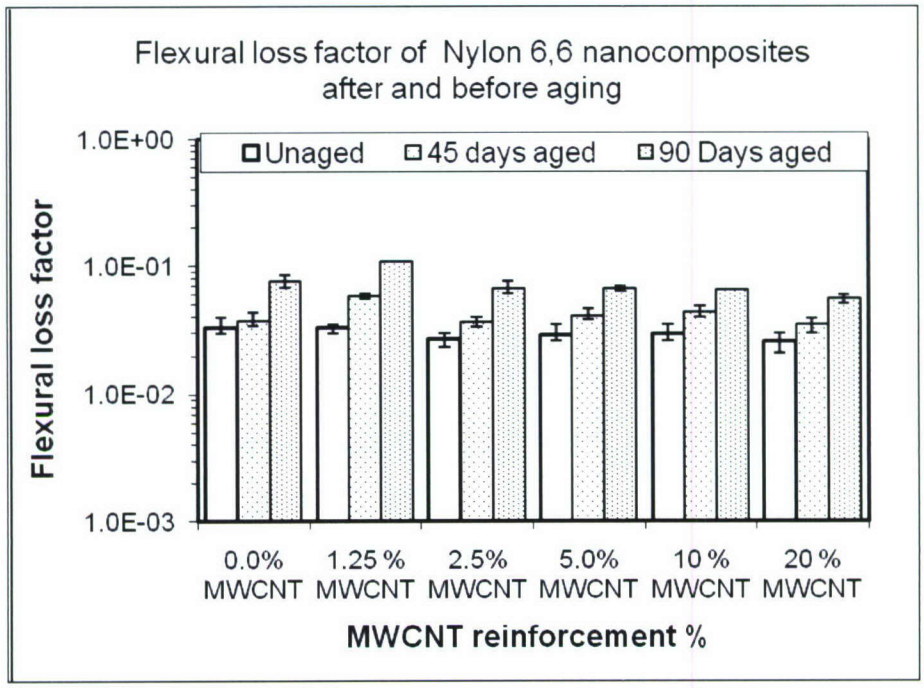

Figure 1.2.8: Flexural loss factor comparison for nylon 6,6 nanocomposites for 45 and 90 days environmental aging.

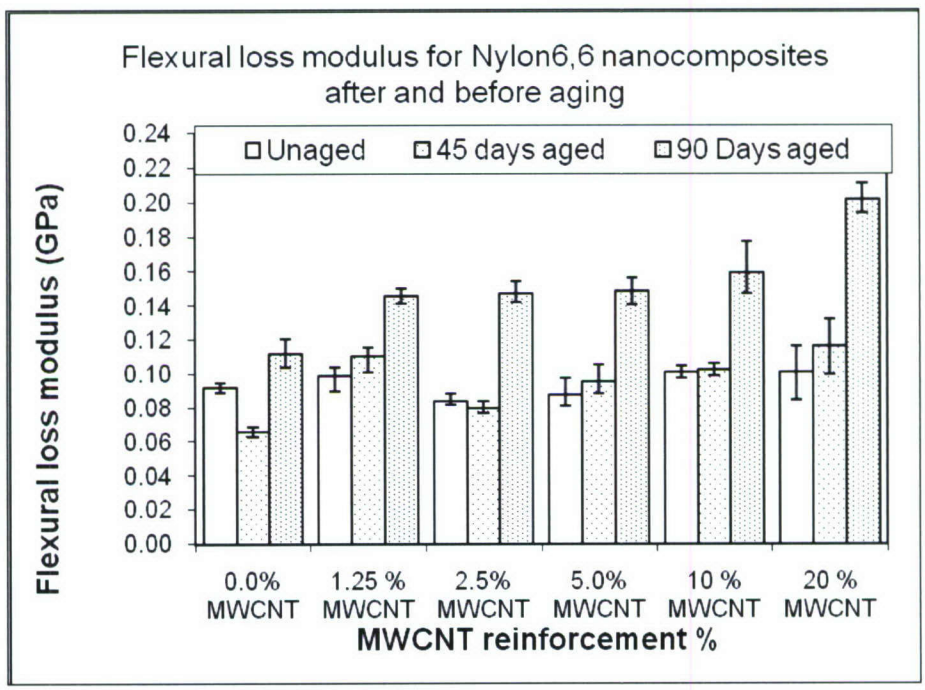

Figure 1.2.9: Flexural loss modulus comparison for nylon 6,6 nanocomposites for 45 and 90 days environmental aging.

Table 1.2.3: Nylon 6,6 nanocomposites 90 days environmental aging results for dynamic flexural tests.

Sample ID	Resonant frequency (Hz)	Flexural loss factor	Flexural dynamic modulus (GPa)	Loss modulus (GPa)
NM00AD01	35.50	7.43E-02	1.39	0.10
NM00AD02	38.50	6.74E-02	1.64	0.11
NM00CD03	35.75	8.53E-02	1.41	0.12
0 % Average	**36.58**	**7.57E-02**	**1.48**	**0.11**
NM12AD01	34.00	1.08E-01	1.39	0.15
NM12AD02	33.44	1.08E-01	1.35	0.15
NM12CD03	33.00	1.08E-01	1.31	0.14
1.25 %	**33.48**	**1.08E-01**	**1.35**	**0.15**
NM25AD01	45.37	6.35E-02	2.27	0.14
NM25AD02	44.75	6.09E-02	2.34	0.14
NM25CD03	42.38	7.53E-02	2.04	0.15
2.5% Average	**44.17**	**6.66E-02**	**2.22**	**0.15**
NM50AD01	44.38	6.91E-02	2.26	0.16
NM50AD02	43.88	6.35E-02	2.21	0.14
NM50CD03	44.25	6.48E-02	2.29	0.15
5.0% Average	**44.17**	**6.58E-02**	**2.26**	**0.15**
NM10AD01	47.19	6.46E-02	2.74	0.18
NM10AD02	44.56	6.47E-02	2.39	0.15
NM10CD03	45.00	6.45E-02	2.28	0.15
10 % Average	**45.58**	**6.46E-02**	**2.47**	**0.16**
NM20JD01	51.50	5.96E-02	3.25	0.19
NM20JD02	56.13	5.11E-02	3.93	0.20
NM20JD03	54.25	5.71E-02	3.70	0.21
20 % Average	**53.96**	**5.59E-02**	**3.63**	**0.20**

For vinyl ester nanocomposites the resonant frequencies for nanoclay reinforcements are lower while for graphite platelets reinforcements they are higher than the virgin polymer. 2.5 wt. percent composites showed higher frequency then their corresponding 1.25 wt. percent ones. The flexural dynamic modulus showed the same trends as the resonant frequencies. The 2.5 wt. percent graphite platelets reinforced composites showed a 33% increase in modulus with their virgin polymer. All the results are shown in Figures 1.2.10 and 1.2.11.

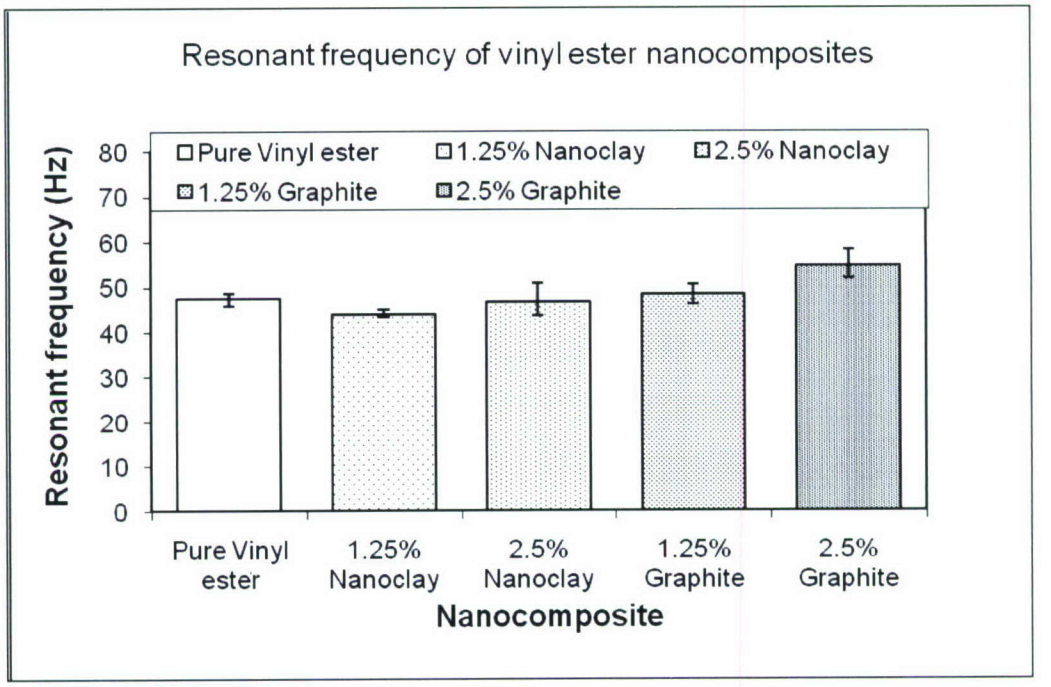

Figure 1.2.10: Resonant frequencies of vinyl ester nanocomposites.

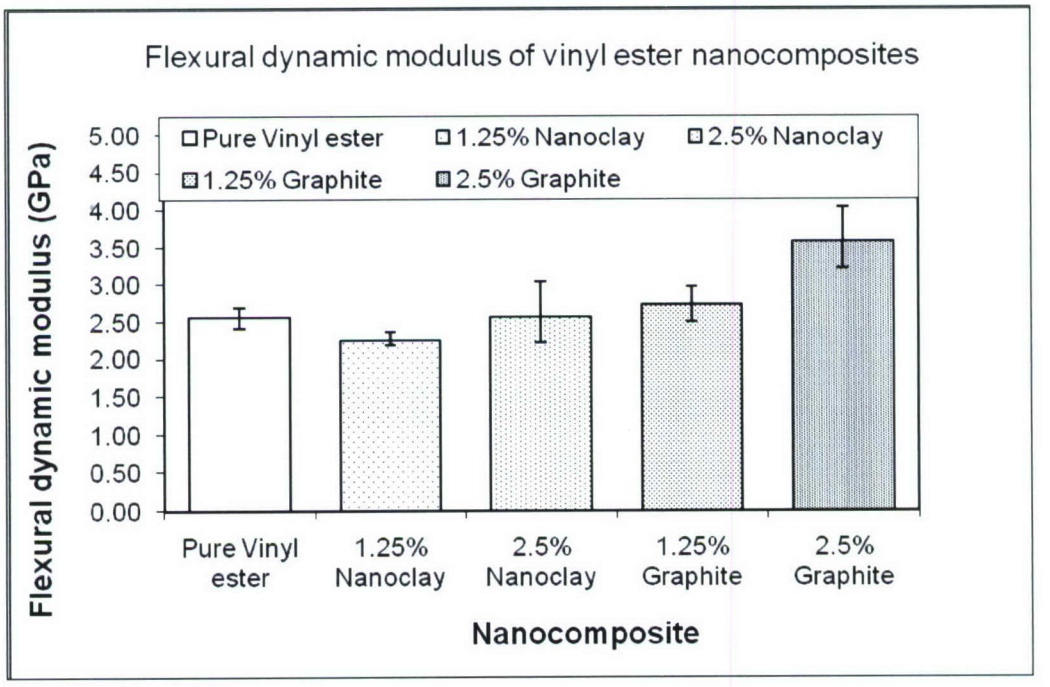

Figure 1.2.11: Flexural dynamic modulus of vinyl ester nanocomposites.

The loss factor did not show much variation with adding of different reinforcements to vinyl ester. The loss modulus observed is lower for nanoclay reinforcements and higher for graphite platelets reinforcements then the virgin polymer. The 2.5 wt. percent graphite platelets composites showed about 20% increase in loss modulus then the virgin polymer. Since both the loss modulus and flexural dynamic modulus are significantly high for graphite platelet nanocomposites, they show potential for dynamic applications. Figure 1.2.12 and Figure 1.2.13 shows the results for flexural loss factor and loss modulus of vinyl ester nanocomposites. Table 1.2.4 lists all the results of dynamic flexural test for vinyl ester nanocomposites with nanoclay and graphite reinforcements.

Table 1.2.4: Results of vinyl ester nanocomposites dynamic flexural tests.

Sample ID	Resonant frequency (Hz)	Flexural loss factor	Flexural dynamic modulus (GPa)	Loss modulus (GPa)
VC00AD01	48.50	3.88E-02	2.68	0.10
VC00AD02	47.69	4.66E-02	2.60	0.12
VC00AD03	45.94	5.04E-02	2.41	0.12
Pure Vinyl ester	**47.38**	**4.52E-02**	**2.56**	**0.12**
VC12AD01	45.06	3.83E-02	2.36	0.09
VC12AD02	43.44	4.01E-02	2.19	0.09
VC12AD03	43.31	4.00E-02	2.18	0.09
1.25% Nanoclay	**43.94**	**3.95E-02**	**2.24**	**0.09**
VC25AD01	45.44	3.67E-02	2.41	0.09
VC25AD02	50.88	4.14E-02	3.03	0.13
VC25CD03	43.56	3.80E-02	2.22	0.08
2.5% Nanoclay	**46.63**	**3.87E-02**	**2.55**	**0.10**
VG12AD01	46.12	4.15E-02	2.49	0.10
VG12BD02	48.25	4.19E-02	2.72	0.11
VG12BD03	50.38	4.42E-02	2.97	0.13
1.25% Graphite	**48.25**	**4.25E-02**	**2.73**	**0.12**
VG25AD01	53.75	3.77E-02	3.45	0.13
VG25BD02	58.25	3.96E-02	4.03	0.16
VG25BD03	52.00	4.40E-02	3.21	0.14
2.5% Graphite	**54.67**	**4.04E-02**	**3.56**	**0.14**

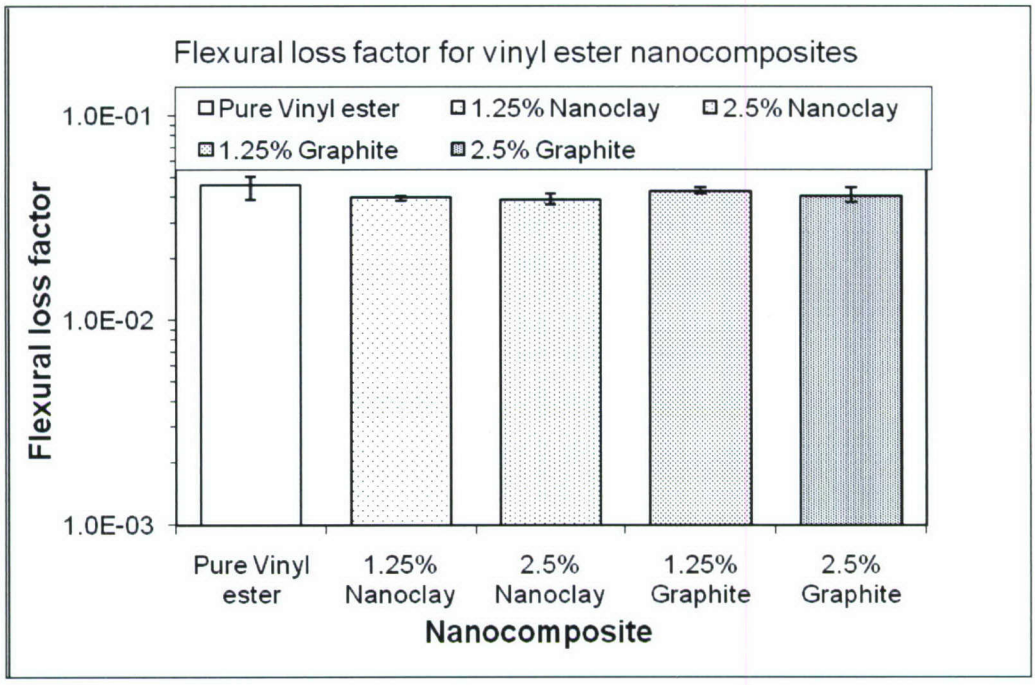

Figure 1.2.12: Flexural loss factor of vinyl ester nanocomposites.

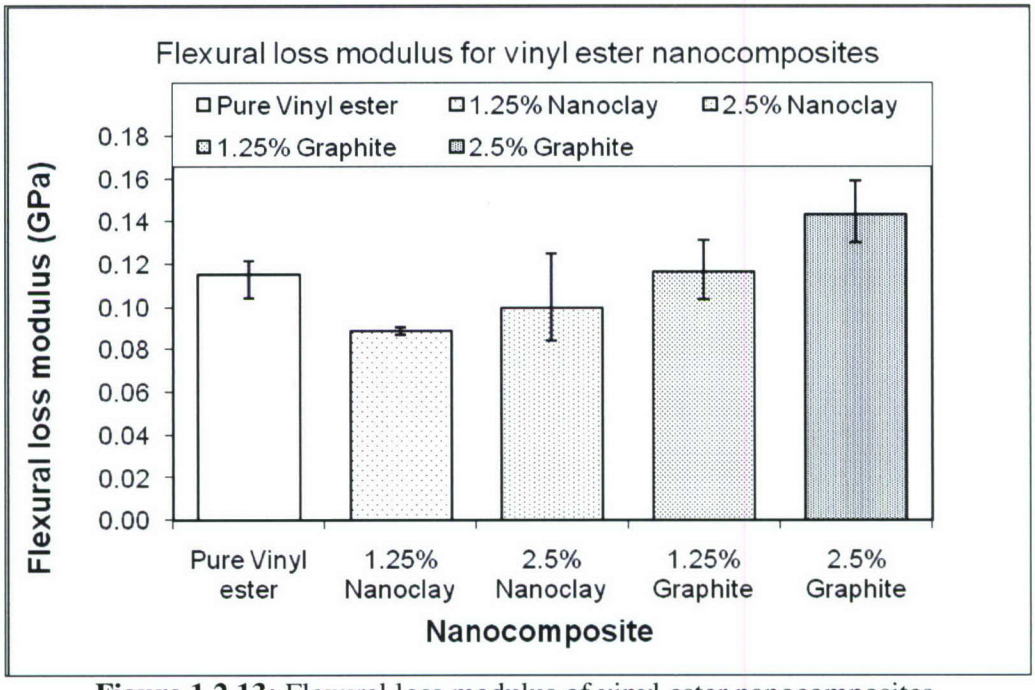

Figure 1.2.13: Flexural loss modulus of vinyl ester nanocomposites.

Vinyl ester with 2.5 wt. percent graphite platelets shows the highest flexural dynamic modulus, loss factor and loss modulus among the 0-2.5 wt. percent nanocomposite configurations under study. The comparison is shown in Figures 1.2.14-1.2.17.

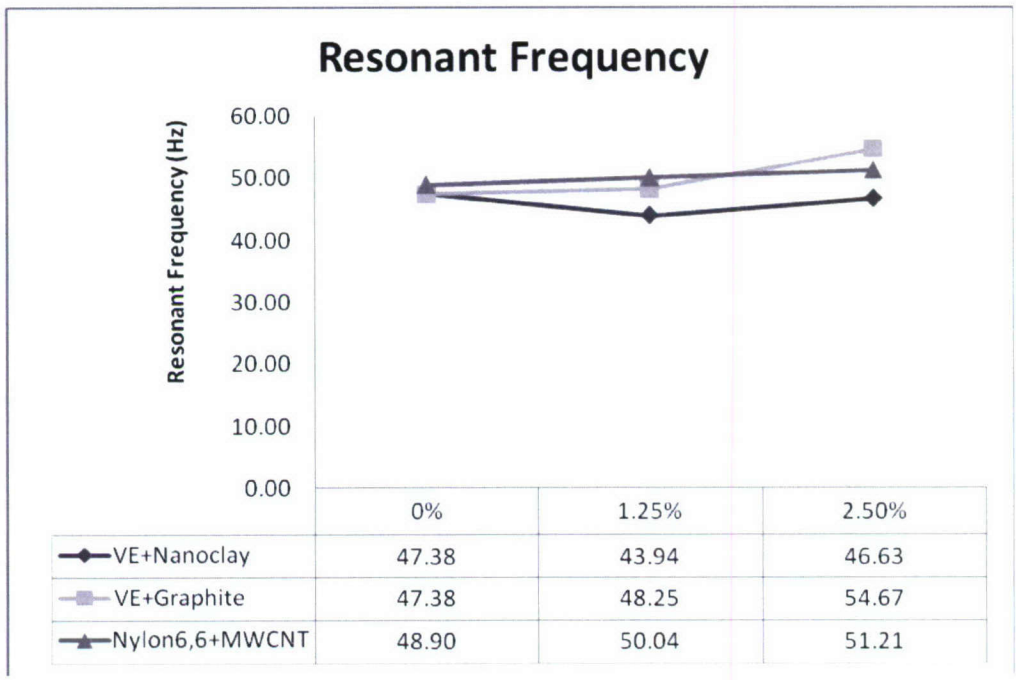

	0%	1.25%	2.50%
VE+Nanoclay	47.38	43.94	46.63
VE+Graphite	47.38	48.25	54.67
Nylon6,6+MWCNT	48.90	50.04	51.21

Figure 1.2.14: Resonant frequenices for nanocomposites in flexural mode.

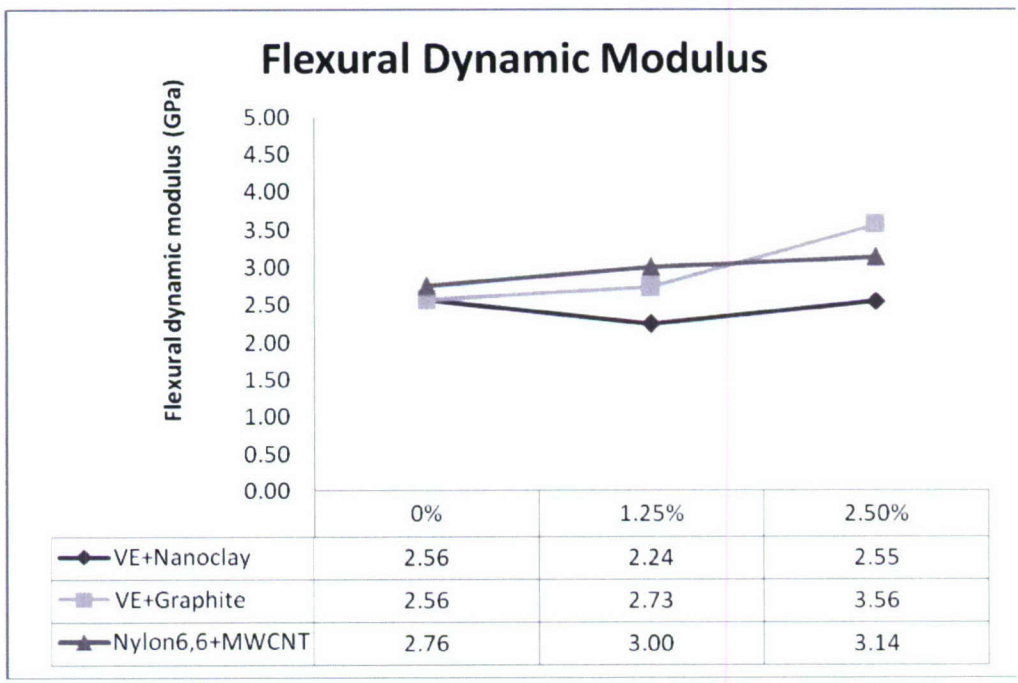

	0%	1.25%	2.50%
VE+Nanoclay	2.56	2.24	2.55
VE+Graphite	2.56	2.73	3.56
Nylon6,6+MWCNT	2.76	3.00	3.14

Figure 1.2.15: Flexural dynamic modulus for different nanocomposites.

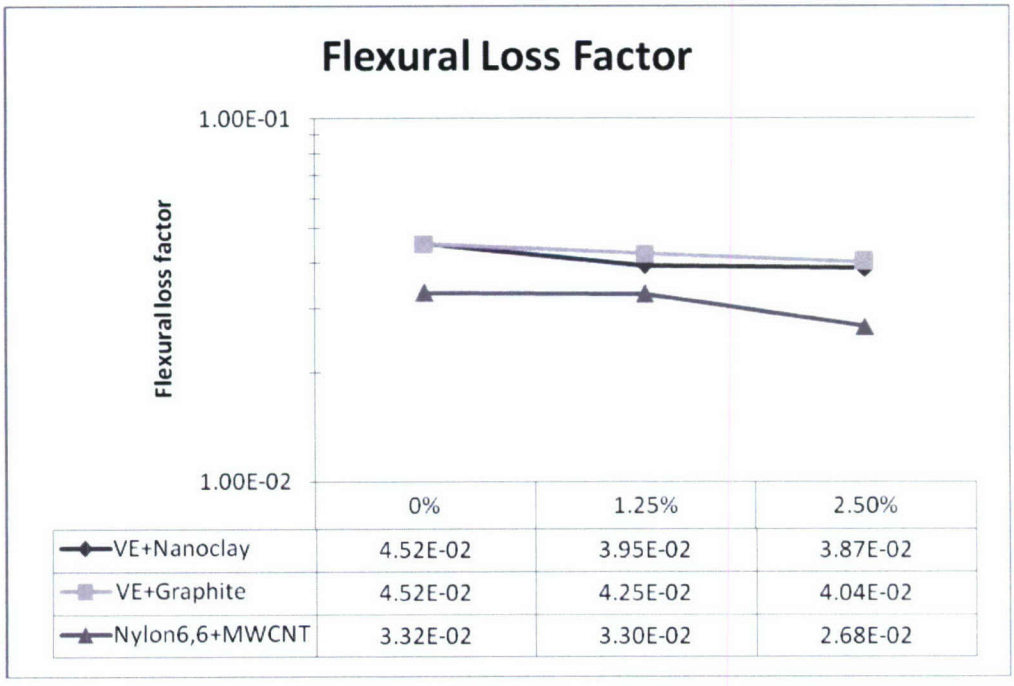

	0%	1.25%	2.50%
VE+Nanoclay	4.52E-02	3.95E-02	3.87E-02
VE+Graphite	4.52E-02	4.25E-02	4.04E-02
Nylon6,6+MWCNT	3.32E-02	3.30E-02	2.68E-02

Figure 1.2.16: Flexural loss factor for different nanocomposites.

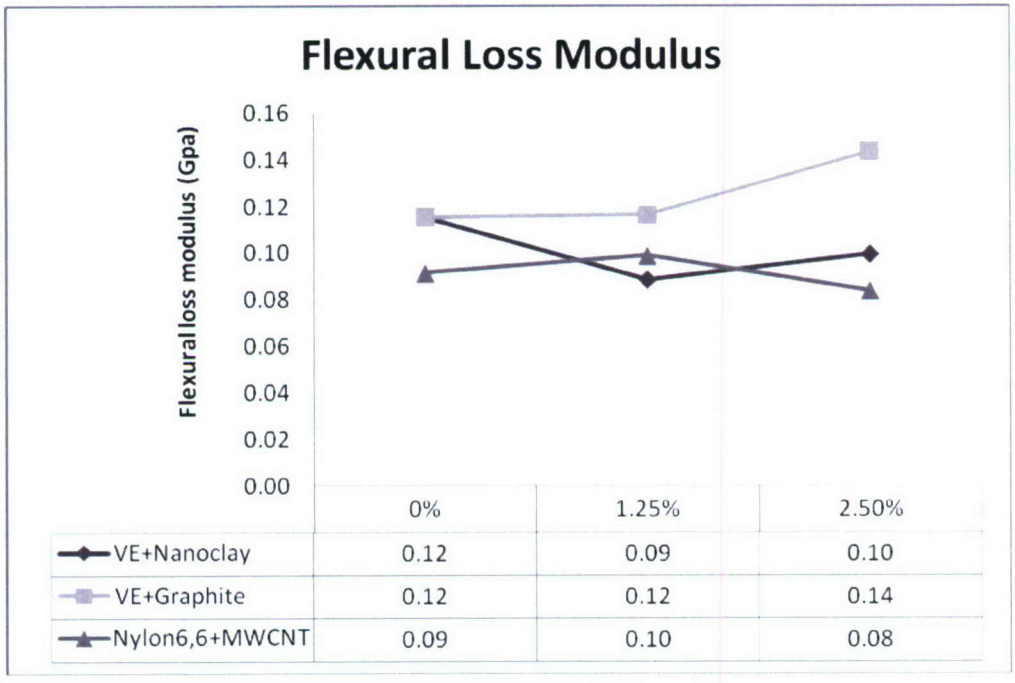

	0%	1.25%	2.50%
VE+Nanoclay	0.12	0.09	0.10
VE+Graphite	0.12	0.12	0.14
Nylon6,6+MWCNT	0.09	0.10	0.08

Figure 1.2.17: Flexural loss modulus for different nanocomposites.

The Eco-Core foam samples showed higher frequencies than nylon 6,6 and vinyl ester nanocomposites which is due to they being lighter. The resonant frequency and flexural dynamic modulus for all the Eco-Core foams is shown in Figures 1.2.18 and 1.2.19. It is observed that among all foams, OM19 has the highest modulus. The loss modulus (Figure 1.2.21) is also highest for the OM19. The loss factor for all the foams is shown in Figure 1.2.20. OM16 has the highest loss factor but the flexural dynamic modulus for the same is much lower as compared to OM19. The loss factor of OM19 is slightly less than OM16. Table 1.2.5 lists all the results for flexural dynamic tests.

Table 1.2.5: Eco-Core foam dynamic test results for flexural dynamic test.

Sample ID	**Resonant Frequency (Hz)**	**Flexural loss factor**	**Flexural dynamic modulus (GPa)**	**Flexural loss modulus (GPa)**
OM11D01	71.50	5.79E-03	2.62	0.015
OM11D02	72.88	5.61E-03	2.72	0.015
OM11 Average	**72.19**	**5.70E-03**	**2.67**	**0.015**
OM12D01	75.56	6.13E-03	3.00	0.018
OM12D02	76.50	6.18E-03	3.06	0.019
OM12 Average	**76.03**	**6.15E-03**	**3.03**	**0.019**
OM16D01	67.37	1.82E-02	2.19	0.040
OM16D02	65.06	2.86E-02	2.04	0.058
OM16 Average	**66.22**	**2.34E-02**	**2.11**	**0.049**
OM18D01	69.63	1.71E-02	2.69	0.046
OM18D02	70.00	2.17E-02	2.72	0.059
OM18 Average	**69.82**	**1.94E-02**	**2.70**	**0.052**
OM19D01	78.19	1.72E-02	3.39	0.059
OM19D02	77.38	1.82E-02	3.32	0.061
OM19 Average	**77.79**	**1.77E-02**	**3.36**	**0.060**
OM21D01	64.38	2.09E-02	2.13	0.044
OM21D02	64.62	2.08E-02	2.14	0.045
OM21 Average	**64.50**	**2.08E-02**	**2.13**	**0.044**

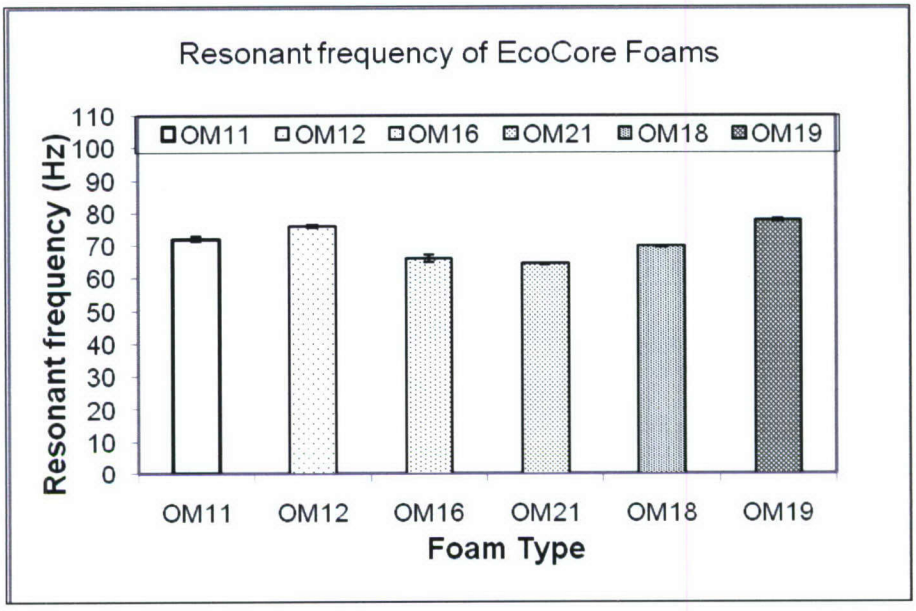

Figure 1.2.18: Resonant frequency of Eco-Core Foams.

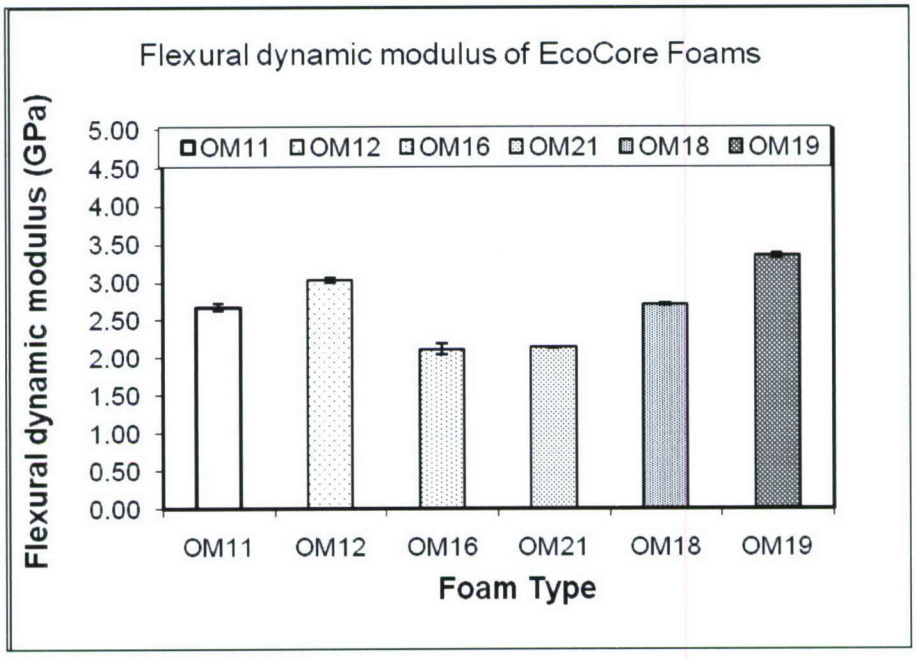

Figure 1.2.19: Flexural dynamic modulus of Eco-Core Foams.

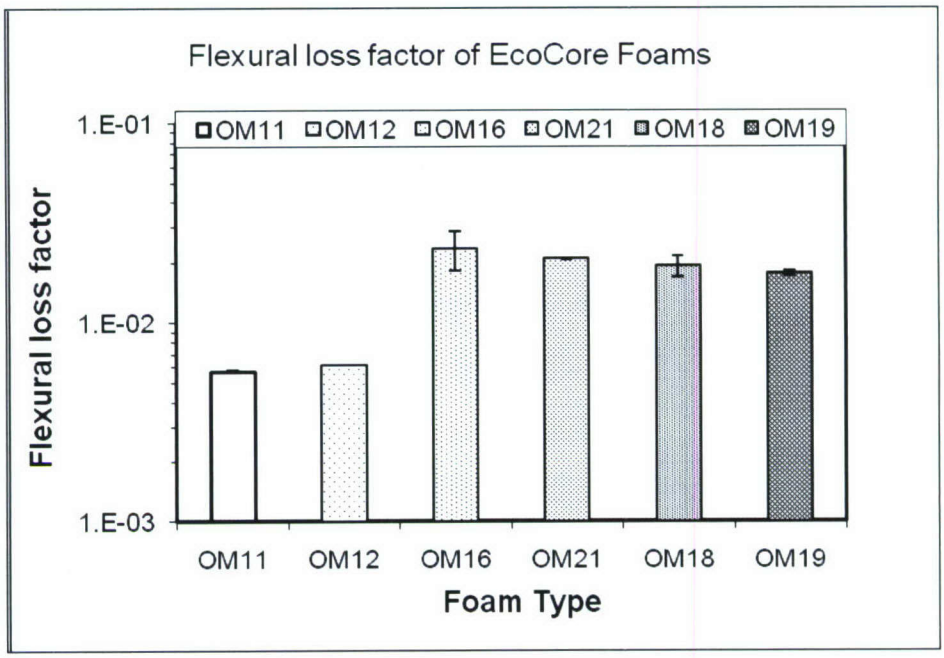

Figure 1.2.20: Flexural loss factor of Eco-Core Foams

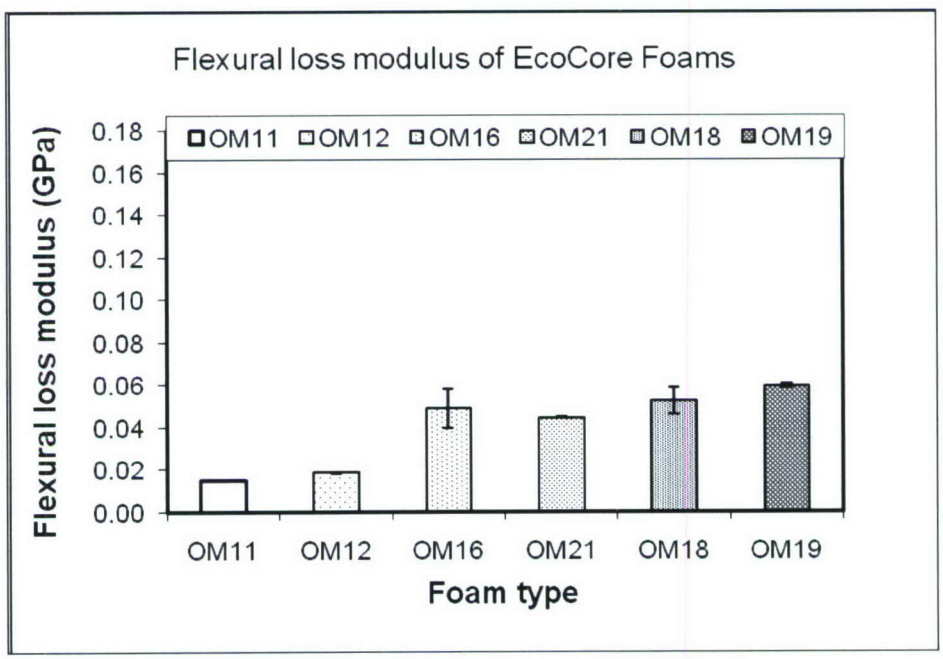

Figure 1.2.21: Flexural loss modulus of Eco-Core Foams.

1.3 Dynamic Extensional Property Measurements:

The same (10"x1"x3/8") flexural samples are also used for computing the dynamic extensional modulus and damping. In this setup, the sample is tested in a free-free condition supported by nylon wires as shown in Figure 1.3.1. Two extra masses are clamped at the ends of the sample with the help of screws for lowering the resonant frequencies. The accelerometer is placed at one end of the sample and an impact is given at the other end. The connections to the analyzer and ICARUS are same as in the flexural measurements. In addition to the specimen dimensions the values of the two masses are also provided as input to the ICARUS which has an algorithm for taking into account the effect of end masses in computing the extensional modulus [1.2, 1.3]. Data is averaged for two tests with three specimens tested from each configuration plate.

The modulus for a free-free setup with end masses at both ends of a vibrating beam is given by [1.2]:

$$E_l = \frac{4\pi^2 L^2 \rho f_n^{\,2}}{\lambda_n^{\,2}}$$

where eigen value λ_n is given by transcendental equation:

$$\tan \lambda_n = \frac{(m_1 + m_2) A\rho l \lambda_n}{m_1 m_2 \lambda_n^{\,2} - (A\rho l)^2}$$

In the above equations l is the length of beam, m_1, m_2 are end masses, A is area of specimen cross-section and ρ is the material mass density.

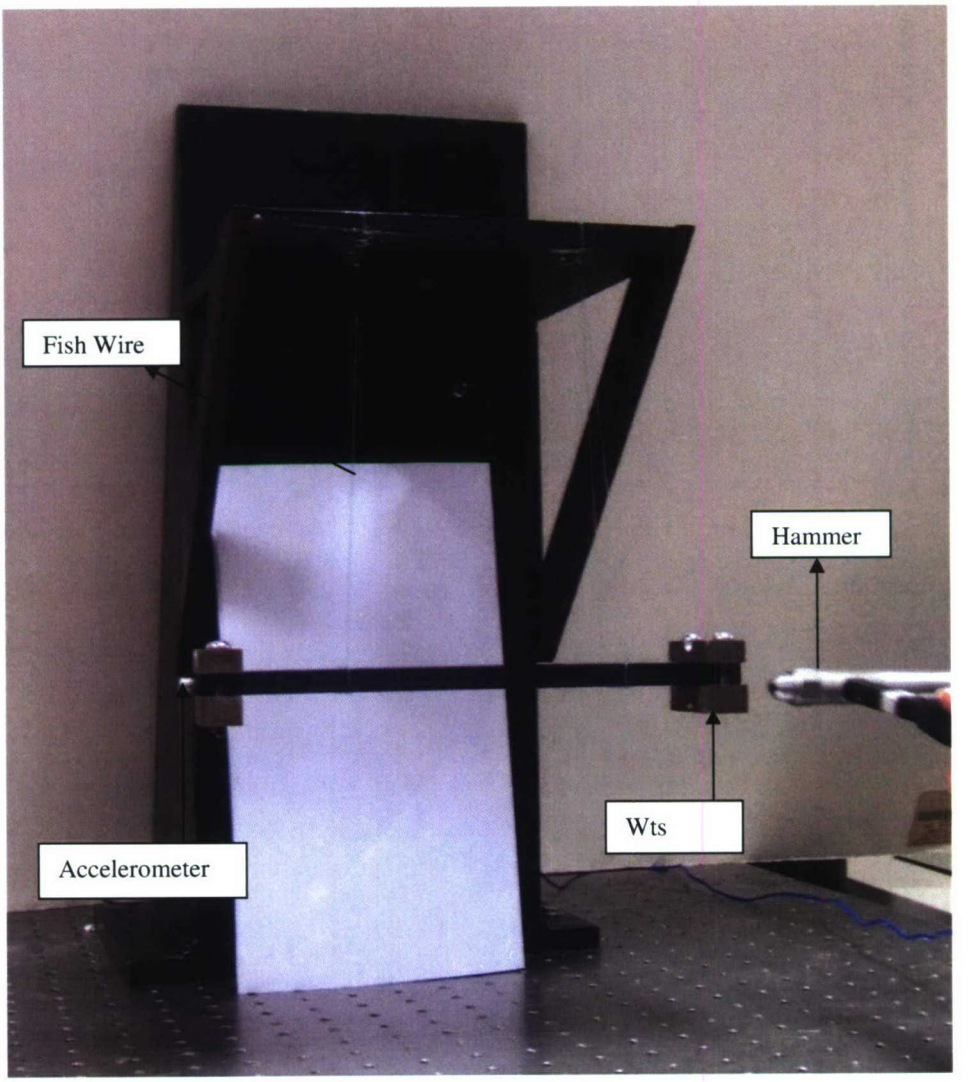

Figure 1.3.1: Experimental setup of extensional modulus and damping measurements

The resonant frequencies showed an upward shift as MWCNTs are added to nylon 6,6, but after 5 wt. percent the values are constant. The extensional dynamic modulus showed the same trend as the resonant frequencies. An increase in modulus of about 30% is observed from pure polymer to 5 wt. percent loadings. Figures 1.3.2 and 1.3.3 show the resonant frequency and dynamic extensional modulus for nylon 6,6 nanocomposites. The loss factor and loss modulus first dropped from 0 to 5 wt. percent loadings then again increased with further loadings. The 1.25 wt. percent composites had very low damping and loss modulus against the trend observed. Figures 1.3.4 and 1.3.5 show the results for nylon 6,6/ MWCNT nanocomposites. All the results are summarized in Table 1.3.1.

Table 1.3.1: Extensional dynamic properties of nylon 6,6 /MWCNT nanocomposites.

Sample ID	Resonant Frequency (Hz)	Extensional loss factor	Extensional dynamic modulus (GPa)	Loss modulus (GPa)
NM00AD01	1003.00	2.48E-02	2.92	0.07
NM00AD02	973.00	4.85E-02	2.75	0.13
NM00CD03	1030.00	1.80E-02	3.12	0.06
0 % Average	**1002.00**	**3.04E-02**	**2.93**	**0.09**
NM12AD01	1075.00	9.09E-03	3.35	0.03
NM12AD02	1059.00	1.26E-02	3.26	0.04
NM12AD03	1081.00	9.37E-03	3.39	0.03
1.25 % Average	**1071.67**	**1.04E-02**	**3.34**	**0.03**
NM25AD01	1128.00	1.11E-02	3.75	0.04
NM25AD02	1102.00	1.47E-02	3.58	0.05
NM25CD03	1010.00	2.09E-02	3.01	0.06
2.5% Average	**1080.00**	**1.56E-02**	**3.45**	**0.05**
NM50AD01	1128.00	1.21E-02	3.78	0.05
NM50AD02	1108.00	1.32E-02	3.62	0.05
NM50CD03	1096.00	1.75E-02	3.63	0.06
5.0% Average	**1110.67**	**1.43E-02**	**3.67**	**0.05**
NM10AD01	1153.00	1.64E-02	3.96	0.06
NM10AD02	1071.00	1.74E-02	3.41	0.06
NM10CD03	1103.00	1.70E-02	3.70	0.06
10 % Average	**1109.00**	**1.69E-02**	**3.69**	**0.06**
NM20JD01	1099.00	3.24E-02	3.64	0.12
NM20JD02	1084.00	2.26E-02	3.48	0.08
NM20JD03	1158.00	2.08E-02	4.05	0.08
20 % Average	**1113.67**	**2.52E-02**	**3.72**	**0.09**

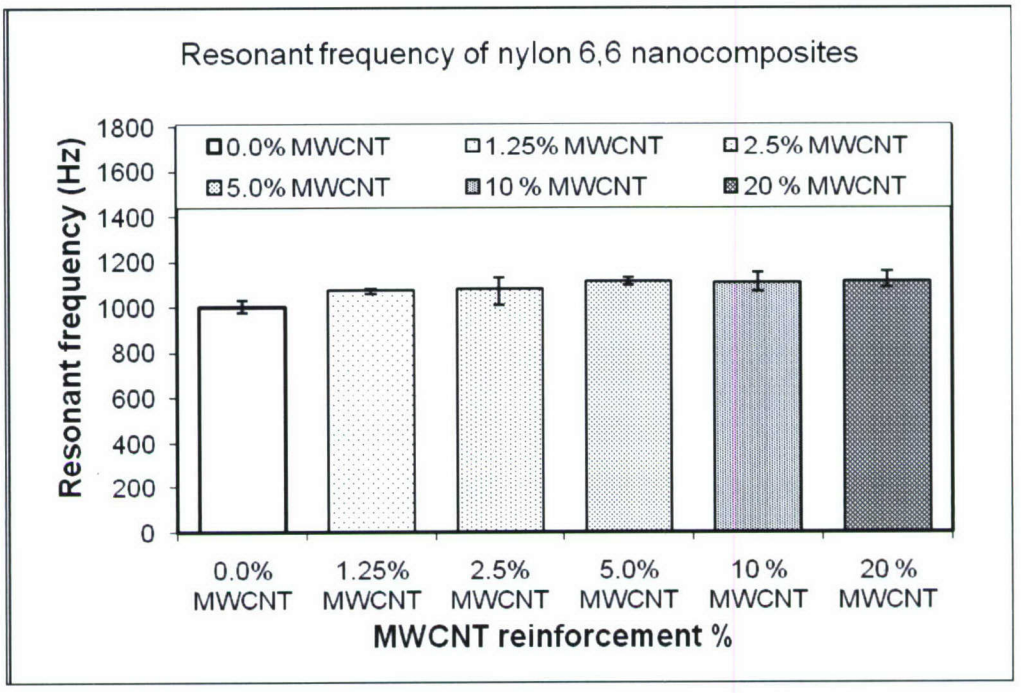

Figure 1.3.2: Resonant frequencies for nylon 6,6/MWCNT extensional dynamic tests.

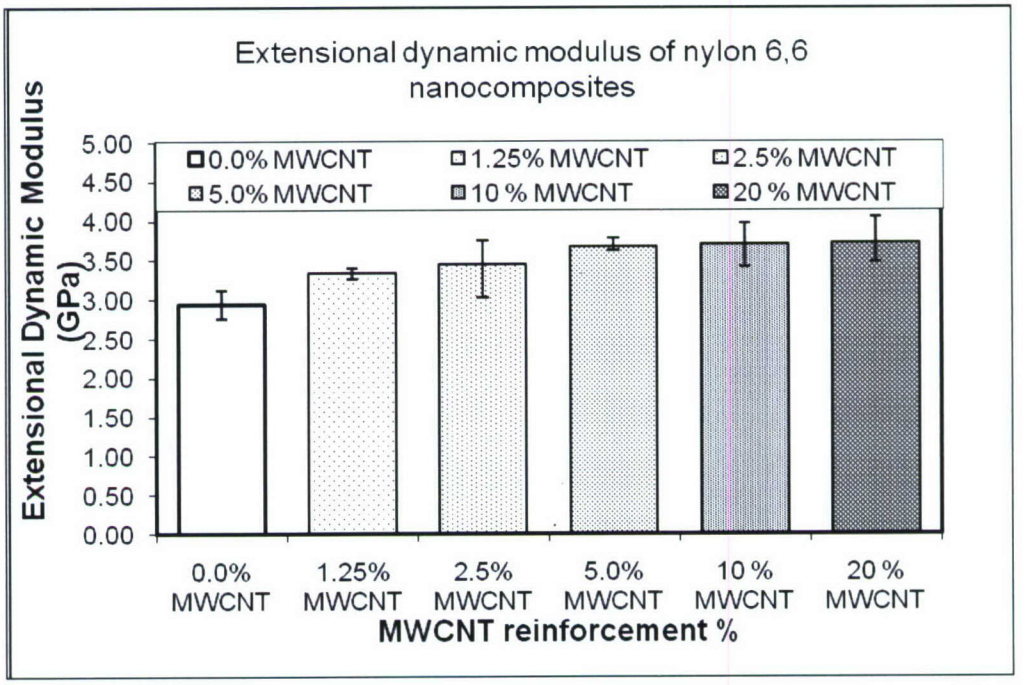

Figure 1.3.3: Extensional dynamic modulus for Nylon6,6 /MWCNT nanocomposites.

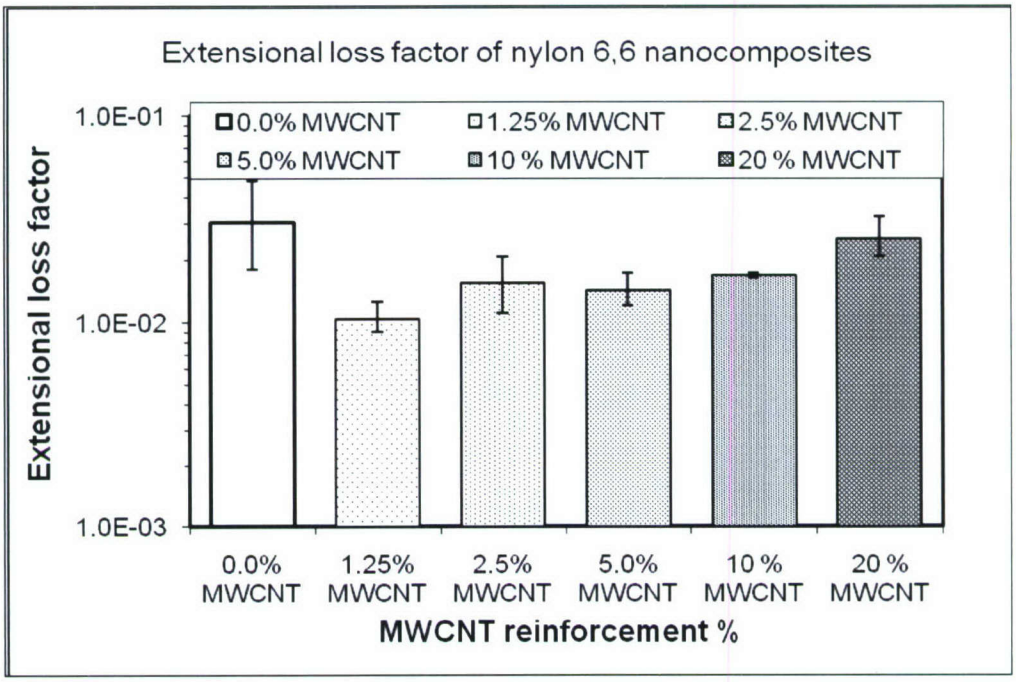

Figure 1.3.4: Extensional loss factor for nylon 6,6/MWNCT nanocomposites.

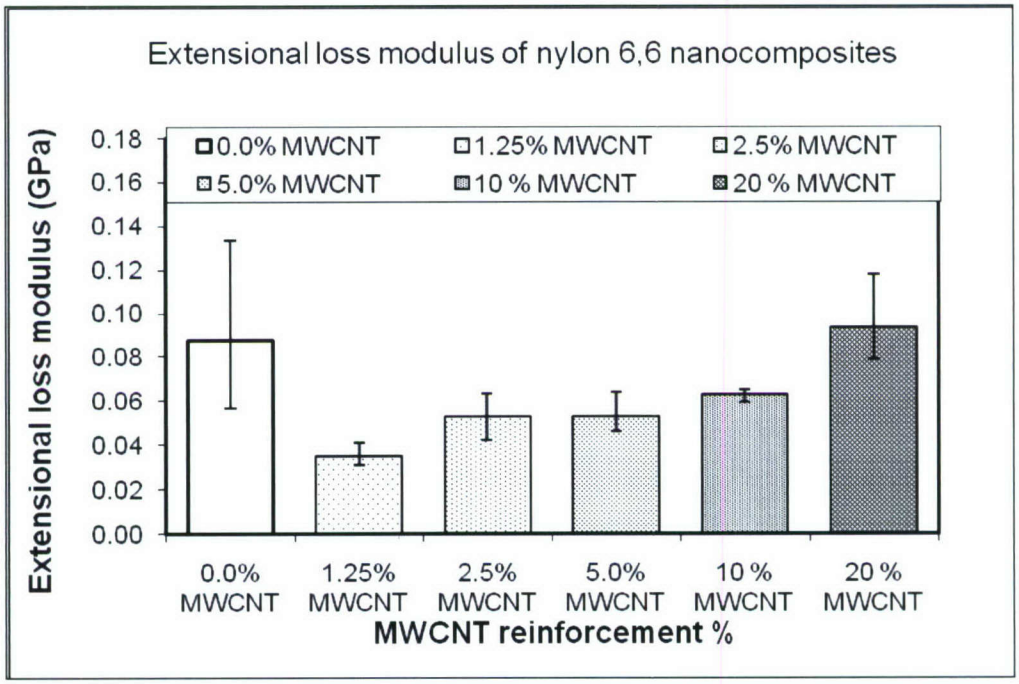

Figure 1.3.5: Extensional loss modulus of nylon 6,6/MWCNT nanocomposites

Figures 1.3.6 and 1.3.7 show the variation of resonant frequencies and dynamic modulus for nylon 6,6 nanocomposites with environmental aging. It is observed that all the configurations showed a decrease in modulus with aging except for 20 wt. percent nanocomposite for 45 days. Also for 90 days aging the modulus further decreased except the 5 wt. percent configurations which showed a slight increase in modulus. The loss factor and loss modulus (Figures 1.3.8 and 1.3.9) both increased with aging. Tables 1.3.1, 1.3.2 and 1.3.3 list the extensional dynamic test results for unaged, 45 days aged and 90 days aged MWCNT/nylon 6,6 nanocomposites respectively.

Table 1.3.2: Extensional dynamic properties of nylon 6,6 /MWCNT nanocomposites after 45 days of environmental aging.

Sample ID	**Resonant frequency (Hz)**	**Loss factor**	**Extensional dynamic modulus (GPa)**	**Loss modulus (GPa)**
NM00AD01	955.30	3.33E-02	2.60	0.09
NM00AD02	925.40	4.18E-02	2.45	0.10
NM00CD03	939.30	3.78E-02	2.51	0.09
0 % Average	**940.00**	**3.76E-02**	**2.52**	**0.09**
NM12AD01	931.70	7.23E-02	2.60	0.19
NM12AD02	941.50	4.89E-02	2.64	0.13
NM12AD03	1007.00	2.97E-02	2.99	0.09
1.25 % Average	**960.07**	**5.03E-02**	**2.74**	**0.14**
NM25AD01	1063.00	2.65E-02	3.26	0.09
NM25AD02	1008.00	3.14E-02	2.92	0.09
NM25CD03	981.10	4.17E-02	2.77	0.12
2.5% Average	**1017.37**	**3.32E-02**	**2.98**	**0.10**
NM50AD01	1099.00	2.94E-02	3.50	0.10
NM50AD02	1054.00	2.55E-02	3.22	0.08
NM50CD03	1092.00	2.587r-2	3.46	0.09
5.0% Average	**1081.67**	**2.74E-02**	**3.39**	**0.09**
NM10AD01	1094.00	2.96E-02	3.48	0.10
NM10AD02	1074.00	3.69E-02	3.36	0.12
NM10CD03	1065.00	3.03E-02	3.31	0.10
10 % Average	**1077.67**	**3.23E-02**	**3.38**	**0.11**
NM20JD01	1208.00	2.17E-02	4.25	0.09
NM20JD02	1133.00	2.03E-02	3.75	0.08
NM20JD03	1172.00	2.80E-02	4.02	0.11
20 % Average	**1171.00**	**2.33E-02**	**4.01**	**0.09**

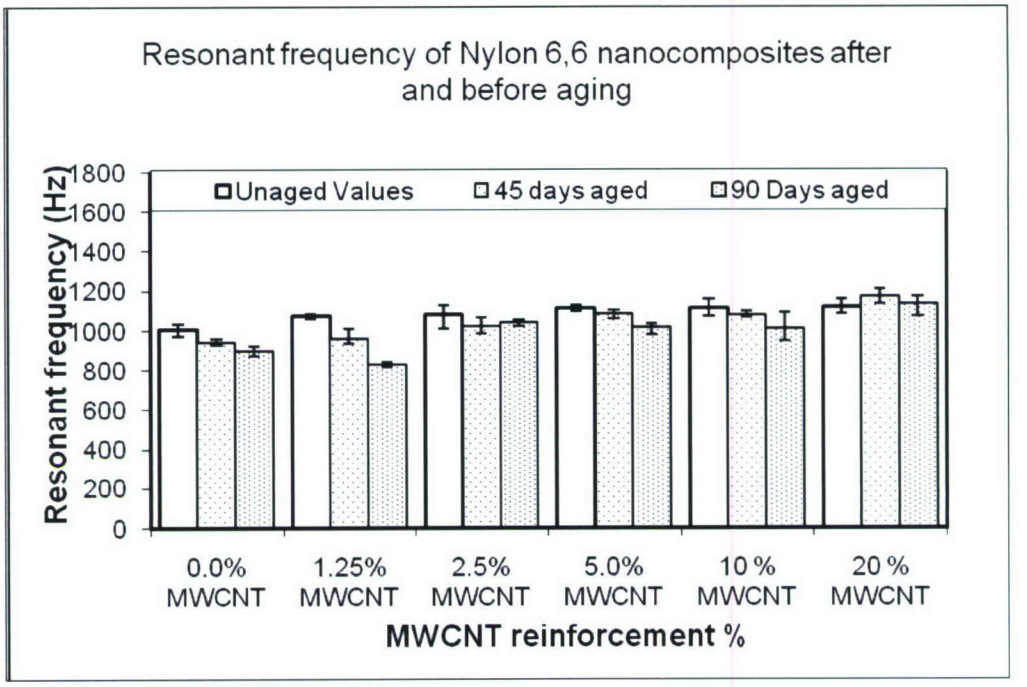

Figure 1.3.6: Extensional resonant frequency of nylon 6,6/MWCNT nanocomposites with aging

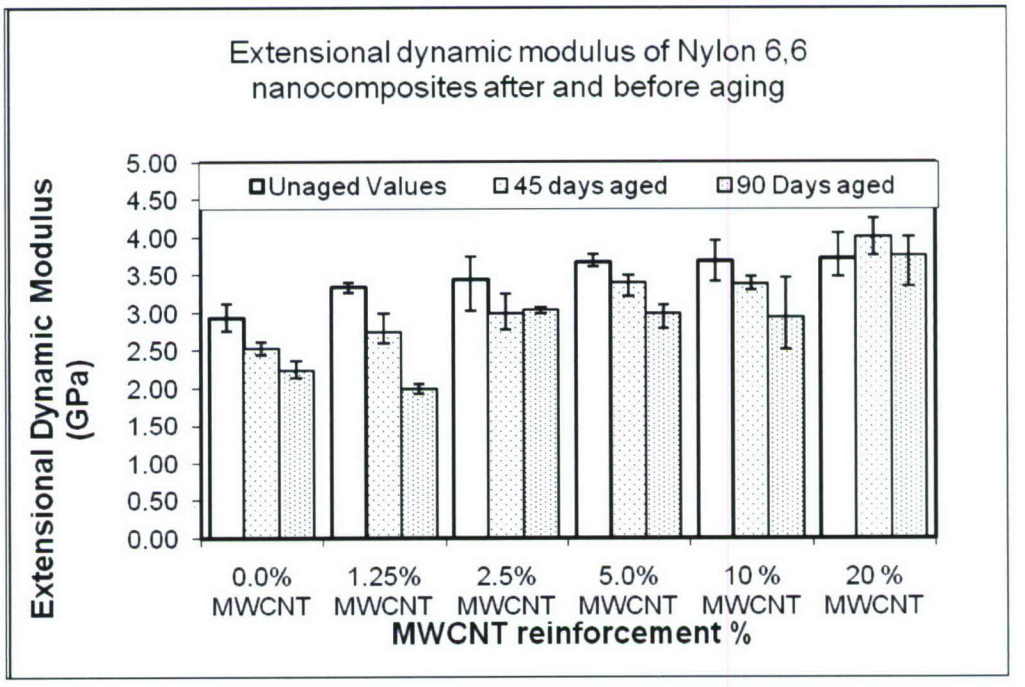

Figure 1.3.7: Extensional dynamic modulus of nylon 6,6/MWCNT nanocomposites with aging

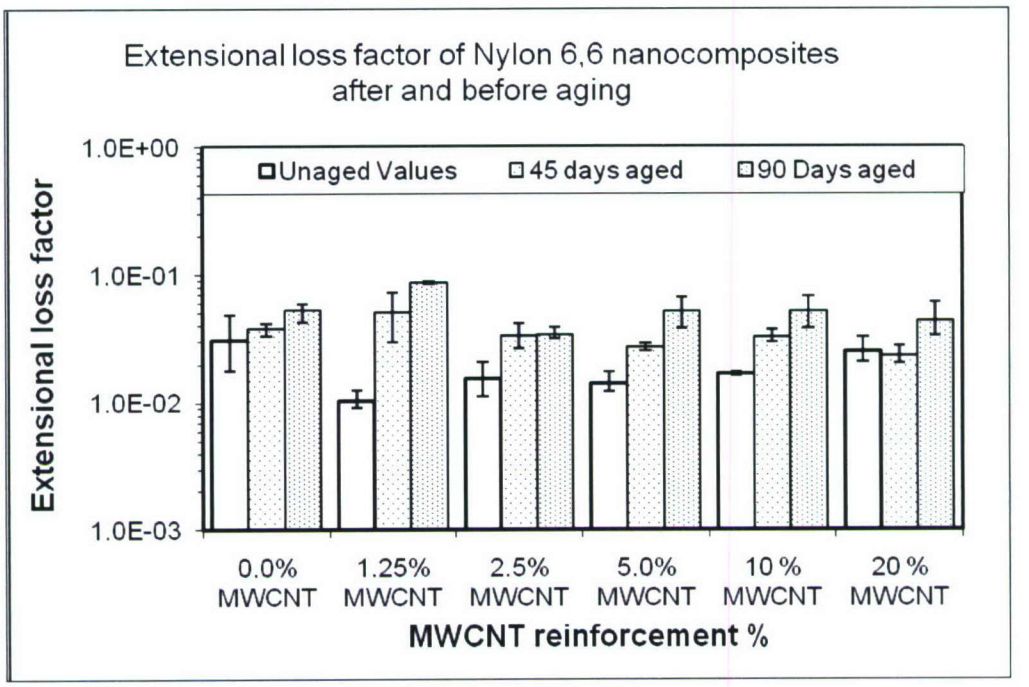

Figure 1.3.8: Extensional loss factor of nylon 6,6/MWCNT nanocomposites with aging

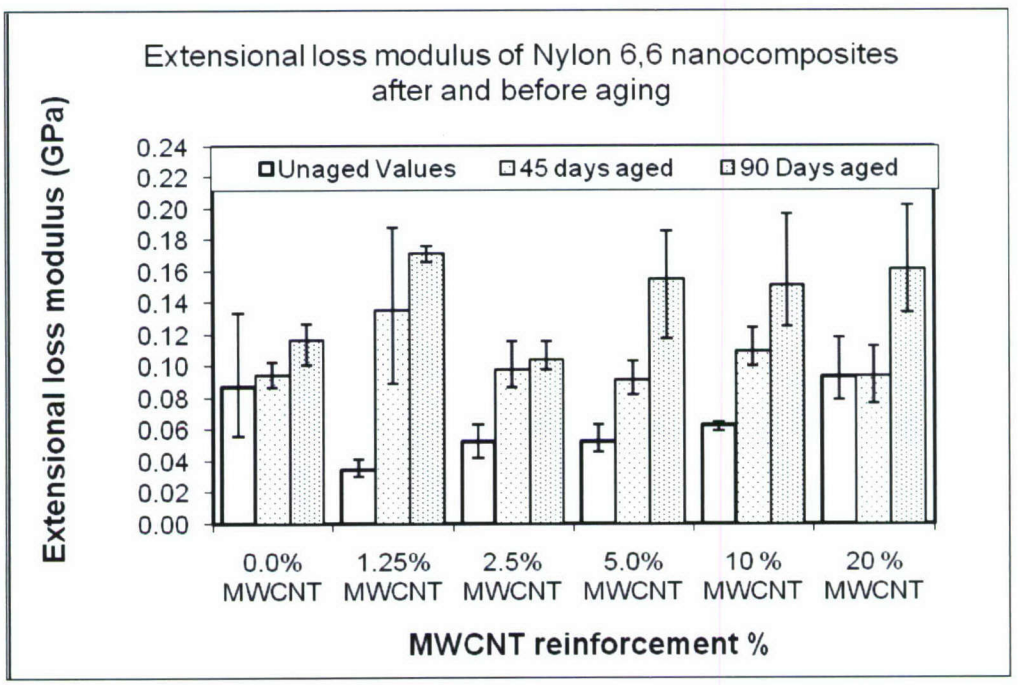

Figure 1.3.9: Extensional loss modulus of nylon 6,6/MWCNT nanocomposites with aging

Table 1.3.3: Extensional dynamic properties of nylon 6,6 /MWCNT nanocomposites after 90 days of environmental aging.

Sample ID	Resonant frequency (Hz)	Loss factor	Extensional dynamic modulus (GPa)	Loss modulus (GPa)
NM00AD01	883.60	5.57E-02	2.18	0.12
NM00AD02	921.90	4.25E-02	2.37	0.10
NM00CD03	873.20	5.94E-02	2.13	0.13
0% Average	**892.90**	**5.25E-02**	**2.23**	**0.12**
NM12AD01	822.40	8.81E-02	1.97	0.17
NM12AD02	814.70	8.59E-02	1.93	0.17
NM12AD03	841.30	8.55E-02	2.06	0.18
1.25 % Average	**826.13**	**8.65E-02**	**1.98**	**0.17**
NM25AD01	1053.00	3.17E-02	3.08	0.10
NM25AD02	1036.00	3.21E-02	3.04	0.10
NM25CD03	1017.00	3.85E-02	3.00	0.12
2.5% Average	**1035.33**	**3.41E-02**	**3.04**	**0.10**
NM50AD01	1027.00	5.29E-02	3.06	0.16
NM50AD02	1032.00	3.77E-02	3.10	0.12
NM50CD03	975.30	6.66E-02	2.79	0.19
5.0% Average	**1011.43**	**5.24E-02**	**2.98**	**0.15**
NM10AD01	1090.00	3.78E-02	3.46	0.13
NM10AD02	985.40	6.86E-02	2.86	0.20
NM10CD03	947.60	4.98E-02	2.51	0.13
10% Average	**1007.67**	**5.21E-02**	**2.94**	**0.15**
NM20JD01	1171.00	3.33E-02	4.01	0.13
NM20JD02	1161.00	3.80E-02	3.92	0.15
NM20JD03	1069.00	6.01E-02	3.36	0.20
20% Average	**1133.67**	**4.38E-02**	**3.76**	**0.16**

For vinyl ester nanocomposites the resonant frequencies as well as the dynamic extensional modulus increased with reinforcements of nanoclay and graphite platelets. The shift is more for graphite platelets than for the nanoclay. This trend is the same as observed before in flexural mode. The 2.5 wt. percent graphite reinforced composites dynamic modulus increased by about 55% with just 2.5 wt. percent reinforcements. The results are shown in Figures 1.3.10 and 1.3.11. The loss factor (damping) on the other hand remained the same for 1.25 wt. percent reinforcements but dropped for 2.5 wt. percent reinforcements as shown in Figures 1.3.12 and 1.3.13. The Table 1.3.4 lists all the extensional tests results for vinyl ester nanocomposites.

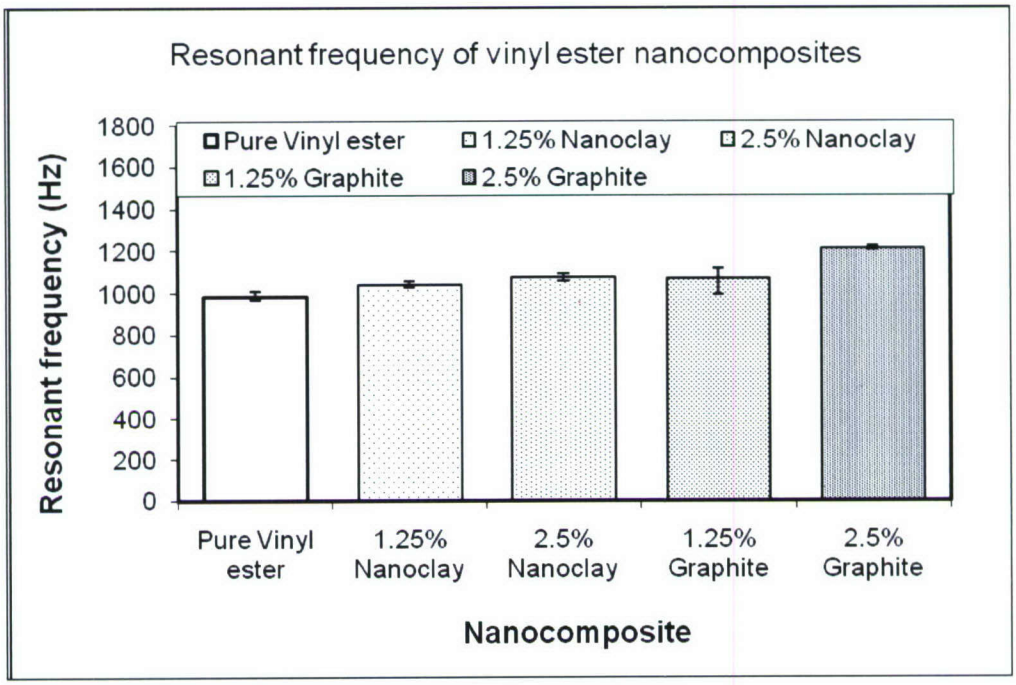

Figure 1.3.10: Resonant frequencies for vinyl ester nanocomposites extensional dynamic tests.

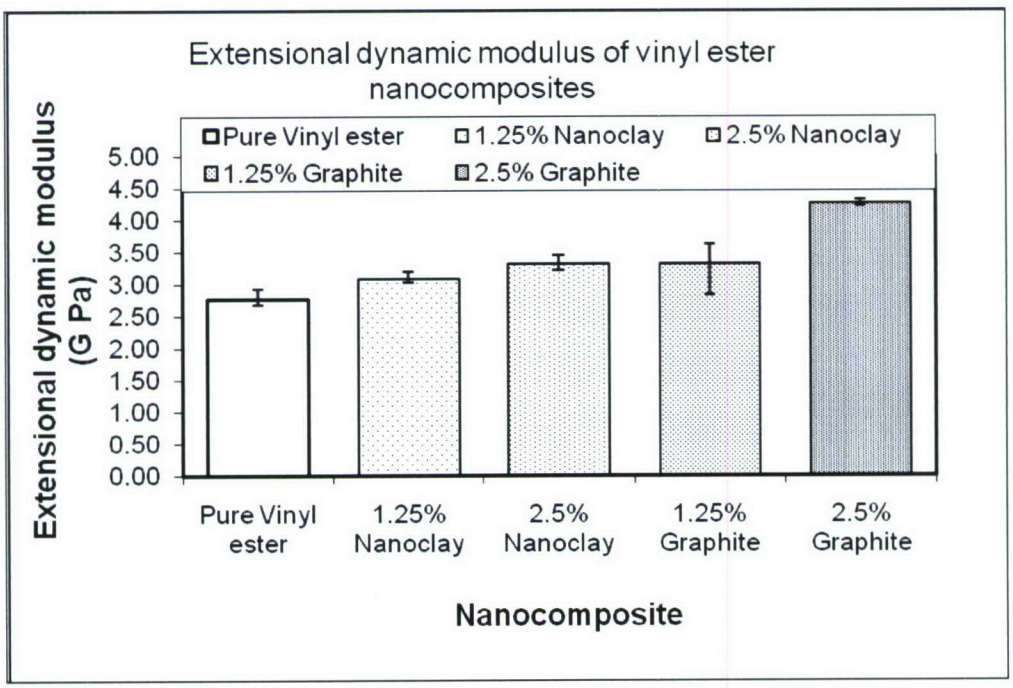

Figure 1.3.11: Extensional dynamic modulus for vinyl ester nanocomposites.

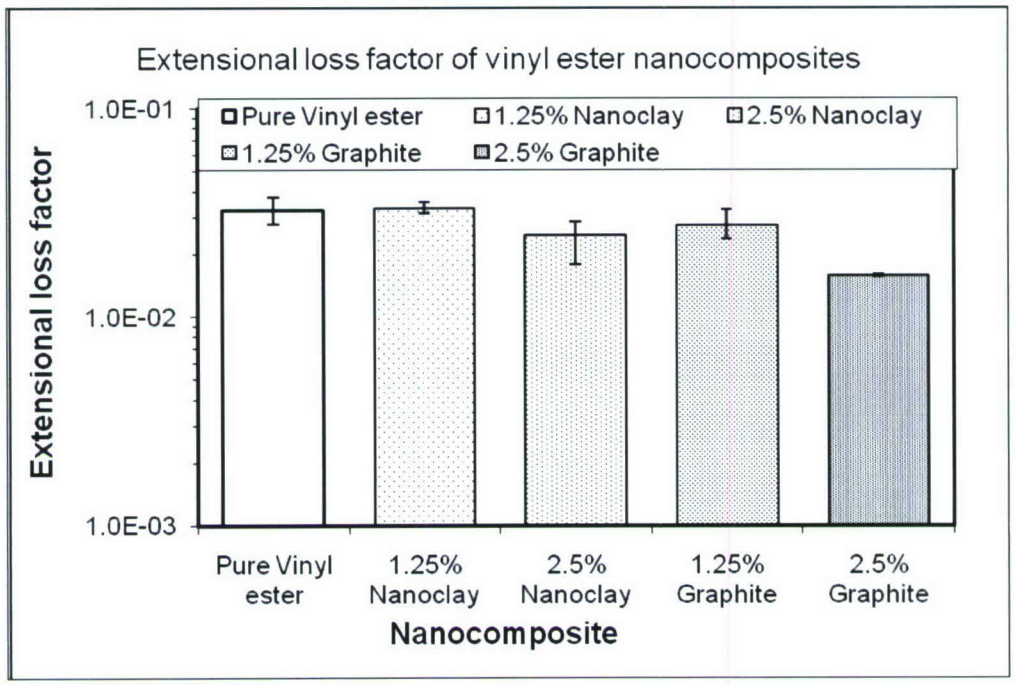

Figure 1.3.12: Extensional loss factor for vinyl ester nanocomposites.

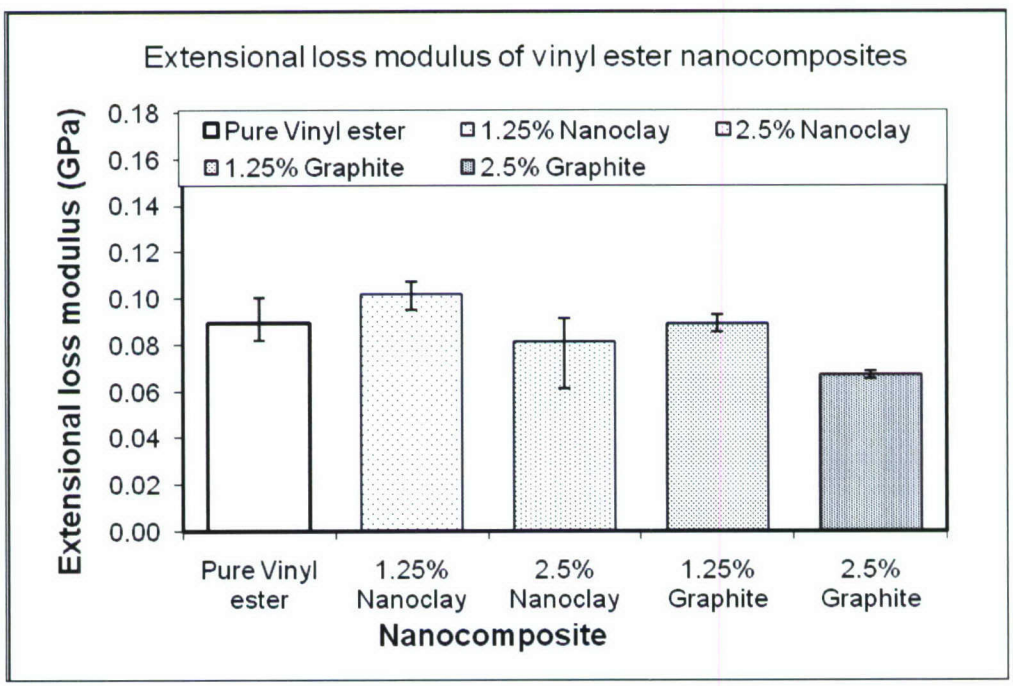

Figure 1.3.13: Extensional loss modulus for vinyl ester nanocomposites.

Table 1.3.4: Extensional dynamic properties of vinyl ester nanocomposites.

Sample ID	Resonant frequency (Hz)	Extensional loss factor	Extensional dynamic modulus (GPa)	Loss modulus (GPa)
VC00AD01	1008.00	2.80E-02	2.92	0.08
VC00AD02	965.40	3.23E-02	2.68	0.09
VC00AD03	964.60	3.75E-02	2.67	0.10
Pure Vinyl Ester	**979.33**	**3.26E-02**	**2.76**	**0.09**
VC12AD01	1024.00	3.56E-02	3.02	0.11
VC12AD02	1028.00	3.13E-02	3.04	0.10
VC12AD03	1055.00	3.23E-02	3.20	0.10
1.25% Nanoclay	**1035.67**	**3.31E-02**	**3.09**	**0.10**
VC25AD01	1093.00	1.77E-02	3.44	0.06
VC25AD02	1073.00	2.74E-02	3.31	0.09
VC25CD03	1055.00	2.86E-02	3.20	0.09
2.5% Nanoclay	**1073.67**	**2.46E-02**	**3.32**	**0.08**
VG12AD01	992.50	3.28E-02	2.83	0.09
VG12BD02	1098.00	2.56E-02	3.50	0.09
VG12AD03	1117.00	2.36E-02	3.62	0.09
1.25% Graphite	**1069.17**	**2.73E-02**	**3.31**	**0.09**
VG25AD01	1204.00	1.59E-02	4.21	0.07
VG25AD02	1219.00	1.59E-02	4.31	0.07
VG25CD03	1204.00	1.56E-02	4.21	0.07
2.5% Graphite	**1209.00**	**1.58E-02**	**4.24**	**0.07**

The three nanocomposites under study namely vinyl ester reinforced with nanoclay, vinyl ester reinforced with graphite platelets and nylon 6,6 reinforced with MWCNT is compared based on the experimental observations made. The vinyl ester with nanoclay showed an increase in frequenices in extensional mode as shown in Figure 1.3.14. The 2.5 wt. percent graphite composites shows a prominent increase in resonant frequency in extensional modes. The extensional modulus (Figure 1.3.15) follows the trend of flexural modulus for all the configurations showing an increase with increasing reinforcements. The loss factor and loss modulus (Figures 1.3.16 and 1.3.17) were highest for vinyl ester/nanoclay composites. The vinyl ester with 2.5 wt. percent graphite platelets had the highest dynamic extnesional modulus with a slight higher damping then 2.5 wt. percent MWCNT/nylon 6,6 nanocompsite. It is to be noted that this is the lightest among all the 2.5 wt. percent nanocomposite configurations studied here.

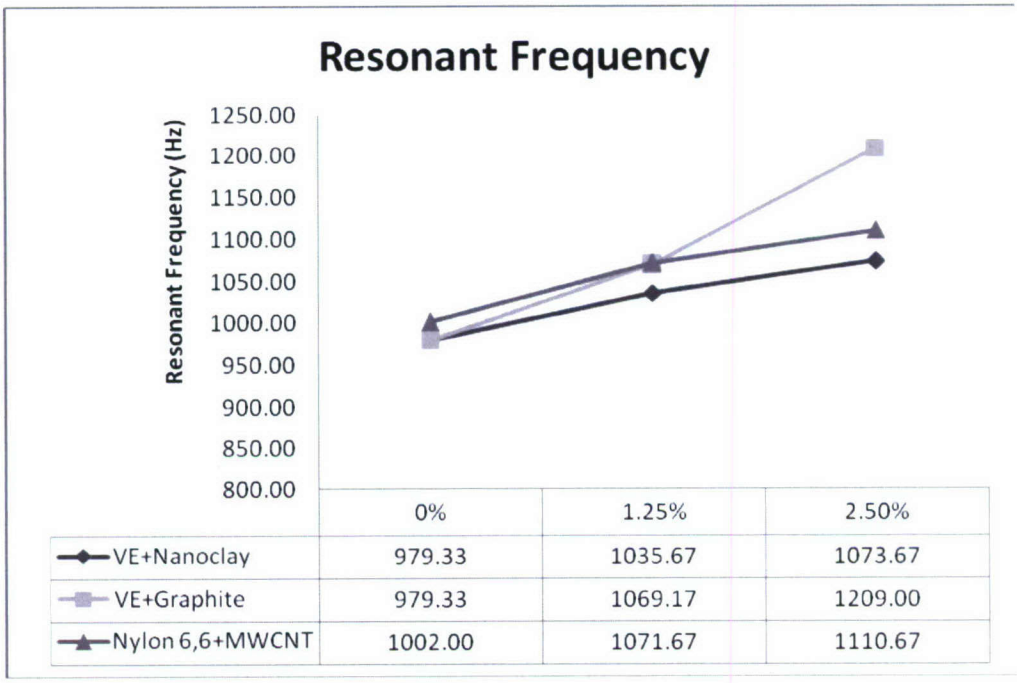

	0%	1.25%	2.50%
VE+Nanoclay	979.33	1035.67	1073.67
VE+Graphite	979.33	1069.17	1209.00
Nylon 6,6+MWCNT	1002.00	1071.67	1110.67

Figure 1.3.14: Comparison of resonant frequencies of nanocomposites.

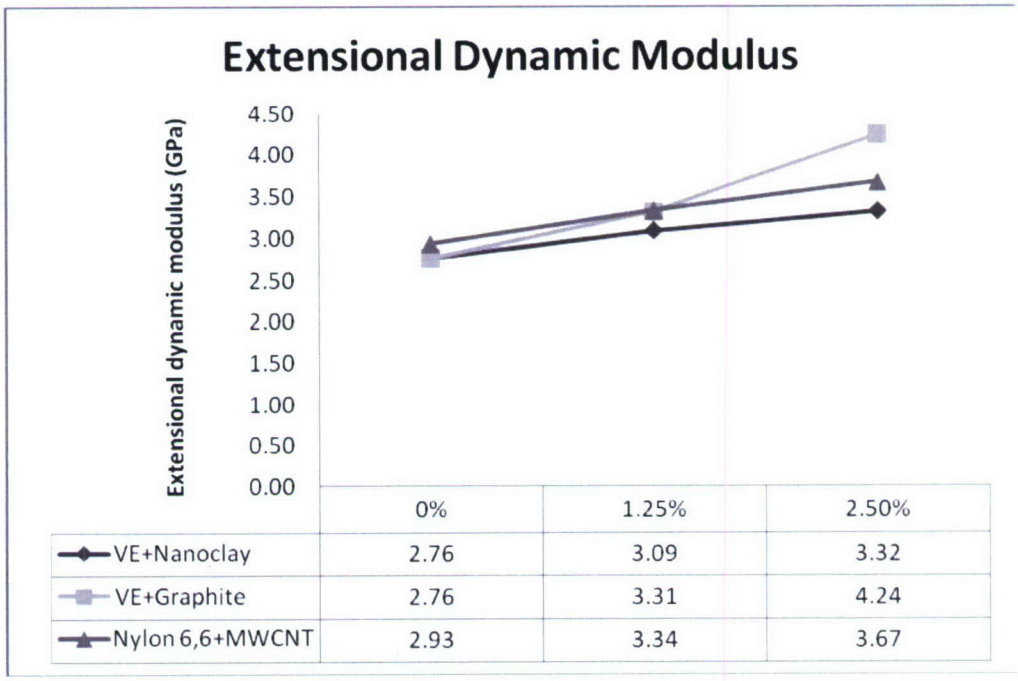

	0%	1.25%	2.50%
VE+Nanoclay	2.76	3.09	3.32
VE+Graphite	2.76	3.31	4.24
Nylon 6,6+MWCNT	2.93	3.34	3.67

Figure 1.3.15: Comparison of extensional dynamic modulus of nanocomposites.

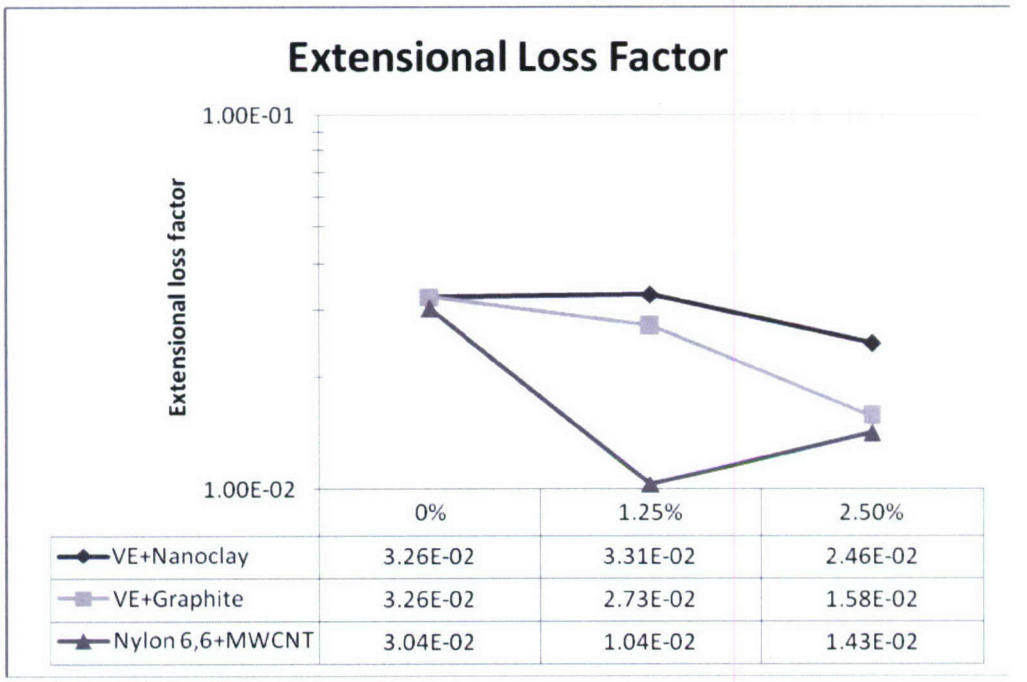

	0%	1.25%	2.50%
VE+Nanoclay	3.26E-02	3.31E-02	2.46E-02
VE+Graphite	3.26E-02	2.73E-02	1.58E-02
Nylon 6,6+MWCNT	3.04E-02	1.04E-02	1.43E-02

Figure 1.3.16: Comparison of extensional loss factor of nanocomposites.

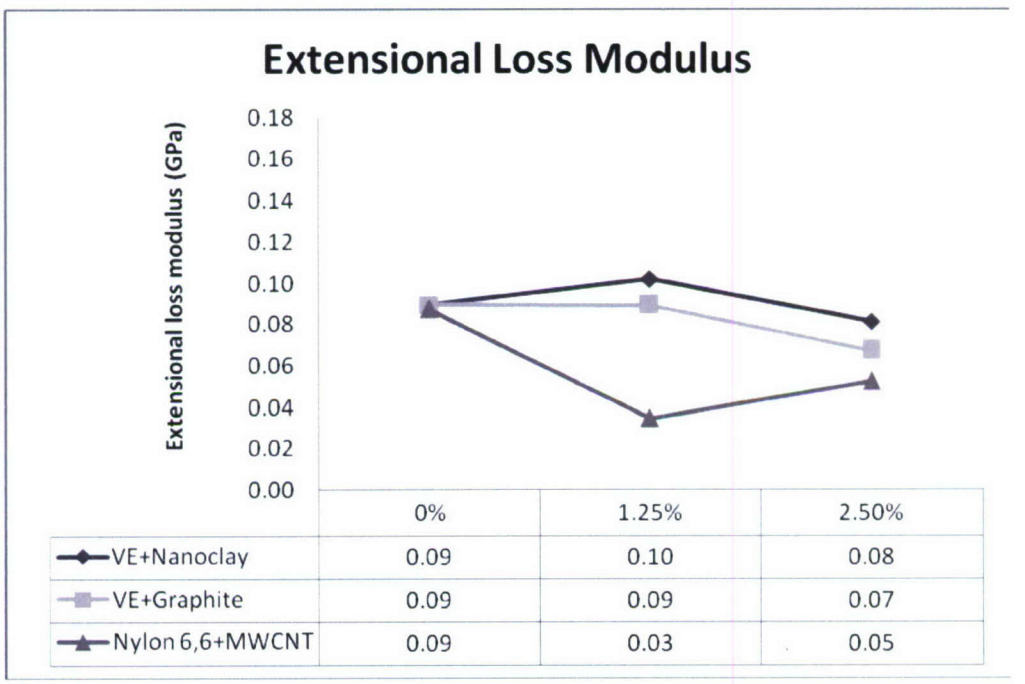

	0%	1.25%	2.50%
VE+Nanoclay	0.09	0.10	0.08
VE+Graphite	0.09	0.09	0.07
Nylon 6,6+MWCNT	0.09	0.03	0.05

Figure 1.3.17: Comparison of extensional loss modulus of nanocomposites.

The extensional properties of Eco-Core foams are shown in Figures 1.3.18 - 1.3.21. Among all the foams tested here OM19 has the most promising properties for dynamic applications. It has the highest extensional dynamic modulus as well as the highest loss factor. The loss modulus of this is prominently higher than the other foams studied here. The numerical values are listed in Table 1.3.5.

Table 1.3.5: Extensional dynamic properties of Eco-Core foams.

Sample ID	**Resonant frequency (Hz)**	**Extensional loss factor**	**Extensional dynamic modulus (GPa)**	**Extensional loss modulus (GPa)**
OM11D01	992.60	7.19E-03	2.78	0.020
OM11D02	975.90	8.50E-03	2.68	0.023
OM11 Average	**984.25**	**7.85E-03**	**2.73**	**0.021**
OM12D01	973.80	5.59E-03	2.67	0.015
OM12D02	994.10	5.72E-03	2.79	0.016
OM12 Average	**983.95**	**5.65E-03**	**2.73**	**0.015**
OM16D01	973.90	5.62E-03	2.65	0.015
OM16D02	984.40	6.13E-03	2.71	0.017
OM16 Average	**979.15**	**5.87E-03**	**2.68**	**0.016**
OM18D01	967.90	6.60E-03	2.63	0.017
OM18D02	977.10	7.88E-03	2.68	0.021
OM18 Average	**972.50**	**7.24E-03**	**2.66**	**0.019**
OM19D01	1098.00	2.50E-02	3.39	0.085
OM19D02	1078.00	1.82E-02	3.27	0.059
OM19 Average	**1088.00**	**2.16E-02**	**3.33**	**0.072**
OM21D01	1037.00	6.08E-03	3.01	0.018
OM21D02	1016.00	1.45E-02	2.89	0.042
OM21 Avergae	**1026.50**	**1.03E-02**	**2.95**	**0.030**

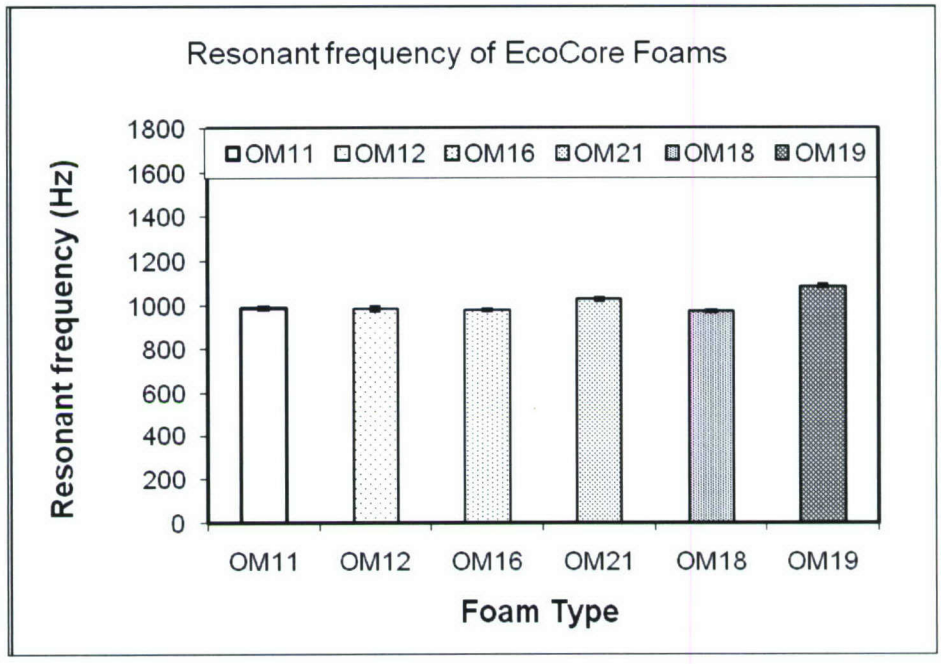

Figure 1.3.18: Resonant frequencies of Eco-Core foams.

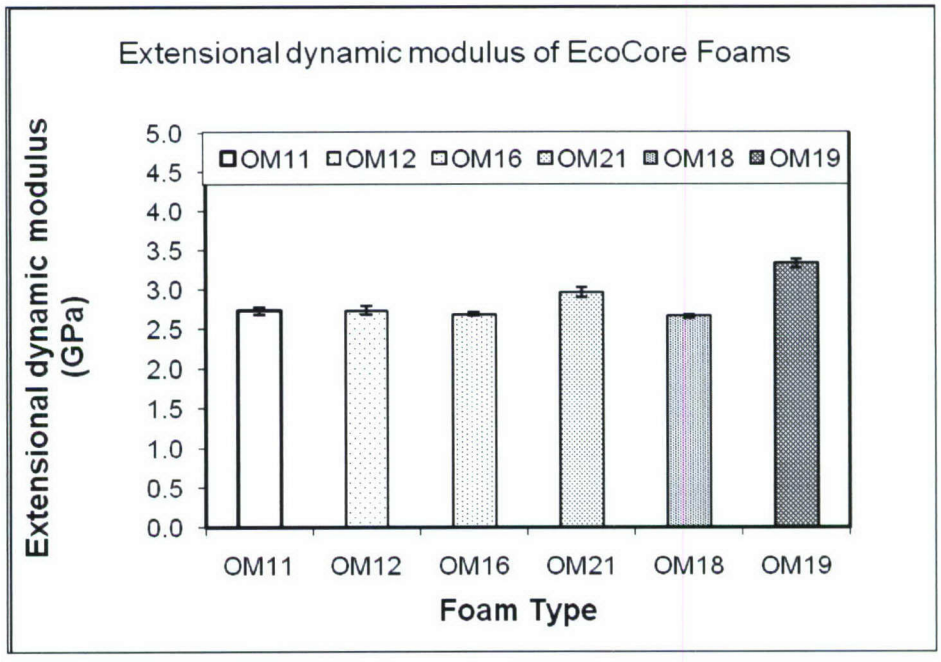

Figure 1.3.19: Extensional dynamic modulus of Eco-Core foams.

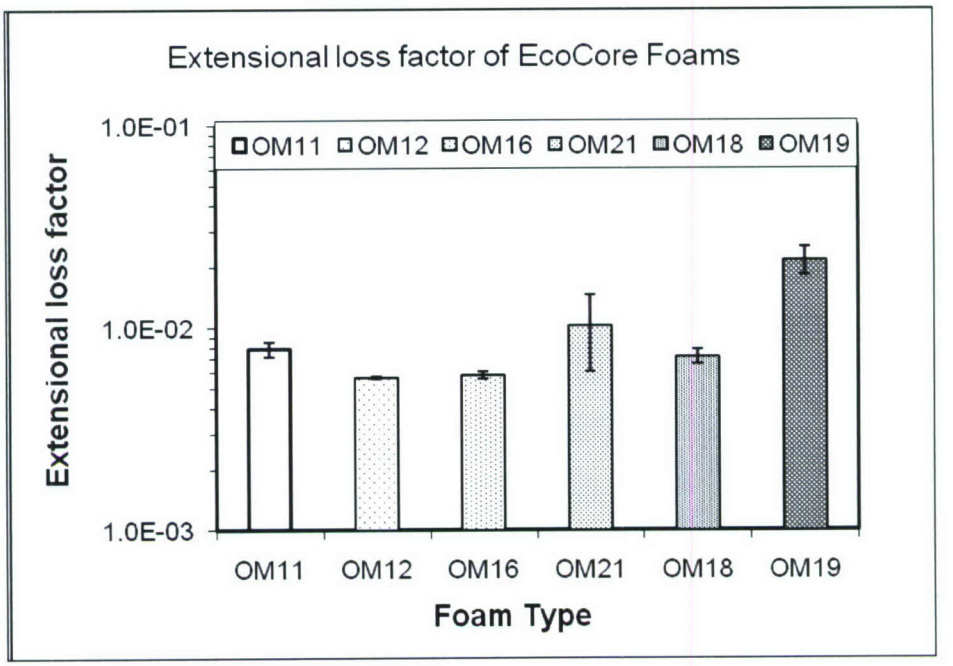

Figure 1.3.20: Extensional loss factor of Eco-Core foams.

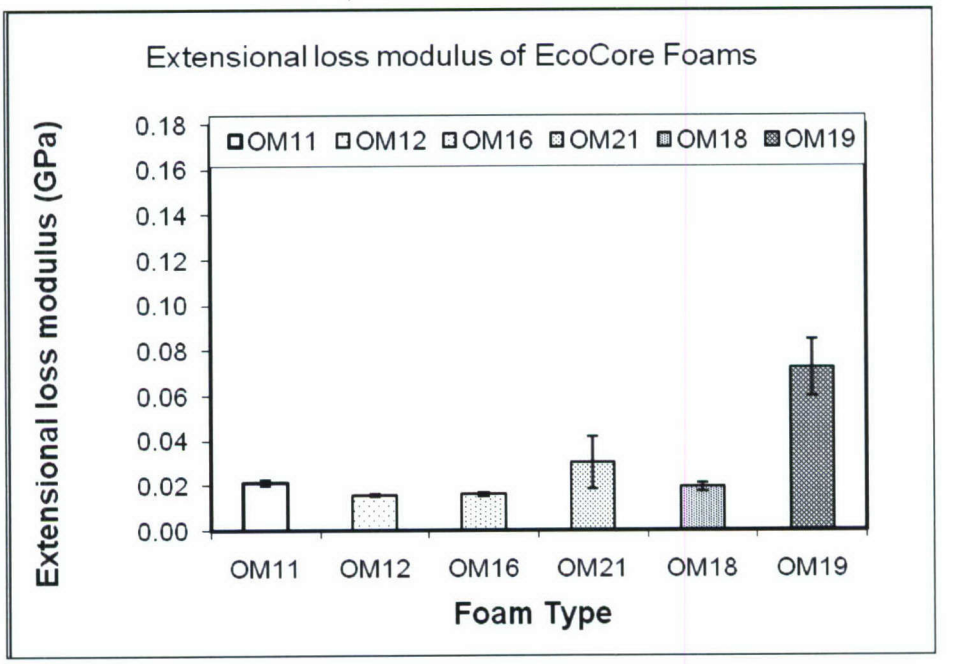

Figure 1.3.21: Extensional loss modulus of Eco-Core foams.

2.0 IMPACT AND ENERGY ABSORPTION

2.1 Specimen Preparation

Specimens for impact testing were prepared in accordance to Section 7 of ASTM D-6110-06: "Standard Test Method for Determining the Charpy Impact Resistance of Notched Specimens of Plastics" [2.1]. Sample dimensions for Charpy impact test specimen are shown in Figure 2.1.1.

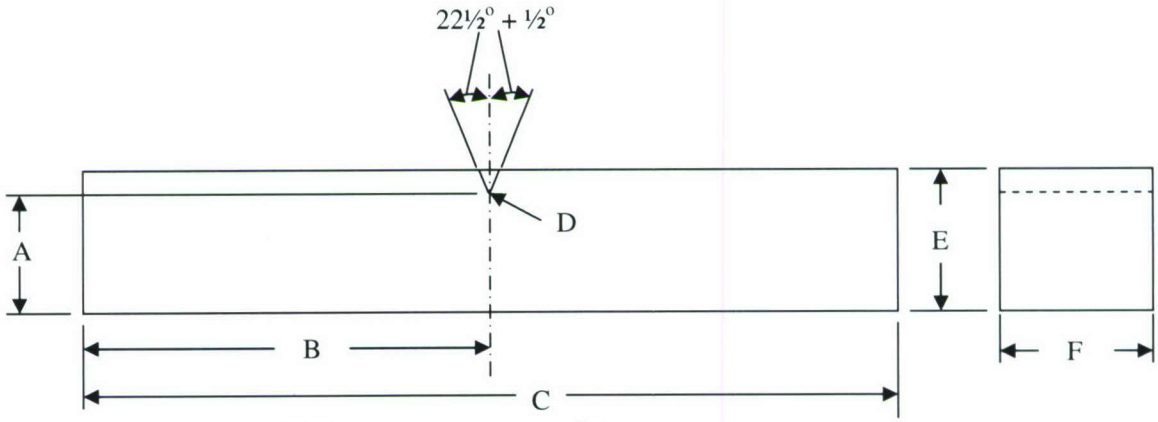

	mm	in.
A	10.16 ± 0.05	.400 ± 0.002
B	63.5 max	2.50 max
	61.0 min	2.40 min
C	127.0 max	5.00 max
	124.5 min	4.90 min
D	.25R ± 0.05	.010R ± 0.002
E	12.70 ± 0.15	0.500 ± 0.006
F	12.7 max	0.500 max
	3.0 min	0.118 min

Figure 2.1.1: Dimensions of simple beam, Charpy type, impact test specimen (ASTM D 6110-06.)

Impact samples were milled to the dimensions of 127 x 9.525 x 12.7 mm (5" x 3/8" x 0.5"), as per ASTM D-6110-06 test requirements. It should be noted that the thickness of as supplied plate was used as width (Dimension F, in Figure 2.1.1) in the tests and the milled 12.7 mm (0.5") dimension (Dimension E) as thickness.

Some specimens were tested un-notched where as others were notched. The notch, where applicable, was cut by special milling cutter with an angle of 45° and a depth of 2.54 mm (0.1") from top of plate, maintaining a dimension of 10.16 ± 0.05 mm (0.400" ± 0.002") for thickness under notch (Dimension A). The specimen notch serves to concentrate the stress and facilitate fracture initiation at the same location, thus reducing data scatter.

All the dimensions except that of notch were taken using digital vernier caliper with least count of 0.01 mm (0.0005"). Notch dimensions of random specimens were verified on comparator for angle, depth & radius. In all other samples, notch depth was measured using vernier caliper and a straight edge. Straight edge was kept on top of the surface and depth was measured using inside jaws of vernier caliper with one jaw on straight edge and another on end of notch.

2.2 Experimental Setup

Impact tests were performed in a drop-wt instrumented impact test system (Dynatup Model 8250) and the test method used was comparable to that of ASTM D6110-06. The difference being that a drop-wt system was used instead of pendulum machine recommended in the standard. A specimen under impact is shown in Figure 2.2.1 and schematic diagram of the setup is shown in Figure 2.2.2.

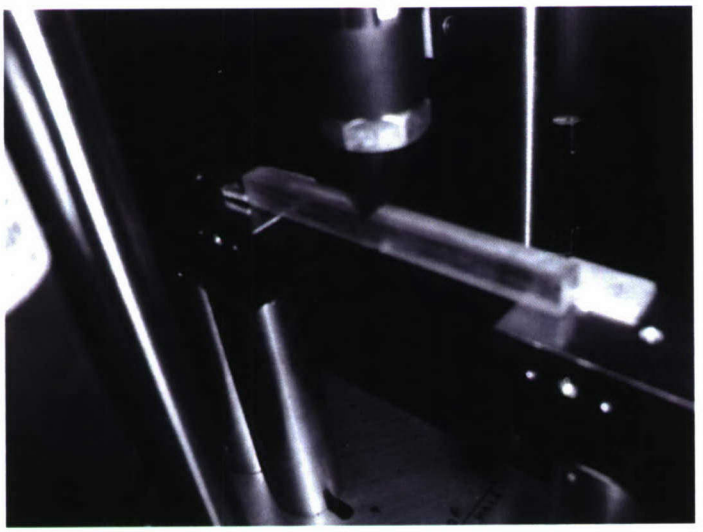

Figure 2.2.1: Sample mounted in Dynatup 8250 impact test system

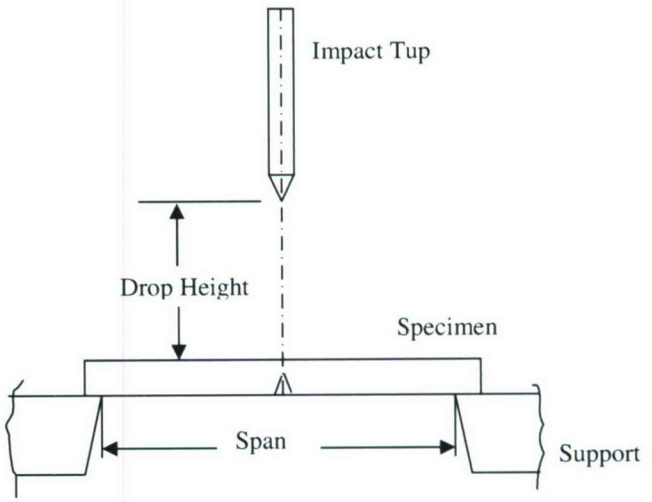

Figure 2.2.2: Schematic of the drop wt impact test

In this test, the 127 mm (5") long specimens were impacted with a steel charpy tup from a suitable drop height. Specimen of dimensions as specified earlier was kept on a steel support fixture having central span (Dimension Span, Figure 2.2.2) of 95.25 mm (3.75") with notch (wherever applicable) facing down, simulating a simply supported beam configuration. It was ensured that the steel tup hits the specimen at the middle both lengthwise as well as widthwise by providing appropriate fixtures.

Impact tests were also performed on nylon 6,6 specimen after freeze-thaw cycling, from 10°F to 50°F at 6 cycles per day according to ASTM standard C666-97 Procedure-A (freezing in water and thawing in water), titled as "Standard Test Method for Resistance of Concrete to Rapid Freezing and Thawing", after 45 days and 90 days in order to check the effect of the environmental aging on the material.

This test method requires the specimen to break completely in a single impact of machine. Impact values cannot be compared for any two materials that experience different types of failure. Therefore, machine needs to be calibrated so as to ensure that all composites under study fracture by using same load cell, drop height, load range etc. For this purpose, certain trials were done to finalize the load, drop height, width and thickness of specimen, filters, notching etc. prior to standardizing the final test.

2.3 Machine Preparation for trial runs

As the material under testing is new and there are no previous records of the impact testing of the material, we cannot estimate the breaking energy. It is to be noted that there should not be more than 15% of energy loss of its capacity, as per ASTM D 6110-06. Energy can be calculated by the formula

$$E = m.g.h$$

where m = drop mass (mass of wt, crosshead & tup)

g = force due to gravity

h = drop height

Instron machine software is used for data acquisition which is activated when a flag is passed through sensors. Flag for data acquisition is set at 6 mm from top of the notch of flag when tup is at a height, where it just touches the specimen as was prescribed by the manufacturer of the machine as shown in Figure 2.3.1.

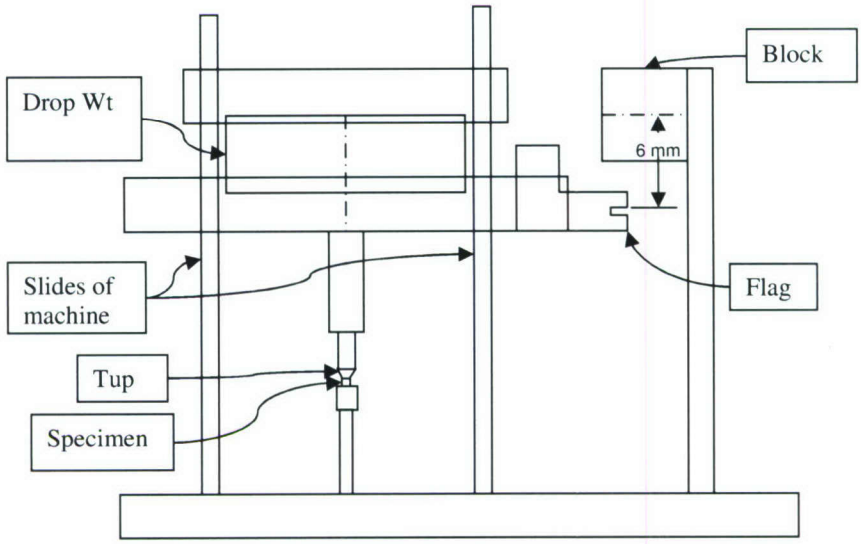

Figure 2.3.1: Schematic of flag setting in drop wt impact testing machine

Velocity test is done before running the experiment in order to cross-check the theoretical calculation with that of actual result. A similar theoretical and actual value in velocity test confirms that the flag setting is correct. Theoretical velocity is calculated by equation

$$V = \sqrt{2 \cdot g \cdot h}$$

where, g = acceleration due to gravity (m/s^2)

h = height of tup from top of specimen (m)

2.4 Standardization of test method

After several trial runs, the cross head wt is set at 2.364 Kg (5.2 lbs) providing a total drop wt of 3.318 Kg (7.3 lbs). It is to be noted that a higher wt of 4.995 Kg (10.99 lbs) providing a total drop wt of 5.95 Kg (13.09 lbs) is used for impacting the un-notched specimen after accelerated aging of 45 days and notched specimen of nylon 6,6 with 1.25 wt percent reinforced MWCNT after 90 days of aging. Load range used for tests is standardized to 4.448 kN (1000 lbs.). Filter is set at 4 KHz and time for data collection was set to 20 mS. The drop height is standardized to 177.8 mm (7") for all matrices except for un-notched specimen of Nylon 6,6 with 1.25% wt reinforced MWCNT after 90 days of accelerated aging for which drop height is set at 355.6 mm (14"). It is to be noted that both notched & un-notched specimens were tested in case of all matrices.

2.5 Impact Test Results

2.5.1 Nylon 6,6 and reinforced nanocomposites

Test results & data for impact experiments on nylon 6,6 and their nanoreinforced composites are shown in Figure 2.5.1.1 to 2.5.1.10 & Table 2.5.1.1 to 2.5.1.10. Graphs below show the trend for two specimens only. It is to be noted that total energy* computed is the energy at a point where load becomes zero after registering maximum load as calculated by the Instron machine software used for data acquisition.

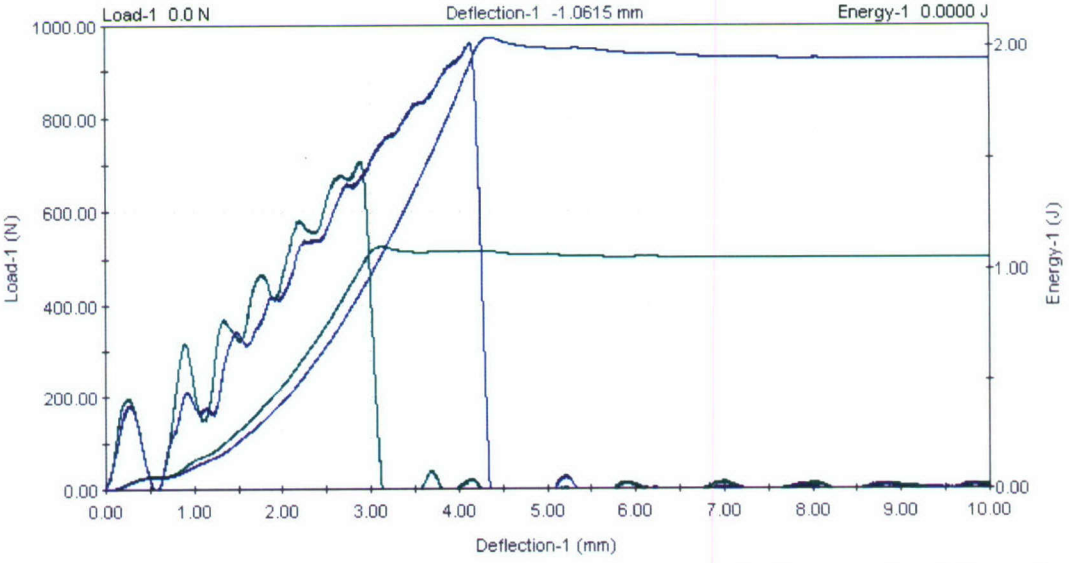

Figure 2.5.1.1: Load & Energy vs Deflection graph for un-notched pure nylon 6,6 specimens

Table 2.5.1.1: Impact characteristics of un-notched pure nylon 6,6 specimens

Specimen ID	Maximum load (N)	Energy to max load (J)	NTT energy to max load (J/mm)	Total energy* (J)	NTT total energy* (J/mm)	Impact energy (J)	Impact velocity (m/s)
NM00AI01	772.6	1.1362	0.0904	1.2507	0.0995	5.8454	1.8771
NM00AI02	707.5	1.0007	0.079	1.103	0.087	5.7715	1.8652
NM00AI03	943.1	1.72	0.1357	1.8669	0.1473	5.7876	1.8678
NM00AI04	829.9	1.3872	0.1092	1.502	0.1183	5.8338	1.8752
NM00AI05	961.9	1.9123	0.1506	2.0431	0.1609	5.7366	1.8595
Average	**843.0**	**1.4313**	**0.113**	**1.5531**	**0.1226**	**5.795**	**1.869**
Median	**829.9**	**1.3872**	**0.1092**	**1.502**	**0.1183**	**5.7876**	**1.8678**

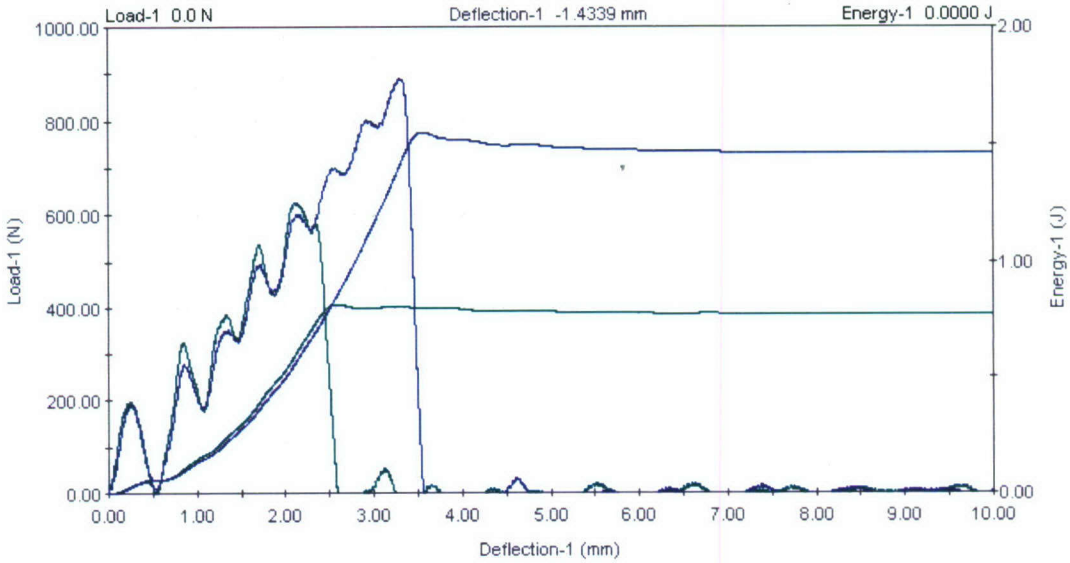

Figure 2.5.1.2: Load & Energy vs Deflection graph for un-notched 1.25 wt percent MWCNT reinforced nylon 6,6 specimens

Table 2.5.1.2: Impact characteristics of un-notched 1.25 wt percent MWCNT reinforced nylon 6,6 specimens

Specimen ID	Maximum load (N)	Energy to max load (J)	NTT energy to max load (J/mm)	Total energy* (J)	NTT total energy* (J/mm)	Impact energy (J)	Impact velocity (m/s)
NM12CI01	634.5	0.5977	0.0477	0.7917	0.0632	5.983	1.8991
NM12CI02	626.7	0.5902	0.0469	0.8144	0.0647	5.9748	1.8977
NM12CI03	890.3	1.4022	0.1114	1.5499	0.1231	5.9072	1.887
NM12CI04	699.5	0.8366	0.0665	0.9272	0.0737	5.9942	1.9008
Average	**712.8**	**0.8567**	**0.0681**	**1.0208**	**0.0812**	**5.9648**	**1.8962**
Median	**667.0**	**0.7171**	**0.0571**	**0.8708**	**0.0692**	**5.9789**	**1.8984**

Note: Data for one sample discarded as it was believed to be a stray case.

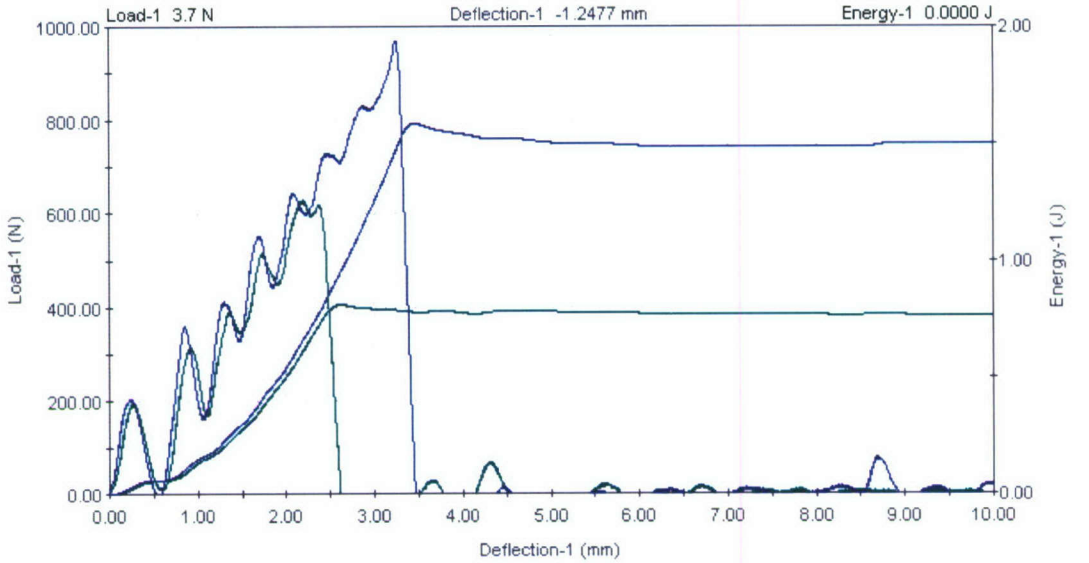

Figure 2.5.1.3: Load & Energy vs Deflection graph for un-notched 2.5 wt percent MWCNT reinforced nylon 6,6 specimens

Table 2.5.1.3: Impact characteristics of un-notched 2.5 wt percent MWCNT reinforced nylon 6,6 specimens

Specimen ID	Maximum load (N)	Energy to max load (J)	NTT energy to max load (J/mm)	Total energy* (J)	NTT total energy* (J/mm)	Impact energy (J)	Impact velocity (m/s)
NM25AI01	937.9	1.5692	0.1241	1.6877	0.1334	5.7214	1.8571
NM25AI02	813.2	1.076	0.0855	1.3261	0.1054	5.7455	1.861
NM25AI03	627.7	0.6142	0.0483	0.8125	0.0638	5.8595	1.8793
NM25AI04	741.8	0.8568	0.0676	1.0713	0.0845	5.7883	1.8679
NM25AI05	968.8	1.4735	0.1163	1.5843	0.125	5.8503	1.8779
Average	**817.9**	**1.1179**	**0.0883**	**1.2964**	**0.1024**	**5.793**	**1.8686**
Median	**813.2**	**1.076**	**0.0855**	**1.3261**	**0.1054**	**5.7883**	**1.8679**

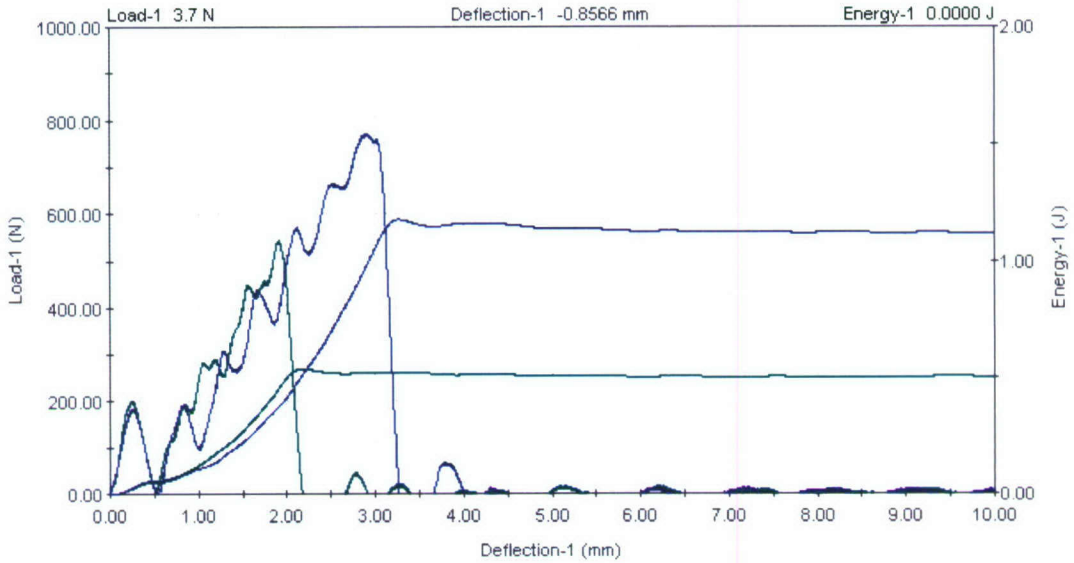

Figure 2.5.1.4: Load & Energy vs Deflection graph for un-notched 5 wt percent MWCNT reinforced nylon 6,6 specimens

Table 2.5.1.4: Impact characteristics of un-notched 5 wt percent MWCNT reinforced nylon 6,6 specimens

Specimen ID	Maximum load (N)	Energy to max load (J)	NTT energy to max load (J/mm)	Total energy* (J)	NTT total energy* (J/mm)	Impact energy (J)	Impact velocity (m/s)
NM50AI01	542.8	0.4579	0.0363	0.5392	0.0428	5.8659	1.8804
NM50AI02	748.8	0.8759	0.0695	0.9922	0.0787	5.8635	1.88
NM50AI03	749.6	0.8485	0.0675	1.0122	0.0805	5.8409	1.8764
NM50AI04	771	0.9754	0.0776	1.1771	0.0936	5.7806	1.8667
NM50AI05	627.4	0.5749	0.0457	0.6649	0.0528	5.7855	1.8674
Average	**687.9**	**0.7465**	**0.0593**	**0.8771**	**0.0697**	**5.8273**	**1.8742**
Median	**748.8**	**0.8485**	**0.0675**	**0.9922**	**0.0787**	**5.8409**	**1.8764**

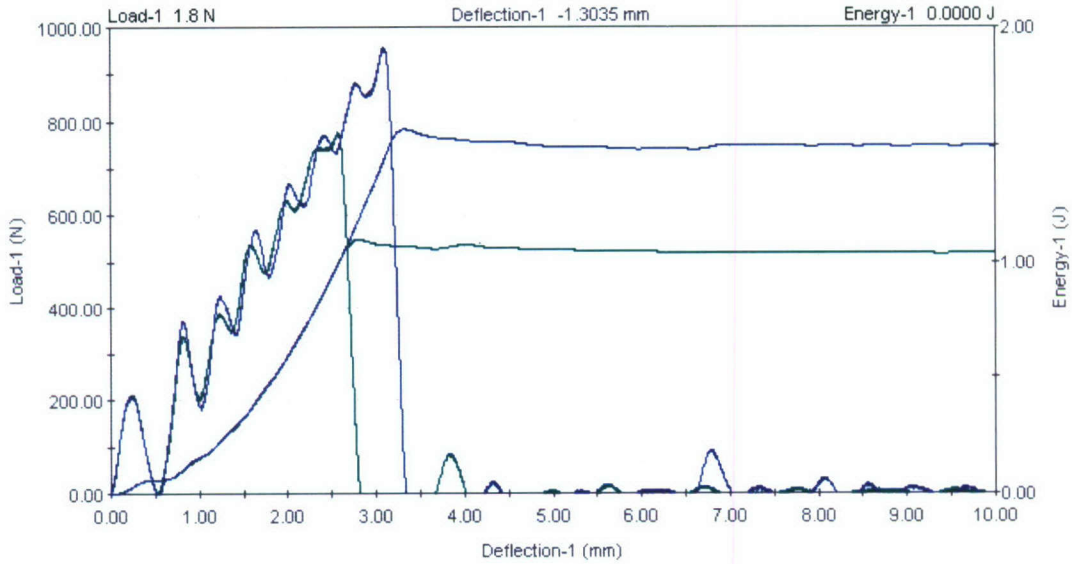

Figure 2.5.1.5: Load & Energy vs Deflection graph for un-notched 10 wt percent MWCNT reinforced nylon 6,6 specimens

Table 2.5.1.5: Impact characteristics of un-notched 10 wt percent MWCNT reinforced nylon 6,6 specimens

Specimen ID	Maximum load (N)	Energy to max load (J)	NTT energy to max load (J/mm)	Total energy* (J)	NTT total energy* (J/mm)	Impact energy (J)	Impact velocity (m/s)
NM10AI01	944.8	1.4517	0.1156	1.5965	0.1271	5.8094	1.8713
NM10AI02	778.7	0.9883	0.0782	1.0955	0.0867	5.7812	1.8667
NM10AI03	882.5	1.3035	0.1032	1.4186	0.1123	5.7987	1.8696
NM10AI04	950.4	1.3721	0.1088	1.4874	0.1179	5.8402	1.8762
NM10AI05	956.7	1.4348	0.1142	1.5664	0.1247	5.7943	1.8689
Average	**902.6**	**1.3101**	**0.104**	**1.4329**	**0.1137**	**5.8048**	**1.8705**
Median	**944.8**	**1.3721**	**0.1088**	**1.4874**	**0.1179**	**5.7987**	**1.8696**

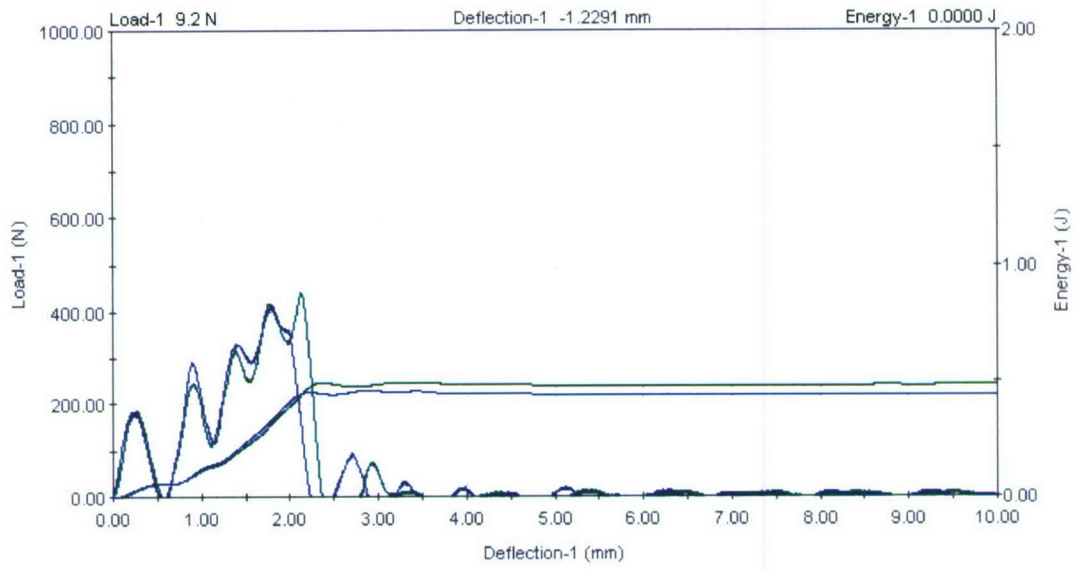

Figure 2.5.1.6: Load & Energy vs Deflection graph for notched pure nylon 6,6 specimens

Table 2.5.1.6: Impact characteristics of notched pure nylon 6,6 specimens

Specimen ID	Maximum load (N)	Energy to max load (J)	NTT energy to max load (J/mm)	Total energy* (J)	NTT total energy* (J/mm)	Impact energy (J)	Impact velocity (m/s)
NM00AI06	393.7	0.3259	0.0321	0.468	0.0461	5.8291	1.8745
NM00AI07	430.5	0.4295	0.0422	0.4895	0.0481	5.799	1.8696
NM00AI08	437.6	0.3399	0.0336	0.4875	0.0482	5.757	1.8628
NM00AI09	441.3	0.4378	0.0428	0.4967	0.0485	5.7846	1.8673
NM00AI10	411.8	0.3347	0.0332	0.4515	0.0448	5.7874	1.8677
Average	**423.0**	**0.3736**	**0.0368**	**0.4786**	**0.0471**	**5.7914**	**1.8684**
Median	**430.5**	**0.3399**	**0.0336**	**0.4875**	**0.0481**	**5.7874**	**1.8677**

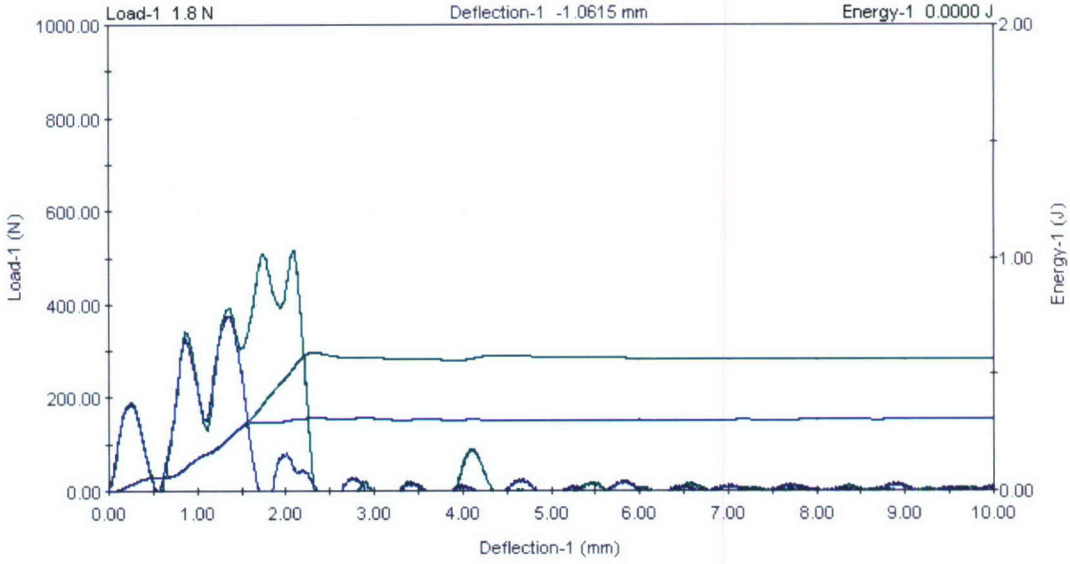

Graph 2.5.1.7: Load & Energy vs Deflection graph for notched 1.25 wt percent MWCNT reinforced nylon 6,6 specimens

Table 2.5.1.7: Impact characteristics of notched 1.25 wt percent MWCNT reinforced nylon 6,6 specimens

Specimen ID	Maximum load (N)	Energy to max load (J)	NTT energy to max load (J/mm)	Total energy* (J)	NTT total energy* (J/mm)	Impact energy (J)	Impact velocity (m/s)
NM12CI06	514.7	0.5309	0.0515	0.5937	0.0576	5.9728	1.8974
NM12CI07	491	0.3692	0.0367	0.4771	0.0474	5.9595	1.8953
NM12CI08	383.7	0.2208	0.0219	0.3274	0.0324	5.9932	1.9007
NM12CI09	381.7	0.3087	0.0312	0.3623	0.0366	5.9382	1.8919
NM12CI10	376.2	0.2289	0.023	0.2983	0.0299	5.9525	1.8942
Average	**429.5**	**0.3317**	**0.0328**	**0.4118**	**0.0408**	**5.9632**	**1.8959**
Median	**383.7**	**0.3087**	**0.0312**	**0.3623**	**0.0366**	**5.9595**	**1.8953**

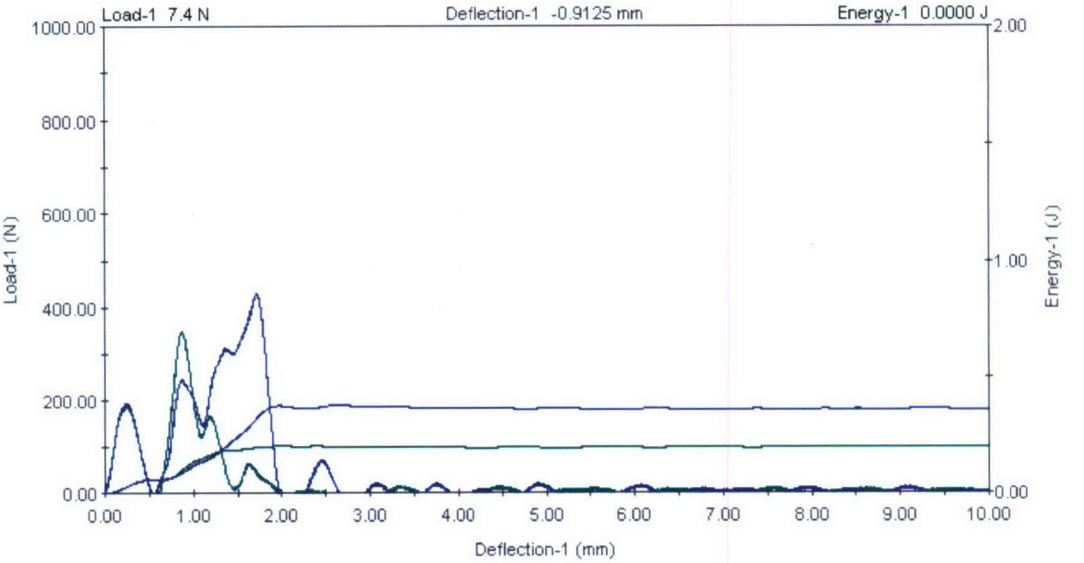

Figure 2.5.1.8: Load & Energy vs Deflection graph for notched 2.5 wt percent MWCNT reinforced nylon 6,6 specimens

Table 2.5.1.8: Impact characteristics of notched 2.5 wt percent MWCNT reinforced nylon 6,6 specimens

Specimen ID	Maximum load (N)	Energy to max load (J)	NTT energy to max load (J/mm)	Total energy* (J)	NTT total energy* (J/mm)	Impact energy (J)	Impact velocity (m/s)
NM25AI06	349.2	0.0978	0.0096	0.2018	0.0199	5.7971	1.8693
NM25AI07	380.4	0.2233	0.0222	0.3116	0.031	5.8457	1.8771
NM25AI08	430.2	0.3159	0.0311	0.3783	0.0373	5.8429	1.8767
NM25AI09	393.3	0.2164	0.0217	0.3064	0.0307	5.8259	1.874
NM25AI10	365.7	0.2076	0.0205	0.2908	0.0287	5.8258	1.8739
Average	**383.7**	**0.2122**	**0.021**	**0.2978**	**0.0295**	**5.8275**	**1.8742**
Median	**380.4**	**0.2164**	**0.0217**	**0.3064**	**0.0307**	**5.8259**	**1.874**

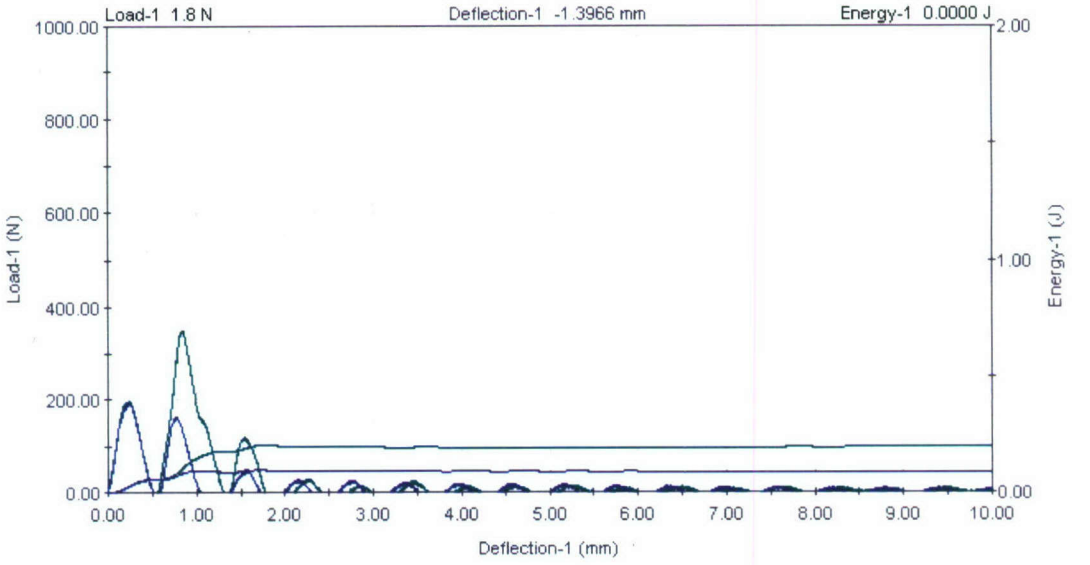

Figure 2.5.1.9: Load & Energy vs Deflection graph for notched 5 wt percent MWCNT reinforced nylon 6,6 specimens

Table 2.5.1.9: Impact characteristics of notched 5 wt percent MWCNT reinforced nylon 6,6 specimens

Specimen ID	Maximum load (N)	Energy to max load (J)	NTT energy to max load (J/mm)	Total energy* (J)	NTT total energy* (J/mm)	Impact energy (J)	Impact velocity (m/s)
NM50AI06	336.3	0.0982	0.0096	0.174	0.0171	5.856	1.8788
NM50AI07	347.3	0.1029	0.0101	0.1644	0.0161	5.8446	1.877
NM50AI08	328.9	0.0996	0.0099	0.1612	0.0161	5.8004	1.8698
NM50AI09	351	0.1003	0.0097	0.1781	0.0173	5.7895	1.8681
NM50AI10	193	0.026	0.0026	0.0551	0.0054	5.8009	1.8699
Average	**311.3**	**0.0854**	**0.0084**	**0.1466**	**0.0144**	**5.8183**	**1.8727**
Median	**336.3**	**0.0996**	**0.0097**	**0.1644**	**0.0161**	**5.8009**	**1.8699**

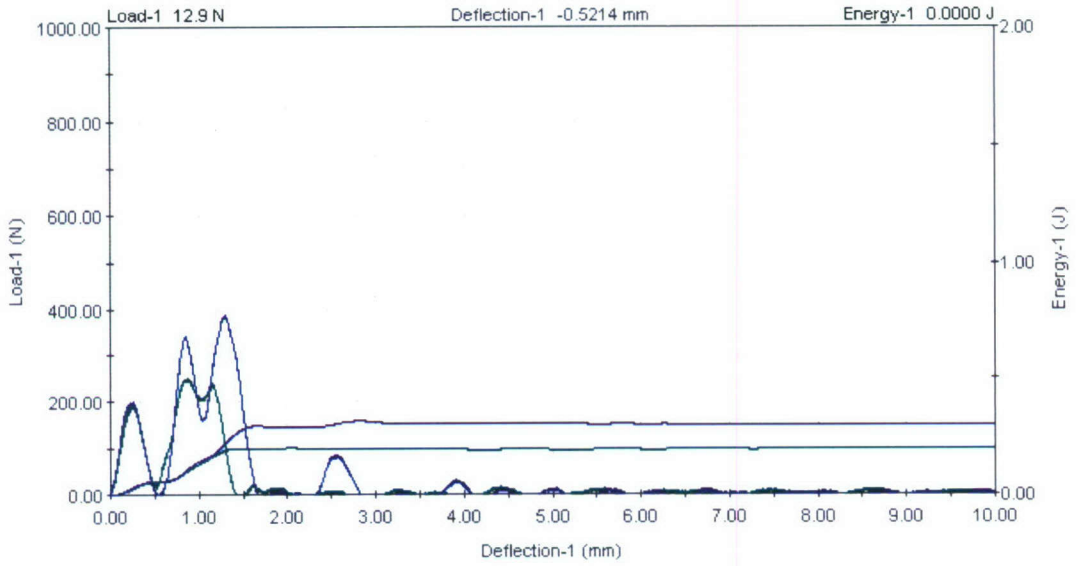

Figure 2.5.1.10: Load & Energy vs Deflection graph for notched 10 wt percent MWCNT reinforced nylon 6,6 specimens

Table 2.5.1.10: Impact characteristics of notched 10 wt percent MWCNT reinforced nylon 6,6 specimens

Specimen ID	Maximum load (N)	Energy to max load (J)	NTT energy to max load (J/mm)	Total energy* (J)	NTT total energy* (J/mm)	Impact energy (J)	Impact velocity (m/s)
NM10AI06	345.3	0.1029	0.0101	0.1686	0.0165	5.8405	1.8763
NM10AI07	249.9	0.1018	0.0102	0.197	0.0197	5.8325	1.875
NM10AI08	334.3	0.1028	0.0103	0.2131	0.0213	5.8786	1.8824
NM10AI09	387.7	0.222	0.0214	0.2947	0.0284	5.8255	1.8739
NM10AI10	345.1	0.1023	0.0102	0.1658	0.0166	5.8589	1.8792
Average	**332.5**	**0.1264**	**0.0124**	**0.2078**	**0.0205**	**5.8472**	**1.8774**
Median	**345.2**	**0.1028**	**0.0102**	**0.197**	**0.0197**	**5.8405**	**1.8763**

2.5.1a Summary of Results

Figure 2.5.1.11 to 2.5.1.15 show the summarized output for Nylon 6,6 and their nano reinforced composite. It is to be noted that 5 notched and 5 un-notched specimens from each category are tested to obtain a statistically significant data while data of 1 un-notched specimen from 1.25 wt percent reinforced composite is discarded.

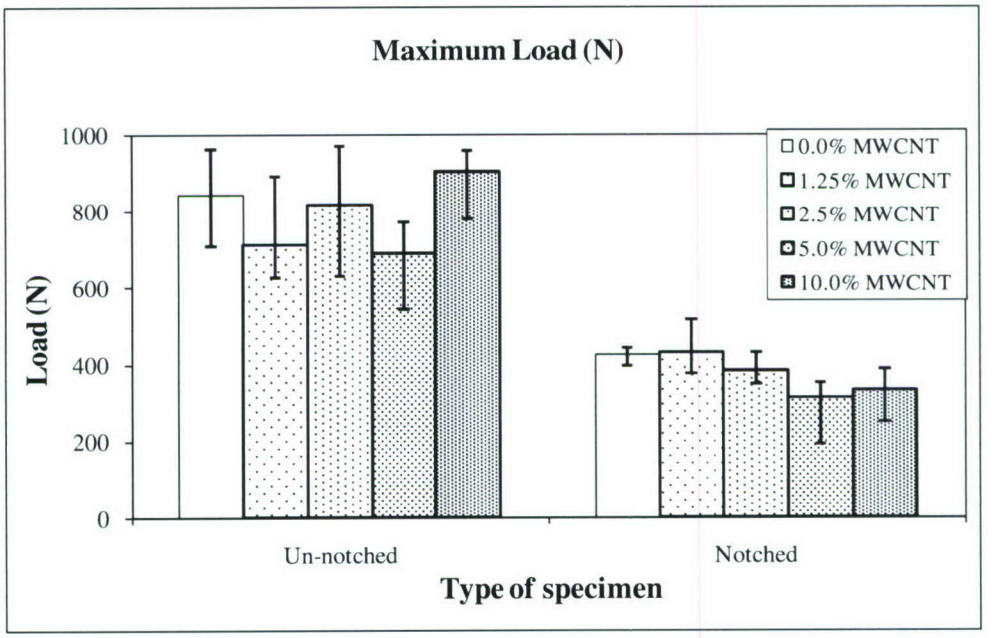

Figure 2.5.1.11: Maximum load comparison for notched & un-notched pure nylon 6,6 and MWCNT reinforced composites.

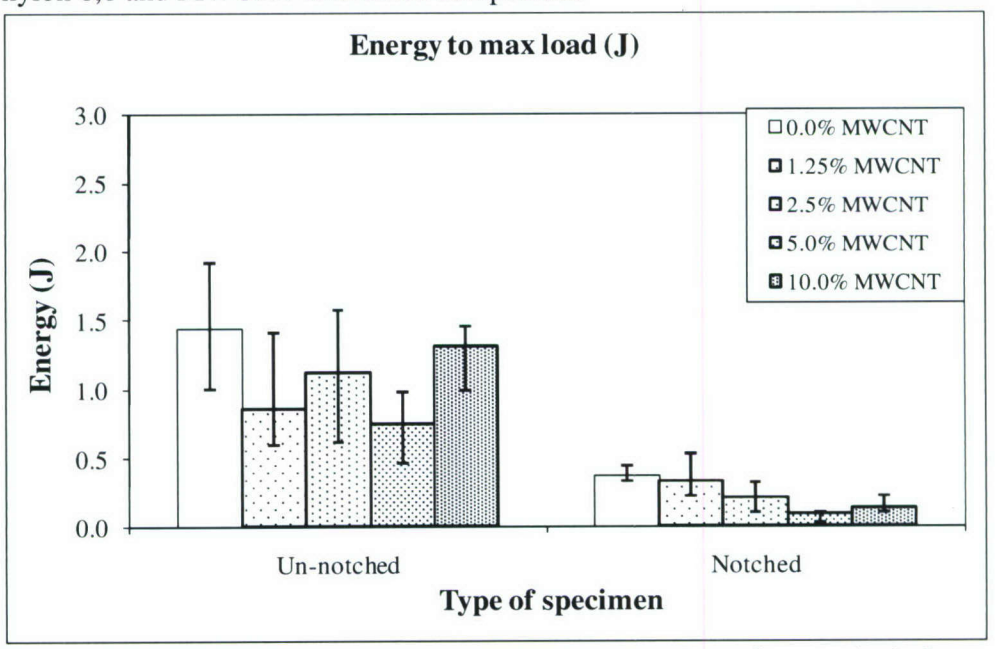

Figure 2.5.1.12: Energy to maximum load comparison for notched & un-notched pure nylon 6,6 and MWCNT reinforced composites.

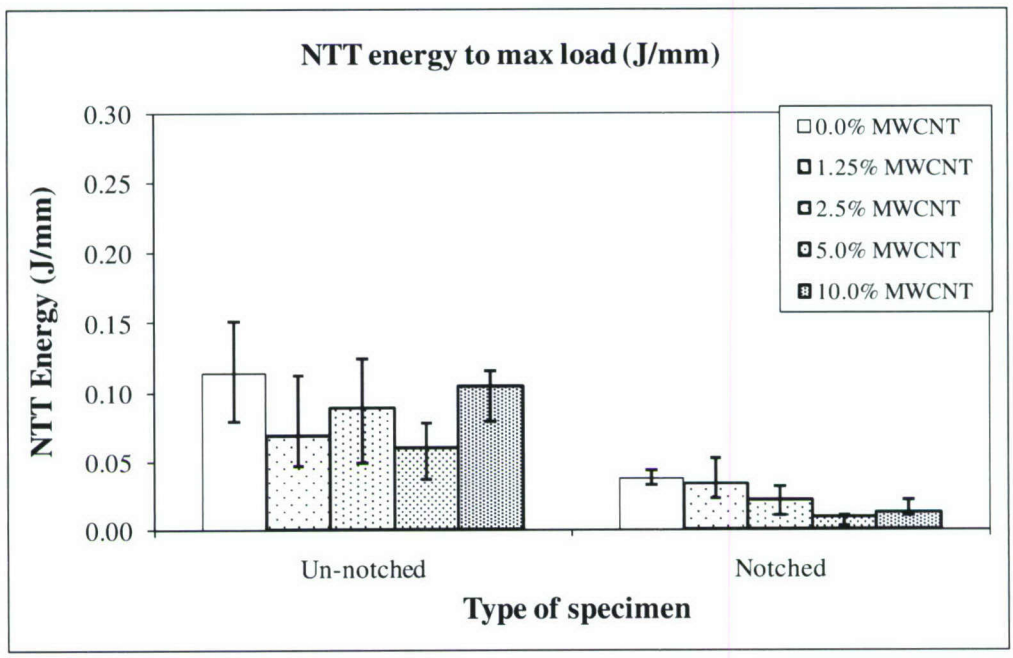

Figure 2.5.1.13: NTT energy to maximum load comparison for notched & un-notched pure nylon 6,6 and MWCNT reinforced composites.

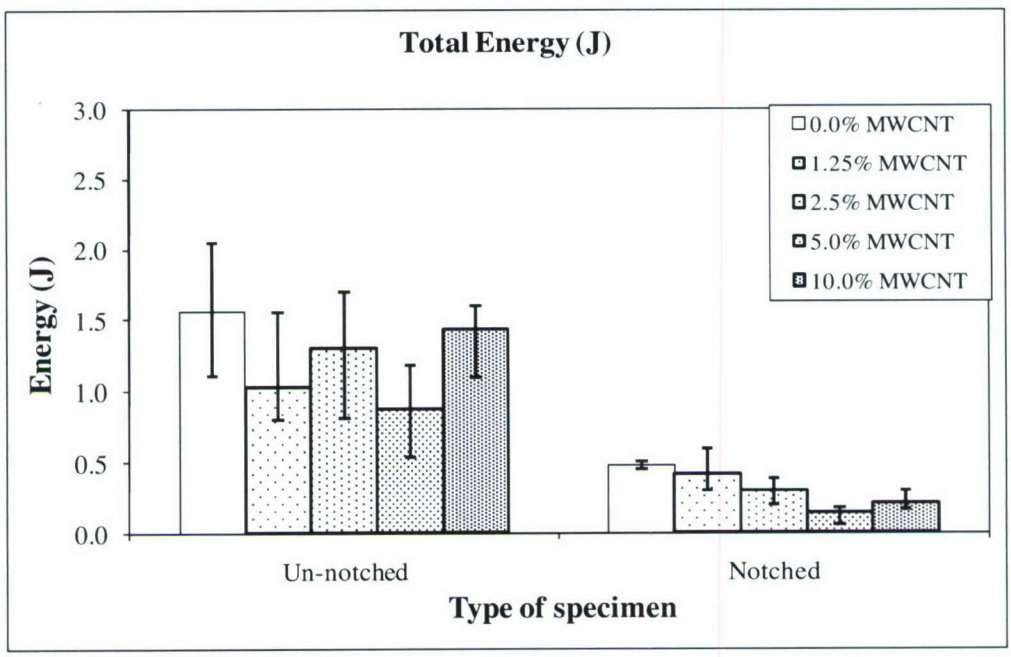

Figure 2.5.1.14: Total energy comparison for notched & un-notched pure nylon 6,6 and MWCNT reinforced composites.

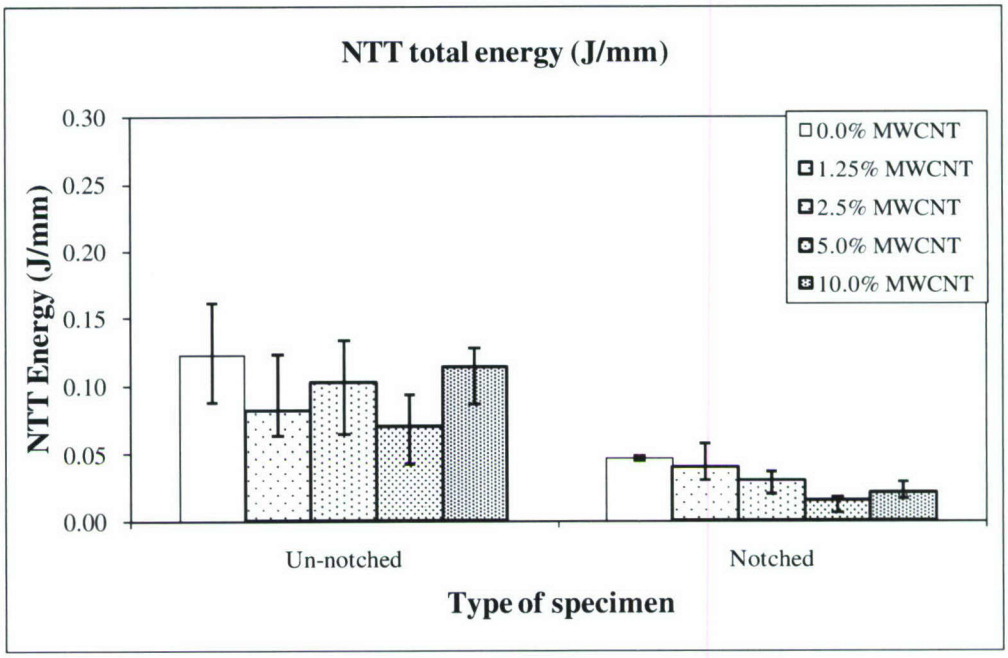

Figure 2.5.1.15: NTT total energy comparison for notched & un-notched pure nylon 6,6 and MWCNT reinforced composites.

2.5.1b Conclusion

It is observed that for notched nylon 6,6 samples load and energy absorption decreases with increase in MWCNT reinforcement. However due to broad scatter band, especially in un-notched sample, no firm conclusion can be presented.

The fractured surface of un-notched sample is observed to be non-uniform while for notched sample, in most cases it was smooth. Analysis of fractured surface using atomic force microscopy (AFM) is in process to determine the effect of presence of MWCNT's in fractured layer, if any.

2.5.2 Notched nylon 6,6 and reinforced nanocomposite after 45 days and 90 days of accelerated aging

Test results and data for impact experiments on notched nylon 6,6 and nanoreinforced composites after 45 days and 90 days of accelerated aging (freeze-thaw cycling as per ASTM C666-97) are shown in Figure 2.5.2.1 to 2.5.2.10 & Table 2.5.2.1 to 2.5.2.10. Graphs below show the trend for two specimens only. It is to be noted that energy* computed is the energy at a point where load becomes zero after registering maximum load as calculated by the Instron machine software. It is also to be noted that drop wt was increased for 1.25 wt percent reinforced sample for 90 days aged sample in order to obtain the complete fracture.

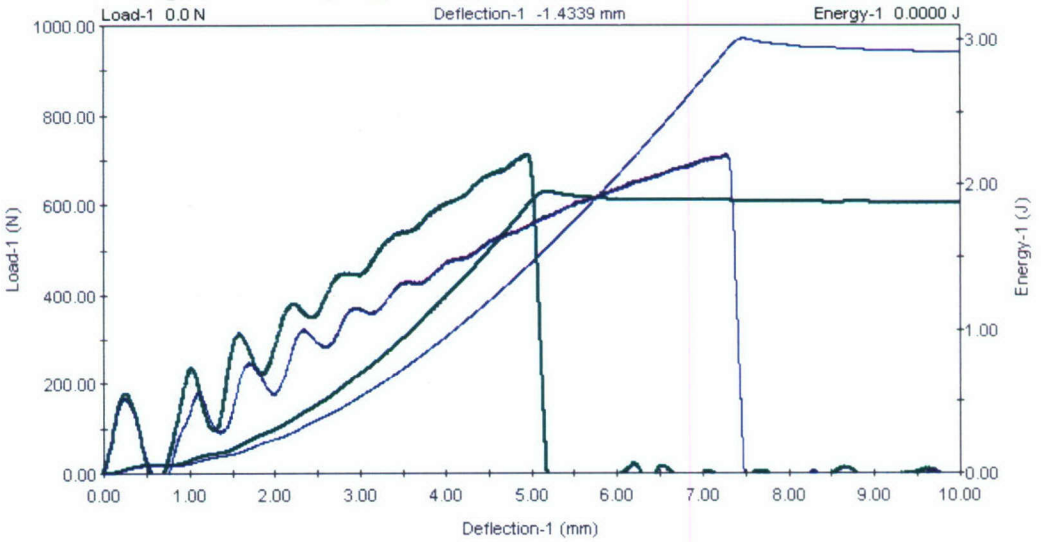

Figure 2.5.2.1: Load & Energy vs Deflection graph for notched pure nylon 6,6 specimens after 45 days of accelerated environmental aging.

Table 2.5.2.1: Impact characteristics of notched pure nylon 6,6 specimens after 45 days of accelerated environmental aging.

Specimen ID	Maximum load (N)	Energy to max load (J)	NTT energy to max load (J/mm)	Total energy* (J)	NTT total energy* (J/mm)	Impact energy (J)	Impact velocity (m/s)
NM00AI16	715.2	1.8513	0.1827	1.9543	0.1928	5.769	1.8648
NM00AI17	713	2.9145	0.2799	3.0083	0.2889	5.738	1.8598
NM00AI18	730	2.1014	0.2058	2.1999	0.2154	5.8101	1.8714
NM00AI19	726.7	2.4984	0.2478	2.5874	0.2566	5.7712	1.8651
NM00AI20	694.6	2.3056	0.2298	2.3983	0.239	5.8306	1.8747
Average	**715.9**	**2.3343**	**0.2292**	**2.4296**	**0.2386**	**5.7838**	**1.8672**
Median	**715.2**	**2.3056**	**0.2298**	**2.3983**	**0.239**	**5.7712**	**1.8651**

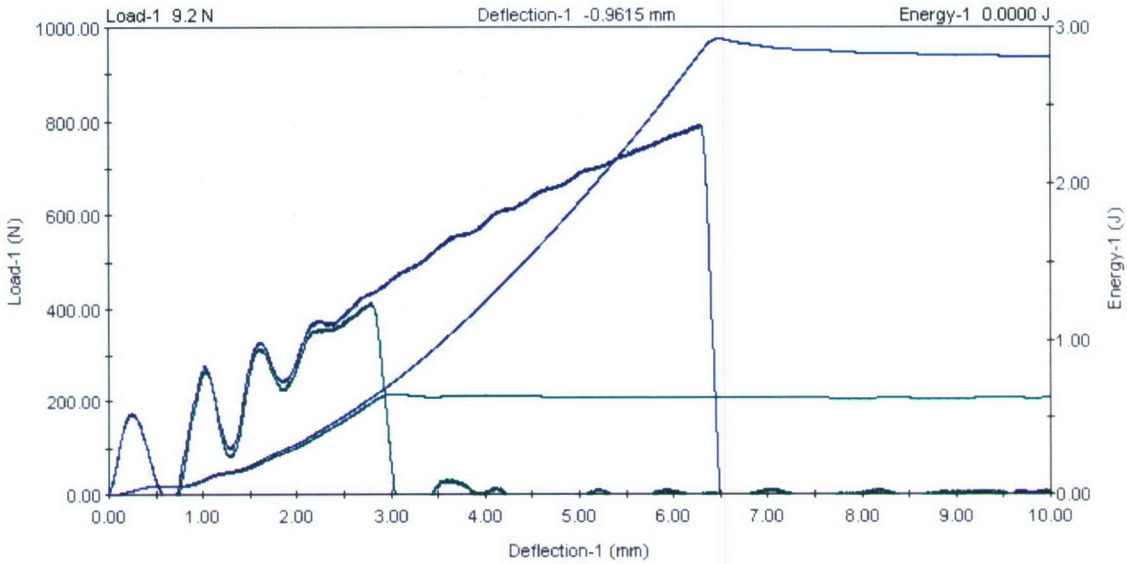

Figure 2.5.2.2: Load & Energy vs Deflection graph for notched 1.25 wt percent MWCNT reinforced nylon 6,6 specimens after 45 days of accelerated environmental aging.

Table 2.5.2.2: Impact characteristics of notched 1.25 wt percent MWCNT reinforced nylon 6,6 specimens after 45 days of accelerated environmental aging.

Specimen ID	Maximum load (N)	Energy to max load (J)	NTT energy to max load (J/mm)	Total energy* (J)	NTT total energy* (J/mm)	Impact energy (J)	Impact velocity (m/s)
NM12AI16	413.3	0.5862	0.0563	0.6496	0.0624	5.9259	1.89
NM12AI17	792	2.8288	0.27	2.9232	0.279	5.965	1.8962
NM12AI18	668.9	1.7185	0.1675	1.8224	0.1776	5.9989	1.9016
NM12AI19	428.2	0.6257	0.061	0.6912	0.0674	5.948	1.8935
NM12AI20	613.5	1.6634	0.1601	1.7642	0.1698	5.9507	1.8939
Average	**583.2**	**1.4845**	**0.143**	**1.5701**	**0.1512**	**5.9577**	**1.895**
Median	**613.5**	**1.6634**	**0.1601**	**1.7642**	**0.1698**	**5.9507**	**1.8939**

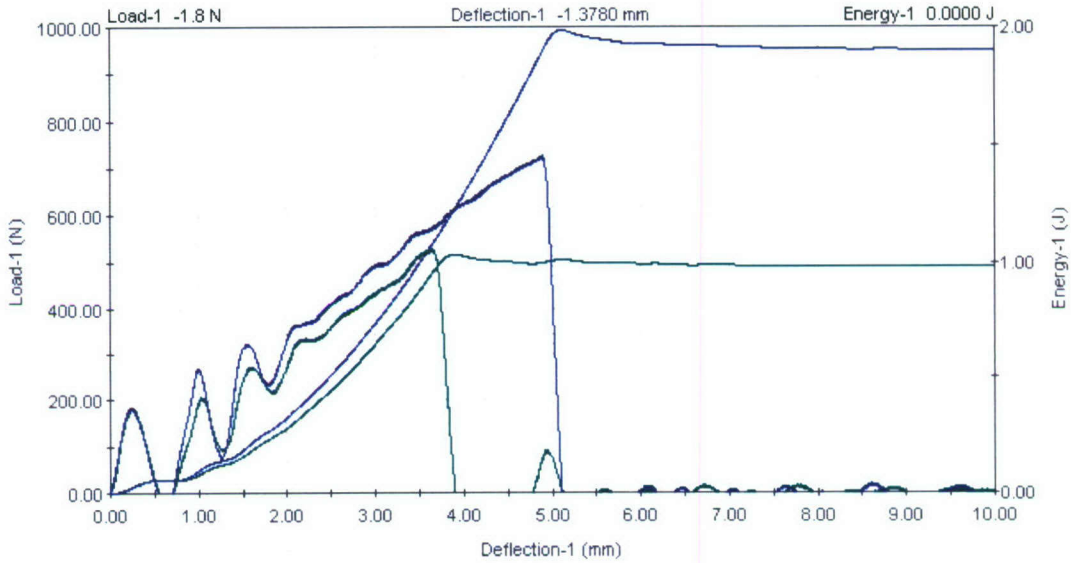

Figure 2.5.2.3: Load & Energy vs Deflection graph for notched 2.5 wt percent MWCNT reinforced nylon 6,6 specimens after 45 days of accelerated environmental aging.

Table 2.5.2.3: Impact characteristics of notched 2.5 wt percent MWCNT reinforced nylon 6,6 specimens after 45 days of accelerated environmental aging.

Specimen ID	Maximum load (N)	Energy to max load (J)	NTT energy to max load (J/mm)	Total energy* (J)	NTT total energy* (J/mm)	Impact energy (J)	Impact velocity (m/s)
NM25AI16	571.2	1.0738	0.107	1.157	0.1153	5.8419	1.8765
NM25AI17	528.5	0.9429	0.0926	1.0328	0.1014	5.8176	1.8726
NM25AI18	690.9	1.6081	0.1579	1.709	0.1678	5.8074	1.871
NM25AI19	665.8	1.4501	0.1424	1.5433	0.1515	5.7848	1.8673
NM25AI20	726.3	1.8916	0.1912	1.9859	0.2007	5.824	1.8736
Average	**636.5**	**1.3933**	**0.1382**	**1.4856**	**0.1474**	**5.8152**	**1.8722**
Median	**665.8**	**1.4501**	**0.1424**	**1.5433**	**0.1515**	**5.8176**	**1.8726**

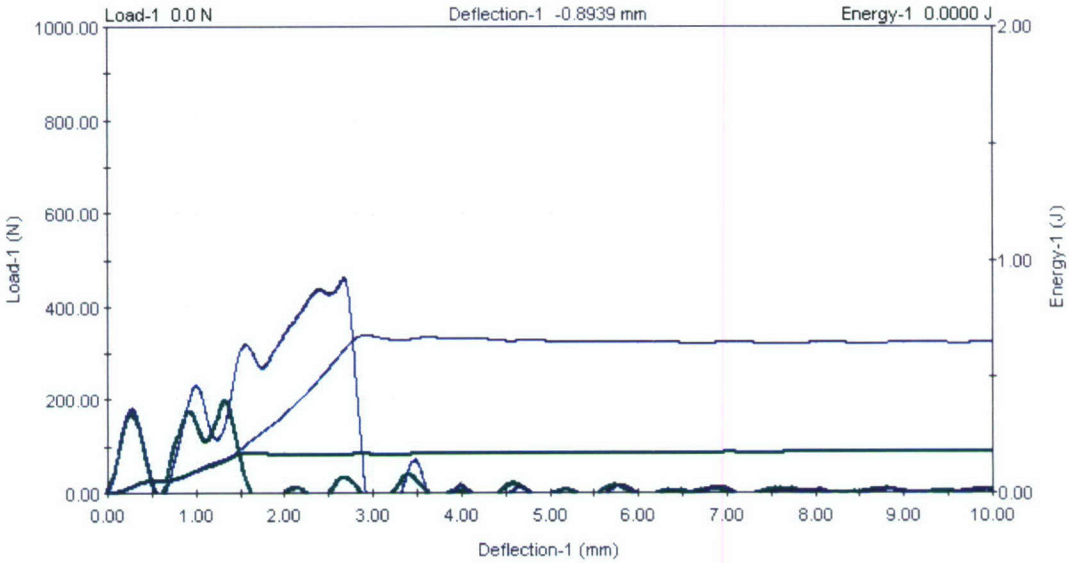

Figure 2.5.2.4: Load & Energy vs Deflection graph for notched 5 wt percent MWCNT reinforced nylon 6,6 specimens after 45 days of accelerated environmental aging.

Table 2.5.2.4: Impact characteristics of notched 5 wt percent MWCNT reinforced nylon 6,6 specimens after 45 days of accelerated environmental aging.

Specimen ID	Maximum load (N)	Energy to max load (J)	NTT energy to max load (J/mm)	Total energy* (J)	NTT total energy* (J/mm)	Impact energy (J)	Impact velocity (m/s)
NM50AI16	200.9	0.1399	0.0142	0.171	0.0174	5.8418	1.8765
NM50AI17	391.2	0.4387	0.0428	0.4925	0.0481	5.8268	1.8741
NM50AI18	462.9	0.6126	0.0607	0.6786	0.0673	5.8439	1.8768
NM50AI19	348.6	0.2103	0.0207	0.3019	0.0298	5.8209	1.8731
NM50AI20	326.8	0.0977	0.0095	0.1889	0.0183	5.83	1.8746
Average	**346.1**	**0.2998**	**0.0296**	**0.3666**	**0.0362**	**5.8327**	**1.875**
Median	**348.6**	**0.2103**	**0.0207**	**0.3019**	**0.0298**	**5.83**	**1.8746**

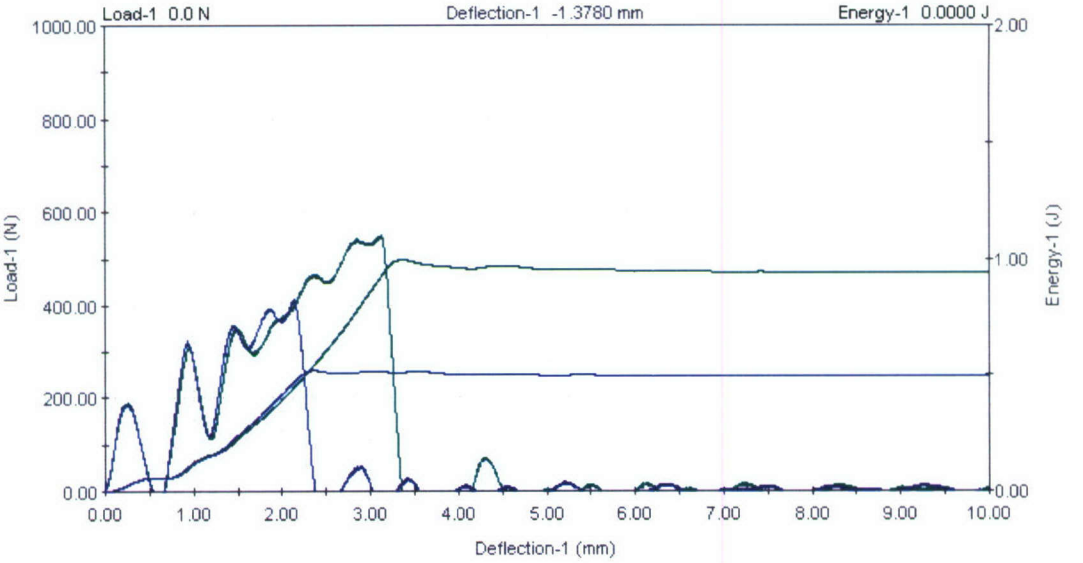

Figure 2.5.2.5: Load & Energy vs Deflection graph for notched 10 wt percent MWCNT reinforced nylon 6,6 specimens after 45 days of accelerated environmental aging.

Table 2.5.2.5: Impact characteristics of notched 10 wt percent MWCNT reinforced nylon 6,6 specimens after 45 days of accelerated environmental aging.

Specimen ID	Maximum load (N)	Energy to max load (J)	NTT energy to max load (J/mm)	Total energy* (J)	NTT total energy* (J/mm)	Impact energy (J)	Impact velocity (m/s)
NM10AI16	490.9	0.657	0.0642	0.7218	0.0705	5.8359	1.8756
NM10AI17	549.9	0.9239	0.0913	0.9957	0.0984	5.803	1.8703
NM10AI18	413.1	0.4689	0.0469	0.5205	0.052	5.7952	1.869
NM10AI19	575.7	0.7589	0.0758	0.9291	0.0928	5.7979	1.8694
NM10AI20	476.3	0.5319	0.0524	0.6047	0.0596	5.7932	1.8687
Average	**501.2**	**0.6681**	**0.0661**	**0.7544**	**0.0747**	**5.805**	**1.8706**
Median	**490.9**	**0.657**	**0.0642**	**0.7218**	**0.0705**	**5.7979**	**1.8694**

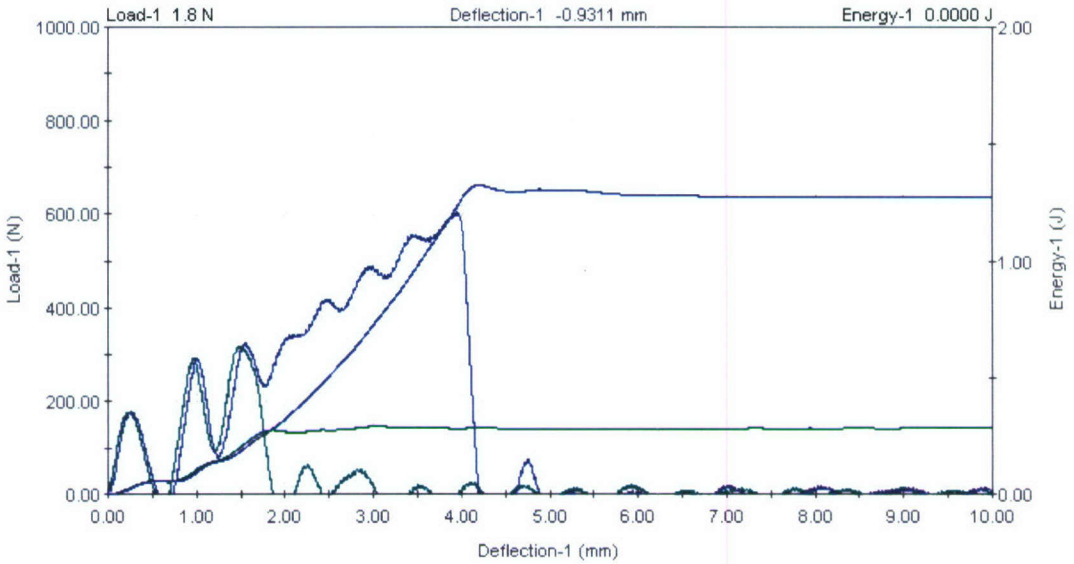

Figure 2.5.2.6: Load & Energy vs Deflection graph for pure notched nylon 6,6 specimens after 90 days of accelerated environmental aging.

Table 2.5.2.6: Impact characteristics of pure notched nylon 6,6 specimens after 90 days of accelerated environmental aging.

Specimen ID	Maximum load (N)	Energy to max load (J)	NTT energy to max load (J/mm)	Total energy* (J)	NTT total energy* (J/mm)	Impact energy (J)	Impact velocity (m/s)
NM00AI26	319.8	0.1952	0.0189	0.2794	0.027	5.9818	1.8989
NM00AI27	603.1	1.2313	0.1207	1.3213	0.1296	5.9557	1.8947
NM00AI28	358.5	0.3462	0.034	0.4294	0.0422	5.9742	1.8976
NM00AI29	496.2	0.6981	0.0679	0.9014	0.0877	5.9638	1.896
NM00AI30	549.7	0.9572	0.0919	1.0359	0.0995	5.9271	1.8902
Average	**465.5**	**0.6856**	**0.0667**	**0.7935**	**0.0772**	**5.9605**	**1.8955**
Median	**496.2**	**0.6981**	**0.0679**	**0.9014**	**0.0877**	**5.9638**	**1.896**

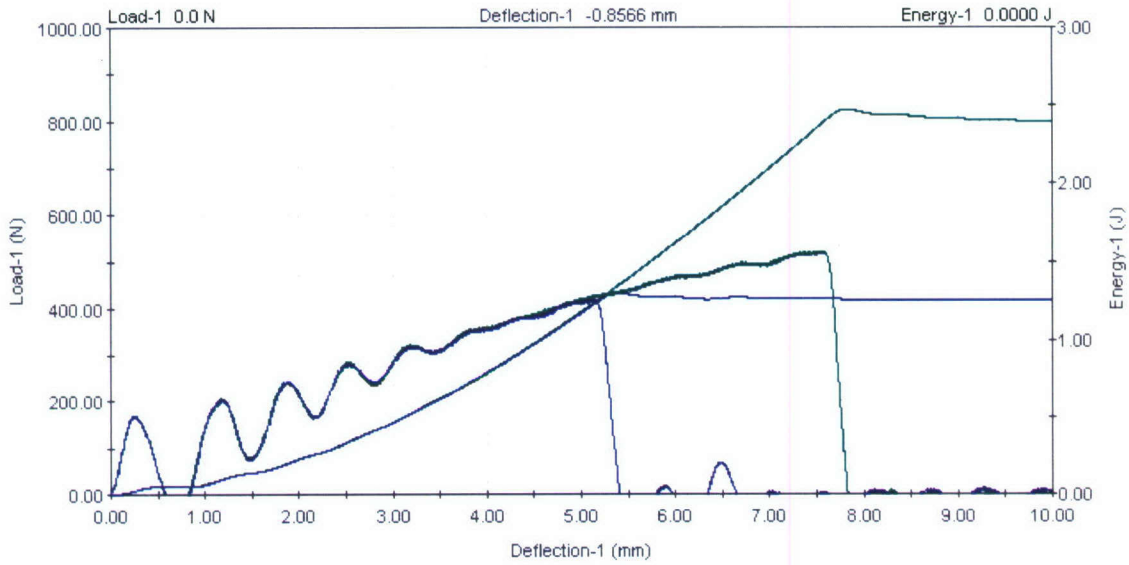

Figure 2.5.2.7: Load & Energy vs Deflection graph for notched 1.25 wt percent MWCNT reinforced nylon 6,6 specimens after 90 days of accelerated environmental aging.

Table 2.5.2.7: Impact characteristics of notched 1.25 wt percent MWCNT reinforced nylon 6,6 specimens after 90 days of accelerated environmental aging.

Specimen ID	Maximum load (N)	Energy to max load (J)	NTT energy to max load (J/mm)	Total energy* (J)	NTT total energy* (J/mm)	Impact energy (J)	Impact velocity (m/s)
NM12CI27	503.5	2.0062	0.1908	2.1339	0.2029	10.7653	1.9043
NM12CI28	520.3	2.3894	0.2294	2.4717	0.2373	10.6119	1.8906
NM12CI30	417.7	1.2083	0.1149	1.2952	0.1232	10.659	1.8948
Average	**480.5**	**1.868**	**0.1784**	**1.9669**	**0.1878**	**10.6787**	**1.8966**
Median	**503.5**	**2.0062**	**0.1908**	**2.1339**	**0.2029**	**10.659**	**1.8948**

Note: It is to be noted that load and drop height was increased to facilitate the failure of the specimen. One sample was damaged in the process and data for another sample was discarded because it was believed to be a stray case.

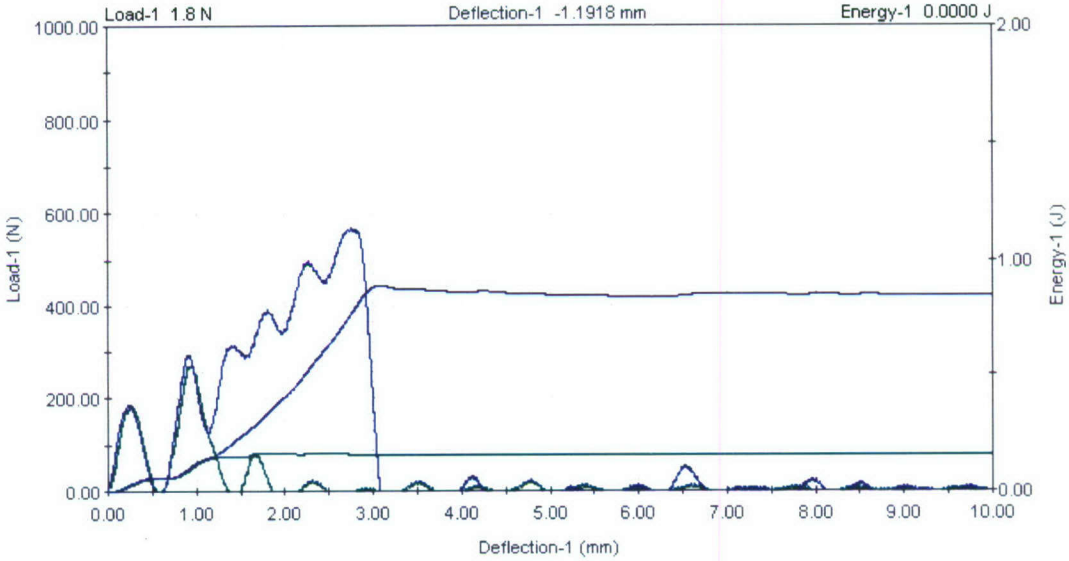

Figure 2.5.2.8: Load & Energy vs Deflection graph for notched 2.5 wt percent MWCNT reinforced nylon 6,6 specimens after 90 days of accelerated environmental aging.

Table 2.5.2.8: Impact characteristics of notched 2.5 wt percent MWCNT reinforced nylon 6,6 specimens after 90 days of accelerated environmental aging.

Specimen ID	Maximum load (N)	Energy to max load (J)	NTT energy to max load (J/mm)	Total energy* (J)	NTT total energy* (J/mm)	Impact energy (J)	Impact velocity (m/s)
NM25AI26	275.6	0.0994	0.0096	0.1503	0.0145	6.0251	1.9057
NM25AI27	329.3	0.1031	0.0099	0.1581	0.0152	5.9779	1.8982
NM25AI28	264.3	0.0902	0.0087	0.1996	0.0192	5.9696	1.8969
NM25AI29	568.1	0.7637	0.0749	0.8847	0.0868	6.0174	1.9045
NM25AI30	310.6	0.1048	0.0101	0.1576	0.0151	5.9769	1.8981
Average	**349.6**	**0.2323**	**0.0226**	**0.3101**	**0.0302**	**5.9934**	**1.9007**
Median	**310.6**	**0.1031**	**0.0099**	**0.1581**	**0.0152**	**5.9779**	**1.8982**

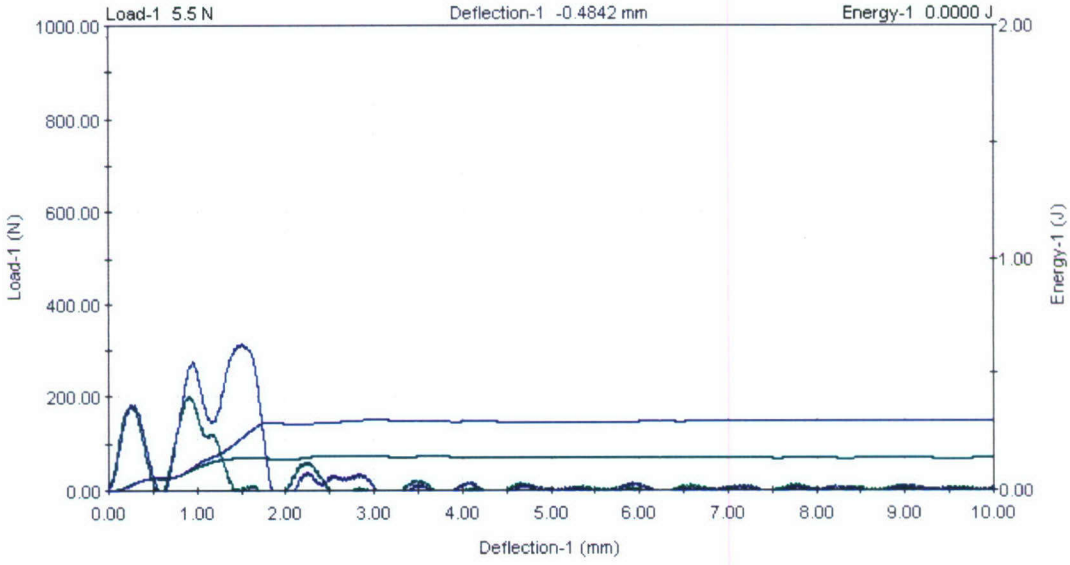

Figure 2.5.2.9: Load & Energy vs Deflection graph for notched 5 wt percent MWCNT reinforced nylon 6,6 specimens after 90 days of accelerated environmental aging.

Table 2.5.2.9: Impact characteristics of notched 5 wt percent MWCNT reinforced nylon 6,6 specimens after 90 days of accelerated environmental aging.

Specimen ID	Maximum load (N)	Energy to max load (J)	NTT energy to max load (J/mm)	Total energy* (J)	NTT total energy* (J/mm)	Impact energy (J)	Impact velocity (m/s)
NM50AI26	200.2	0.0839	0.0081	0.1379	0.0133	5.9802	1.8986
NM50AI27	290	0.0933	0.009	0.2039	0.0196	6.009	1.9032
NM50AI28	229.8	0.0873	0.0084	0.1375	0.0133	5.9673	1.8966
NM50AI29	314.1	0.2246	0.022	0.2925	0.0287	6.0037	1.9023
NM50AI30	251.6	0.0928	0.0089	0.1632	0.0157	5.9804	1.8986
Average	**257.2**	**0.1164**	**0.0113**	**0.187**	**0.0181**	**5.9881**	**1.8999**
Median	**251.6**	**0.0928**	**0.0089**	**0.1632**	**0.0157**	**5.9804**	**1.8986**

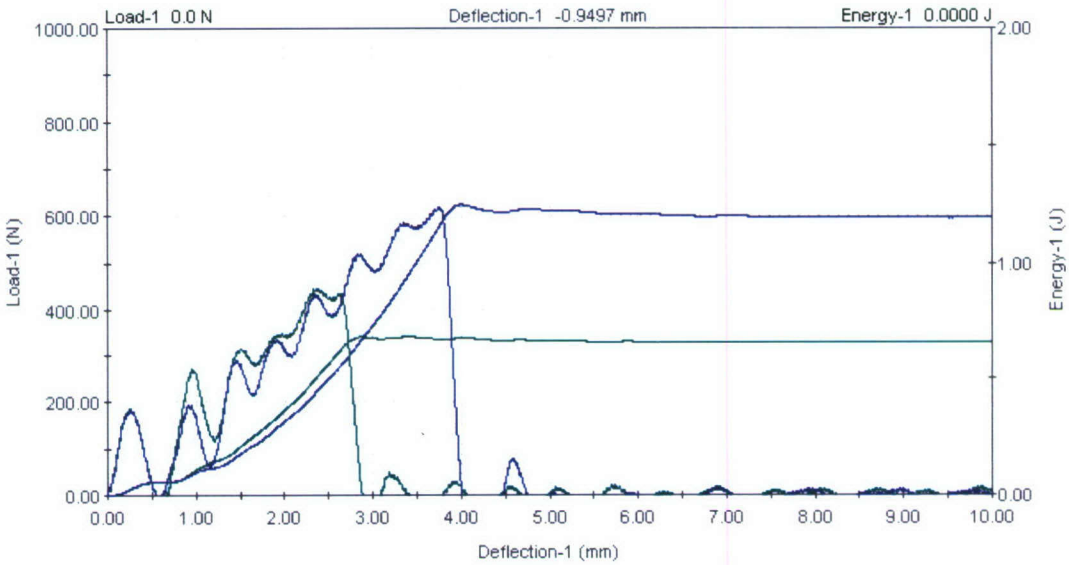

Figure 2.5.2.10: Load & Energy vs Deflection graph for notched 10 wt percent MWCNT reinforced nylon 6,6 specimens after 90 days of accelerated environmental aging.

Table 2.5.2.10: Impact characteristics of notched 10 wt percent MWCNT reinforced nylon 6,6 specimens after 90 days of accelerated environmental aging.

Specimen ID	Maximum load (N)	Energy to max load (J)	NTT energy to max load (J/mm)	Total energy* (J)	NTT total energy* (J/mm)	Impact energy (J)	Impact velocity (m/s)
NM10AI26	492.2	0.5201	0.0499	0.7199	0.0691	5.9696	1.8969
NM10AI27	444.7	0.4914	0.0481	0.6834	0.0669	5.9878	1.8998
NM10AI28	619	1.1468	0.1101	1.2476	0.1198	5.9465	1.8932
NM10AI29	472.3	0.4976	0.0475	0.5796	0.0553	5.9419	1.8925
NM10AI30	506.9	0.6937	0.0665	0.768	0.0737	6.0055	1.9026
Average	**507.0**	**0.6699**	**0.0644**	**0.7997**	**0.077**	**5.9703**	**1.897**
Median	**492.2**	**0.5201**	**0.0499**	**0.7199**	**0.0691**	**5.9696**	**1.8969**

2.5.2a Summary of Results

Figure 2.5.2.11 to 2.5.2.15 show the summarized output for effects of environmental aging on notched nylon 6,6 and their matrices with nano reinforced composite. It is to be noted that 5 notched specimens were tested for accelerated aging of 45 days and 90 days while data of 2 specimens from 90 days aging test from 1.25 wt percent reinforced composite is discarded.

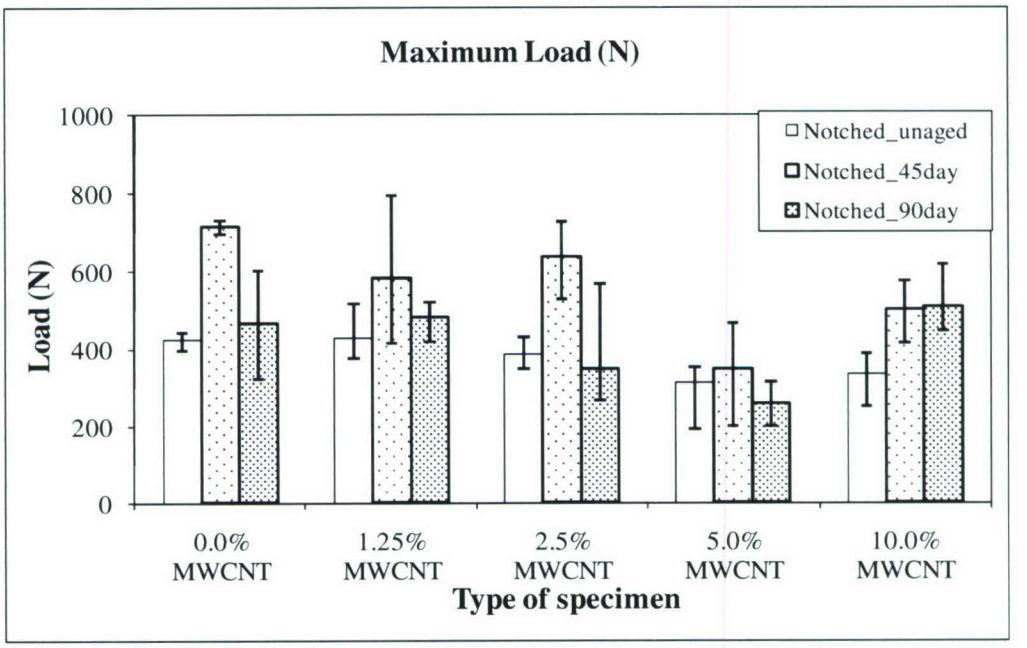

Figure 2.5.2.11: Maximum load comparison for notched nylon 6,6 and MWCNT reinforced composites with effects of aging.

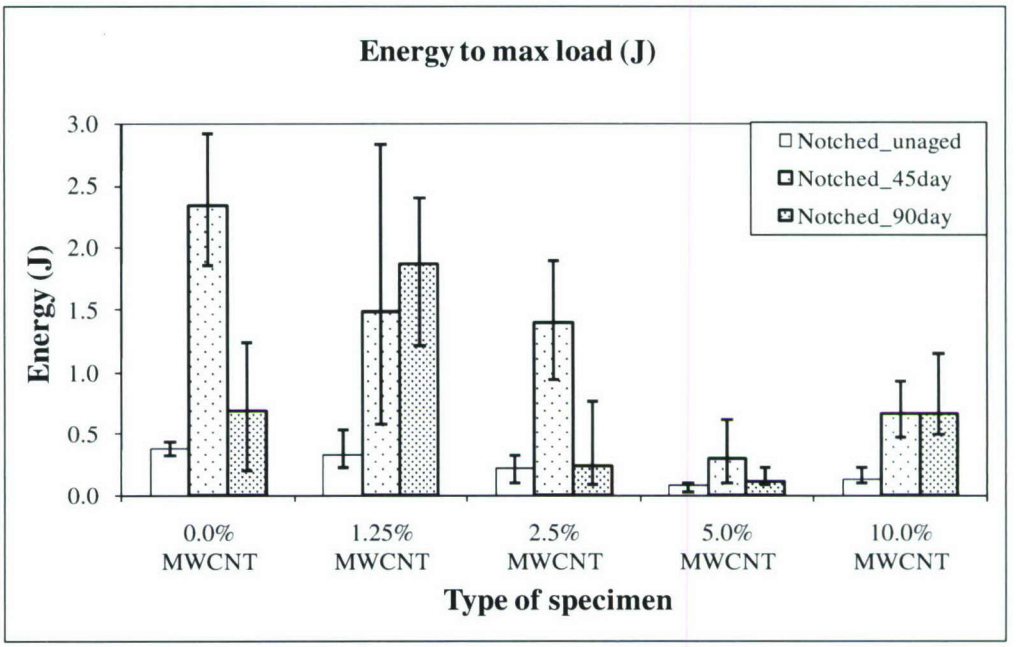

Figure 2.5.2.12: Energy to maximum load comparison for notched nylon 6,6 and MWCNT reinforced composites with effects of aging.

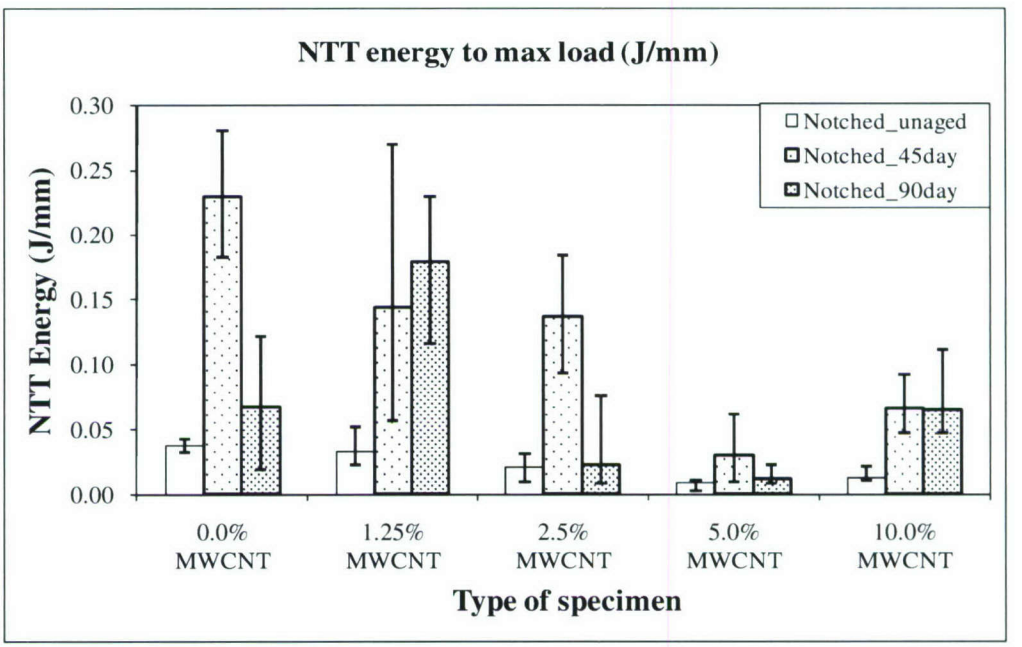

Figure 2.5.2.13: NTT energy to maximum load comparison for notched nylon 6,6 and MWCNT reinforced composites with effects of aging.

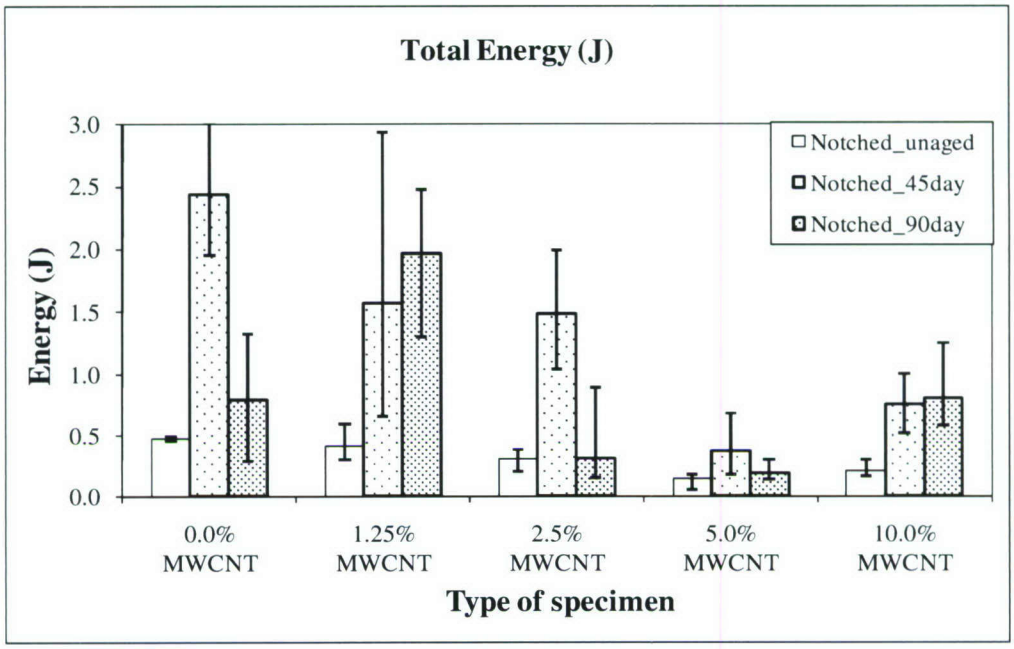

Figure 2.5.2.14: Total energy comparison for notched nylon 6,6 and MWCNT reinforced composites with effects of aging.

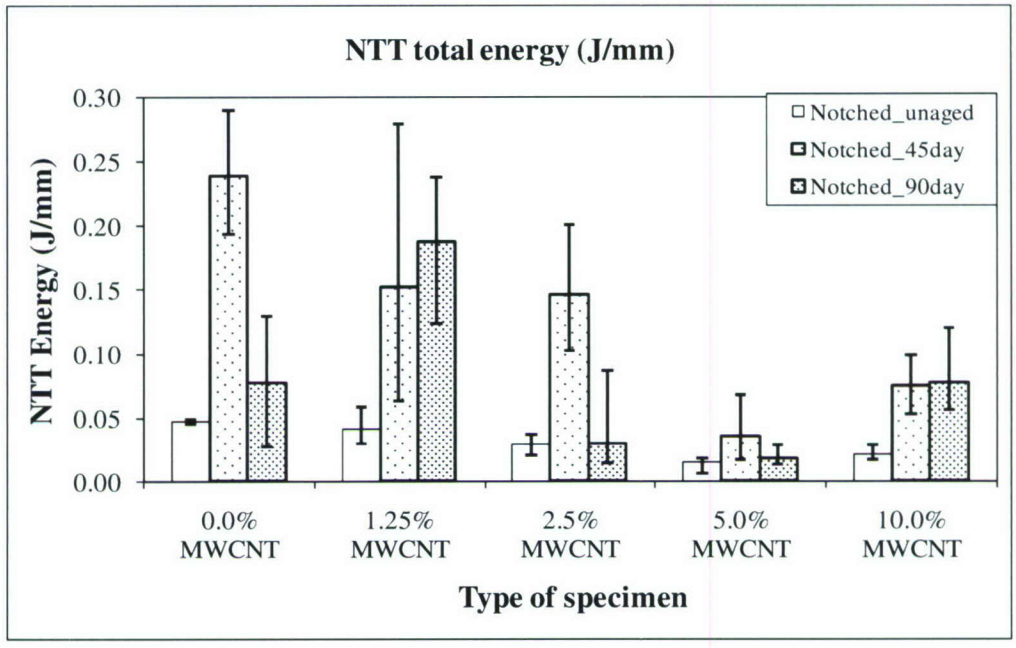

Figure 2.5.2.15: NTT total energy comparison for notched nylon 6,6 and MWCNT reinforced composites with effects of aging.

2.5.2b Conclusion

It is evident from the graphs that maximum load and energy absorption have increased significantly after 45 days of environmental aging for all nanocomposites. However, after 90 days of accelerated aging the maximum load decreased, closer to that of unaged specimens except for 10 wt percent nanocomposite.

Energy absorption increased after 45 days of accelerated aging and then decreased after 90 days of accelerated aging in all nanocomposites except 1.25 wt percent and 10 wt percent nanocomposites. Due to broad scatter band, no firm conclusion can be drawn.

2.5.3 Un-notched Nylon 6,6 and reinforced nanocomposite after 45 days and 90 days of accelerated aging

Test results and data for impact experiments on un-notched Nylon 6,6 and nanoreinforced composites after 45 days and 90 days of accelerated aging are shown in Figure 2.5.3.1 to 2.5.3.10 & Table 2.5.3.1 to 2.5.3.10. Figures show the trend for two specimens only. It is to be noted that energy* computed is the energy at a point where load becomes zero after registering maximum load as calculated by the Instron machine software.

It is to be noted that drop wt was increased to 5.95 Kg (13.09 lbs) for all 45 days aged samples and 90 days aged sample of 1.25 wt percent reinforced composite in order to obtain the complete fracture. Drop height was also increased to 355.6 mm (14") in 90 days aged sample of 1.25 wt percent reinforced composite.

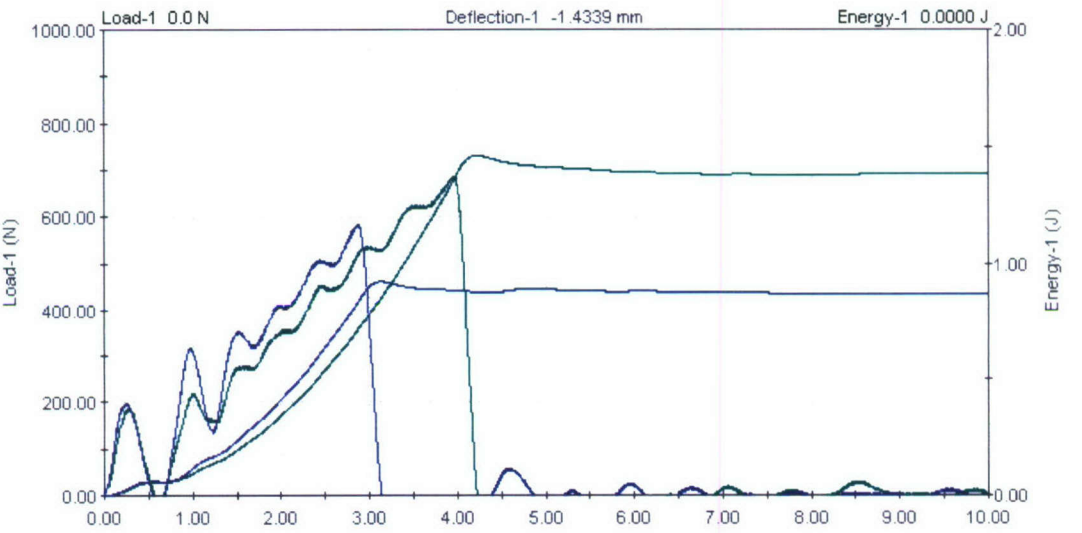

Figure 2.5.3.1: Load & Energy vs Deflection graph for un-notched pure nylon 6,6 specimens after 45 days of accelerated environmental aging.

Table 2.5.3.1: Impact characteristics of un-notched pure nylon 6,6 specimens after 45 days of accelerated environmental aging.

Specimen ID	Maximum load (N)	Energy to max load (J)	NTT energy to max load (J/mm)	Total energy* (J)	NTT total energy* (J/mm)	Impact energy (J)	Impact velocity (m/s)
NM00AI11	686.1	1.3624	0.1068	1.4649	0.1149	10.734	1.9015
NM00AI12	587.4	0.9762	0.0766	1.058	0.0831	10.6727	1.8961
NM00AI13	595.4	0.7824	0.0622	0.8624	0.0685	10.6889	1.8975
NM00AI14	582.2	0.8283	0.065	0.9234	0.0725	10.6774	1.8965
Average	**612.8**	**0.9873**	**0.0777**	**1.0772**	**0.0847**	**10.6932**	**1.8979**
Median	**591.4**	**0.9023**	**0.0708**	**0.9907**	**0.0778**	**10.6831**	**1.897**

Note: Only 4 samples were tested due to one sample damaged during machine set-up.

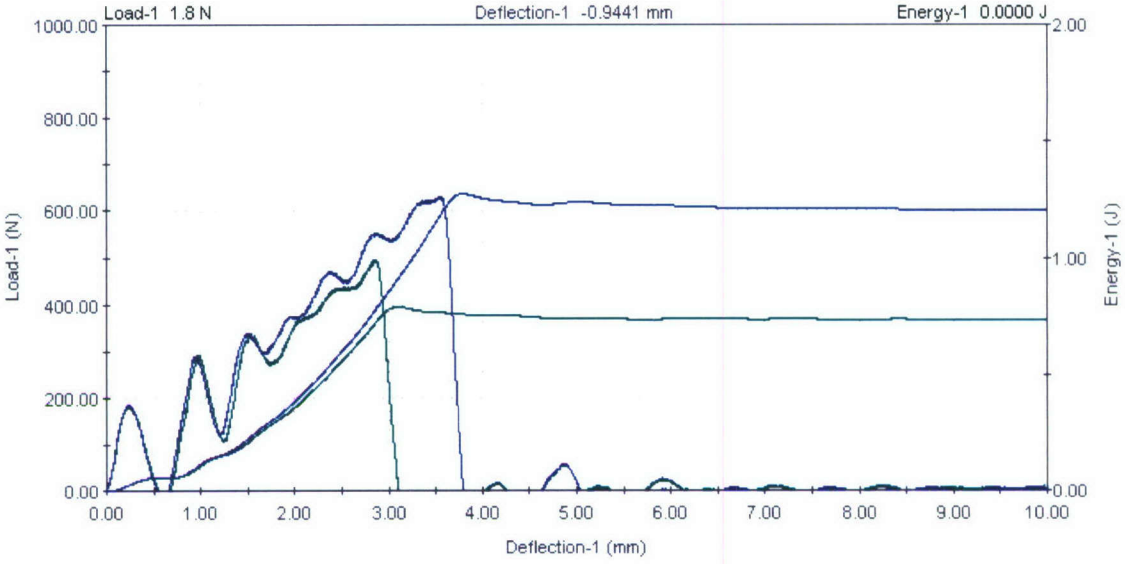

Figure 2.5.3.2: Load & Energy vs Deflection graph for un-notched 1.25 wt percent MWCNT reinforced nylon 6,6 specimens after 45 days of accelerated environmental aging.

Table 2.5.3.2: Impact characteristics of un-notched 1.25 wt percent MWCNT reinforced nylon 6,6 specimens after 45 days of accelerated environmental aging.

Specimen ID	Maximum load (N)	Energy to max load (J)	NTT energy to max load (J/mm)	Total energy* (J)	NTT total energy* (J/mm)	Impact energy (J)	Impact velocity (m/s)
NM12AI11	495.7	0.7226	0.0564	0.7915	0.0618	5.9659	1.8963
NM12AI12	543.5	0.9342	0.0736	1.0138	0.0798	5.9154	1.8883
NM12AI13	619.2	1.0712	0.0837	1.1955	0.0934	5.9226	1.8894
NM12AI14	629.9	1.1769	0.0919	1.2712	0.0993	5.8996	1.8858
Average	**572.1**	**0.9762**	**0.0764**	**1.068**	**0.0836**	**5.9259**	**1.89**
Median	**581.4**	**1.0027**	**0.0786**	**1.1047**	**0.0866**	**5.919**	**1.8889**

Note: Only 4 samples were tested due to one sample damaged during machine set-up.

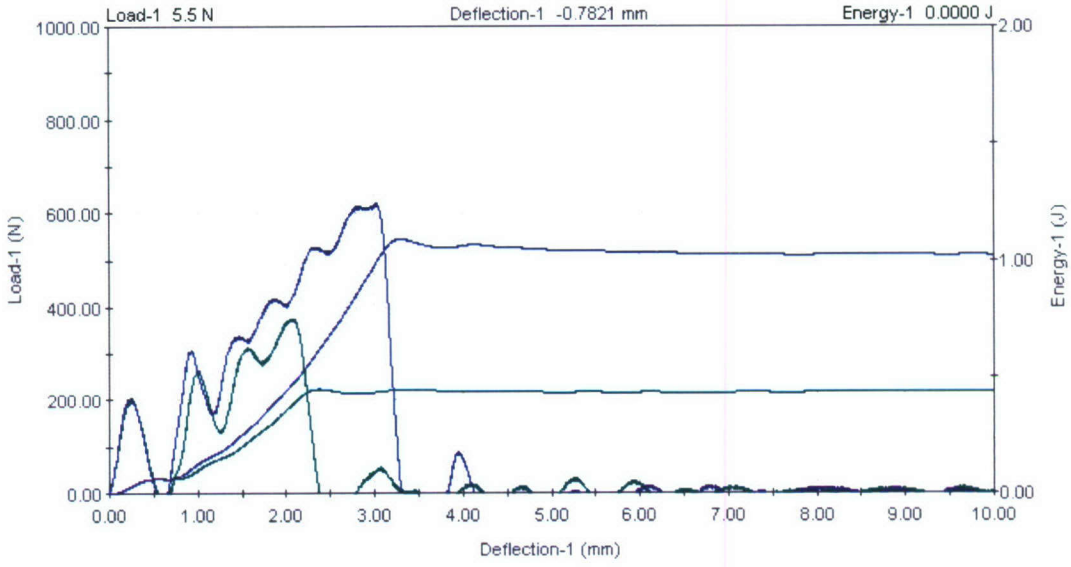

Figure 2.5.3.3: Load & Energy vs Deflection graph for un-notched 2.5 wt percent MWCNT reinforced nylon 6,6 specimens after 45 days of accelerated environmental aging.

Table 2.5.3.3: Impact characteristics of un-notched 2.5 wt percent MWCNT reinforced nylon 6,6 specimens after 45 days of accelerated environmental aging.

Specimen ID	Maximum load (N)	Energy to max load (J)	NTT energy to max load (J/mm)	Total energy* (J)	NTT total energy* (J/mm)	Impact energy (J)	Impact velocity (m/s)
NM25AI11	392	0.443	0.0348	0.5012	0.0394	10.6048	1.89
NM25AI12	375.4	0.371	0.029	0.4488	0.0351	10.6964	1.8982
NM25AI13	429	0.3783	0.0297	0.4995	0.0392	10.6411	1.8932
NM25AI14	621.3	0.9849	0.0778	1.0892	0.086	10.689	1.8975
NM25AI15	428.8	0.3915	0.0307	0.46	0.0361	10.6917	1.8977
Average	**449.3**	**0.5137**	**0.0404**	**0.5998**	**0.0472**	**10.6646**	**1.8953**
Median	**428.8**	**0.3915**	**0.0307**	**0.4995**	**0.0392**	**10.689**	**1.8975**

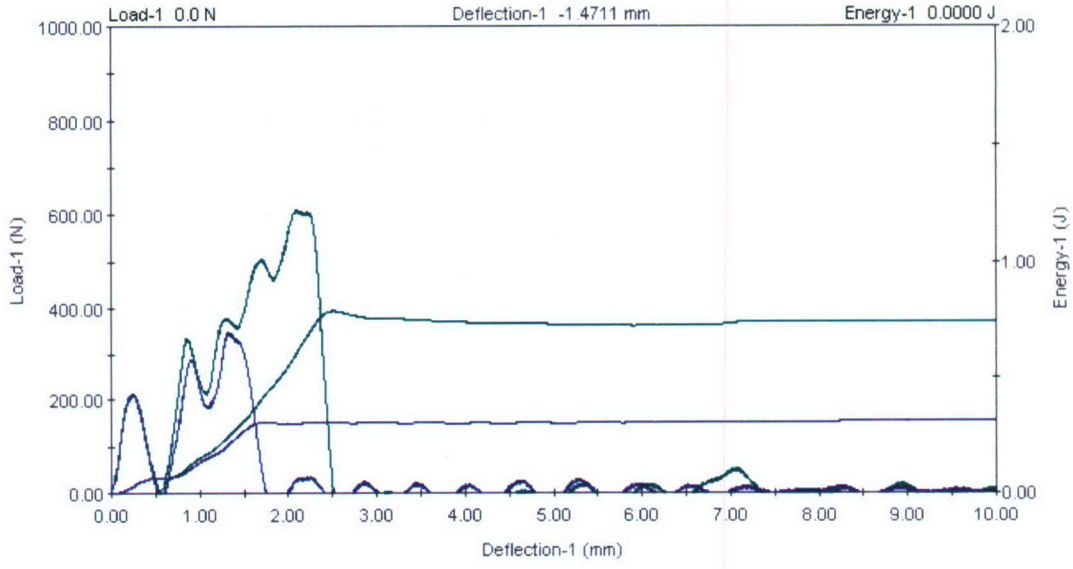

Figure 2.5.3.4: Load & Energy vs Deflection graph for un-notched 5 wt percent MWCNT reinforced nylon 6,6 specimens after 45 days of accelerated environmental aging.

Table 2.5.3.4: Impact characteristics of un-notched 5 wt percent MWCNT reinforced nylon 6,6 specimens after 45 days of accelerated environmental aging.

Specimen ID	Maximum load (N)	Energy to max load (J)	NTT energy to max load (J/mm)	Total energy* (J)	NTT total energy* (J/mm)	Impact energy (J)	Impact velocity (m/s)
NM50AI11	440.3	0.3656	0.0287	0.4908	0.0385	10.6137	1.8908
NM50AI12	612.1	0.6132	0.0483	0.7882	0.0621	10.6962	1.8981
NM50AI13	486.6	0.3901	0.0307	0.4814	0.0378	10.6783	1.8966
NM50AI14	349.7	0.2103	0.0165	0.3057	0.024	10.7461	1.9026
NM50AI15	441.7	0.3695	0.0289	0.5256	0.0412	10.6769	1.8964
Average	**466.1**	**0.3897**	**0.0306**	**0.5183**	**0.0407**	**10.6822**	**1.8969**
Median	**441.7**	**0.3695**	**0.0289**	**0.4908**	**0.0385**	**10.6783**	**1.8966**

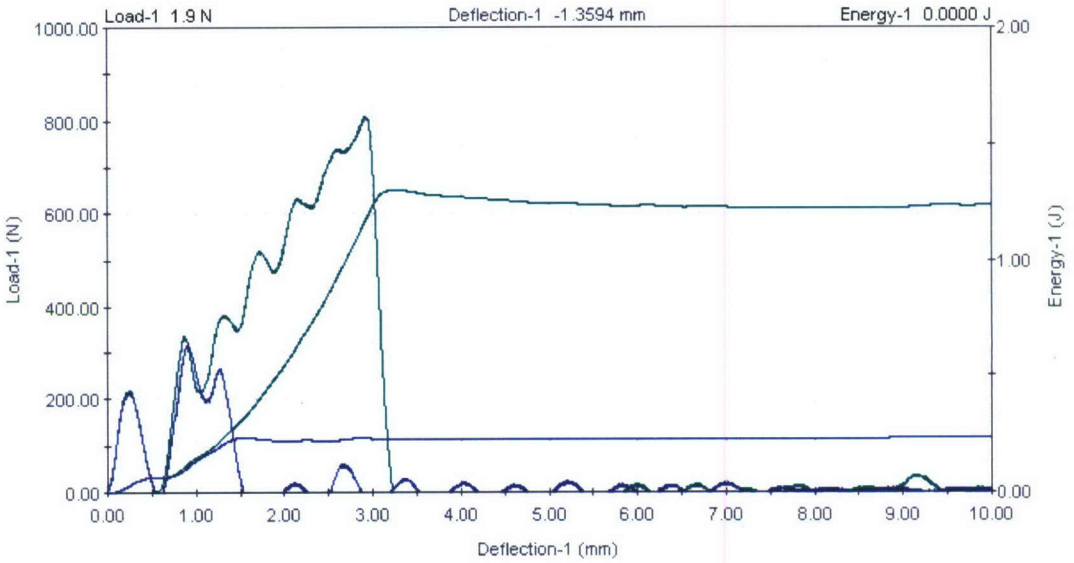

Figure 2.5.3.5: Load & Energy vs Deflection graph for un-notched 10 wt percent MWCNT reinforced nylon 6,6 specimens after 45 days of accelerated environmental aging.

Table 2.5.3.5: Impact characteristics of un-notched 10 wt percent MWCNT reinforced nylon 6,6 specimens after 45 days of accelerated environmental aging.

Specimen ID	Maximum load (N)	Energy to max load (J)	NTT energy to max load (J/mm)	Total energy* (J)	NTT total energy* (J/mm)	Impact energy (J)	Impact velocity (m/s)
NM10AI11	692	0.7993	0.0628	1.0137	0.0797	10.6821	1.8969
NM10AI12	808.5	1.1635	0.0915	1.3005	0.1023	10.7291	1.9011
NM10AI13	316.7	0.108	0.0085	0.2328	0.0183	10.6513	1.8942
NM10AI14	667.9	0.8906	0.0697	1.002	0.0784	10.6792	1.8966
NM10AI15	626.6	0.8111	0.0638	0.9091	0.0715	10.6616	1.8951
Average	**622.3**	**0.7545**	**0.0593**	**0.8916**	**0.07**	**10.6807**	**1.8968**
Median	**667.9**	**0.8111**	**0.0638**	**1.002**	**0.0784**	**10.6792**	**1.8966**

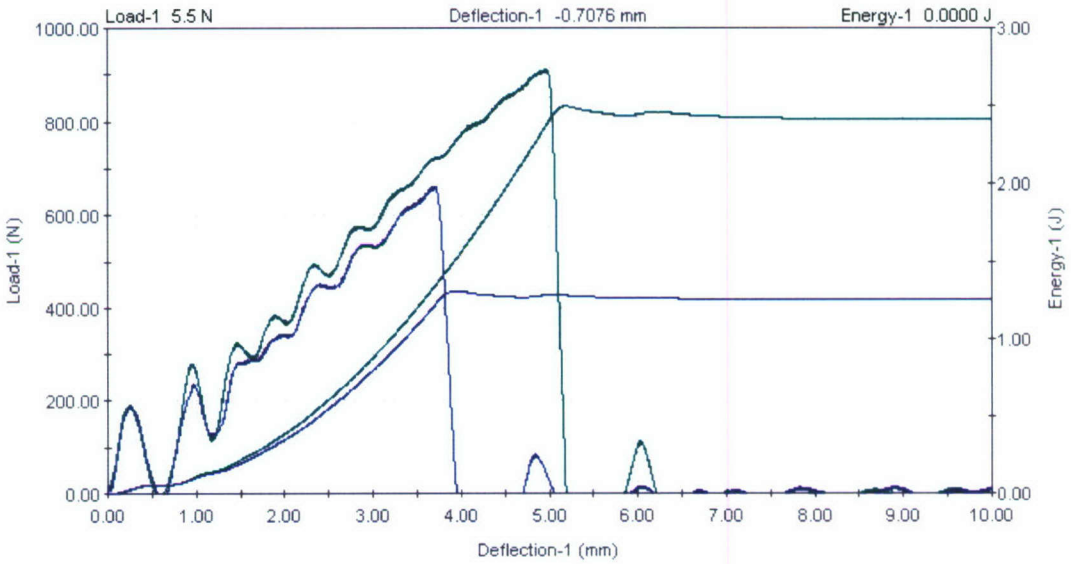

Figure 2.5.3.6: Load & Energy vs Deflection graph for un-notched pure nylon 6,6 specimens after 90 days of accelerated environmental aging.

Table 2.5.3.6: Impact characteristics of un-notched pure nylon 6,6 specimens after 90 days of accelerated environmental aging.

Specimen ID	Maximum load (N)	Energy to max load (J)	NTT energy to max load (J/mm)	Total energy* (J)	NTT total energy* (J/mm)	Impact energy (J)	Impact velocity (m/s)
NM00AI21	769.6	1.7466	0.1372	1.8516	0.1455	5.913	1.8879
NM00AI22	886.2	1.9243	0.1511	2.048	0.1608	5.8803	1.8827
NM00AI23	911	2.3617	0.1854	2.4984	0.1961	5.9476	1.8934
NM00AI24	661.6	1.2108	0.0952	1.3088	0.103	5.9917	1.9004
Average	**807.1**	**1.8108**	**0.1422**	**1.9267**	**0.1513**	**5.9332**	**1.8911**
Median	**827.9**	**1.8354**	**0.1442**	**1.9498**	**0.1531**	**5.9303**	**1.8907**

Note: Only 4 samples were tested due to one sample damaged during machine set-up.

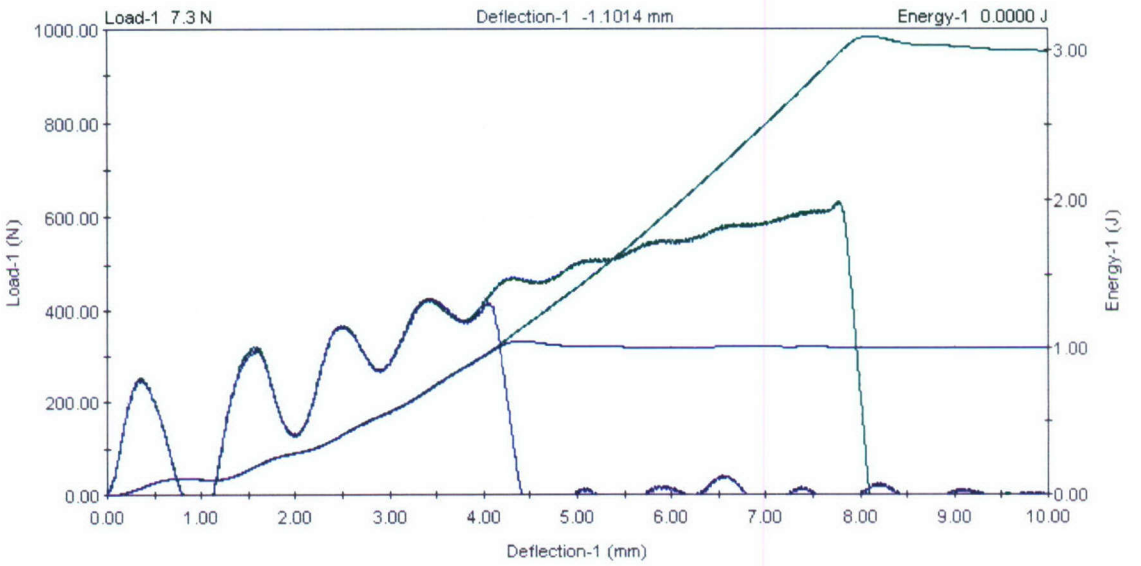

Figure 2.5.3.7: Load & Energy vs Deflection graph for un-notched 1.25 wt percent MWCNT reinforced nylon 6,6 specimens after 90 days of accelerated environmental aging.

Table 2.5.3.7: Impact characteristics of un-notched 1.25 wt percent MWCNT reinforced nylon 6,6 specimens after 90 days of accelerated environmental aging.

Specimen ID	Maximum load (N)	Energy to max load (J)	NTT energy to max load (J/mm)	Total energy* (J)	NTT total energy* (J/mm)	Impact energy (J)	Impact velocity (m/s)
NM12CI22	633.4	2.9723	0.2299	3.0973	0.2396	21.2477	2.6753
NM12CI23	425.3	0.7243	0.0559	1.0497	0.081	21.1675	2.6702
Average	**529.3**	**1.8483**	**0.1429**	**2.0735**	**0.1603**	**21.2076**	**2.6728**
Median	**529.3**	**1.8483**	**0.1429**	**2.0735**	**0.1603**	**21.2076**	**2.6728**

Note: Data of only 2 samples is presented due to 1 sample damaged during machine set-up, 1 sample did not fractured and data of 1 sample was discarded because it is believed to be a stray case.

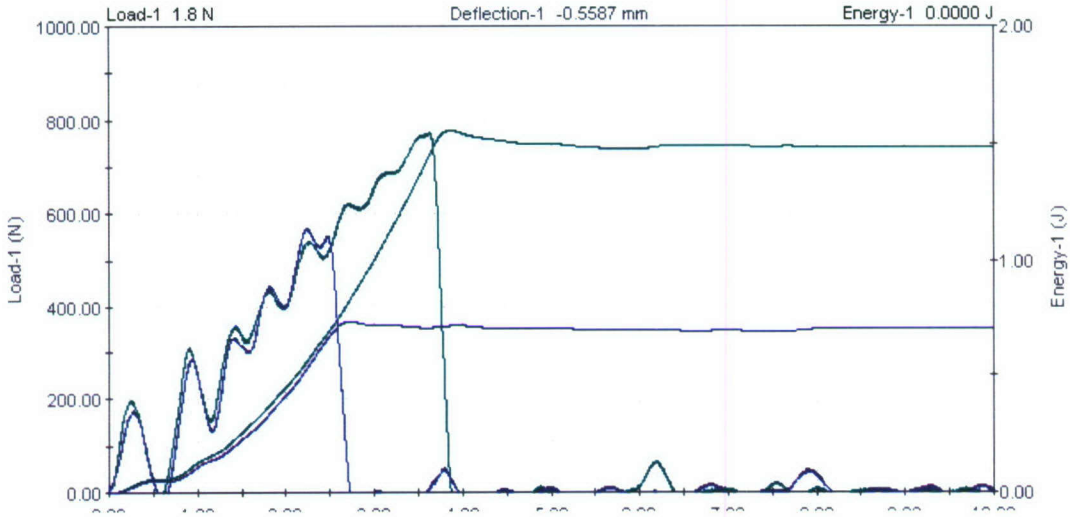

Figure 2.5.3.8: Load & Energy vs Deflection graph for un-notched 2.5 wt percent MWCNT reinforced nylon 6,6 specimens after 90 days of accelerated environmental aging.

Table 2.5.3.8: Impact characteristics of un-notched 2.5 wt percent MWCNT reinforced nylon 6,6 specimens after 90 days of accelerated environmental aging.

Specimen ID	Maximum load (N)	Energy to max load (J)	NTT energy to max load (J/mm)	Total energy* (J)	NTT total energy* (J/mm)	Impact energy (J)	Impact velocity (m/s)
NM25AI21	607.9	0.7972	0.0626	0.9143	0.0718	5.9511	1.894
NM25AI22	775.1	1.4479	0.1137	1.5559	0.1221	5.9897	1.9001
NM25AI23	688.8	0.8505	0.0668	1.035	0.0813	5.9553	1.8947
NM25AI24	567.8	0.5253	0.0413	0.7359	0.0579	5.9773	1.8981
Average	**659.9**	**0.9052**	**0.0711**	**1.0603**	**0.0833**	**5.9684**	**1.8967**
Median	**648.4**	**0.8239**	**0.0647**	**0.9746**	**0.0765**	**5.9663**	**1.8964**

Note: Only 4 samples were tested due to one sample damaged during machine set-up.

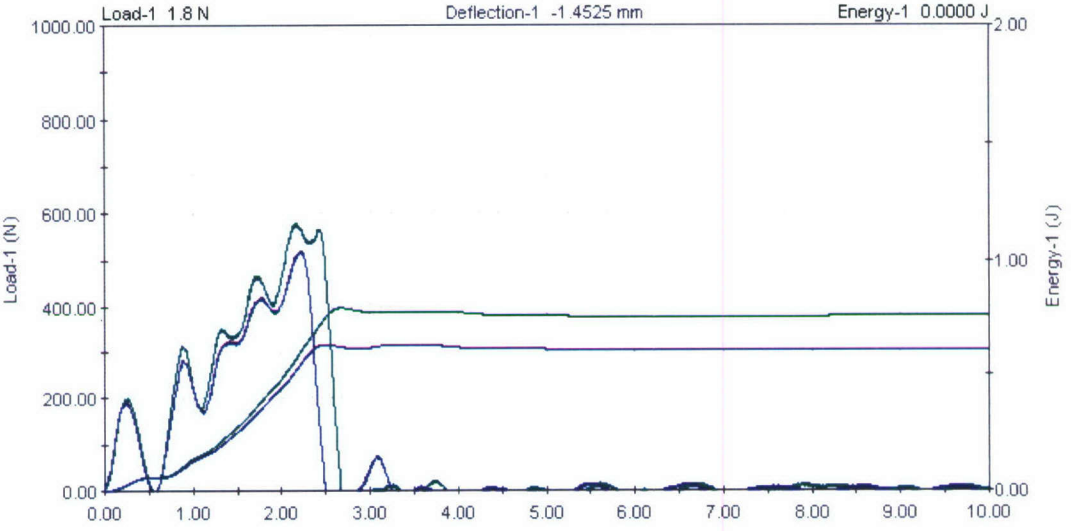

Figure 2.5.3.9: Load & Energy vs Deflection graph for un-notched 5 wt percent MWCNT reinforced nylon 6,6 specimens after 90 days of accelerated environmental aging.

Table 2.5.3.9: Impact characteristics of un-notched 5 wt percent MWCNT reinforced nylon 6,6 specimens after 90 days of accelerated environmental aging.

Specimen ID	Maximum load (N)	Energy to max load (J)	NTT energy to max load (J/mm)	Total energy* (J)	NTT total energy* (J/mm)	Impact energy (J)	Impact velocity (m/s)
NM50AI22	534.5	0.5562	0.0436	0.6786	0.0532	5.9828	1.899
NM50AI23	578.6	0.5728	0.0448	0.7962	0.0623	5.9733	1.8975
NM50AI24	517.9	0.5414	0.0425	0.6321	0.0496	5.9667	1.8965
NM50AI25	536	0.7003	0.0549	0.7774	0.0609	5.9769	1.8981
Average	**541.8**	**0.5927**	**0.0464**	**0.7211**	**0.0565**	**5.9749**	**1.8978**
Median	**535.3**	**0.5645**	**0.0442**	**0.728**	**0.057**	**5.9751**	**1.8978**

Note: Only 4 samples were tested due to one sample damaged during machine set-up.

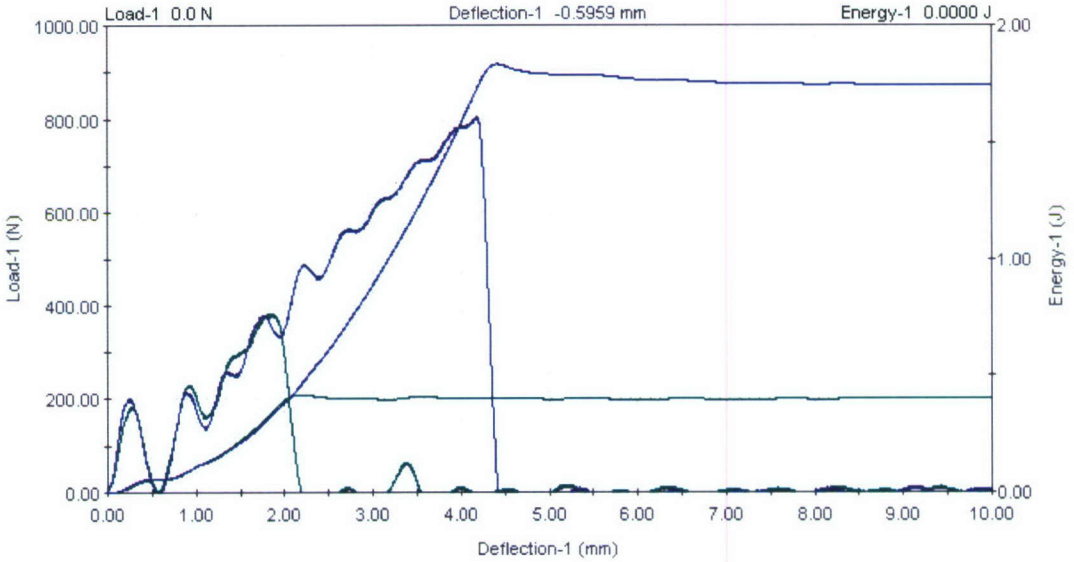

Figure 2.5.3.10: Load & Energy vs Deflection graph for un-notched 10 wt percent MWCNT reinforced nylon 6,6 specimens after 90 days of accelerated environmental aging.

Table 2.5.3.10: Impact characteristics of un-notched 10 wt percent MWCNT reinforced nylon 6,6 specimens after 90 days of accelerated environmental aging.

Specimen ID	Maximum load (N)	Energy to max load (J)	NTT energy to max load (J/mm)	Total energy* (J)	NTT total energy* (J/mm)	Impact energy (J)	Impact velocity (m/s)
NM10AI21	572.8	0.7831	0.0612	0.8622	0.0674	5.9716	1.8972
NM10AI22	382	0.3437	0.0269	0.4193	0.0328	5.9758	1.8979
NM10AI23	804.9	1.7231	0.135	1.8341	0.1437	5.9682	1.8967
NM10AI24	442.6	0.3646	0.0286	0.5348	0.042	5.9601	1.8954
NM10AI25	799.4	1.5411	0.1206	1.6385	0.1282	5.9523	1.8942
Average	**600.3**	**0.9511**	**0.0745**	**1.0578**	**0.0828**	**5.9656**	**1.8963**
Median	**572.8**	**0.7831**	**0.0612**	**0.8622**	**0.0674**	**5.9682**	**1.8967**

2.5.3a Summary of Results

Figure 2.5.3.11 to 2.5.3.15 show the summarized output for effects of environmental aging on un-notched nylon 6,6 and their matrices with reinforced composite. It is to be noted that 5 specimens were tested for accelerated aging of 45 days and 90 days while data of 1 specimen each from 45 days aging test of pure nylon 6,6 and 1.25 wt percent reinforced composite and 1 specimen each from 90 days aging test of pure nylon 6,6, 1.25 wt percent reinforced composite and 2.5 wt percent reinforced composite was discarded.

It is also to be noted that drop wt was increased to 5.95 Kg (13.09 lbs) in case of testing of specimens with 45 day aging except for 1.25 wt percent reinforced matrix. Drop height was also increased to 355.6 mm (14") for 1.25 wt percent reinforced matrix after 90 days aging.

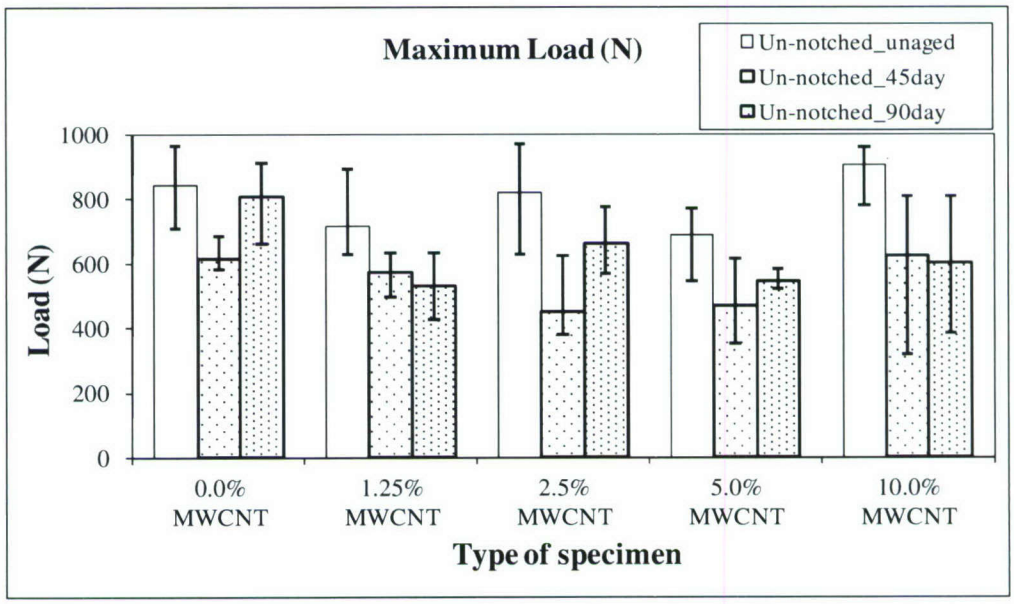

Figure 2.5.3.11: Maximum load comparison for un-notched nylon 6,6 and MWCNT reinforced composites with effects of aging.

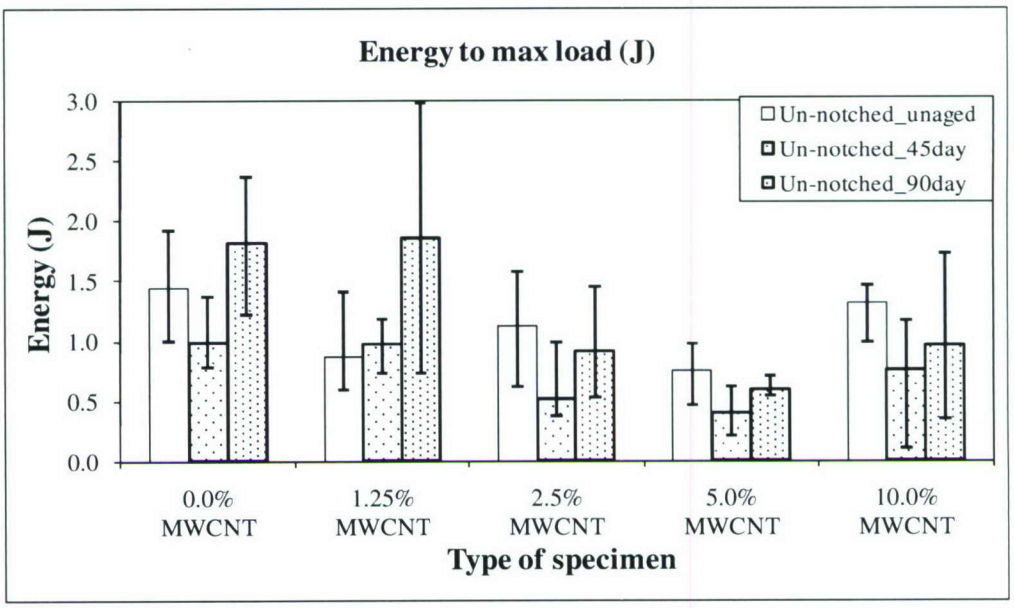

Figure 2.5.3.12: Energy to maximum load comparison for un-notched nylon 6,6 and MWCNT reinforced composites with effects of aging.

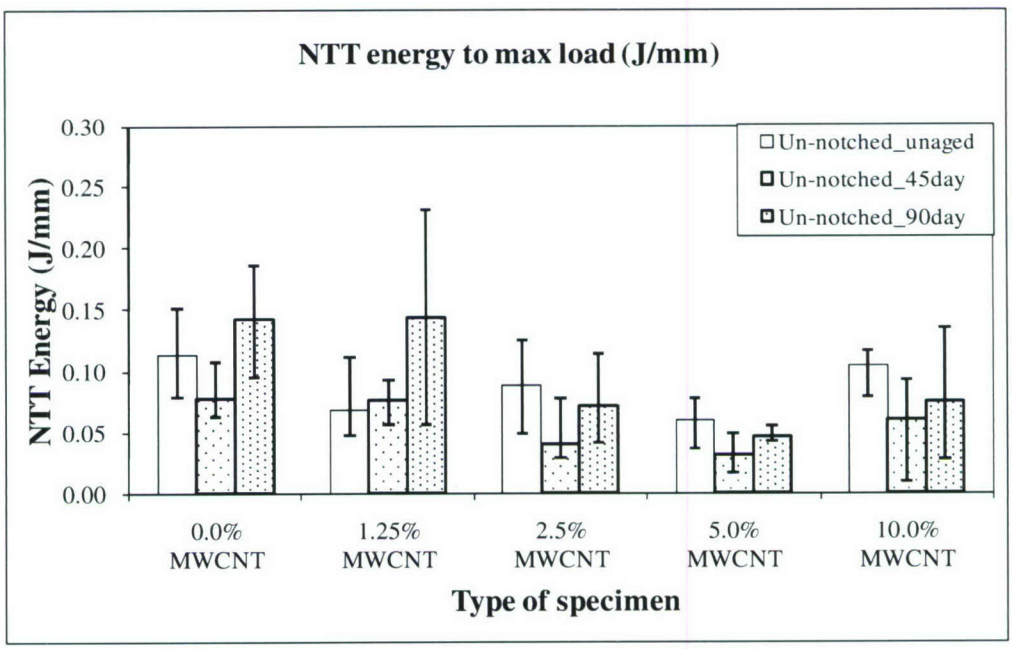

Figure 2.5.3.13: NTT energy to maximum load comparison for un-notched nylon 6,6 and MWCNT reinforced composites with effects of aging.

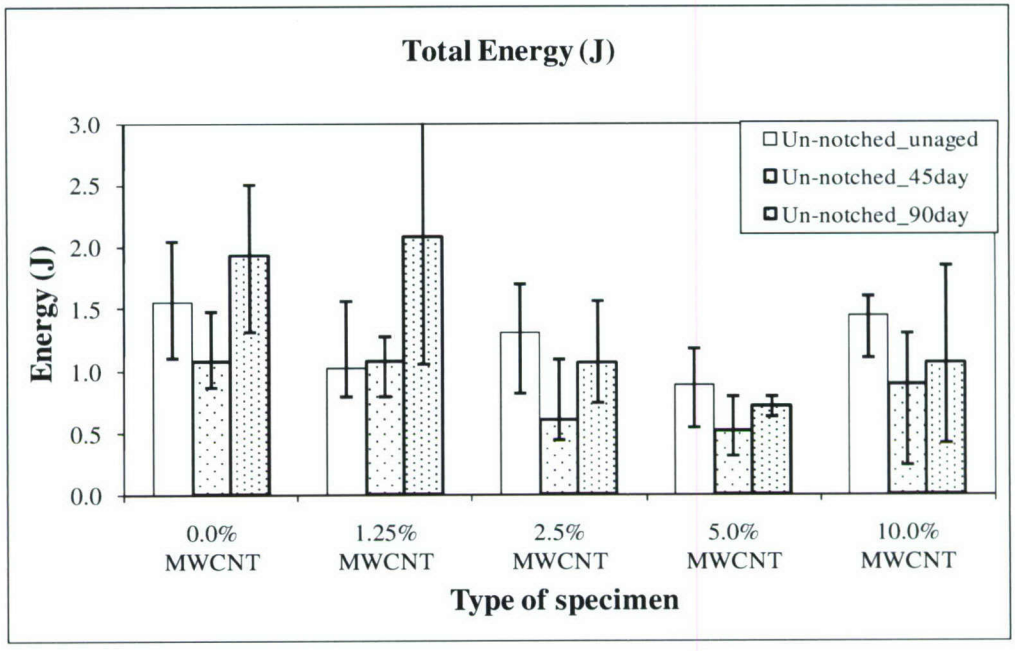

Figure 2.5.3.14: Total energy comparison for un-notched nylon 6,6 and MWCNT reinforced composites with effects of aging.

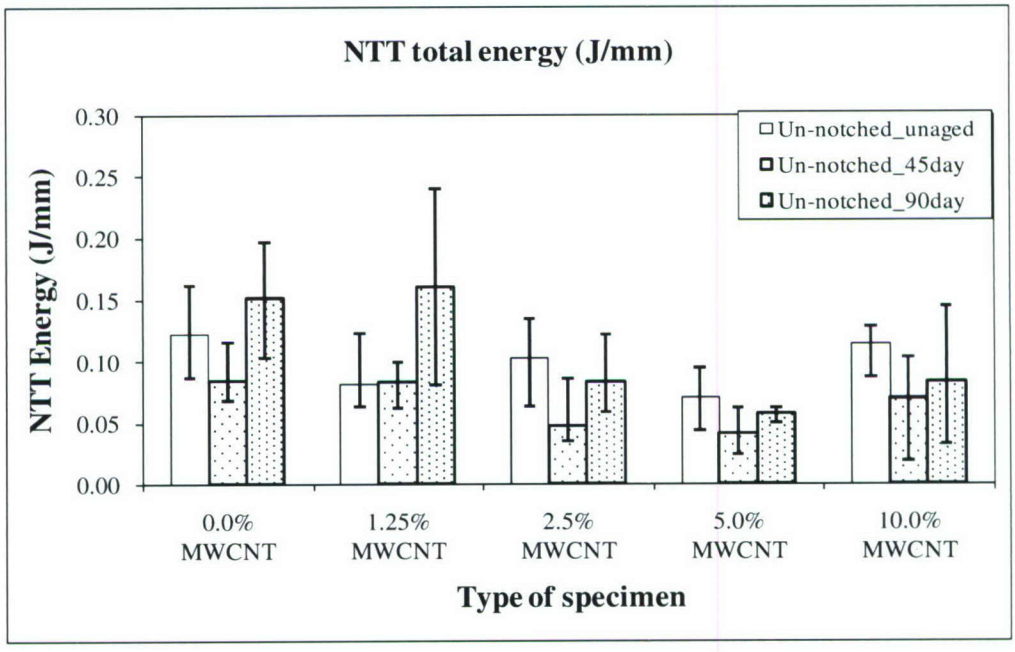

Figure 2.5.3.15: NTT total energy comparison for un-notched nylon 6,6 and MWCNT reinforced composites with effects of aging.

2.5.3b Conclusion

It was observed that energy absorption reduced after 45 days of aging and again increased after 90 days of aging in all matrices other than that of 1.25 wt percent reinforced matrix. Similar trend was observed with that of load with the exception of 1.25 wt percent and 10 wt percent reinforced matrices. These results are observed to be opposite to that of trends observed in testing of notched specimens. However, no firm conclusion can be drawn because of the broad scatter band.

2.5.4 Vinyl ester and reinforced nanocomposites

Test results & data for impact experiments on vinyl ester and nanoreinforced composites with nanoclay and graphite platelets are shown in Figure 2.5.4.1 to 2.5.4.10 & Table 2.5.4.1 to 2.5.4.10. Figures below show the trend for two specimens only. It is to be noted that total energy* computed is the energy at a point where load becomes zero after registering maximum load as calculated by the Instron machine software used for data acquisition.

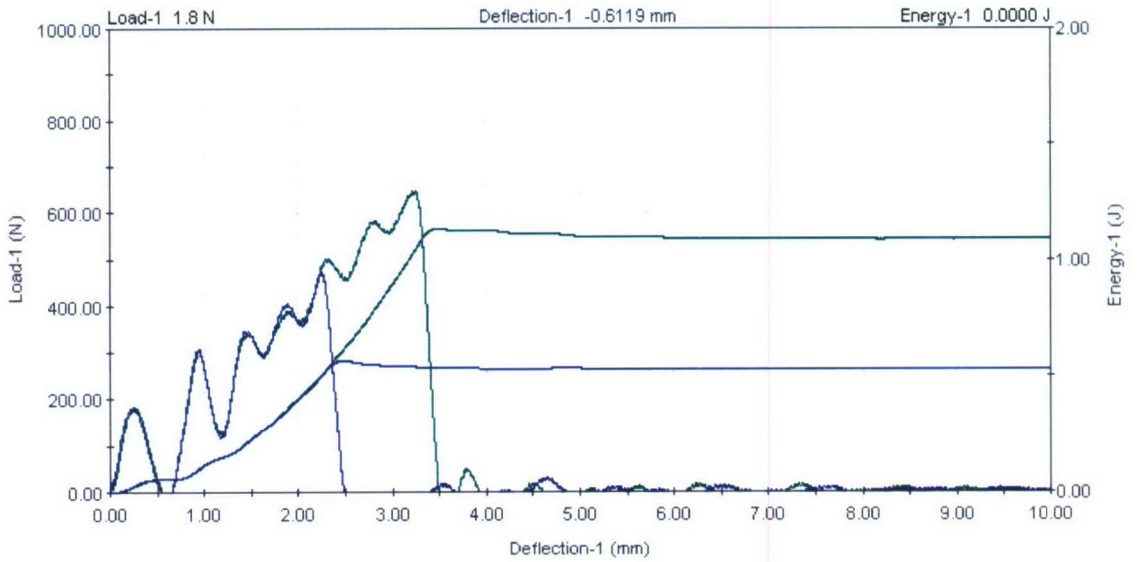

Figure 2.5.4.1: Load & Energy vs Deflection graph for un-notched pure vinyl ester specimens

Table 2.5.4.1: Impact characteristics of un-notched pure vinyl ester specimens

Specimen ID	Maximum load (N)	Energy to max load (J)	NTT energy to max load (J/mm)	Total energy* (J)	NTT total energy* (J/mm)	Impact energy (J)	Impact velocity (m/s)
VC00AI01	515.5	0.6826	0.0537	0.7529	0.0593	5.8802	1.8827
VC00AI02	484.5	0.512	0.0404	0.6586	0.052	5.9151	1.8882
VC00AI03	566.7	0.7513	0.0592	0.9313	0.0733	5.9528	1.8942
VC00AI04	645.7	1.0215	0.0804	1.133	0.0892	5.9637	1.896
VC00AI05	475.1	0.5019	0.0395	0.5664	0.0446	6.0003	1.9018
Average	**537.5**	**0.6939**	**0.0547**	**0.8084**	**0.0637**	**5.9424**	**1.8926**
Median	**515.5**	**0.6826**	**0.0537**	**0.7529**	**0.0593**	**5.9528**	**1.8942**

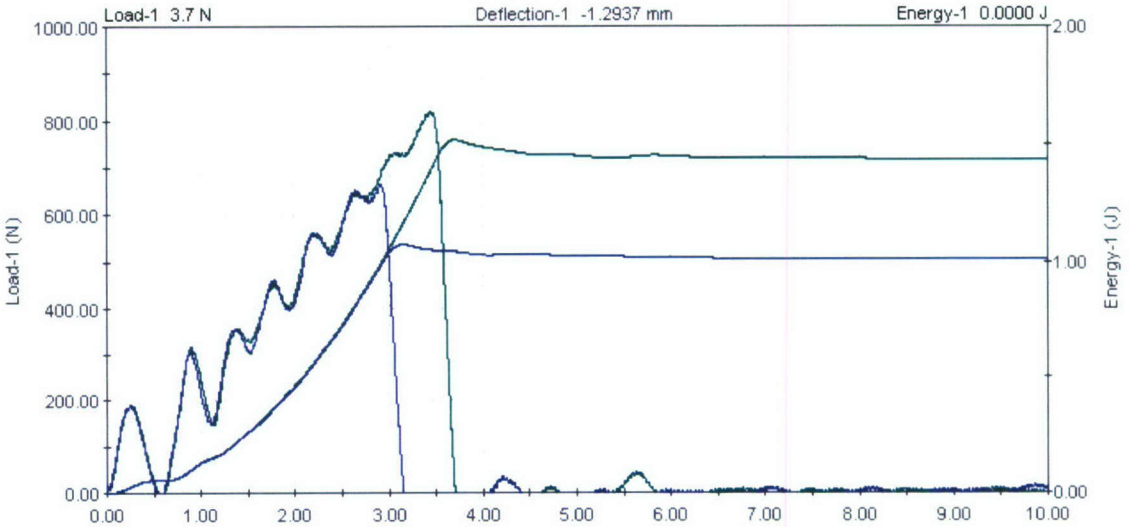

Figure 2.5.4.2: Load & Energy vs Deflection graph for un-notched 1.25 wt percent nanoclay reinforced vinyl ester specimens

Table 2.5.4.2: Impact characteristics of un-notched 1.25 wt percent nanoclay reinforced vinyl ester specimens

Specimen ID	Maximum load (N)	Energy to max load (J)	NTT energy to max load (J/mm)	Total energy* (J)	NTT total energy* (J/mm)	Impact energy (J)	Impact velocity (m/s)
VC12AI01	814.5	1.3623	0.1075	1.4886	0.1175	5.9931	1.9006
VC12AI02	705.7	1.0214	0.0807	1.1112	0.0878	5.8972	1.8854
VC12AI03	819	1.3841	0.1094	1.517	0.1199	5.9192	1.8889
VC12AI04	800.7	1.3194	0.1042	1.4245	0.1125	6.0036	1.9023
VC12AI05	665.4	0.9757	0.077	1.0725	0.0846	5.9737	1.8976
Average	**761.1**	**1.2126**	**0.0958**	**1.3228**	**0.1045**	**5.9573**	**1.895**
Median	**800.7**	**1.3194**	**0.1042**	**1.4245**	**0.1125**	**5.9737**	**1.8976**

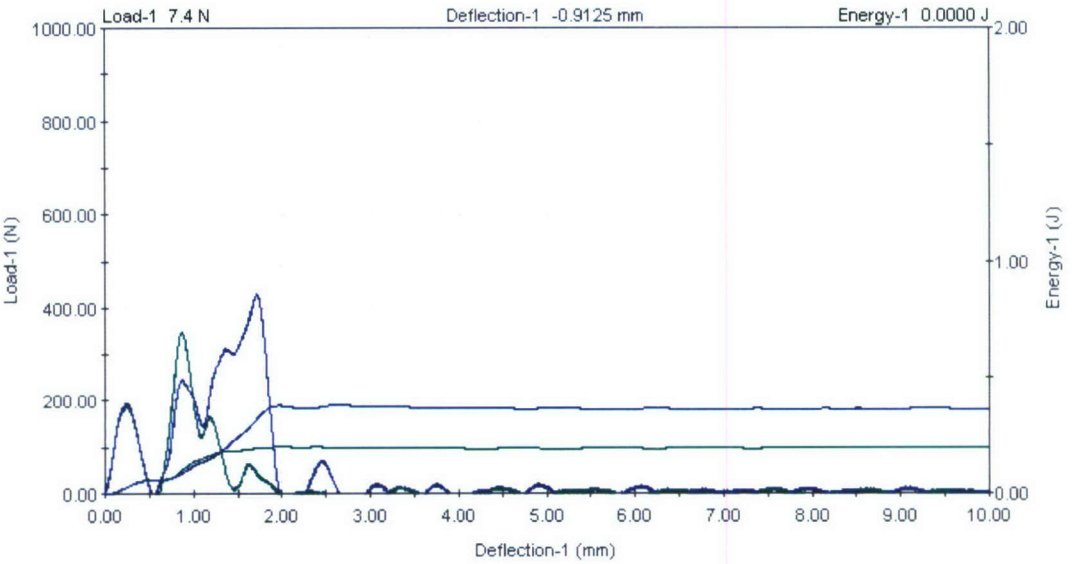

Figure 2.5.4.3: Load & Energy vs Deflection graph for un-notched 2.5 wt percent nanoclay reinforced vinyl ester specimens

Table 2.5.4.3: Impact characteristics of un-notched 2.5 wt percent nanoclay reinforced vinyl ester specimens

Specimen ID	Maximum load (N)	Energy to max load (J)	NTT energy to max load (J/mm)	Total energy* (J)	NTT total energy* (J/mm)	Impact energy (J)	Impact velocity (m/s)
VC25AI01	850.5	1.381	0.1094	1.492	0.1182	6.0712	1.913
VC25AI02	858.3	1.4086	0.1123	1.6247	0.1295	6.0101	1.9034
VC25AI03	843.2	1.36	0.1077	1.4723	0.1166	5.9926	1.9006
VC25AI04	861.5	1.3827	0.1092	1.5093	0.1192	5.9722	1.8973
VC25AI05	841.4	1.335	0.1053	1.4525	0.1146	5.9568	1.8949
Average	**851.0**	**1.3735**	**0.1088**	**1.5101**	**0.1196**	**6.0006**	**1.9018**
Median	**850.5**	**1.381**	**0.1092**	**1.492**	**0.1182**	**5.9926**	**1.9006**

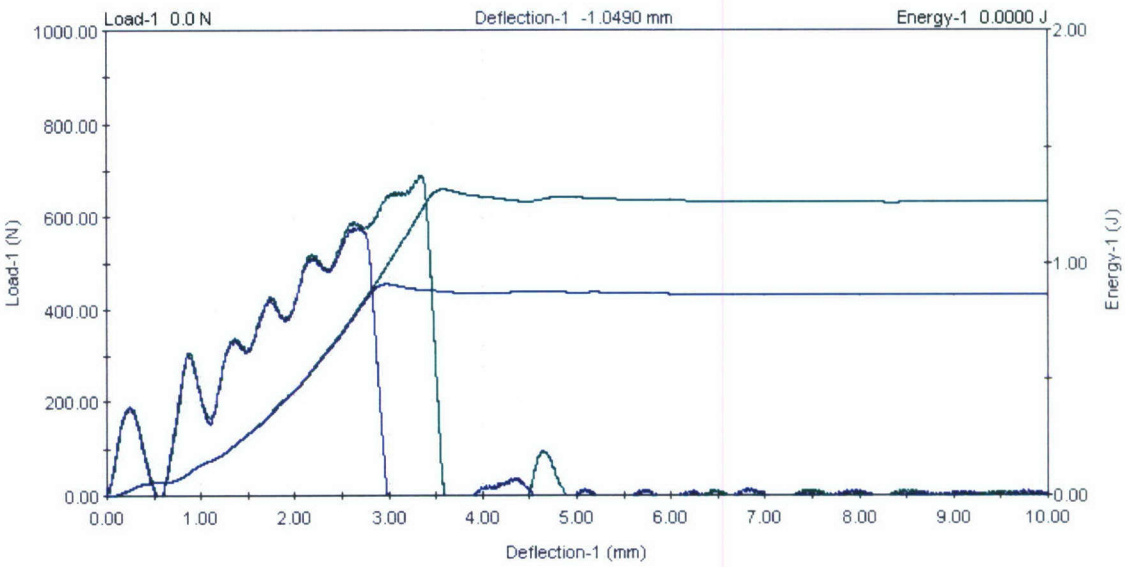

Figure 2.5.4.4: Load & Energy vs Deflection graph for un-notched 1.25 wt percent graphite platelets reinforced vinyl ester specimens

Table 2.5.4.4: Impact characteristics of un-notched 1.25 wt percent graphite platelets reinforced vinyl ester specimens

Specimen ID	Maximum load (N)	Energy to max load (J)	NTT energy to max load (J/mm)	Total energy* (J)	NTT total energy* (J/mm)	Impact energy (J)	Impact velocity (m/s)
VG12AI01	689.9	1.2117	0.0958	1.3198	0.1043	5.9544	1.8945
VG12AI02	700.5	1.0488	0.0829	1.1688	0.0924	5.9075	1.887
VG12AI03	577.7	0.7664	0.0603	0.9086	0.0715	5.9287	1.8904
VG12AI04	711.9	1.1032	0.087	1.2869	0.1014	5.9682	1.8967
VG12AI05	671.6	1.0408	0.0823	1.227	0.097	5.9528	1.8943
Average	**670.3**	**1.0342**	**0.0816**	**1.1822**	**0.0933**	**5.9423**	**1.8926**
Median	**689.9**	**1.0488**	**0.0829**	**1.227**	**0.097**	**5.9528**	**1.8943**

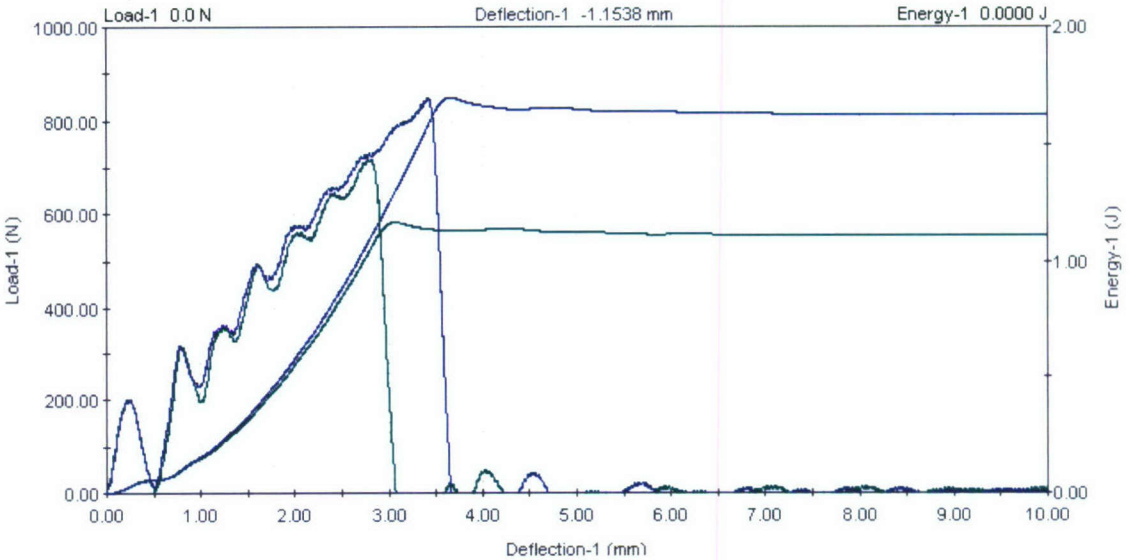

Figure 2.5.4.5: Load & Energy vs Deflection graph for un-notched 2.5 wt percent graphite platelets reinforced vinyl ester specimens

Table 2.5.4.5: Impact characteristics of un-notched 2.5 wt percent graphite platelets reinforced vinyl ester specimens

Specimen ID	Maximum load (N)	Energy to max load (J)	NTT energy to max load (J/mm)	Total energy* (J)	NTT total energy* (J/mm)	Impact energy (J)	Impact velocity (m/s)
VG25AI01	818	1.4558	0.1149	1.5791	0.1246	5.9427	1.8926
VG25AI02	810.7	1.4628	0.1158	1.5806	0.1251	6.0261	1.9059
VG25AI03	768.6	1.2585	0.0996	1.3784	0.1091	6.009	1.9032
VG25AI04	717.4	1.0305	0.0816	1.165	0.0923	6.0144	1.904
VG25AI05	848.7	1.5816	0.1243	1.6975	0.1334	5.9438	1.8928
Average	**792.7**	**1.3578**	**0.1072**	**1.4801**	**0.1169**	**5.9872**	**1.8997**
Median	**810.7**	**1.4558**	**0.1149**	**1.5791**	**0.1246**	**6.009**	**1.9032**

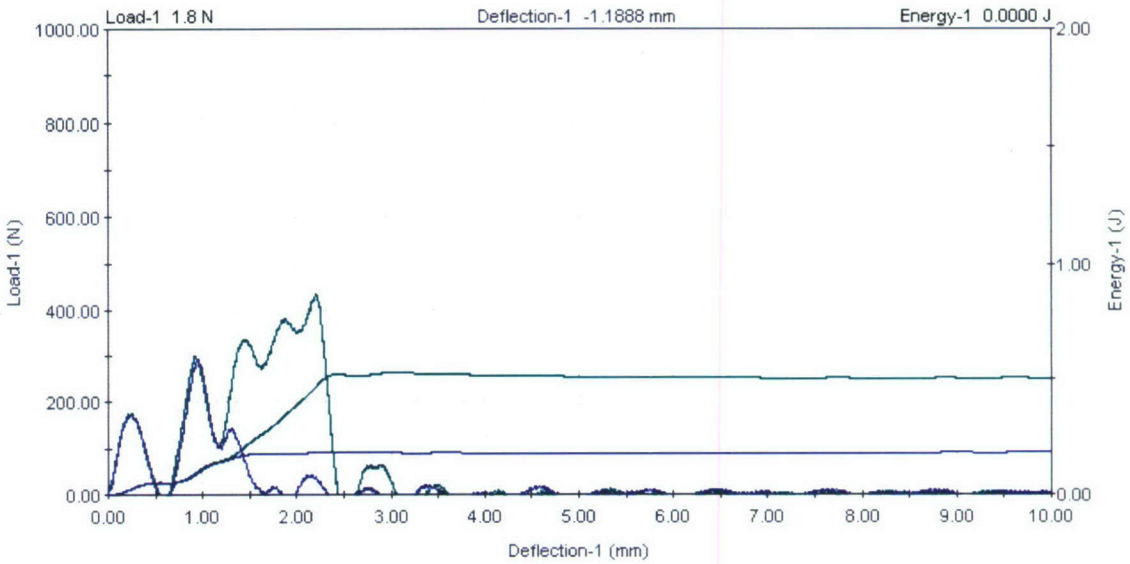

Figure 2.5.4.6: Load & Energy vs Deflection graph for notched pure vinyl ester specimens

Table 2.5.4.6: Impact characteristics of notched pure vinyl ester specimens

Specimen ID	Maximum load (N)	Energy to max load (J)	NTT energy to max load (J/mm)	Total energy* (J)	NTT total energy* (J/mm)	Impact energy (J)	Impact velocity (m/s)
VC00AI06	395.5	0.4557	0.045	0.5093	0.0503	5.9325	1.891
VC00AI07	366.6	0.3369	0.0336	0.4468	0.0445	5.9429	1.8927
VC00AI08	434.6	0.4655	0.0457	0.5234	0.0514	5.9536	1.8944
VC00AI09	368.6	0.3268	0.0325	0.4092	0.0407	5.9634	1.8959
VC00AI10	293.4	0.0937	0.0092	0.1768	0.0174	5.9534	1.8943
Average	**371.7**	**0.3357**	**0.0332**	**0.4131**	**0.0409**	**5.9492**	**1.8937**
Median	**368.6**	**0.3369**	**0.0336**	**0.4468**	**0.0445**	**5.9534**	**1.8943**

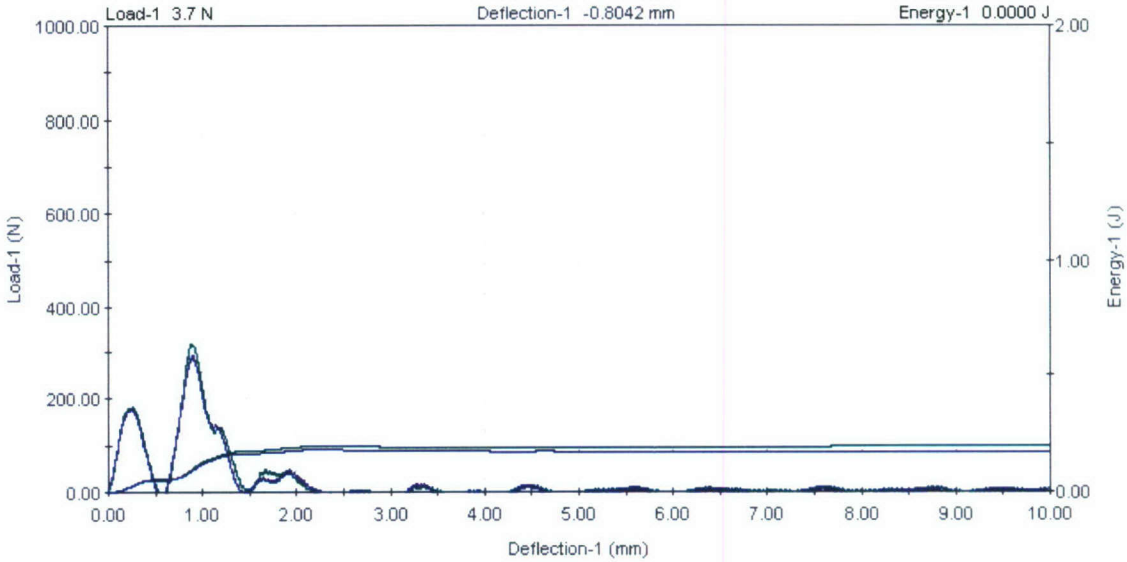

Figure 2.5.4.7: Load & Energy vs Deflection graph for notched 1.25 wt percent nanoclay reinforced vinyl ester specimens

Table 2.5.4.7: Impact characteristics of notched 1.25 wt percent nanoclay reinforced vinyl ester specimens

Specimen ID	Maximum load (N)	Energy to max load (J)	NTT energy to max load (J/mm)	Total energy* (J)	NTT total energy* (J/mm)	Impact energy (J)	Impact velocity (m/s)
VC12AI06	310.2	0.0935	0.0094	0.1636	0.0165	5.9986	1.9015
VC12AI07	304.6	0.0949	0.0096	0.1944	0.0196	5.9441	1.8929
VC12AI08	319.4	0.0943	0.0094	0.1959	0.0196	5.978	1.8983
VC12AI09	291.7	0.096	0.0097	0.1641	0.0165	5.9496	1.8937
VC12AI10	305.1	0.0916	0.0092	0.1631	0.0164	6.0018	1.902
Average	**306.2**	**0.0941**	**0.0095**	**0.1762**	**0.0177**	**5.9744**	**1.8977**
Median	**305.1**	**0.0943**	**0.0094**	**0.1641**	**0.0165**	**5.978**	**1.8983**

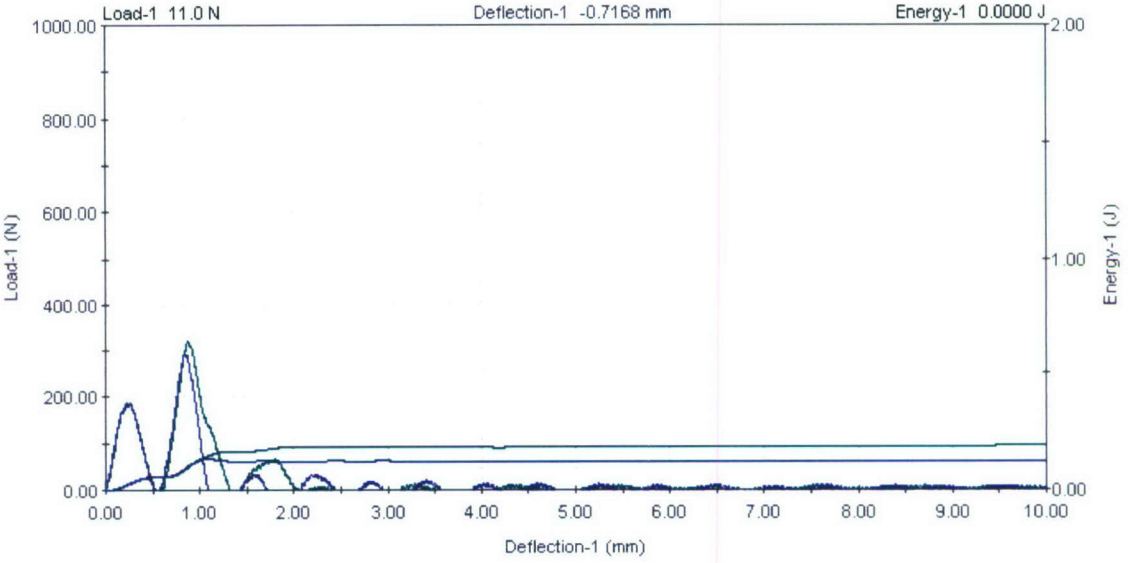

Figure 2.5.4.8: Load & Energy vs Deflection graph for un-notched 2.5 wt percent nanoclay reinforced vinyl ester specimens

Table 2.5.4.8: Impact characteristics of un-notched 2.5 wt percent nanoclay reinforced vinyl ester specimens

Specimen ID	Maximum load (N)	Energy to max load (J)	NTT energy to max load (J/mm)	Total energy* (J)	NTT total energy* (J/mm)	Impact energy (J)	Impact velocity (m/s)
VC25AI06	317.7	0.0954	0.0097	0.1628	0.0165	5.9718	1.8973
VC25AI07	321.6	0.0964	0.0096	0.163	0.0162	5.9774	1.8982
VC25AI08	321.4	0.1028	0.0105	0.17	0.0174	6.0023	1.9021
VC25AI09	294	0.0946	0.0095	0.1598	0.0161	5.9924	1.9005
VC25AI10	293.9	0.092	0.0092	0.132	0.0132	6.0129	1.9038
Average	**309.7**	**0.0962**	**0.0097**	**0.1575**	**0.0159**	**5.9914**	**1.9004**
Median	**317.7**	**0.0954**	**0.0096**	**0.1628**	**0.0162**	**5.9924**	**1.9005**

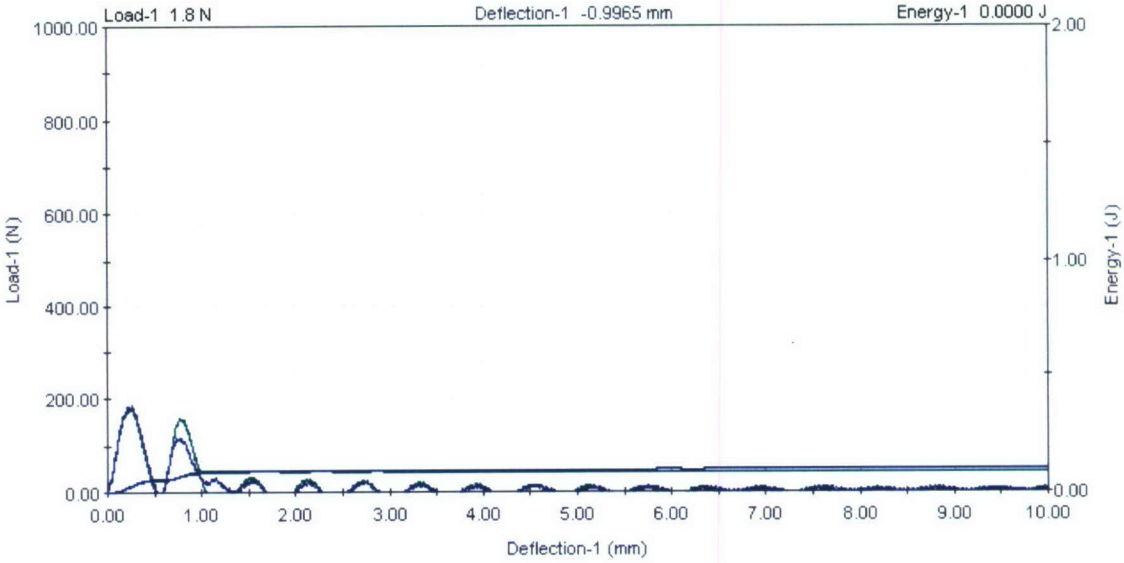

Figure 2.5.4.9: Load & Energy vs Deflection graph for notched 1.25 wt percent graphite platelets reinforced vinyl ester specimens

Table 2.5.4.9: Impact characteristics of notched 1.25 wt percent graphite platelets reinforced vinyl ester specimens

Specimen ID	Maximum load (N)	Energy to max load (J)	NTT energy to max load (J/mm)	Total energy* (J)	NTT total energy* (J/mm)	Impact energy (J)	Impact velocity (m/s)
VG12AI06	180	0.0281	0.0029	0.0518	0.0053	5.8175	1.8726
VG12AI07	185.6	0.0293	0.003	0.0542	0.0055	5.9583	1.8951
VG12AI08	182	0.0267	0.0026	0.053	0.0052	5.9598	1.8954
VG12AI09	180.2	0.0247	0.0025	0.0518	0.0053	5.9951	1.901
VG12AI10	182	0.0218	0.0022	0.0528	0.0053	5.9482	1.8935
Average	**182.0**	**0.0261**	**0.0026**	**0.0527**	**0.0053**	**5.9358**	**1.8915**
Median	**182.0**	**0.0267**	**0.0026**	**0.0528**	**0.0053**	**5.9583**	**1.8951**

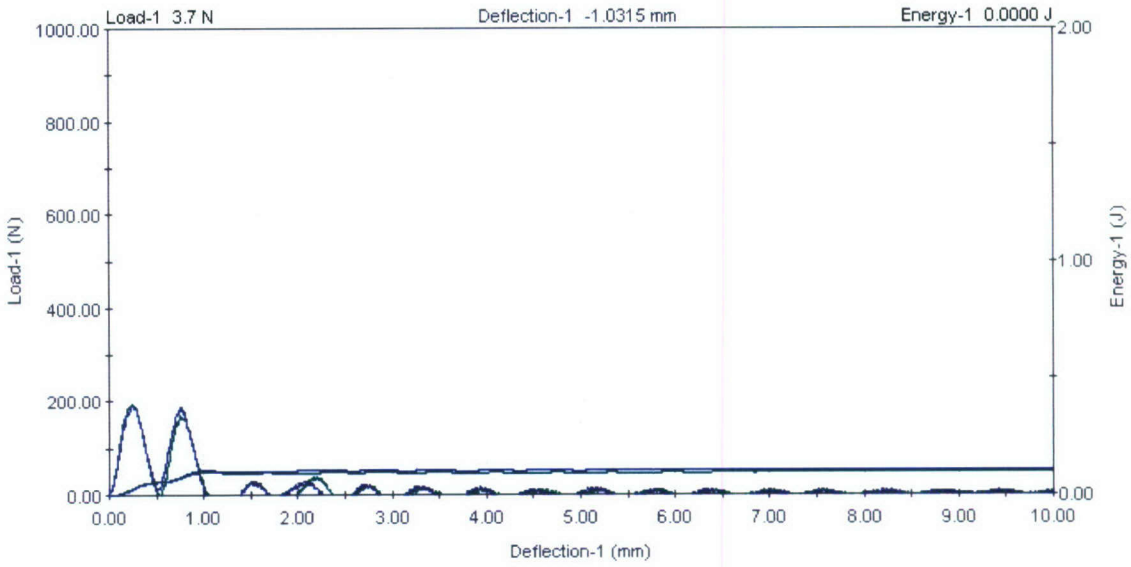

Figure 2.5.4.10: Load & Energy vs Deflection graph for notched 2.5 wt percent graphite platelets reinforced vinyl ester specimens

Table 2.5.4.10: Impact characteristics of notched 2.5 wt percent graphite platelets reinforced vinyl ester specimens

Specimen ID	Maximum load (N)	Energy to max load (J)	NTT energy to max load (J/mm)	Total energy* (J)	NTT total energy* (J/mm)	Impact energy (J)	Impact velocity (m/s)
VG25AI06	194.7	0.0264	0.0026	0.0542	0.0052	5.9239	1.8896
VG25AI07	194.8	0.0267	0.0027	0.0546	0.0054	5.9374	1.8918
VG25AI09	194.8	0.025	0.0025	0.0545	0.0054	5.9549	1.8946
VG25AI10	189.3	0.0237	0.0023	0.1036	0.01	5.9501	1.8938
VG25AI12	195.1	0.0272	0.0027	0.0951	0.0096	5.9359	1.8916
Average	**193.7**	**0.0258**	**0.0025**	**0.0724**	**0.0071**	**5.9405**	**1.8923**
Median	**194.8**	**0.0264**	**0.0026**	**0.0546**	**0.0054**	**5.9374**	**1.8918**

2.5.4a Summary of Results

Figure 2.5.4.11 to 2.5.4.15 show the summarized output for vinyl ester and nanoreinforced composites with nanoclay and graphite platelets. It is to be noted that 5 notched & 5 un-notched specimens from each category were tested to obtain statistically significant data.

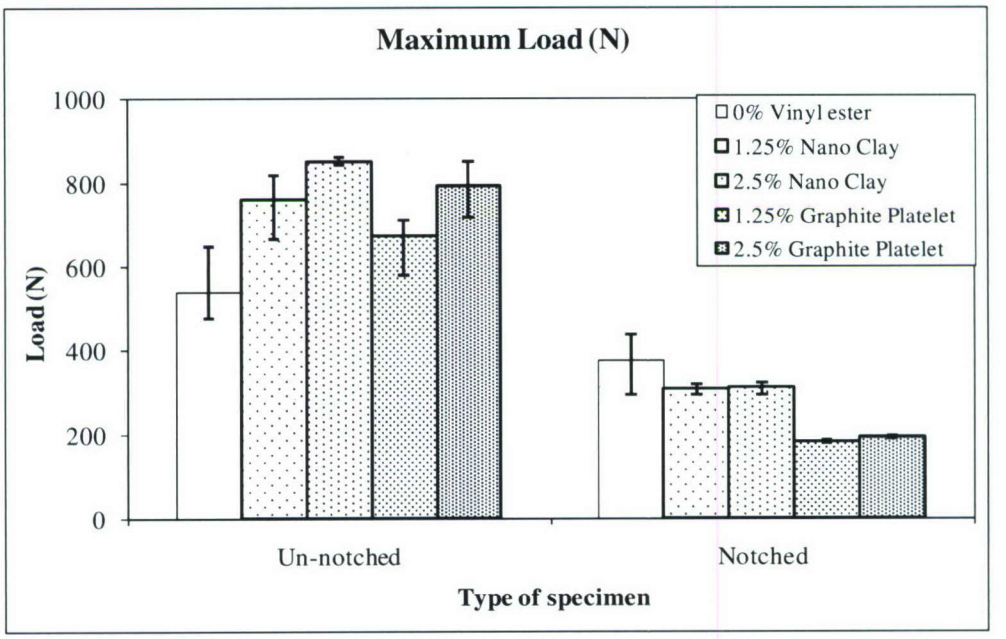

Figure 2.5.4.11: Maximum load comparison for notched & un-notched pure vinyl ester and nanoclay and graphite platelets reinforced composites

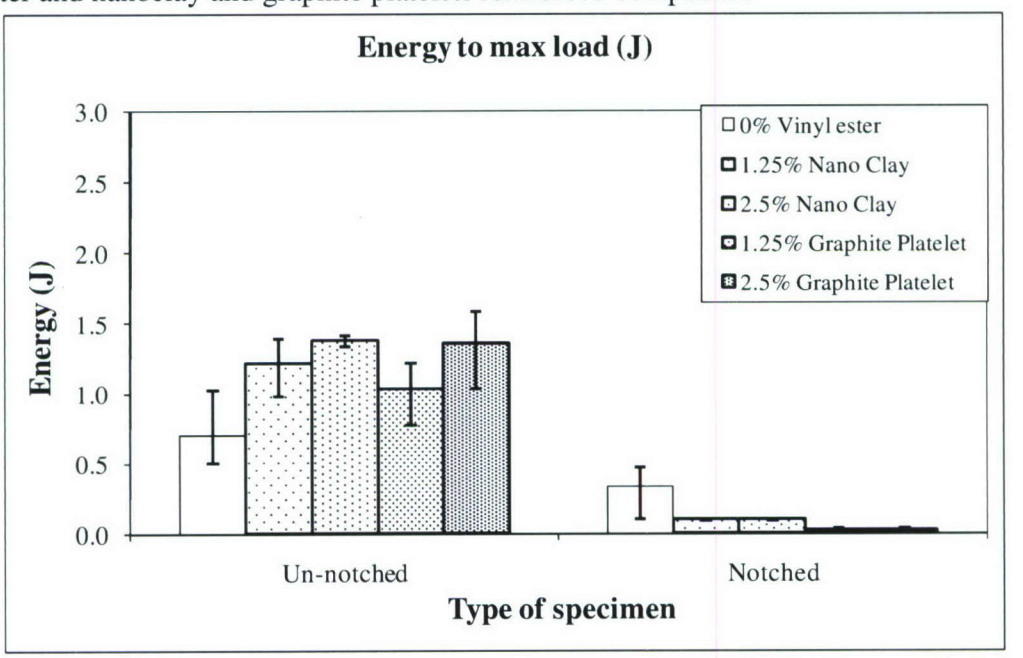

Figure 2.5.4.12: Energy to maximum load comparison for notched & un-notched pure vinyl ester and nanoclay and graphite platelets reinforced composites

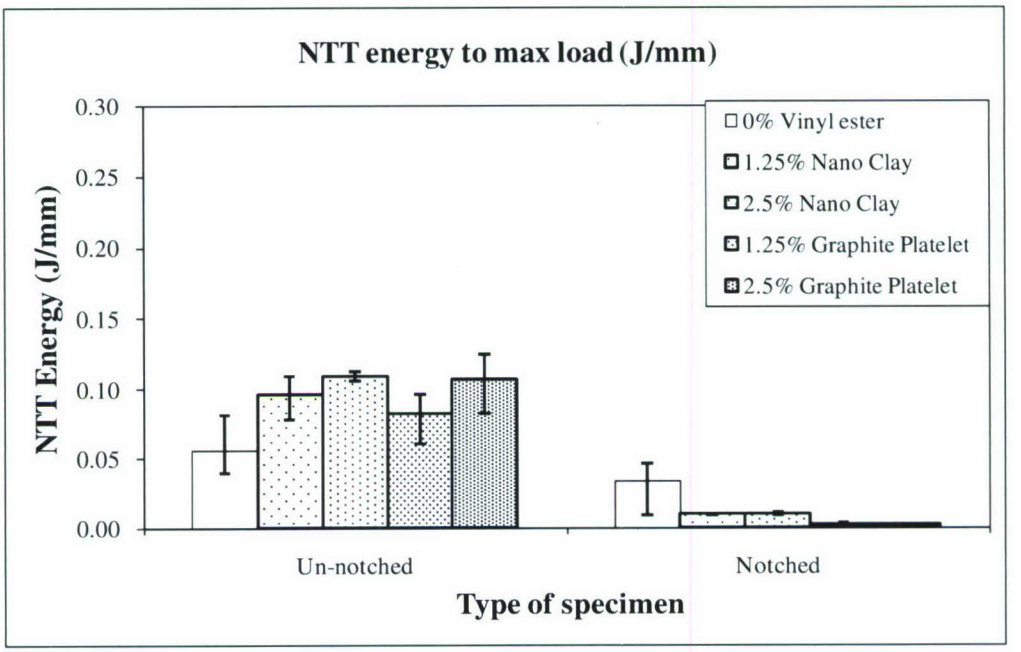

Figure 2.5.4.13: NTT energy to maximum load comparison for notched & un-notched vinyl ester and nanoclay and graphite platelets reinforced composites

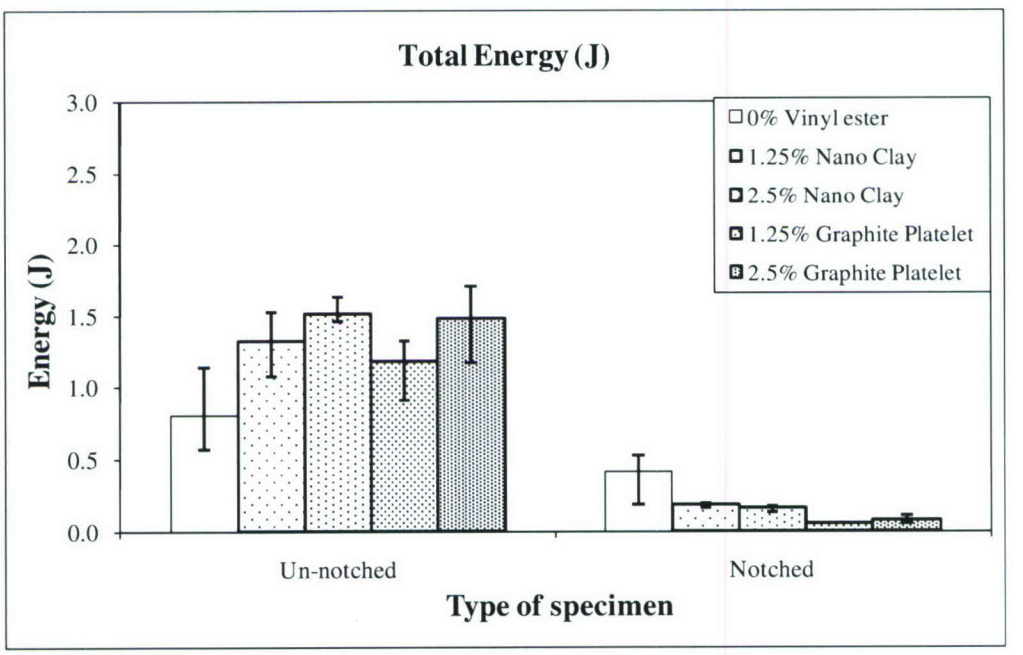

Figure 2.5.4.14: Total energy comparison for notched & un-notched pure vinyl ester and nanoclay and graphite platelets reinforced composites

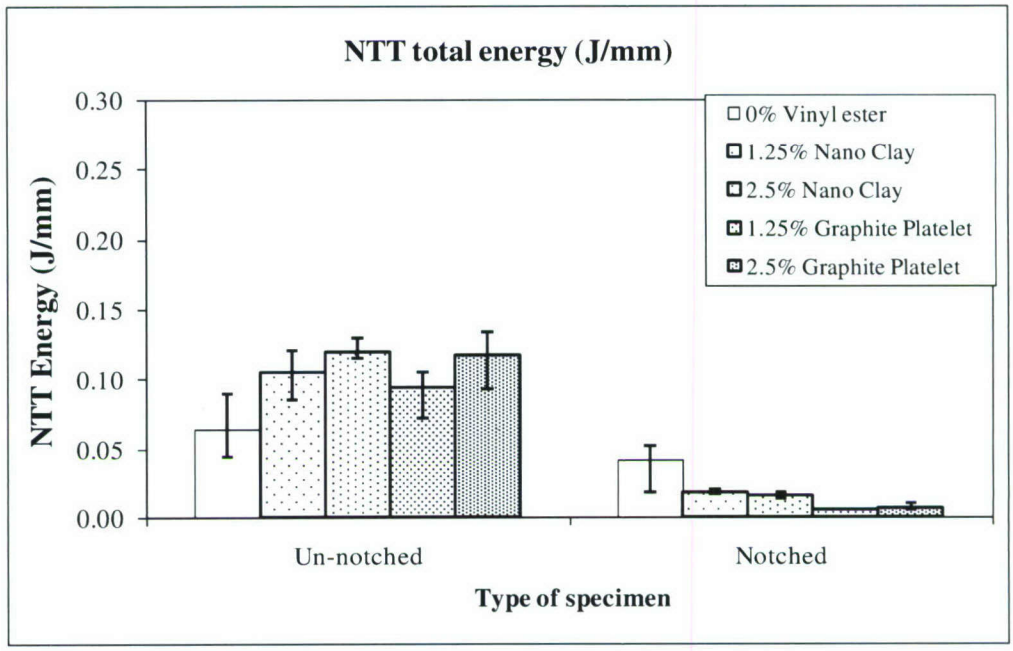

Figure 2.5.4.15: NTT total energy comparison for notched & un-notched pure vinyl ester and nanoclay and graphite platelets reinforced composites

2.5.4b Conclusion

It is observed that in un-notched specimens, reinforcement of nano-clay and graphite platelets increases the load and energy in comparison to that of pure vinyl ester. This increase is observed to be more with nanoclay reinforcement than that with graphite platelets reinforcement. Notched specimens, however, show a decrease in both load and energy absorption suggesting that the nanocomposites are notch-sensitive.

Further, it was observed that in case of notched sample with graphite platelets there is another load peak after the first peak goes down to 0 N but less than maximum load, as can be seen in Figure 2.5.4.9 & 2.5.4.10. This second peak is less than the first one and due to this reason, total energy consumed as computed by the software is less. However, in two of the 2.5% graphite reinforced samples (VG25AI10 & VG25AI12), first peak did not go down to 0 N. Hence, total energy reported in this case may be higher than that of other specimens. It is once again to be noted that total energy computed by the Instron machine software is the energy at a point where load becomes zero after registering maximum load.

2.5.5 Comparison of Nylon 6,6 and Vinyl ester impact characteristics

Maximum load and energy comparison for notched and un-notched specimen of nylon 6,6 and vinyl ester is shown below.

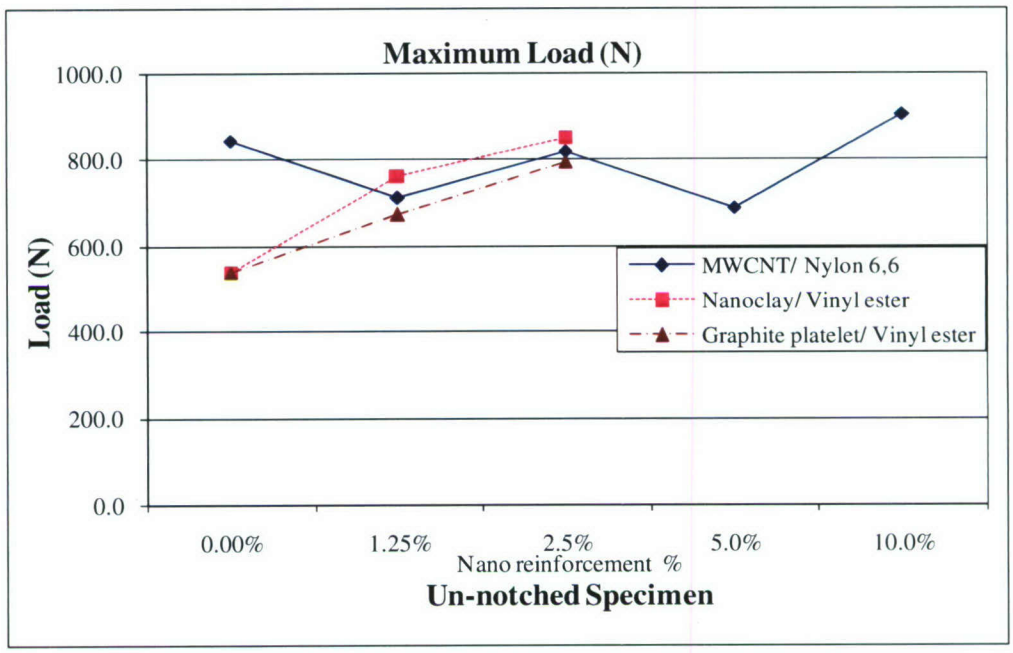

Figure 2.5.5.1: Maximum load comparison for un-notched MWCNT/ nylon 6,6, nanoclay/ vinyl ester and graphite platelet/ vinyl ester

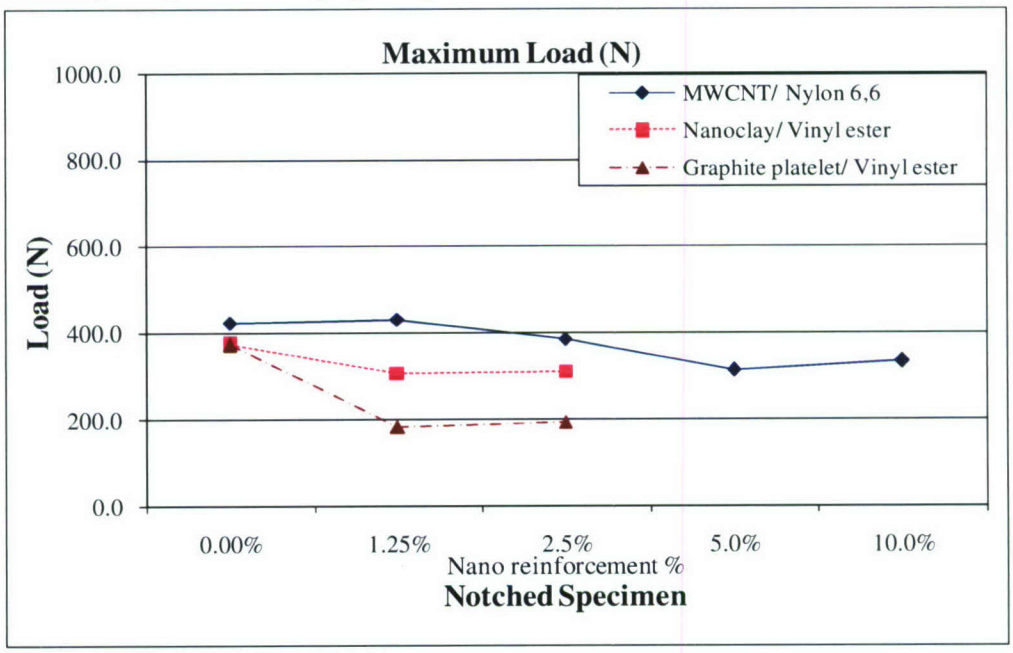

Figure 2.5.5.2: Maximum load comparison for notched MWCNT/ nylon 6,6, nanoclay/ vinyl ester and graphite platelet/ vinyl ester

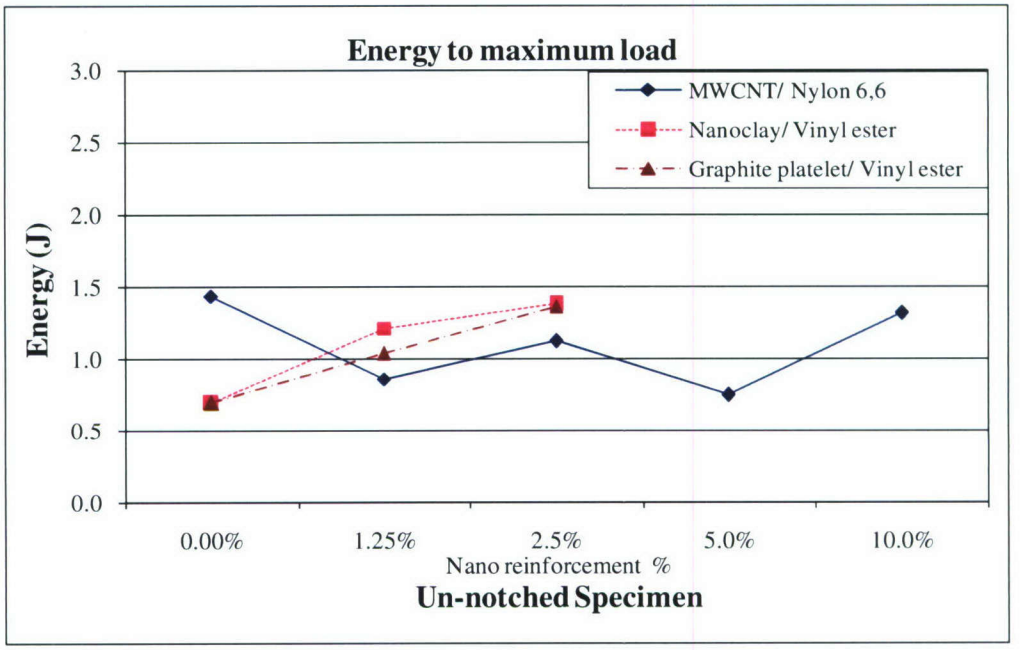

Figure 2.5.5.3: Energy to maximum load comparison for un-notched MWCNT/ nylon 6,6, nanoclay/ vinyl ester and graphite platelet/ vinyl ester

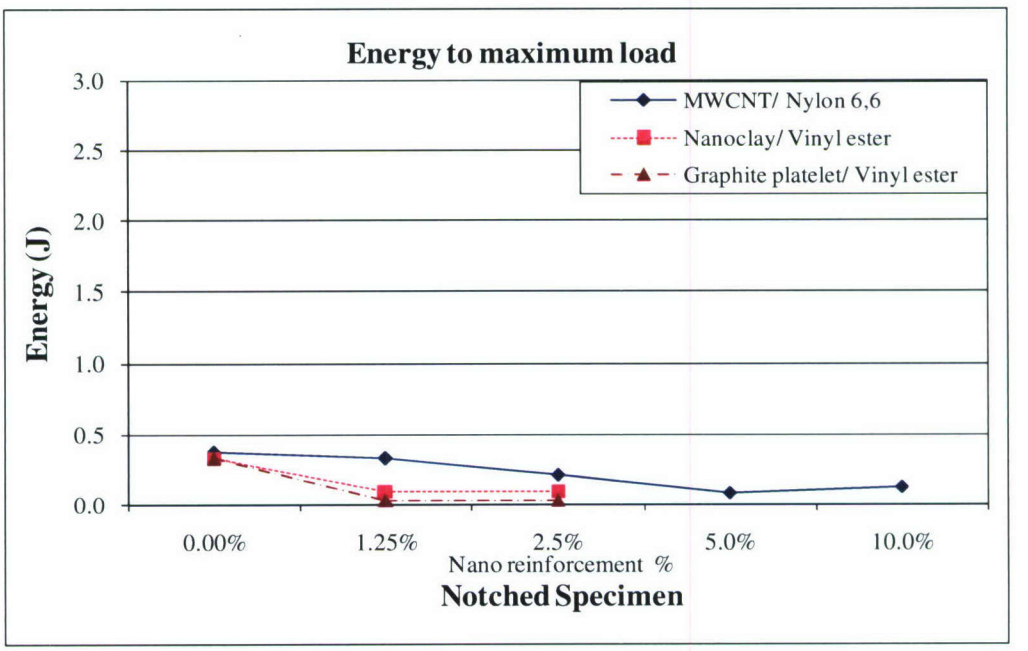

Figure 2.5.5.4: Energy to maximum load comparison for notched MWCNT/ nylon 6,6, nanoclay/ vinyl ester and graphite platelet/ vinyl ester

2.5.5a Conclusion

It can be observed from these graphs that for un-notched specimens, increase in reinforcement of nylon 6,6 shows a fluctuating effect on maximum load and energy to maximum load. However, in notched case, increase in reinforcement shows an adverse effect on load and energy absorption. No firm conclusions can be drawn because of broad scatter band.

In case of vinyl ester, maximum load and energy to maximum load increases with increase in reinforcement of nanoclay and graphite platelets. This increase is observed to be more in nanoclay reinforcement than that of graphite platelets and is more than that of nylon 6,6 with similar reinforcement of MWCNT. At the same time notched samples of vinyl ester with nanoclay and graphite platelets shows a decrease in maximum load and energy to maximum load. This suggests these nanocomposites are notch-sensitive.

2.5.6 Eco-Core foams

Test results & data for the experiments on Eco-Core foams are shown in Figure 2.5.6.1 to 2.5.6.12 & Table 2.5.6.1 to 2.5.6.12. Graphs below show the trend for two specimens only. It is to be noted that energy* computed is the energy at a point where load becomes zero after registering maximum load as calculated by the Instron machine software.

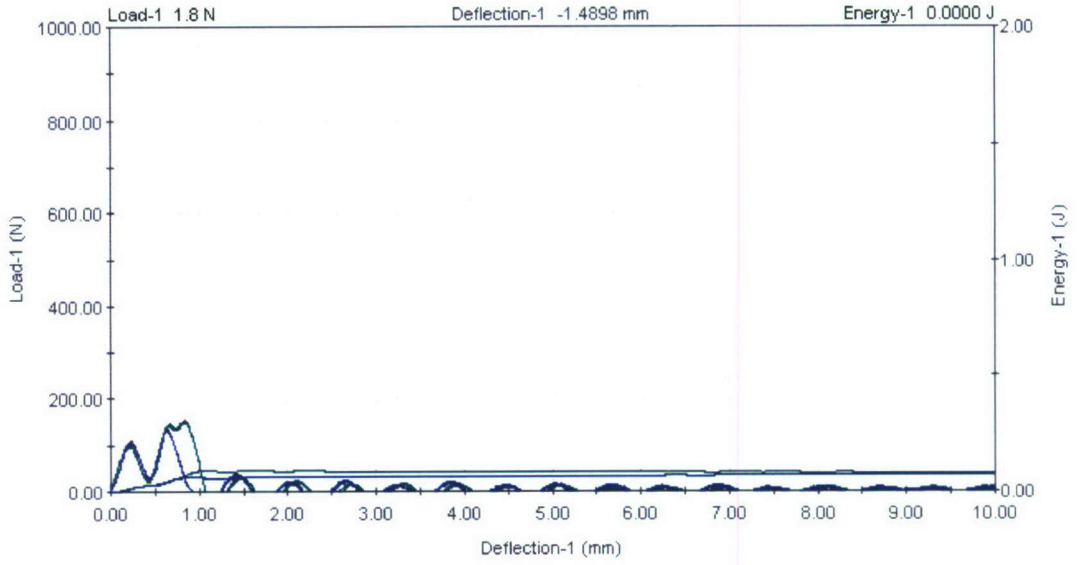

Figure 2.5.6.1: Load & Energy vs Deflection graph for un-notched Eco-Core flyash with phenolic resin (no added fibers) with 1 ply phenolic resin coated glass fiber veil (on top & bottom) for plate OM11

Table 2.5.6.1: Impact characteristics of un-notched Eco-Core flyash with phenolic resin (no added fibers) with 1 ply phenolic resin coated glass fiber veil (on top & bottom) for plate OM11

Specimen ID	Maximum load (N)	Energy to max load (J)	NTT energy to max load (J/mm)	Total energy* (J)	NTT total energy* (J/mm)	Impact energy (J)	Impact velocity (m/s)
OM11I01	154.8	0.0491	0.0039	0.0841	0.0066	5.8346	1.8754
OM11I02	144.3	0.045	0.0035	0.0788	0.0062	5.8083	1.8711
OM11I03	155.3	0.0688	0.0055	0.0909	0.0072	5.8259	1.874
OM11I04	135.2	0.043	0.0034	0.0621	0.0049	5.8548	1.8786
OM11I05	149.9	0.0473	0.0038	0.0821	0.0065	5.7799	1.8665
Average	**147.9**	**0.0506**	**0.004**	**0.0796**	**0.0063**	**5.8207**	**1.8731**
Median	**149.9**	**0.0473**	**0.0038**	**0.0821**	**0.0065**	**5.8259**	**1.874**

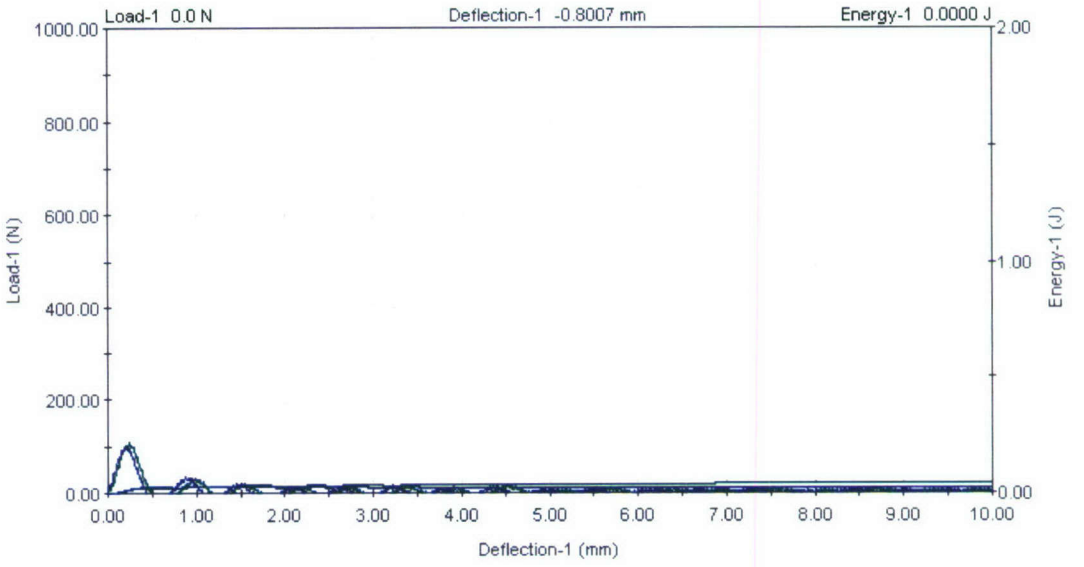

Figure 2.5.6.2: Load & Energy vs Deflection graph for notched Eco-Core flyash with phenolic resin (no added fibers) with 1 ply phenolic resin coated glass fiber veil (on top & bottom) for plate OM11

Table 2.5.6.2: Impact characteristics of notched Eco-Core flyash with phenolic resin (no added fibers) with 1 ply phenolic resin coated glass fiber veil (on top & bottom) for plate OM11

Specimen ID	Maximum load (N)	Energy to max load (J)	NTT energy to max load (J/mm)	Total energy* (J)	NTT total energy* (J/mm)	Impact energy (J)	Impact velocity (m/s)
OM11I07	103.9	0.012	0.0012	0.0265	0.0027	5.8083	1.8711
OM11I08	105.9	0.0124	0.0013	0.0265	0.0027	5.8328	1.8751
OM11I09	109.6	0.0142	0.0014	0.0278	0.0028	5.8164	1.8724
OM11I10	100.4	0.0113	0.0011	0.0243	0.0025	5.4552	1.8134
Average	**105.0**	**0.0125**	**0.0013**	**0.0263**	**0.0027**	**5.7282**	**1.858**
Median	**105.0**	**0.0122**	**0.0012**	**0.0265**	**0.0027**	**5.8124**	**1.8718**

Note: Result of 1 sample was discarded due to damage occurred while testing.

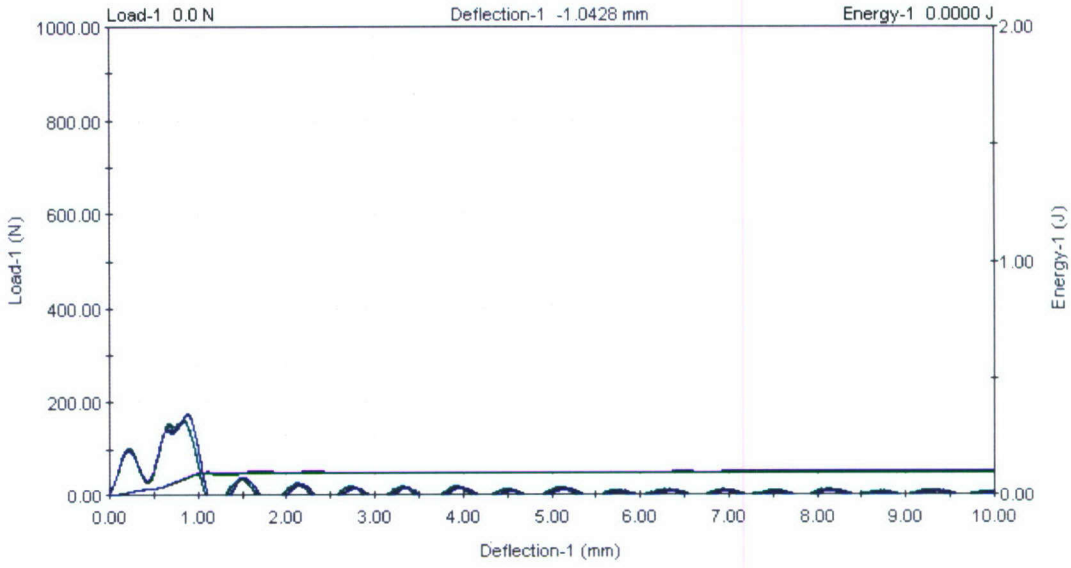

Figure 2.5.6.3: Load & Energy vs Deflection graph for un-notched Eco-Core flyash with phenolic resin (no added fibers) with 1 ply phenolic resin coated glass fiber veil (on top & bottom) for plate OM12

Table 2.5.6.3: Impact characteristics of un-notched Eco-Core flyash with phenolic resin (no added fibers) with 1 ply phenolic resin coated glass fiber veil (on top & bottom) for plate OM12

Specimen ID	Maximum load (N)	Energy to max load (J)	NTT energy to max load (J/mm)	Total energy* (J)	NTT total energy* (J/mm)	Impact energy (J)	Impact velocity (m/s)
OM12I01	162.9	0.0726	0.0058	0.0969	0.0077	5.7776	1.8662
OM12I02	168.4	0.076	0.006	0.1005	0.0079	5.7927	1.8686
OM12I03	168.5	0.0728	0.0057	0.0978	0.0077	5.7939	1.8688
OM12I04	177.4	0.0778	0.0061	0.1025	0.0081	5.7772	1.8661
Average	**169.3**	**0.0748**	**0.0059**	**0.0994**	**0.0079**	**5.7854**	**1.8674**
Median	**168.4**	**0.0744**	**0.0059**	**0.0991**	**0.0078**	**5.7852**	**1.8674**

Note: Result of 1 sample was discarded due to damage occurred while testing.

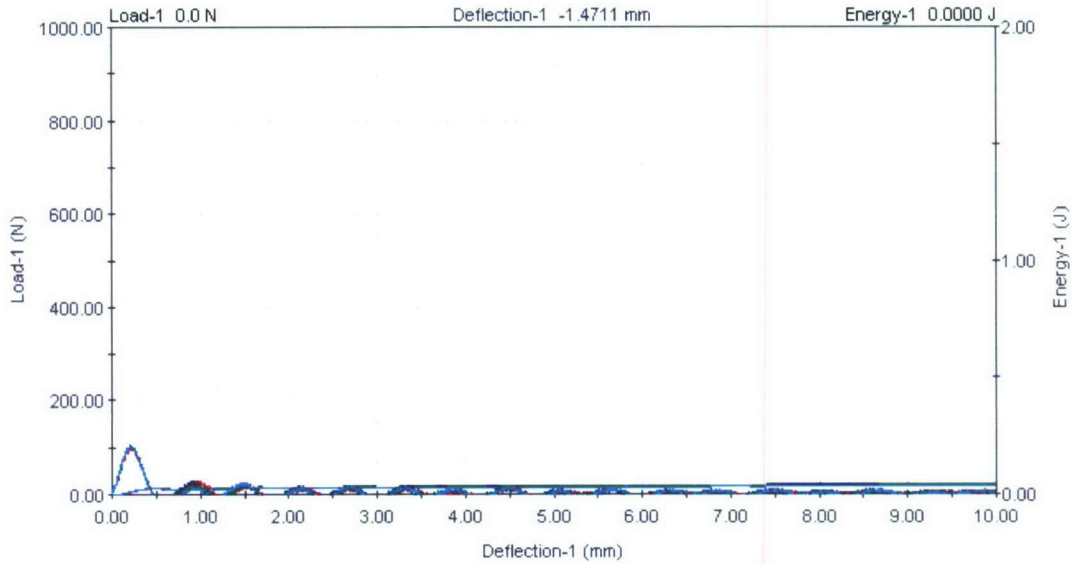

Figure 2.5.6.4: Load & Energy vs Deflection graph for notched Eco-Core flyash with phenolic resin (no added fibers) with 1 ply phenolic resin coated glass fiber veil (on top & bottom) for plate OM12

Table 2.5.6.4: Impact characteristics of notched Eco-Core flyash with phenolic resin (no added fibers) with 1 ply phenolic resin coated glass fiber veil (on top & bottom) for plate OM12

Specimen ID	Maximum load (N)	Energy to max load (J)	NTT energy to max load (J/mm)	Total energy* (J)	NTT total energy* (J/mm)	Impact energy (J)	Impact velocity (m/s)
OM12I06	104.1	0.0117	0.0012	0.0263	0.0026	5.8012	1.87
OM12I07	104.2	0.0119	0.0012	0.0264	0.0027	5.7713	1.8652
OM12I08	100.4	0.0111	0.0011	0.0255	0.0026	5.7927	1.8686
OM12I09	106	0.0124	0.0012	0.0268	0.0027	5.8127	1.8718
OM12I10	102.4	0.0115	0.0012	0.0263	0.0026	5.8059	1.8707
Average	**103.4**	**0.0117**	**0.0012**	**0.0262**	**0.0026**	**5.7967**	**1.8693**
Median	**104.1**	**0.0117**	**0.0012**	**0.0263**	**0.0026**	**5.8012**	**1.87**

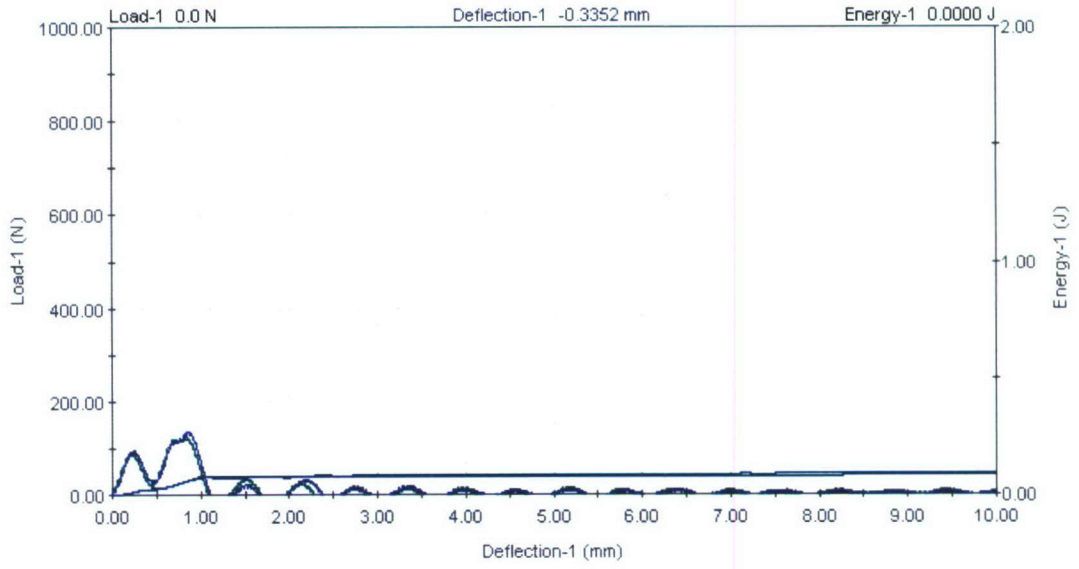

Figure 2.5.6.5: Load & Energy vs Deflection graph for un-notched Eco-Core flyash w/ phenolic resin (0% wt. 0.125-in chopped glass fiber) with no covering for plate OM16

Table 2.5.6.5: Impact characteristics of un-notched Eco-Core flyash w/ phenolic resin (0% wt. 0.125-in chopped glass fiber) with no covering for plate OM16

Specimen ID	Maximum load (N)	Energy to max load (J)	NTT energy to max load (J/mm)	Total energy* (J)	NTT total energy* (J/mm)	Impact energy (J)	Impact velocity (m/s)
OM16I01	128.7	0.0533	0.0042	0.0751	0.006	5.9239	1.8897
OM16I02	125.1	0.0536	0.0043	0.0749	0.0059	5.9807	1.8987
OM16I03	138	0.0594	0.0047	0.0803	0.0064	5.9546	1.8945
OM16I04	136.1	0.059	0.0047	0.0796	0.0063	5.9173	1.8886
OM16I05	128.6	0.0565	0.0045	0.0763	0.0061	5.9756	1.8979
Average	**131.3**	**0.0564**	**0.0045**	**0.0772**	**0.0061**	**5.9504**	**1.8939**
Median	**128.7**	**0.0565**	**0.0045**	**0.0763**	**0.0061**	**5.9546**	**1.8945**

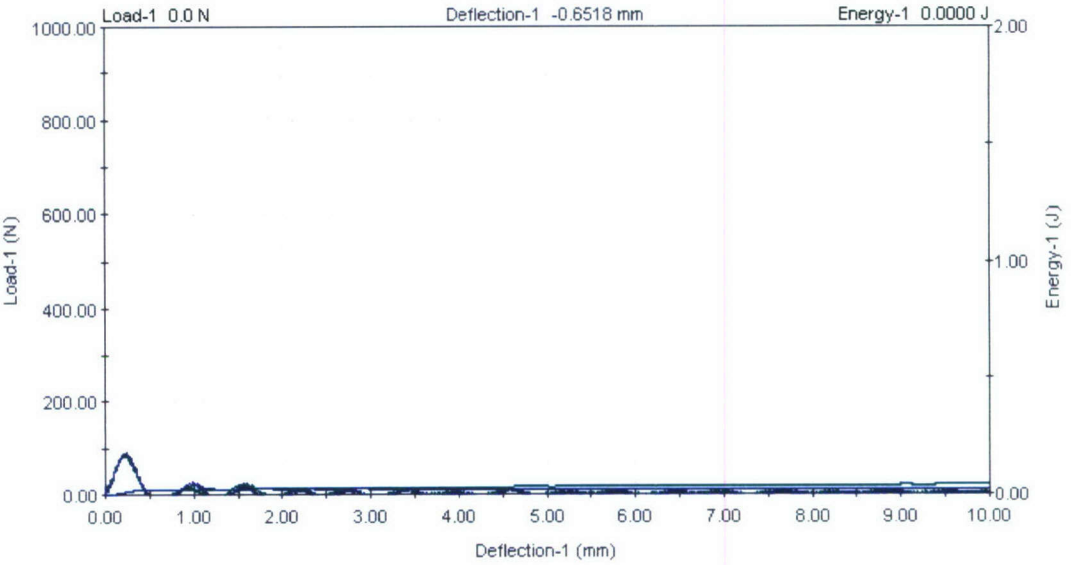

Figure 2.5.6.6: Load & Energy vs Deflection graph for notched Eco-Core flyash w/ phenolic resin (0% wt. 0.125-in chopped glass fiber) with no covering for plate OM16

Table 2.5.6.6: Impact characteristics of notched Eco-Core flyash w/ phenolic resin (0% wt. 0.125-in chopped glass fiber) with no covering for plate OM16

Specimen ID	Maximum load (N)	Energy to max load (J)	NTT energy to max load (J/mm)	Total energy* (J)	NTT total energy* (J/mm)	Impact energy (J)	Impact velocity (m/s)
OM16I06	90	0.0109	0.0011	0.0232	0.0023	5.9287	1.8904
OM16I07	86.4	0.0099	0.001	0.0223	0.0022	5.9384	1.892
OM16I08	90	0.0109	0.0011	0.023	0.0023	5.9907	1.9003
OM16I09	90.1	0.012	0.0012	0.023	0.0022	5.9663	1.8964
Average	**89.2**	**0.0109**	**0.0011**	**0.0229**	**0.0022**	**5.956**	**1.8948**
Median	**90.0**	**0.0109**	**0.0011**	**0.023**	**0.0022**	**5.9524**	**1.8942**

Note: Result of 1 sample was discarded due to damage while testing.

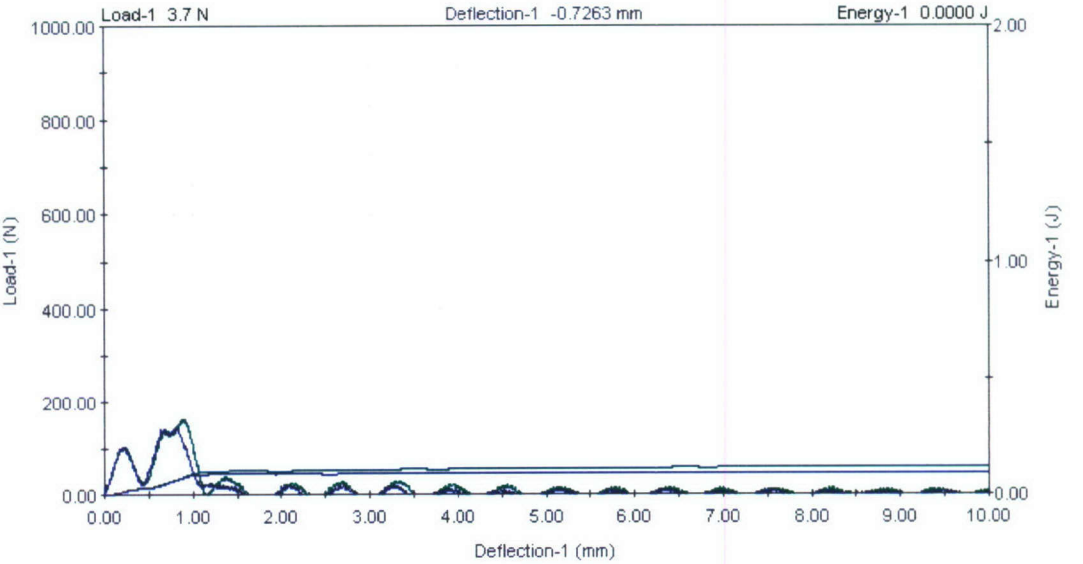

Figure 2.5.6.7: Load & Energy vs Deflection graph for un-notched Eco-Core flyash with phenolic resin (with 6% wt. 0.125-in chopped glass fibers) with no covering for plate OM21

Table 2.5.6.7: Impact characteristics of un-notched Eco-Core flyash with phenolic resin (with 6% wt. 0.125-in chopped glass fibers) with no covering for plate OM21

Specimen ID	Maximum load (N)	Energy to max load (J)	NTT energy to max load (J/mm)	Total energy* (J)	NTT total energy* (J/mm)	Impact energy (J)	Impact velocity (m/s)
OM21I01	147.1	0.0654	0.0052	0.088	0.007	5.9774	1.8982
OM21I02	161.9	0.073	0.0058	0.0971	0.0077	5.9609	1.8955
OM21I03	143.4	0.0661	0.0052	0.0947	0.0075	5.956	1.8948
OM21I04	143.3	0.0659	0.0052	0.094	0.0074	5.9899	1.9001
OM21I05	143.5	0.0492	0.0039	0.0938	0.0074	5.9462	1.8932
Average	**147.8**	**0.0639**	**0.0051**	**0.0935**	**0.0074**	**5.9661**	**1.8964**
Median	**143.5**	**0.0659**	**0.0052**	**0.094**	**0.0074**	**5.9609**	**1.8955**

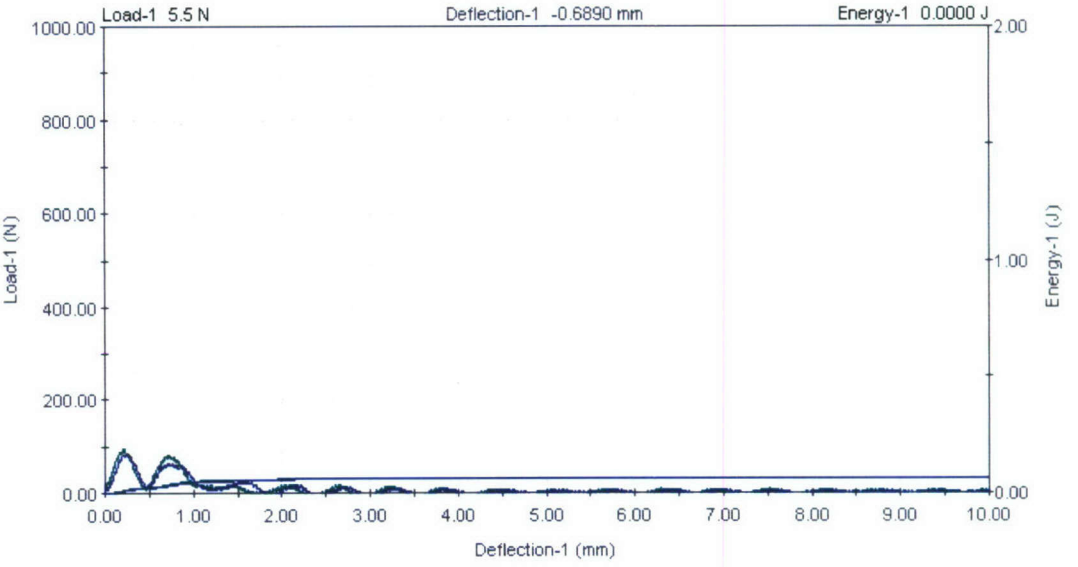

Figure 2.5.6.8: Load & Energy vs Deflection graph for notched Eco-Core flyash with phenolic resin (with 6% wt. 0.125-in chopped glass fibers) with no covering for plate OM21

Table 2.5.6.8: Impact characteristics of notched Eco-Core flyash with phenolic resin (with 6% wt. 0.125-in chopped glass fibers) with no covering for plate OM21

Specimen ID	Maximum load (N)	Energy to max load (J)	NTT energy to max load (J/mm)	Total energy* (J)	NTT total energy* (J/mm)	Impact energy (J)	Impact velocity (m/s)
OM21I06	93.7	0.0101	0.001	0.0453	0.0045	5.9699	1.897
OM21I07	91.9	0.0122	0.0012	0.0487	0.0048	6.0075	1.9029
OM21I08	93.8	0.0116	0.0012	0.0598	0.0059	5.9692	1.8969
OM21I09	90.1	0.0118	0.0012	0.0611	0.0061	5.9701	1.897
OM21I10	86.5	0.0112	0.0011	0.0588	0.0059	5.9712	1.8972
Average	**91.2**	**0.0114**	**0.0011**	**0.0547**	**0.0054**	**5.9776**	**1.8982**
Median	**91.9**	**0.0116**	**0.0012**	**0.0588**	**0.0059**	**5.9701**	**1.897**

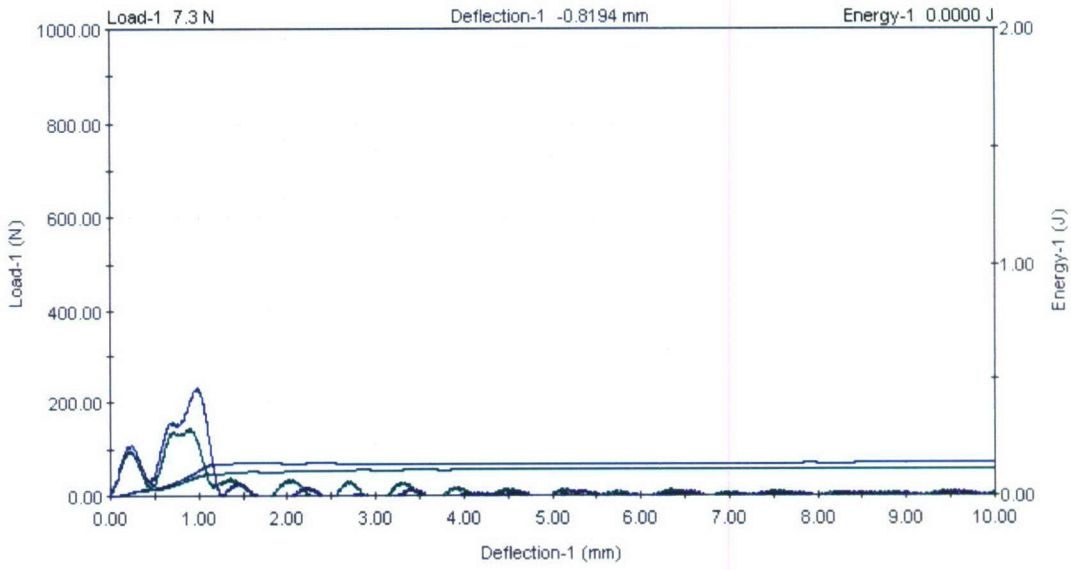

Figure 2.5.6.9: Load & Energy vs Deflection graph for un-notched Eco-Core flyash with phenolic resin (with 6% wt. 0.125-in chopped glass fibers) with 1-ply covering of phenolic resin-coated glass fiber veil (on top/bottom surface) for plate OM18

Table 2.5.6.9: Impact characteristics of un-notched Eco-Core flyash with phenolic resin (with 6% wt. 0.125-in chopped glass fibers) with 1-ply covering of phenolic resin-coated glass fiber veil (on top/bottom surface) for plate OM18

Specimen ID	Maximum load (N)	Energy to max load (J)	NTT energy to max load (J/mm)	Total energy* (J)	NTT total energy* (J/mm)	Impact energy (J)	Impact velocity (m/s)
OM18I01	163.2	0.0702	0.0056	0.1107	0.0088	5.9104	1.8875
OM18I02	144.9	0.0695	0.0055	0.1029	0.0082	5.9436	1.8928
OM18I03	185.3	0.0848	0.0067	0.1092	0.0087	5.9388	1.892
OM18I04	233	0.1055	0.0084	0.1365	0.0108	5.9493	1.8937
OM18I05	152.3	0.0687	0.0054	0.0928	0.0073	5.9838	1.8992
Average	**175.8**	**0.0798**	**0.0063**	**0.1104**	**0.0088**	**5.9452**	**1.893**
Median	**163.2**	**0.0702**	**0.0056**	**0.1092**	**0.0087**	**5.9436**	**1.8928**

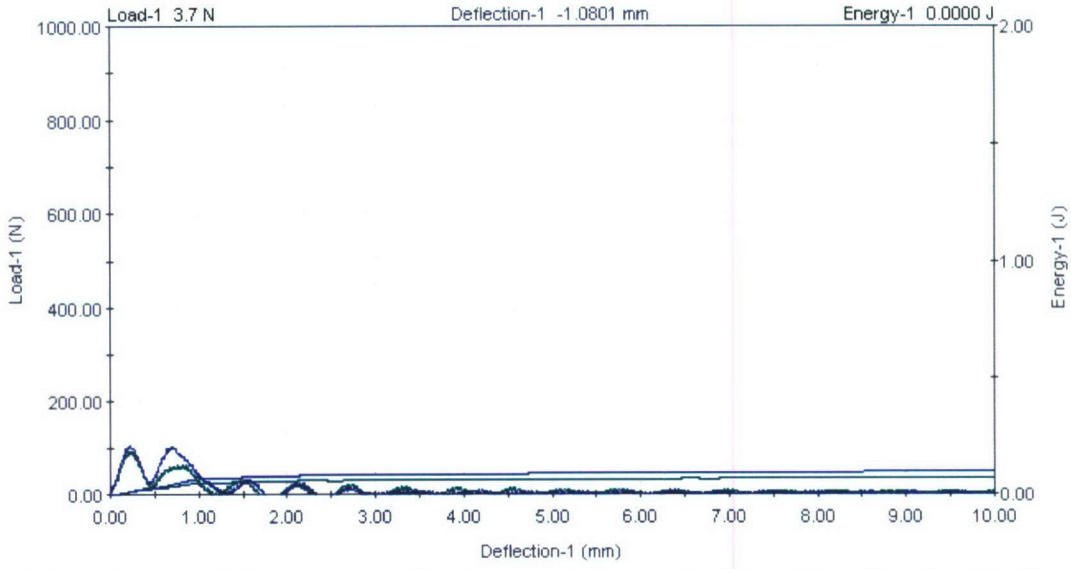

Figure 2.5.6.10: Load & Energy vs Deflection graph for notched Eco-Core flyash with phenolic resin (with 6% wt. 0.125-in chopped glass fibers) with 1-ply covering of phenolic resin-coated glass fiber veil (on top/bottom surface) for plate OM18

Table 2.5.6.10: Impact characteristics of notched Eco-Core flyash with phenolic resin (with 6% wt. 0.125-in chopped glass fibers) with 1-ply covering of phenolic resin-coated glass fiber veil (on top/bottom surface) for plate OM18

Specimen ID	Maximum load (N)	Energy to max load (J)	NTT energy to max load (J/mm)	Total energy* (J)	NTT total energy* (J/mm)	Impact energy (J)	Impact velocity (m/s)
OM18I06	102.7	0.0116	0.0011	0.0613	0.006	5.9614	1.8956
OM18I07	102.7	0.0129	0.0013	0.05	0.0049	5.9155	1.8883
OM18I08	99.1	0.0136	0.0013	0.0604	0.0059	5.9845	1.8993
OM18I09	91.8	0.01	0.001	0.0517	0.0052	5.9517	1.8941
OM18I10	104.5	0.0121	0.0012	0.0724	0.0071	5.9967	1.9012
Average	**100.2**	**0.012**	**0.0012**	**0.0592**	**0.0058**	**5.962**	**1.8957**
Median	**102.7**	**0.0121**	**0.0012**	**0.0604**	**0.0059**	**5.9614**	**1.8956**

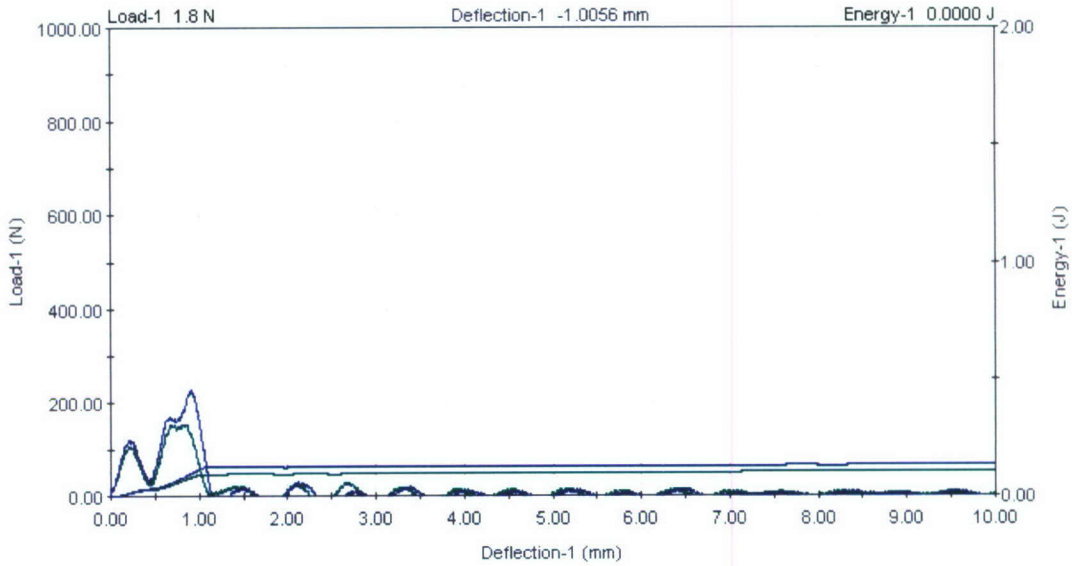

Figure 2.5.6.11: Load & Energy vs Deflection graph for un-notched Eco-Core flyash with phenolic resin (with 6% wt. 0.125-in chopped glass fibers) with 1-ply covering of phenolic resin-coated glass fiber veil (on top/bottom surface) for plate OM19

Table 2.5.6.11: Impact characteristics of un-notched Eco-Core flyash with phenolic resin (with 6% wt. 0.125-in chopped glass fibers) with 1-ply covering of phenolic resin-coated glass fiber veil (on top/bottom surface) for plate OM19

Specimen ID	Maximum load (N)	Energy to max load (J)	NTT energy to max load (J/mm)	Total energy* (J)	NTT total energy* (J/mm)	Impact energy (J)	Impact velocity (m/s)
OM19I01	152.3	0.0467	0.0037	0.0939	0.0075	5.9879	1.8998
OM19I02	229.3	0.098	0.0078	0.1277	0.0102	5.9866	1.8996
OM19I03	176.2	0.0522	0.0042	0.1042	0.0083	6.0103	1.9034
OM19I04	174.3	0.0554	0.0044	0.1035	0.0082	6.0069	1.9028
OM19I05	194.5	0.0874	0.007	0.1121	0.0089	5.9686	1.8968
Average	**185.3**	**0.068**	**0.0054**	**0.1083**	**0.0086**	**5.9921**	**1.9005**
Median	**176.2**	**0.0554**	**0.0044**	**0.1042**	**0.0083**	**5.9879**	**1.8998**

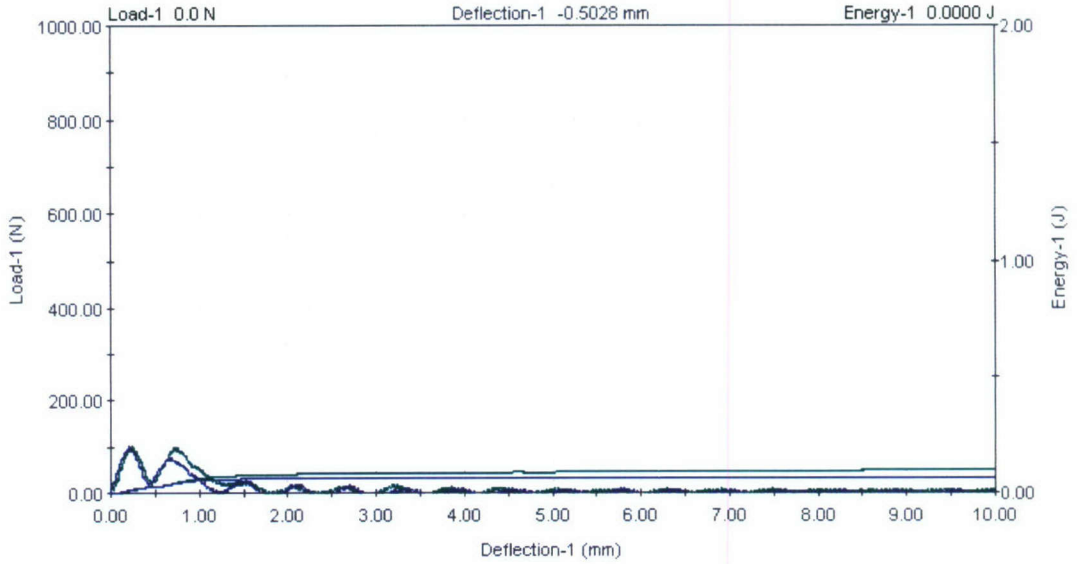

Figure 2.5.6.12: Load & Energy vs Deflection graph for notched Eco-Core flyash with phenolic resin (with 6% wt. 0.125-in chopped glass fibers) with 1-ply covering of phenolic resin-coated glass fiber veil (on top/bottom surface) for plate OM19

Table 2.5.6.12: Impact characteristics of notched Eco-Core flyash with phenolic resin (with 6% wt. 0.125-in chopped glass fibers) with 1-ply covering of phenolic resin-coated glass fiber veil (on top/bottom surface) for plate OM19

Specimen ID	Maximum load (N)	Energy to max load (J)	NTT energy to max load (J/mm)	Total energy* (J)	NTT total energy* (J/mm)	Impact energy (J)	Impact velocity (m/s)
OM19I06	111.9	0.0128	0.0012	0.0617	0.006	5.9679	1.8966
OM19I07	110.1	0.0149	0.0015	0.0736	0.0072	6.0035	1.9023
OM19I08	100.9	0.0134	0.0013	0.0795	0.0077	5.9345	1.8913
OM19I09	108.3	0.0139	0.0014	0.0725	0.0071	5.9688	1.8968
OM19I10	100.9	0.0122	0.0012	0.0575	0.0057	5.9963	1.9012
Average	**106.4**	**0.0134**	**0.0013**	**0.069**	**0.0067**	**5.9742**	**1.8976**
Median	**108.3**	**0.0134**	**0.0013**	**0.0725**	**0.0071**	**5.9688**	**1.8968**

2.5.6a Summary of Results

Figures 2.5.6.13 to 2.5.6.17 show the summarized output for Eco-Core foams. It is to be noted that 5 notched & 5 un-notched specimens from each category were tested in order to obtain a statistically significant data. However, data of 1 specimen each from notched OM11 and OM16 and un-notched OM12 has been discarded due to damage during testing.

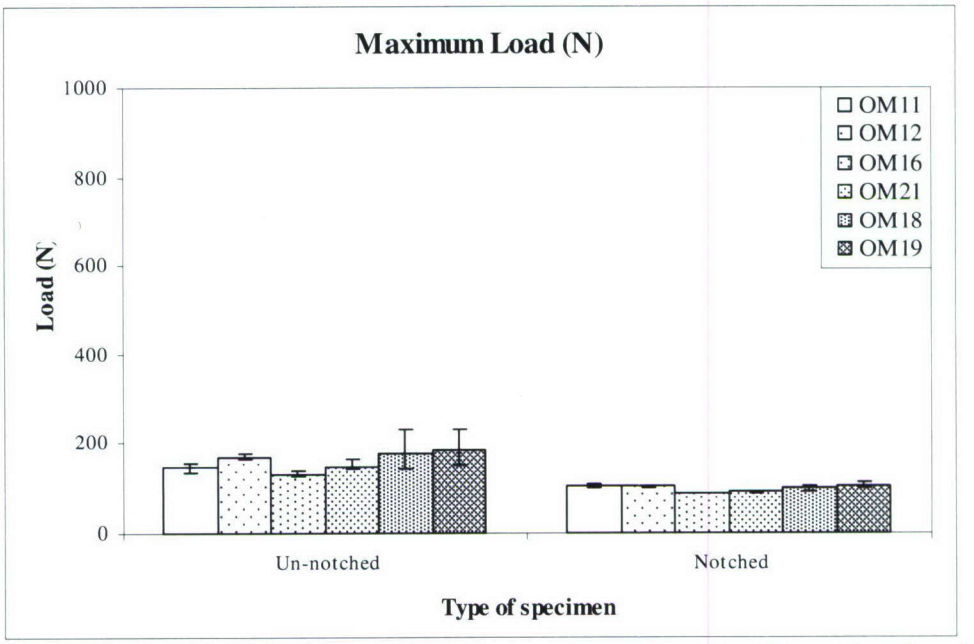

Figure 2.5.6.13: Maximum load comparison for Eco-Core flyash with different configurations for notched & un-notched specimens.

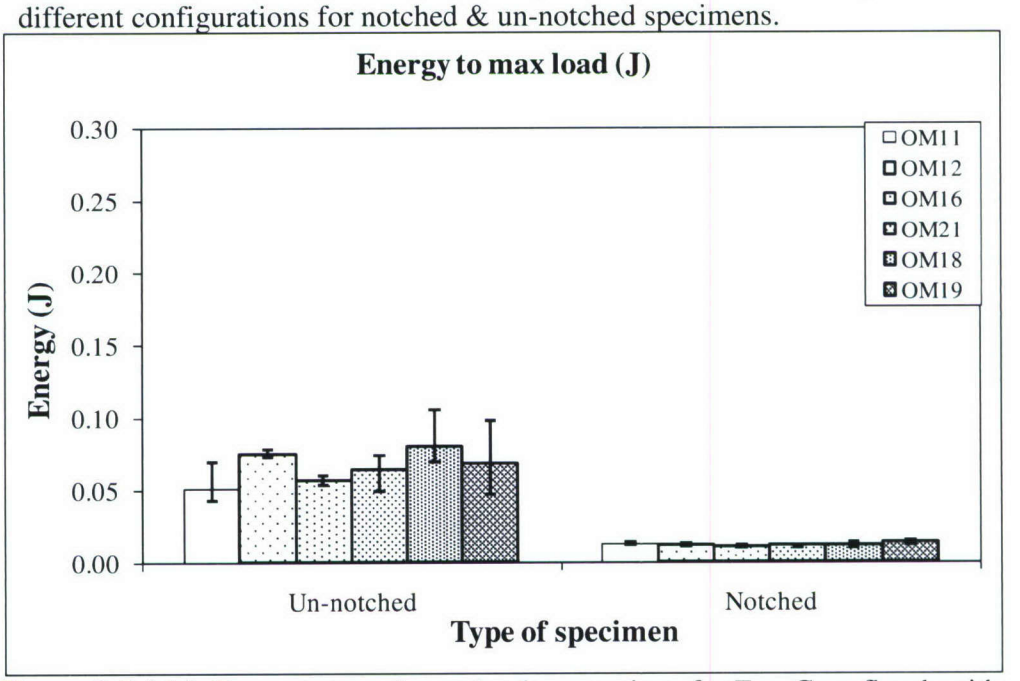

Figure 2.5.6.14: Energy to maximum load comparison for Eco-Core flyash with different configurations for notched & un-notched specimens

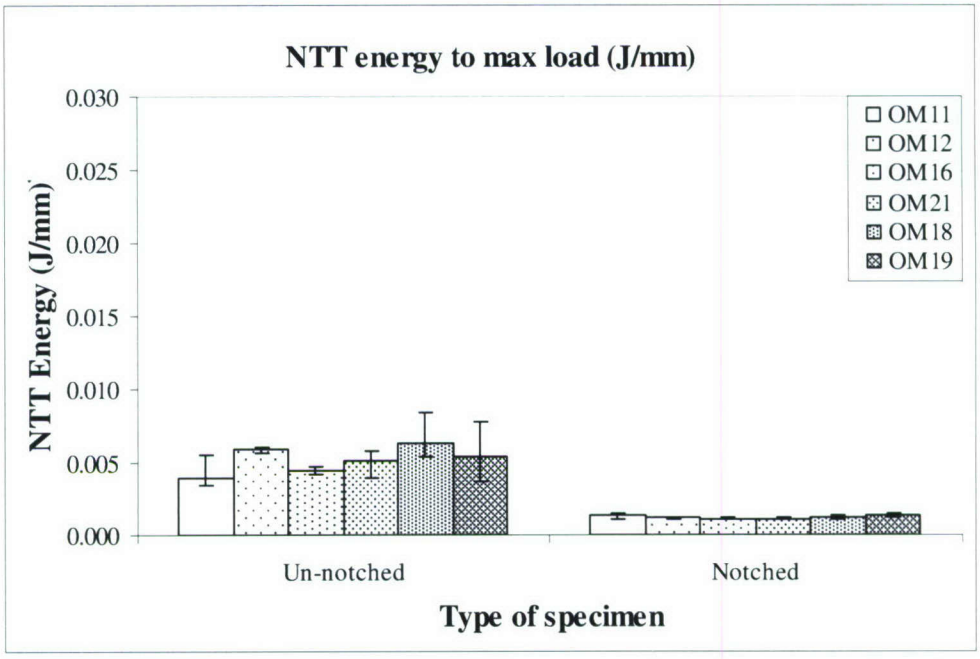

Figure 2.5.6.15: NTT energy to maximum load comparison for Eco-Core flyash with different configurations for notched & un-notched specimens

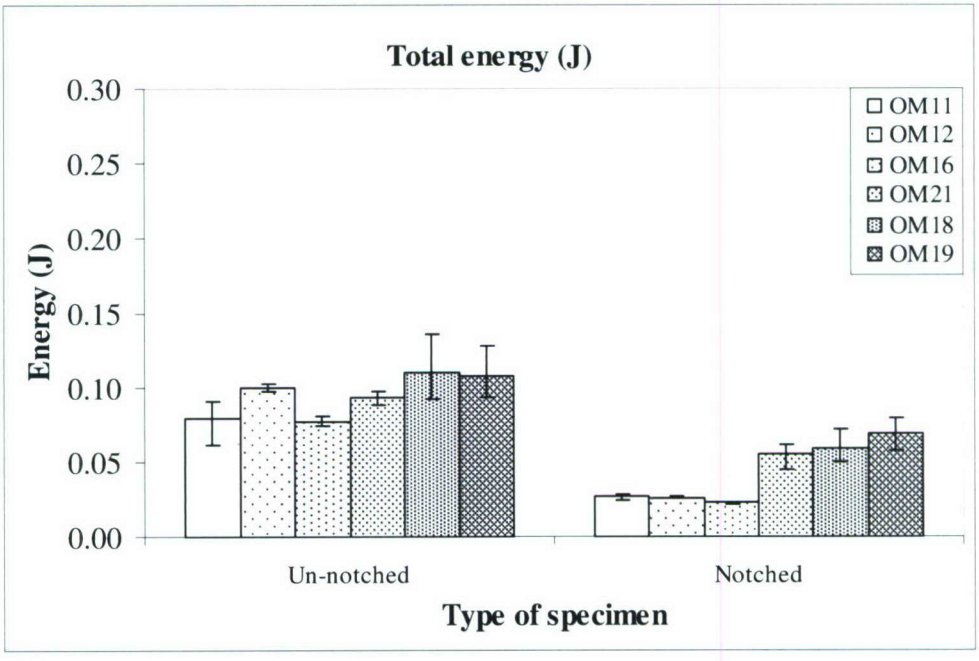

Figure 2.5.6.16: Total Energy comparison for Eco-Core flyash with different configurations for notched & un-notched specimens

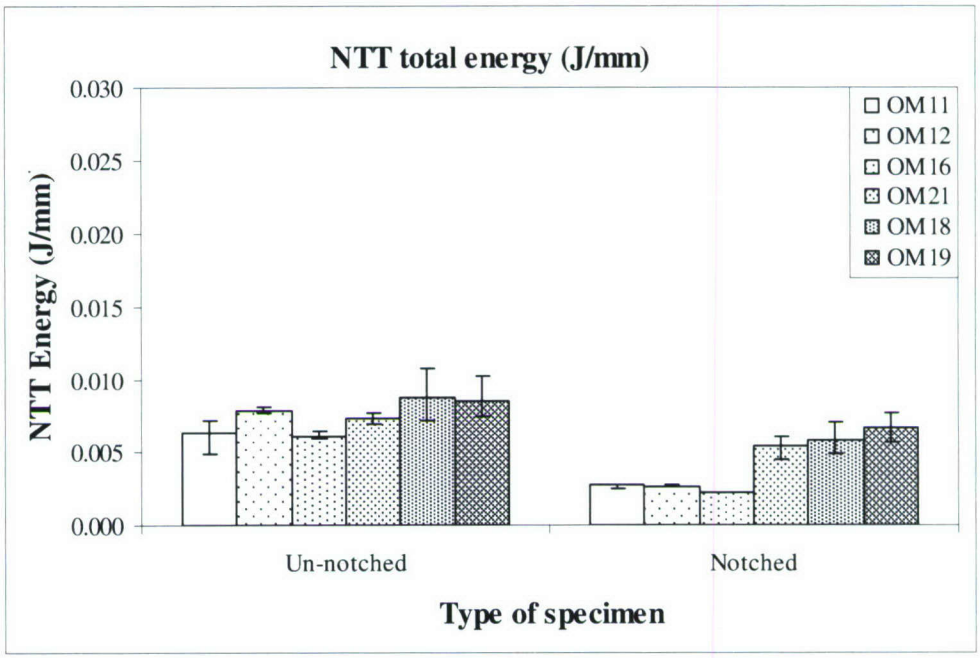

Figure 2.5.6.17: NTT total energy comparison for Eco-Core flyash with different configurations for notched & un-notched specimens

2.5.6b Conclusion

It was observed that OM12, OM18 & OM19 showed better load and energy absorption in case of un-notched specimen as compared to other configuration. However, total energy absorbed before failure reduced drastically in OM12. Hence, OM18 and OM19 look to be better material for good impact properties.

3.0 ELECTROCHEMICAL IMPEDANCE SPECTROSCOPY (EIS)

Recently, EIS in situ sensors has been used to predict deterioration of coating, moisture ingress and crack propagation at interfaces of adhesively jointed materials [3.1]. Early detection of corrosion initiation is of great importance to overcome structural deficiencies. The simplest method for detecting debonding can be achieved by direct comparison of raw impedance [3.2]. Usually, the impedance typically increases in magnitude as the cracks propagate. However, additional information may be obtained from the impedance spectra by using equivalent circuit analysis. It is found that the resistive components in the equivalent circuit used are function of moisture content and that the capacitance parameter is function of both moisture content and bonded area [3.3-3.4].

In this project, the EIS technique was used to study the long-term behavior of nano reinforced composites with different wt percentage of MWCNT subjected to extreme service conditions of freezing and thawing cycling from -12°C to 10°C at 6 cycles per day, according to ASTM C666- Procedure A (freezing in water and thawing in water) for 45 and 90 days.

3.1 Electrical Impedance

Electrochemical impedance is defined as the resistance to a current in an electrochemical cell. By measuring an *AC* current across the electrodes due to an applied *AC* voltage, electrical impedance *Z* may be obtained as a complex ratio of the *AC* voltage *V(t)* to the response current *I(t)* .

For an *AC* voltage, *V (t)* and impedance magnitude *Z* can be expressed as:

$$V(t) = V_o\, e^{j\omega t} = V_o\, (\cos\omega t + j\sin\omega t) \qquad (3.1)$$

$$Z = \frac{V(t)}{I(t)} \qquad (3.2)$$

Where ω is the excitation frequency in *Hz*, and V_o is the amplitude of the voltage signal.

The response current and impedance are given by:

$$I(t) = I_o\, \left[\cos(\omega t - \phi) + j\sin(\omega t - \phi)\right] \qquad (3.3)$$

$$Z = Z_o(\cos\phi + j\sin\phi) \qquad (3.4)$$

Z_o, ϕ are the magnitude and phase angle respectively which are functions of the excitation frequency. It is common to display the impedance by directly plotting the variation of the magnitude (Bode) or the phase against the excitation frequency.

$$Z = \sqrt{(Z_R)^2 + \frac{1}{(\omega C)^2}} \tag{3.5}$$

Alternatively, constant phase element (*CPE*) is often used in equivalent circuits. This may be either resistance or capacitor. The impedance of *CPE* is defined as:

$$Z_{CPE} = A(j\omega)^{-\alpha} \tag{3.6}$$

α has a maximum value of 1 (capacitive behavior) and minimum value of zero (resistive behavior)

3.2 EIS measurements

Specimens with dimensions of *25.4 mm* x *25.4 mm* x *9.5 mm* were cut from the reinforced nylon 6,6 of different wt percent of MWCNT. Two ends of copper tape were bonded on the top and bottom surfaces of each specimen and attached to pair of electrodes as shown in Figure 3.1. The sensor electrodes serve as a counter and working electrodes for the EIS measurements, which allows conventional EIS data acquisition in ambient environment instead of the immersion conditions required by traditional electrodes.

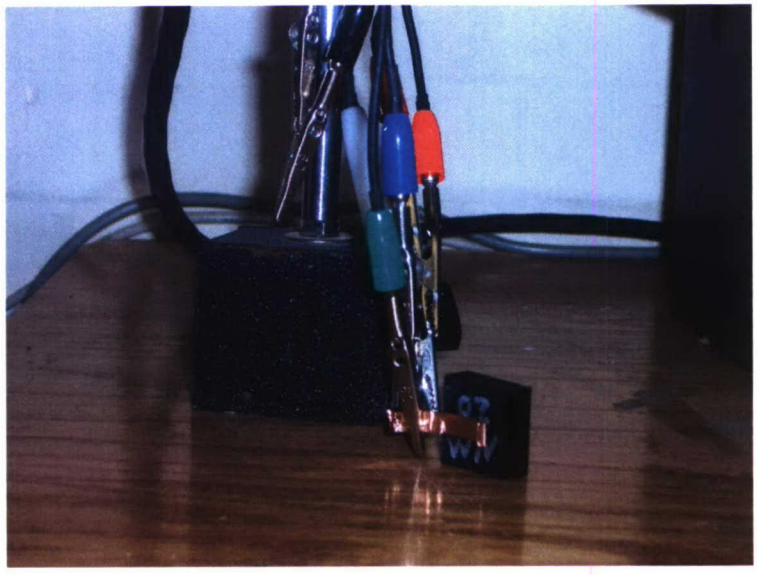

Figure 3.1: Experimental setup for the EIS system.

An alternating *AC* voltage was applied across the electrodes terminals. The impedance spectra were obtained over a range of frequencies from 0.1 Hz to100 kHz using the Gamry EIS 300 Electrochemical Impedance Spectroscopy Software. The Gamry Instrument Echem Analyst software included with the EIS300 Electrochemical Impedance Software includes a graphical Model Editor. This Model Editor was used to visually build an equivalent circuit model. The spectra were customarily performed in the Bode magnitude plot (impedance magnitude versus frequency). Phase angle plots (phase angle versus frequency) were used to confirm interpretation of the magnitude plot.

3.3.1 Raw impedance spectra

Figure 3.2 shows the raw impedance spectra for the un-aged (baseline) nylon 6,6 specimens with different MWCNT wt percent. It was observed that the impedance decreases in magnitude as the MWCNT wt percent increases.

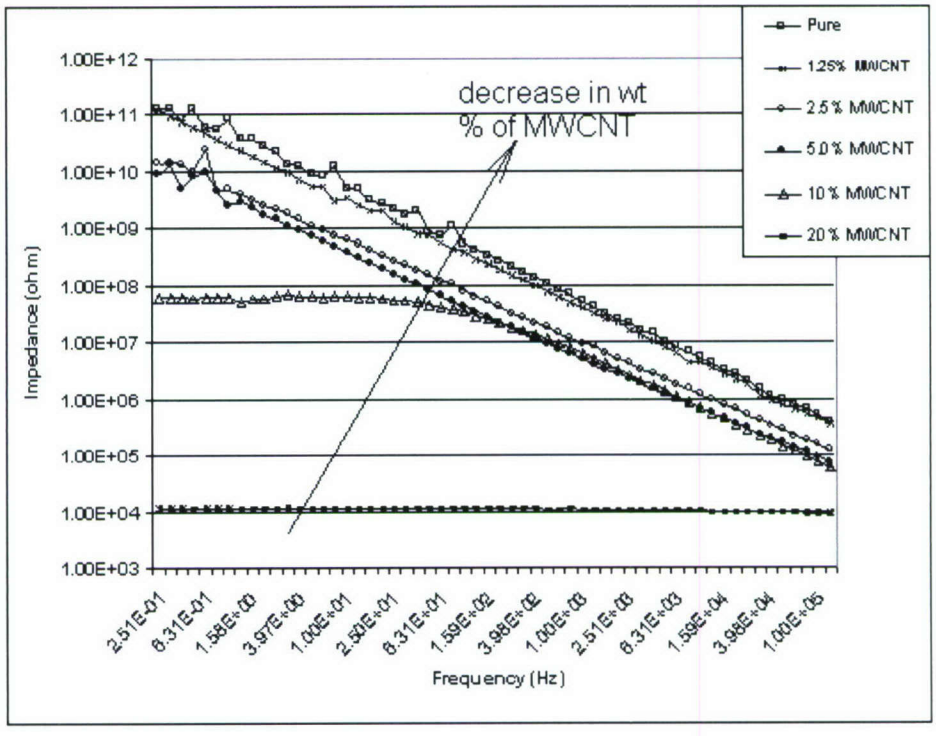

Figure 3.2: Impedance spectra for un-aged nylon 6,6 with different wt percent of MWCNT.

Effect of aging is shown in Figures 3.3-3.9, which show a capacitive spectrum in nature (slope of -1 on the log impedance-frequency plot) with high impedance at low frequency. In the case of 0 wt percent (Figure 3.3), the spectrum behavior reflects a polymer (nylon 6,6) with no pathways of low resistance, meaning that the pure nylon 6,6 has the greatest impedance magnitude over the whole frequency range. However, the effect of 45 days aging is more pronounced in the case of pure nylon 6,6 rather than that associated with the higher reinforced MWCNT composites. This is because the pure nylon had the maximum moisture uptake (wt percent) when subjected to environmental aging. For example, pure nylon's specimen experienced 61% drop in impedance magnitude after 45 days of aging time while the one with1.25 wt percent MWCNT decreased by 16% of the baseline impedance magnitude when excited at 50 Hz. Similarly, the impedance magnitude for the 10 wt percent nano composite reduced by 10% after 45 days aging, as seen in impedance spectra Figures (Figures 3.3-3.8). Tables 3.1-3.3 show the moisture absorption wt percent for each aged specimen.

Another observation is that the impedance corresponding to the 0, 1.25 and 10 wt percent nano composites decreases in magnitude considerably over the low frequency range when subjected to longer period of freezing and thawing while others specimens (2.5, 5 and 20 wt percents) experienced a slight drop in impedance magnitude. For example, pure nylon6,6 shows a 66% impedance reduction at 50 Hz when exposed to freeze-thaw cycling for 90 days compared to 60% off when it was subjected to 45 days aging at the same excitation frequency. Moreover, the impedance for the 1.25 wt percent specimen reduced by 71% of the baseline value after 90 days aging compared to 16% off corresponding to 45 days- aging. The impedance magnitude of the 10 wt percent decreased by 72.5% for the 90 days aged specimen. That is due to the fact that at low frequencies, the current flow in the electrochemical cell is dominated by the movement of ions and different moisture levels affect the rate of ion transport [3.5].

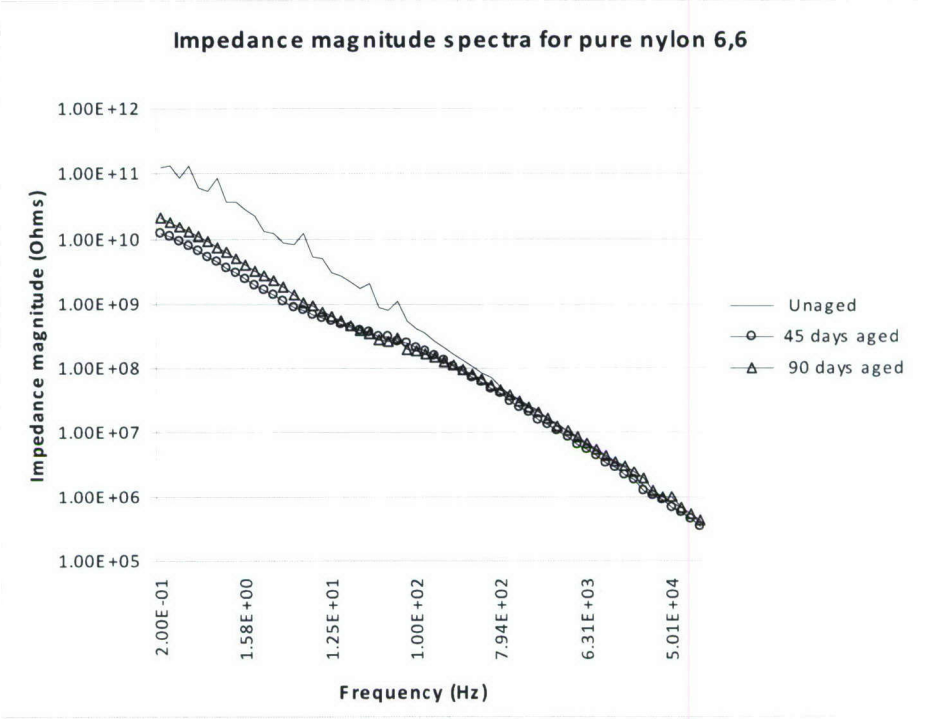

Figure 3.3: Impedance spectra variation for pure nylon 6,6.

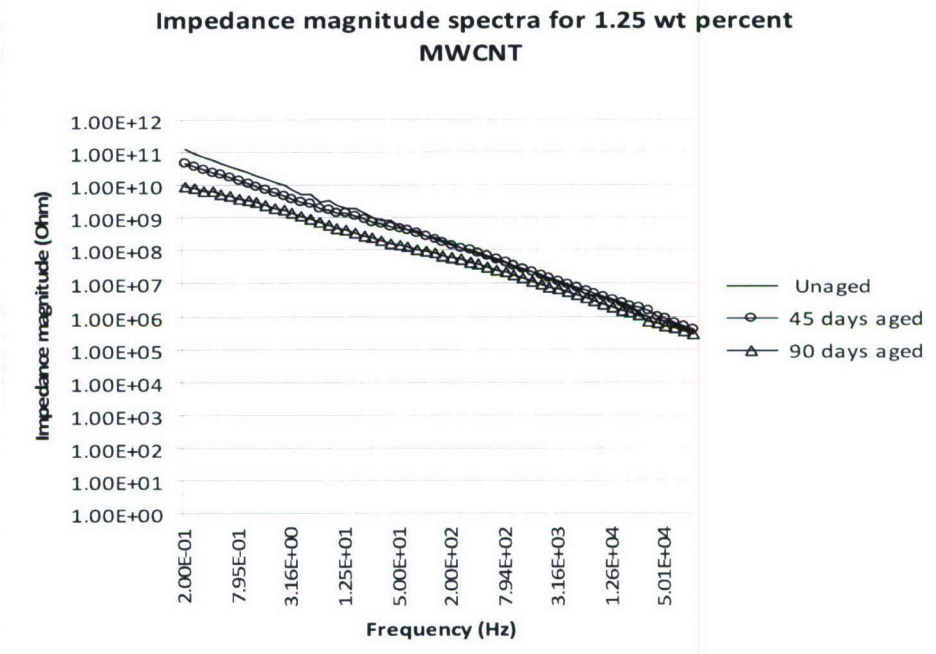

Figure 3.4: Impedance spectra variation for 1.25 wt percent (MWCNT).

Effect of enviromental aging on nylon 6,6 reinforced with 2.5 wt percent (MWCNT) was almost negligible. Spectra for the baseline specimens and the aged ones were collapsed into one spectra, though the mentiond specimen had a moisture uptake of 2.7 and 4 wt percent coresponding to 45 and 90 days of environmental aging respectively (Figure 3.5).

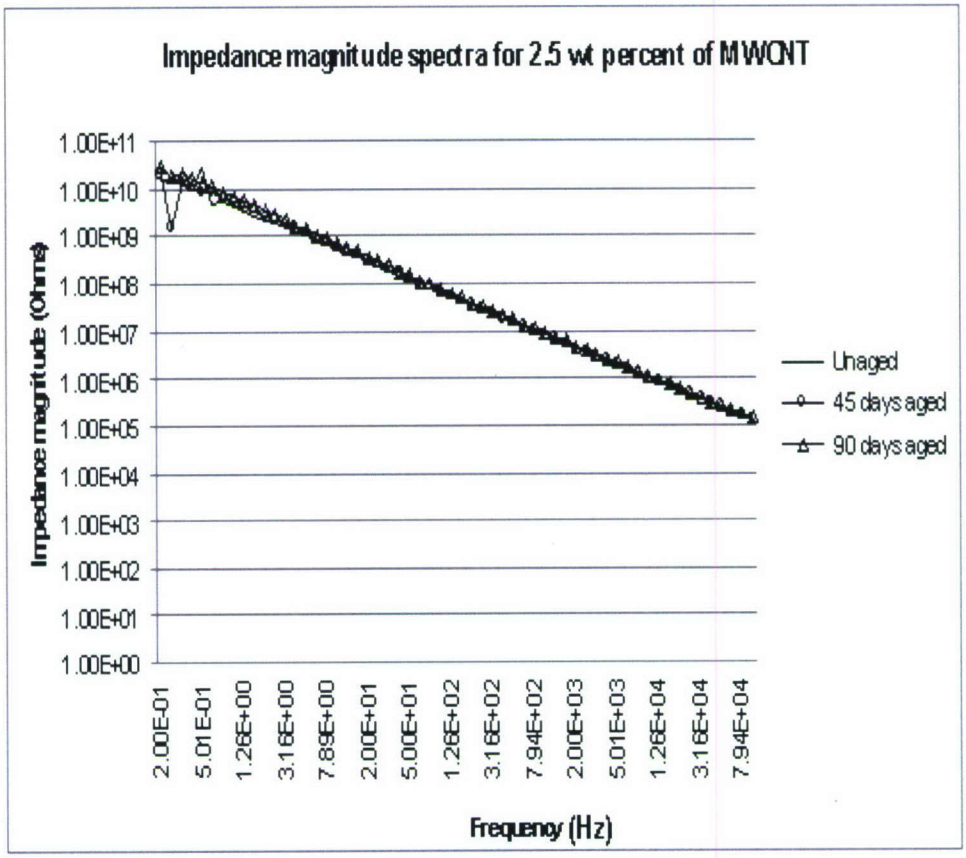

Figure 3.5: Impedance spectra variation for the 2.5 wt percent (MWCNT).

Table 3.1: Measured data of the un-aged (baseline) specimens.

Specimen	Nano wt %	Length mm	Width mm	Thickness mm	Weight gm	Average wt (gm)
NM00CE01	0	25.44	25.39	10.05	7.38	7.15
NM00AE02		25.51	25.58	10.00	7.45	
NM12CE01	1.25	24.98	25.19	9.86	7.12	7.12
NM12CE01		25.05	25.10	9.92	7.12	
NM25CE01	2.5	25.54	25.54	9.96	7.53	7.43
NM25AE02		25.38	25.71	9.96	7.32	
NM50CE01	5	25.66	25.37	9.91	7.60	7.55
NM50AE02		25.56	25.43	9.91	7.51	
NM10CE01	10	25.36	25.59	9.80	7.60	7.59
NM10AE02		25.68	25.20	9.84	7.57	
NM20JE01	20	25.28	25.18	9.77	7.86	7.85
NM20JE02		25.40	25.02	9.85	7.84	

Table 3.2: Measured data of the 45 days-aged specimens.

Specimen	Nano wt %	Length mm	Width mm	Thickness mm	Weight gm	Average wt (gm)	Moisture absorption (wt %)
NM00CE01	0	25.66	25.19	10.07	7.53	7.57	5.9
NM00AE02		25.76	25.26	10.16	7.61		
NM12CE01	1.25	25.02	25.00	10.00	7.70	7.44	4.5
NM12CE01		25.77	25.74	10.14	7.18		
NM25CE01	2.5	25.54	25.44	10.00	7.62	7.63	2.7
NM25AE02		25.67	25.40	10.00	7.64		
NM50CE01	5	25.58	25.50	10.00	7.67	7.69	1.9
NM50AE02		25.59	25.52	10.02	7.70		
NM10CE01	10	25.55	25.52	9.91	7.81	7.76	2.2
NM10AE02		25.59	25.12	9.93	7.71		
NM20JE01	20	25.31	25.01	9.83	7.84	7.94	1.1
NM20JE02		25.52	25.41	9.81	8.04		

Table 3.3: Measured data for 90 days-aged specimens.

Specimen	Nano wt %	Length mm	Width mm	Thickness mm	Weight gm	Average wt (gm)	Moisture absorption (wt %)
NM00CE01	0	25.28	25.82	10.00	7.55	7.62	6.6
NM00AE02		25.48	25.73	9.88	7.69		
NM12CE01	1.25	25.24	25.21	10.06	7.37	7.64	7.3
NM12CE01		26.09	26.07	10.12	7.91		
NM25CE01	2.5	25.54	25.44	10.06	7.84	7.73	4.0
NM25AE02		25.69	25.74	9.89	7.62		
NM50CE01	5	25.35	25.44	9.92	7.79	7.78	3.0
NM50AE02		25.73	25.36	9.96	7.76		
NM10CE01	10	25.68	25.24	9.96	7.80	7.81	2.9
NM10AE02		25.73	25.44	9.76	7.81		
NM20JE01	20	25.80	25.08	9.78	7.95	8.02	2.2
NM20JE02		25.28	25.64	9.78	8.08		

Figure 3.6 shows a linear correlation between moisture uptake (wt-percent) and the percentage change in impedance magnitude over the very low frequency range (2 *Hz*) for all the aged specimens. It can be seen that the effect of moisture uptake becomes more pronounced for cases of lower weight fraction of MWCNT, because this will be associated with larger amount of porous polymer. For example, pure nylon 6,6 had the greatest moisture uptake (5.9 wt- percent) and its impedance magnitude had been changed by 93% after 45 days- aging. On the other hand, aged reinforced composites had smaller impedance change with less wt fraction of moisture uptake compared to pure nylon. Hence, EIS approach may be used to monitor moisture ingression in nano-composites. Summary of the results are shown in tables 3.4 and 3.5.

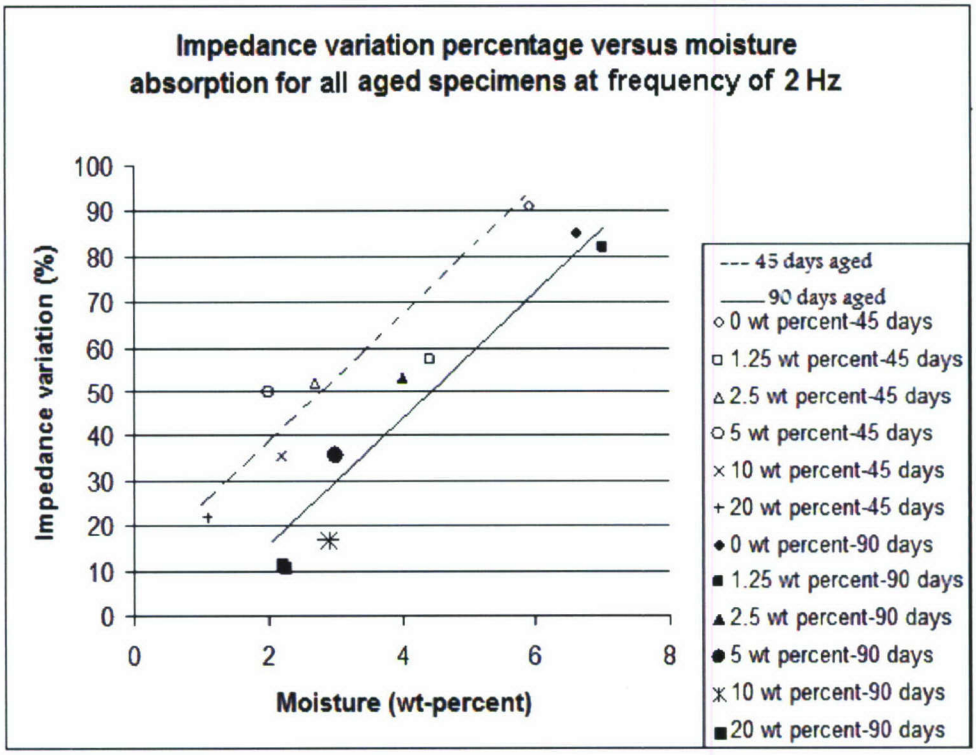

Figure 3.6: Impedance variation percentage versus moisture (wt- percent) for the aged specimens with different MWCNT at excitation frequency of 2 Hz.

Table 3.4: Moisture absorption (wt percent) and *Z* variation (%) for the 45 days aged specimens at excitation frequency of 2 Hz.

Nano wt %	Moisture absorption wt %	Z variation (%)
0	5.9	91
1.25	4.5	53
2.5	2.7	52
5	1.9	50
10	2.2	36
20	1.1	22

Table 3.5: Moisture absorption (wt percent) and Z variation (%) for the 90 days-aged specimens at excitation frequency of 2 Hz.

Nano wt%	Moisture absorption wt %	Z variation (%)
0	6.6	85
1.25	7.3	82
2.5	4	53
5	3	36
10	2.9	17
20	2.2	12

Figure 3.7 shows the impedance magnitude spectra for the case of nylon 6,6 with 5 wt percent of MWCNT. The impedance spectrum is a capacitive in nature (slope of -1 on the log impedance-frequency plot) similar to the spectra mode for 0, 1.25 and 2.5 wt percent. The difference is that the effect of aging over the impedance magnitude spectra is almost negligible for the 5 wt percent MWCNT.

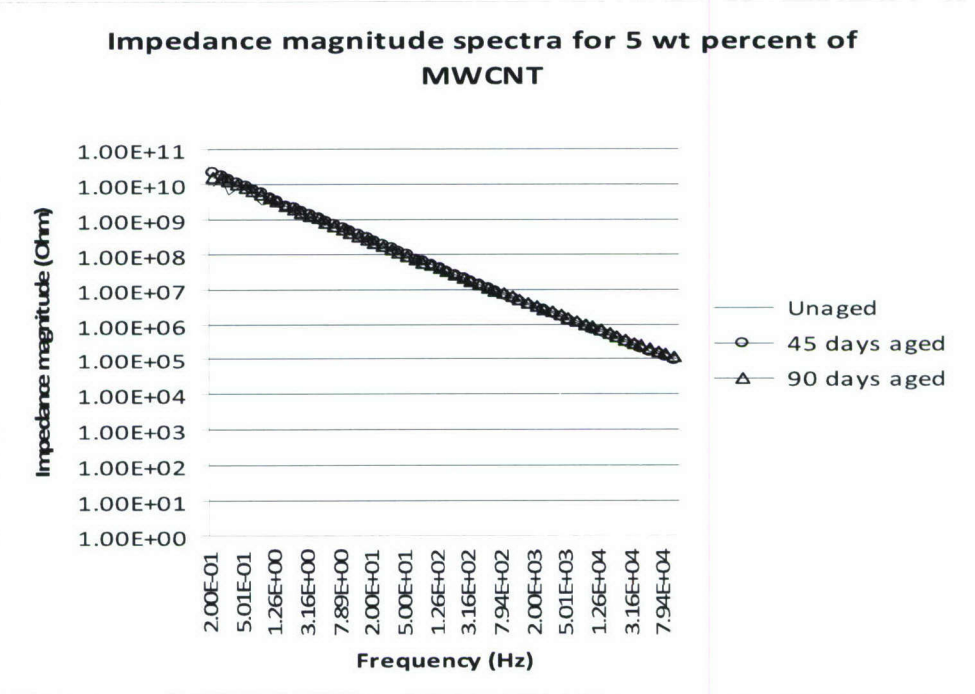

Figure 3.7: Impedance spectra variation for the 5.0 wt percent (MWCNT).

The impedance magnitude spectrum associated with the case of nylon 6,6 reinforced with 10 wt percent of MWCNT is shown in Figure 3.8. The material behaves in a resistive manner over the low frequency range and a capacitive one over the mid to high frequency ranges. As the polymer absorbs moisture, the low-frequency impedance spectrum decreases in magnitude and becomes more resistive and independent of frequency. This is similar to other results obtained by Harichandran et al. [3.6]. This behavior reflects moisture ingress into the pores of the nylon 6,6 and formation of pathways of relatively low resistance and that exactly what was observed for the 10 wt percent MWCNT

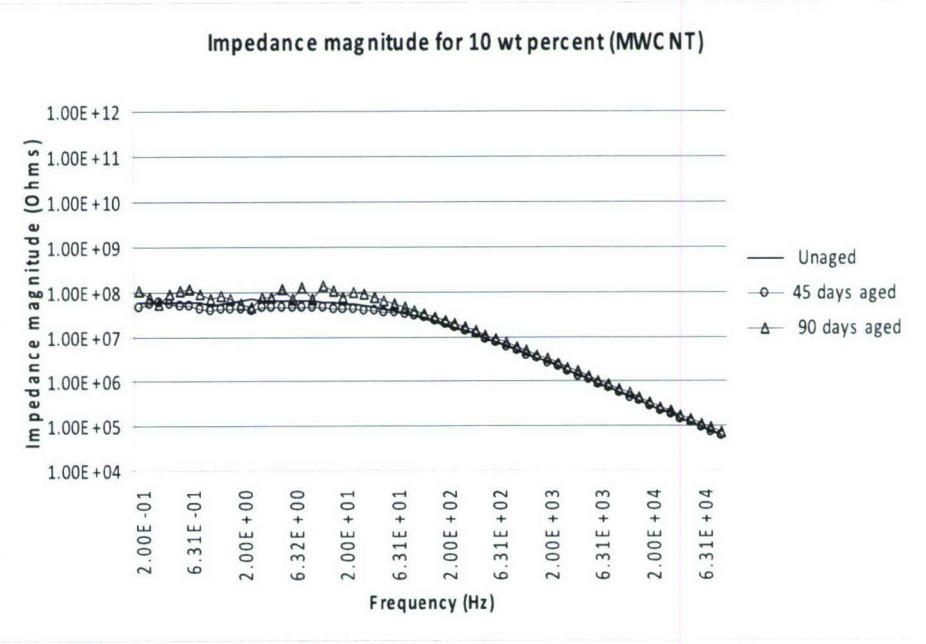

Figure 3.8: Impedance spectra variation for the 10 wt percent (MWCNT).

In Figure 3.9, the impedance spectrum looks to be almost uniform over the whole frequency range. That is in turn reflects the pure resistive behavior of the 20 wt percent MWCNT. Generally, it can be predicted that the impedance spectrum would behave more likely in a resistive manner for the higher MWCNT wt percent composites.

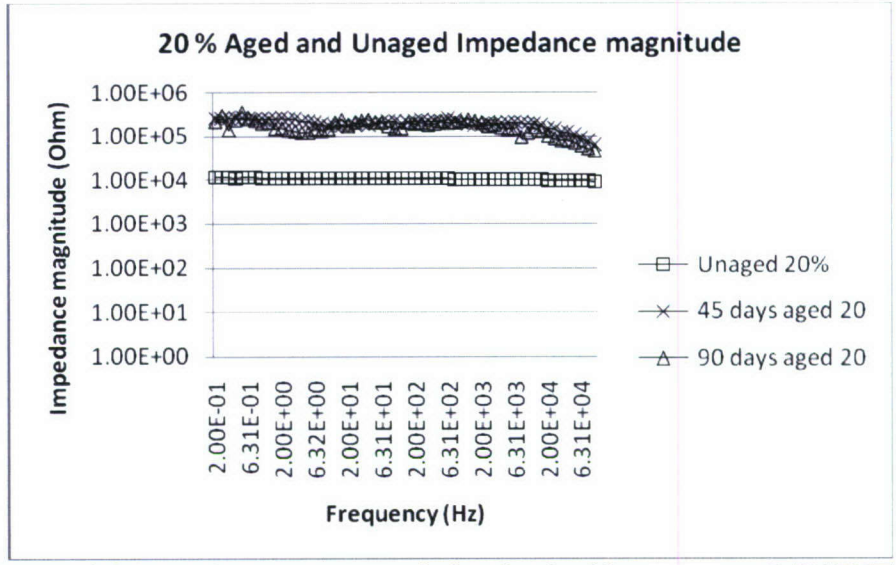

Figure 3.9: Impedance spectra variation for the 20 wt percent (MWCNT).

3.3.2 Raw phase spectra

From Figure 3.10, the phase angle is basically ranging from 0 to $-\pi/2$ for the un-aged specimens (baseline samples). Phase angle has almost a uniform value of $-\pi/2$ for those specimens with 0, 1.25, 2.5 and 5.0 wt percent MWCNT over the whole frequency range. Accordingly, those specimens most probably behave as a capacitor because their phase angle equals to $-\pi/2$. However, the phase spectra for the 20 wt percent remains constant at 0, acting extremely as pure resistor regardless of the frequency range applied, and for the 10 wt percent, the equivalent circuit element is neither resistive nor capacitive, but a combination of both resistor and capacitor can be used to fit the un-aged impedance spectra.

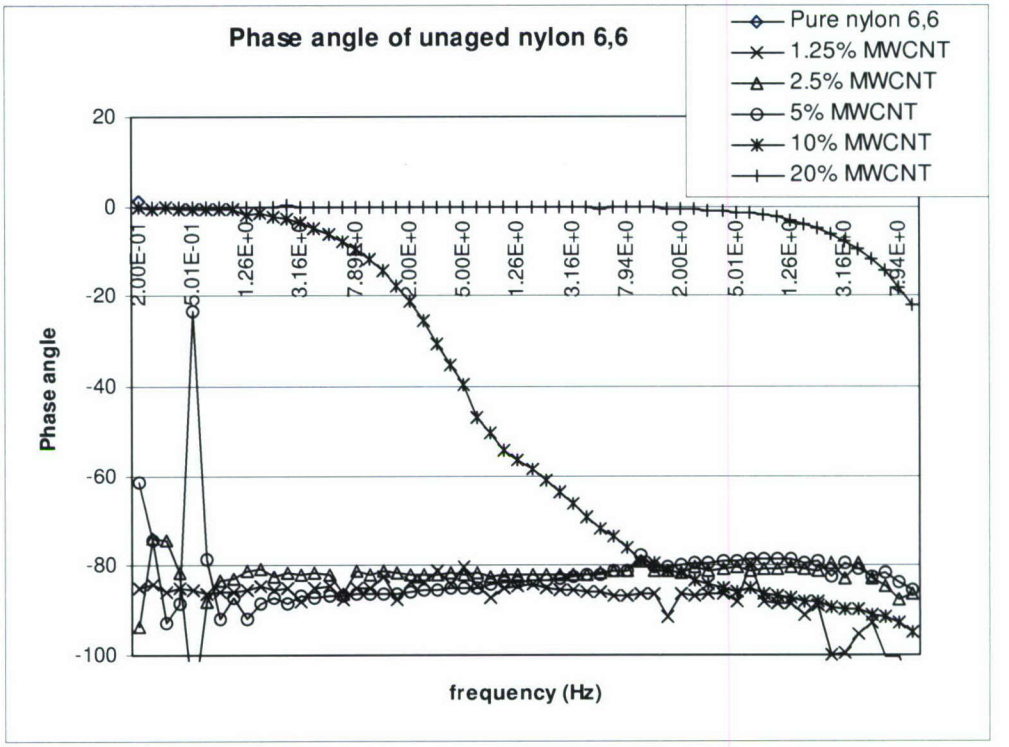

Figure 3.10: Phase spectra for baseline nylon 6,6 with different MWCNT wt percent.

The aging effect on the impedance phase spectra is interpreted through Figures 3.11 to 3.16 for 0, 1.25, 2.5, 5, 10 and 20 wt percent reinforcements of (MWCNT) respectively, Phase plots for 0, 1.25 wt percent show the effect of aging on the phase angle is of greater consideration over the low frequency range (1.26 Hz-50 Hz) than that for the mid freq range (50 Hz -2000 Hz).

Phase angle does not vary much under the aging effect for 2.5, 5, 10 and 20 wt percent specimens. However, the impedance phase spectra for 10 wt percent sample over the mid to high frequency ranges were more sensitive to environmental aging as seen in figure 3.15.

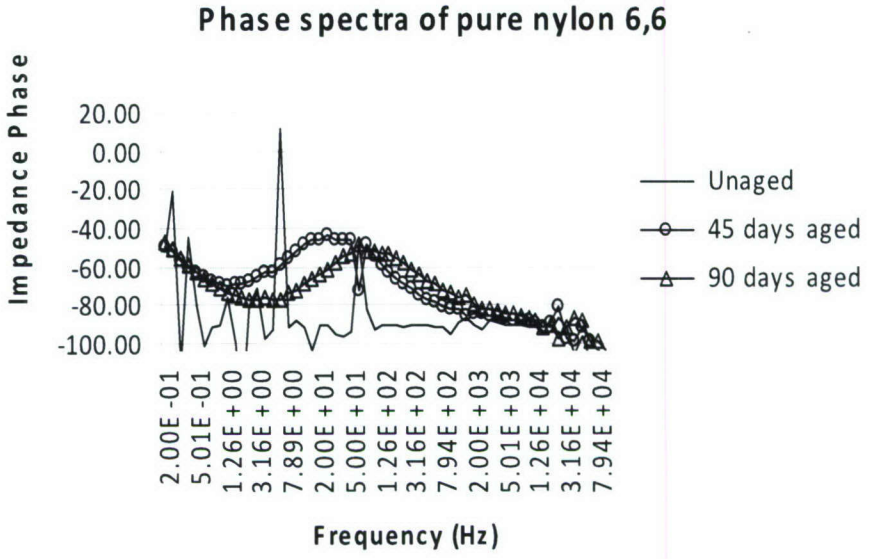

Figure 3.11: Phase spectra of pure nylon 6,6.

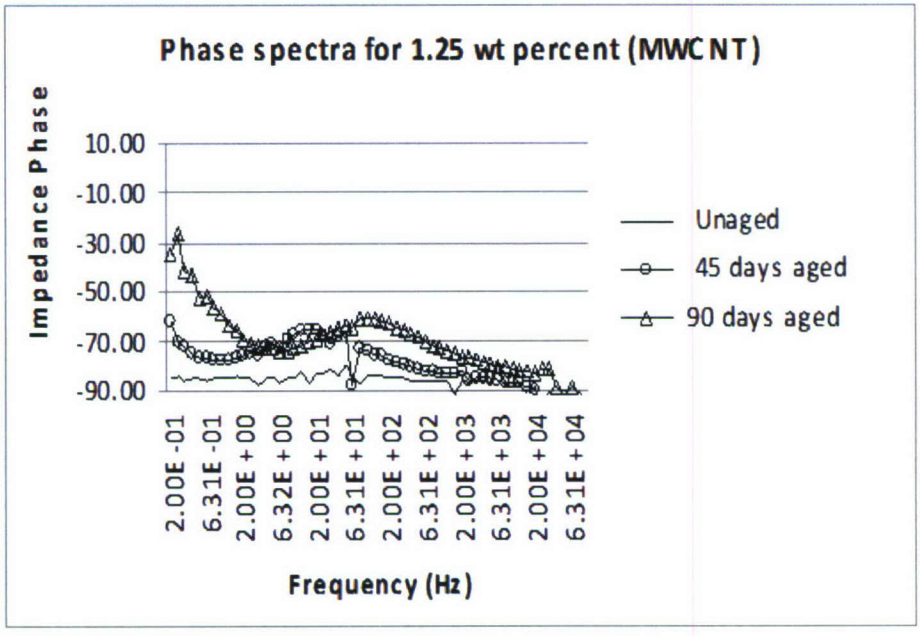

Figure 3.12: Phase spectra for 1.25 wt percent (MWCNT).

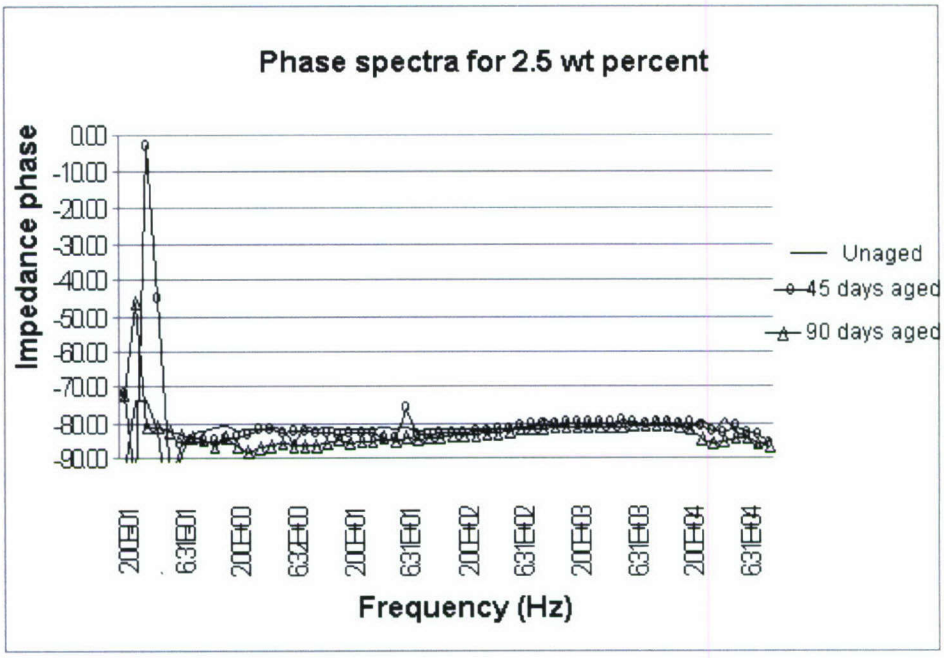

Figure 3.13: Phase spectra for 2.5 wt percent (MWCNT).

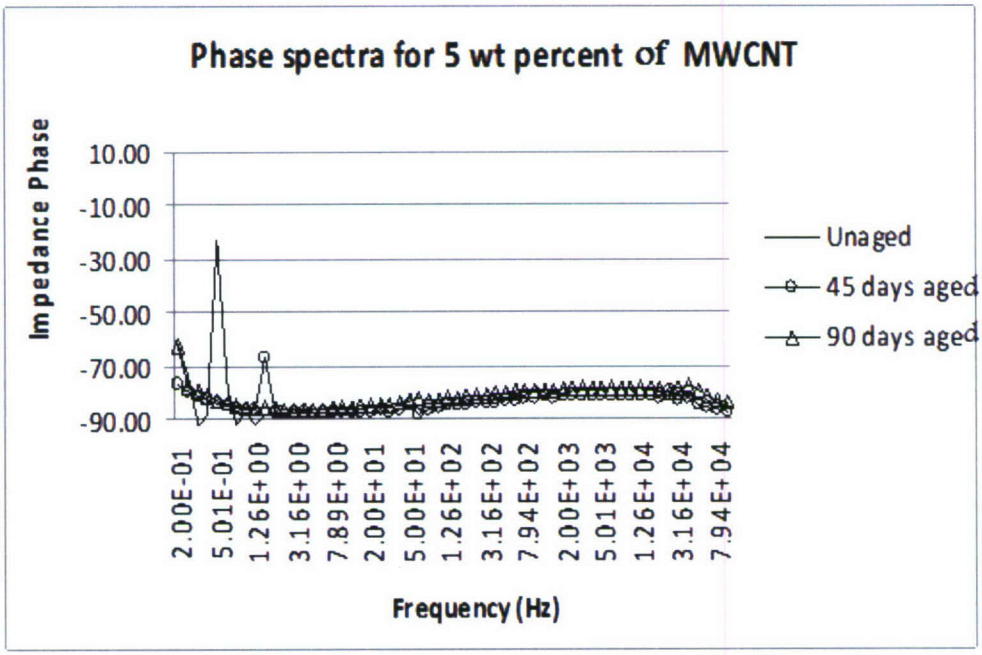

Figure 3.14: Phase spectra for 5 wt percent (MWCNT).

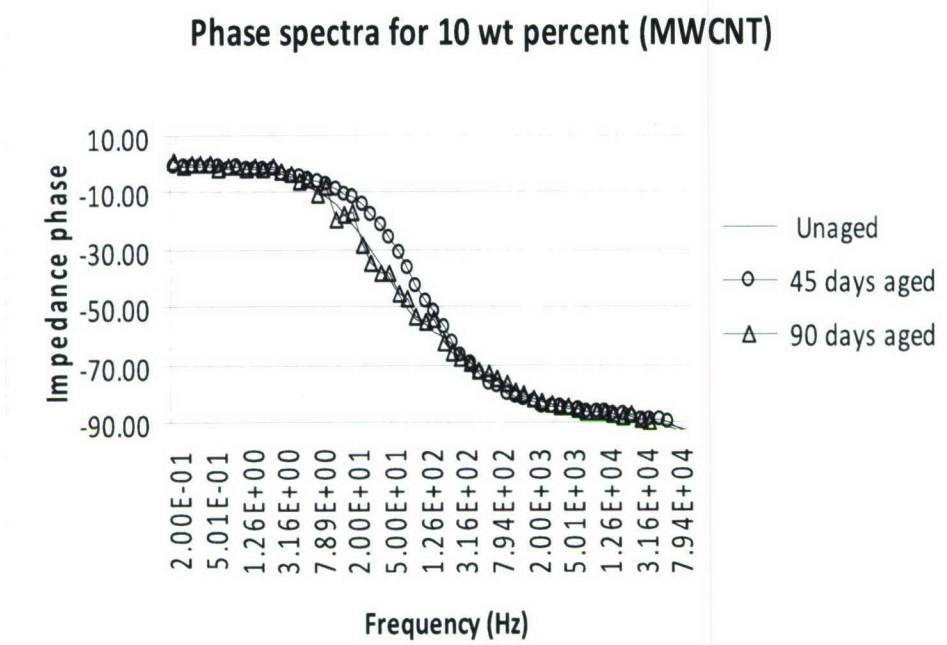

Figure 3.15: Phase spectra for 10 wt percent (MWCNT).

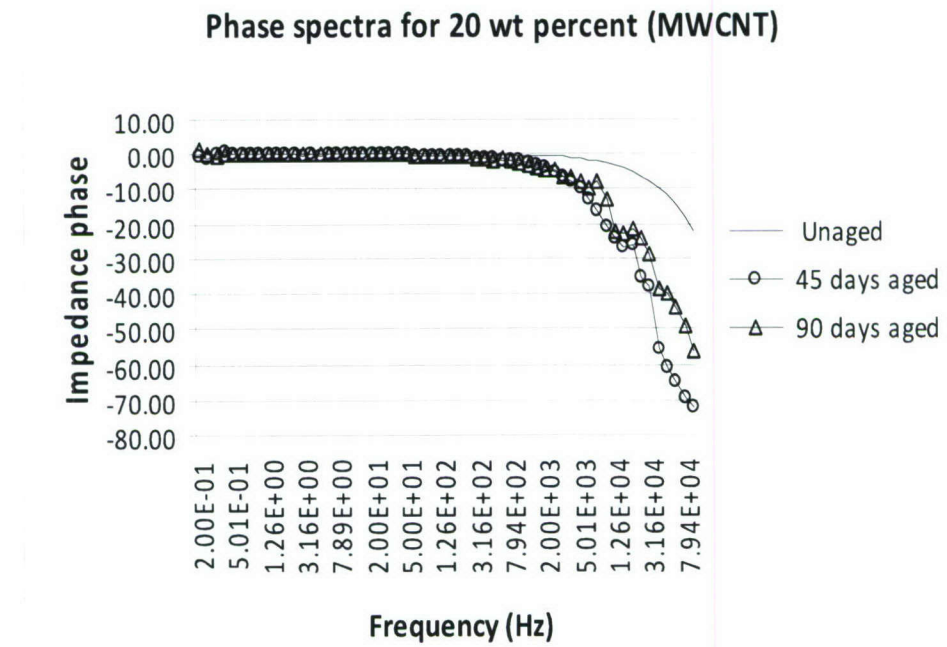

Figure 3.16: Phase spectra for 20 wt percent (MWCNT).

3.4.1 Equivalent circuit analysis

In the experiment, an alternating *AC* potential was applied across the working and reference electrodes and the impedance spectrum was measured as a function of excitation frequency. There are two methods of analyzing the data. The first method is direct comparison of the raw impedance spectra. The common presentations are the Bode (impedance magnitude) diagram, Phase plot, and real and imaginary impedance plots. The second method, which has been done also in this work, is the use of a lumped parameter equivalent circuit model in order to analyze the data, the parameters of the equivalent circuit which has an a predictable impedance (Bode and phase) similar to that of the measured impedance are evaluated.

The most common method used to analyze EIS impedance and phase spectra is the equivalent circuit modeling. Several cell elements and cell characteristics contribute to the EIS spectrum. A list of possible elements includes:

- Electrode double layer capacitance
- Electrode kinetics
- Diffusion layer

The behavior of each element mentioned above is described in terms of electrical component (resistor, capacitor). The most important step in this process is to predict the system elements that will play a role in the cell's impedance. The arrangement of the elements into logical series and parallel combination is a critical to the success of the fitted model.

3.4.2 Fitting the model to the raw data

Once a model is found represent the raw data, a non linear least square program is used to fit the model to the experimental data. Two fitting algorithms are built inside the Echem Analyst: the Levenberg-Marquardt algorithm and the Simplex algorithm [3.7].

One of the most difficult tasks in equivalent circuit modeling is determining the initial values of the model's parameters. If the initial values are far from optimal values, the best fitting might not get fully accomplished.

The steps for fitting a model to a data when the form of the model is known, like the 'paint' model shown in Figure 3.17.The fitting algorithm in EIS analysis requires initial

values that are within a decade or two of their final values before it would fit properly. Therefore, initial values of the fitting parameters should be based on a logical understanding of the behavior of the elements in the circuit.

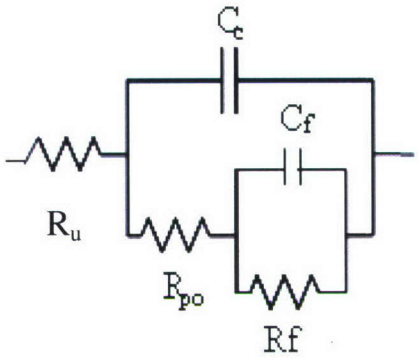

Figure 3.17: The equivalent circuit model 'paint'.

Typically, we try to find areas in the Bode curve where the model's impedance is dominated by one element in the circuit, then the approximate estimate for that element at that frequency could be easily estimated.

Figure 3.18 shows one of the original EIS spectra in a Bode format. Gamry recommends that the initial estimate for fitting parameters be tested in the Bode diagram. Keeping in mind that the impedance of a capacitor approaches zero at high frequency and infinity at low frequency, since the capacitive impedance is given by $Z = -\frac{1}{j\omega C}$. Both Cc and C_f are in parallel with a resistor, when the capacitor impedance is high, the resistor's impedance dominates. At the lowest frequency, the impedance magnitude is around 6×10^7 ohms and the phase near zero, that particular value could be translated to be a resistor element only while no phase angle incorporated there. Consequently this is the sum of R_u, R_{po} and R_f. Then a reasonable estimate of R_f would be 6×10^7 ohms.

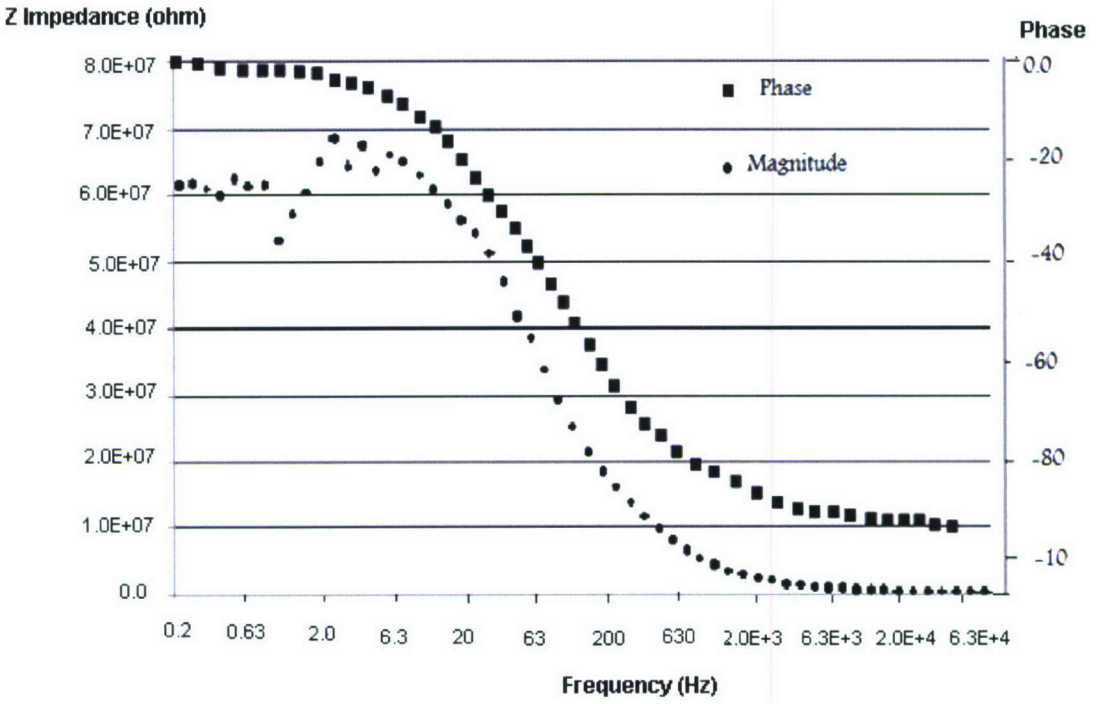

Figure 3.18: Original spectrum of phase and magnitude outputs for the 10 wt percent MWCNT specimen.

Referring to Figure 3.18, the drop in the impedance magnitude after 20 Hz frequency is due to the capacitance effect of C_f. At 20 Hz, the impedance of the EIS is about 5.5×10^7 ohms. Applying that to the impedance equation for a capacitor and using $f = 20$ Hz.

$$Zc = \frac{1}{(j\ .w\ .C_f)} = \frac{1}{2\ \pi.\ f.\ C_f} = \frac{1}{6.28\times20\times C_f}$$

$C_f = 1.45\times10^{-10}$ Farads

Therefore, two seed values were obtained so far which are R_f and C_f.

The middle portion of the impedance spectrum has a capacitive characteristic because the curve is decaying rapidly. From Figure 3.18, the impedance at 100 Hz is around 4×10^7 ohms. Following the same procedure above, but with an impedance value of 4×10^7 ohms at 100 Hz, the calculated value for Cc is 4×10^{-11} Farads.

After a set of all seed values are obtained, the initial values of the equivalent circuit were adjusted and locked to get the best fitted model that matches the raw impedance and phase spectra.

3.4.3 Equivalent circuit results

In Figure 3.19, the solid fitted curve represents the R_{po} response against the MWCNT wt percent for the baseline specimens, whereas the dotted line corresponds to the R_{po} response for the aged specimens. Two observations are noticed from Figure 3.19. Firstly, the equivalent circuit element R_{po} profile decreases exponentially as the MWCNT wt percent increases. Secondly, R_{po} is not so sensitive to environmental aging.

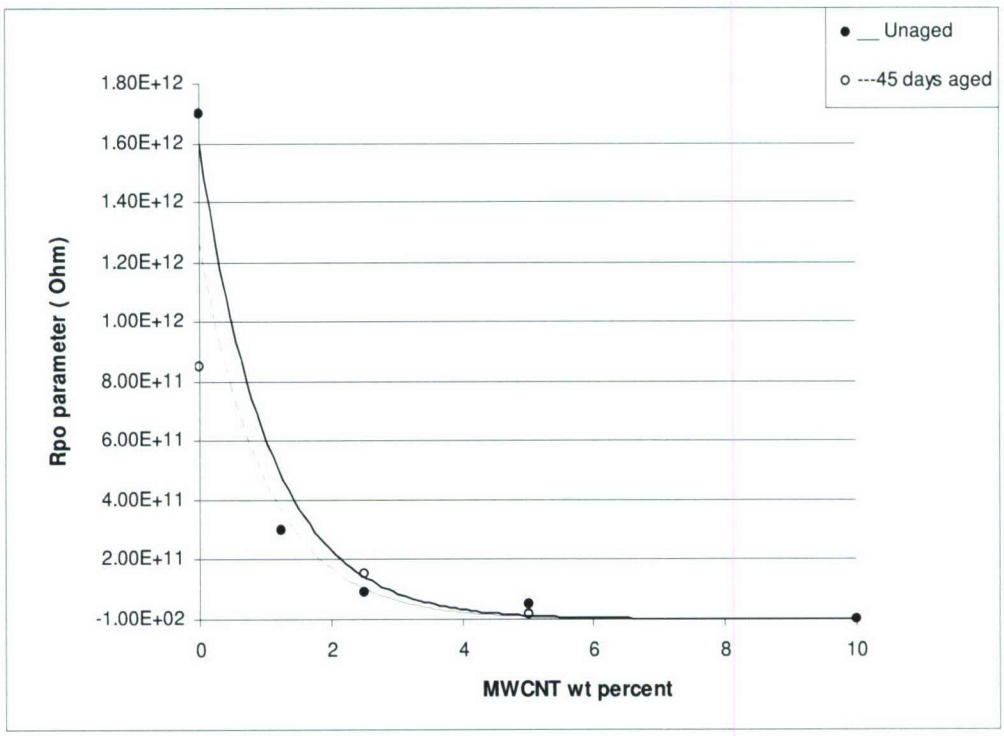

Figure 3.19: Fitted resistance R_{po} versus wt percent of MWCNT for different ages.

Cc is the most sensitive capacitor element in the equivalent circuit model used in the EIS analysis. From Figures 3.20 and 3.21, one can conclude that the Cc response to the MWCNT wt percent is more pronounced than that to the aging exposure.

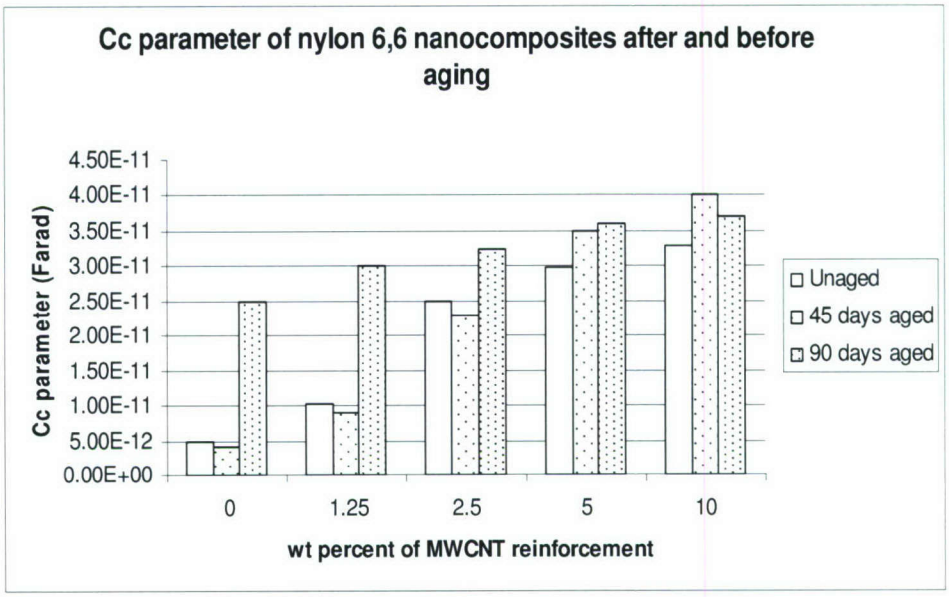

Figure 3.20: Fitted Cc element versus MWCNT wt percent for different ages.

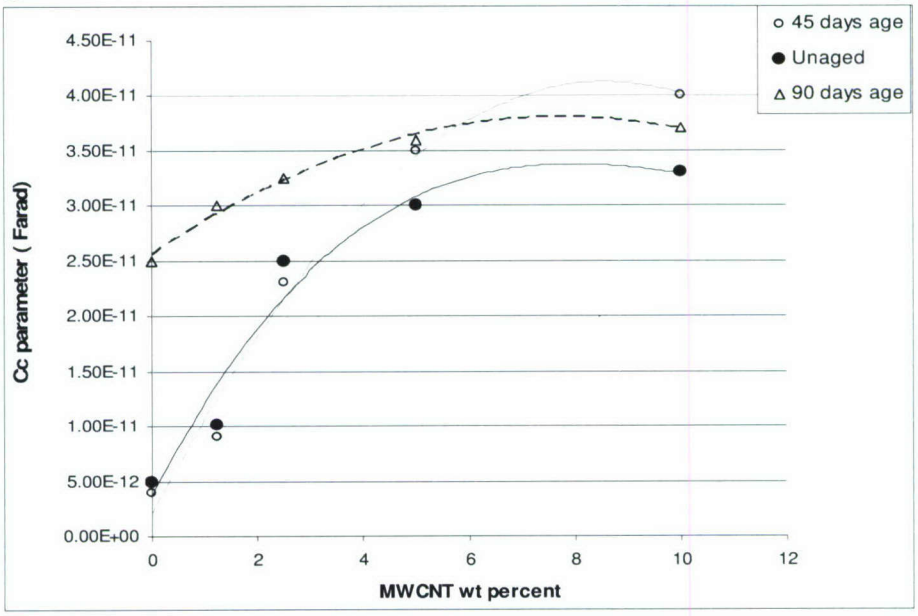

Figure 3.21: Fitted parameter *Cc* versus MWCNT for different ages.

In Figure 3.22, the capacitance *Cc* was plotted versus aging exposure time for all MWCNT reinforced specimens. It was observed that the slope of the capacitance profile decreases smoothly as the wt percent of MWCNT increases. It is expected to have a straight line profile of *Cc* corresponding to a wt percent around four where *Cc* would be insensitive to environmental aging.

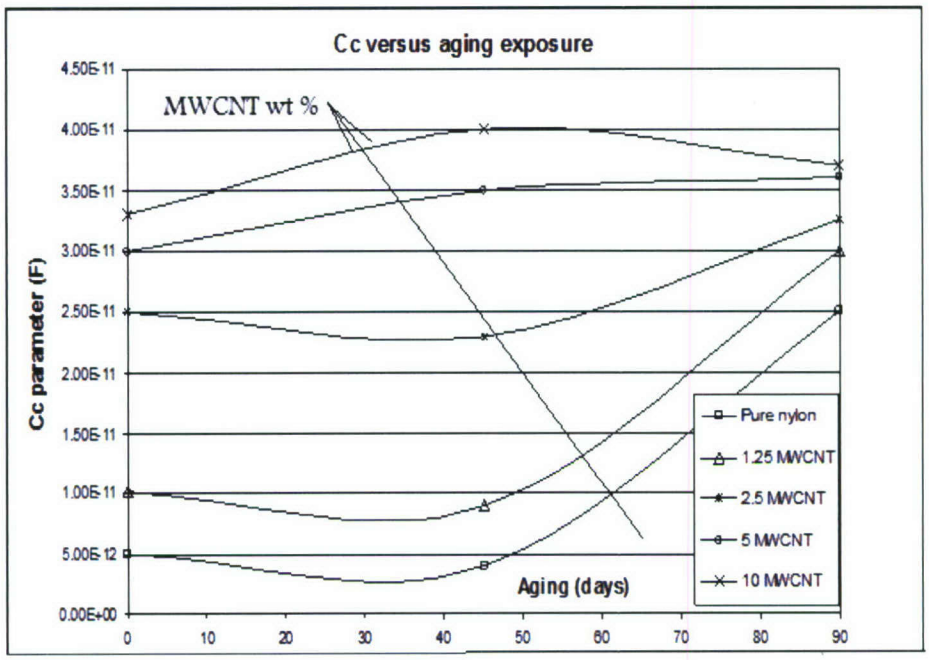

Figure 3.22: Fitted parameter *Cc* versus aging exposure.

3.4.4 Equivalent circuit elements and dynamic flexural properties of nylon 6,6

Referring back to Section 1, (Tables: 1.2.1 and 1.2.3). An attempt to find a relation between the flexural dynamic modulus which has been evaluated experimentally in Section one, and the lumped parameter *Cc* resulted from the equivalent circuit analysis. A linear fitted relation was observed between the flexural dynamic modulus and the *Cc* capacity resulted from the predicted equivalent circuit for both baseline and aged specimens (Figure 3.23). Dynamic storage modulus correspondent to both aged and un-aged specimens increases linearly when *Cc* increases which associated with increase in the MWCNT wt percent.

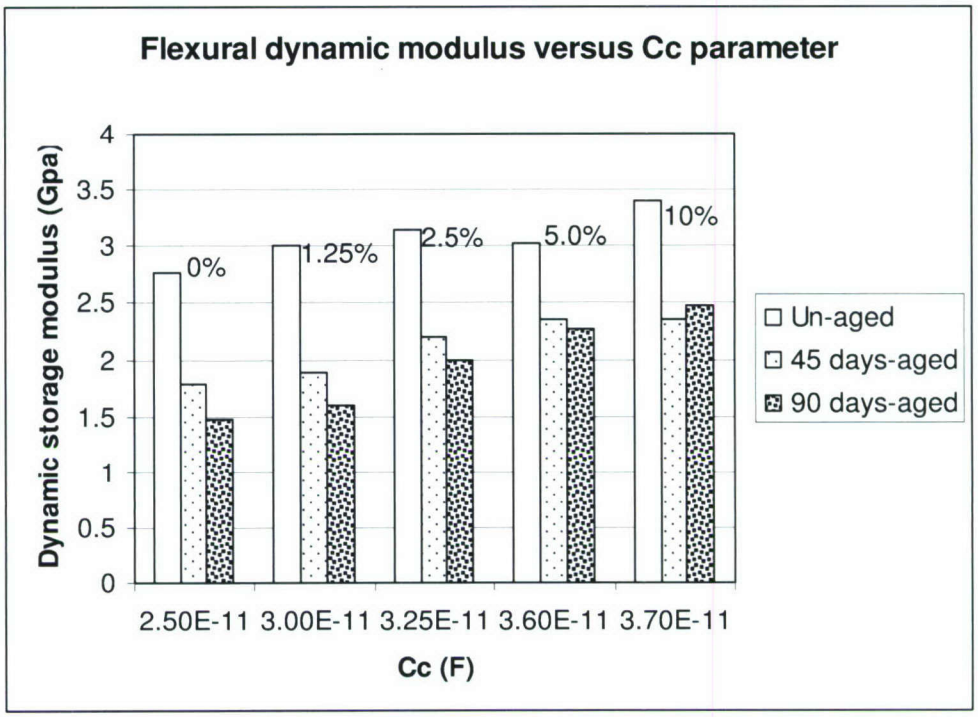

Figure 3.23: Flexural dynamic modulus versus Cc parameter.

3.5 Conclusion

Electrochemical impedance spectroscopy technique has been used to evaluate the effect of freeze-thaw aging and moisture ingression on electrochemical properties of nylon 6,6 reinforced with multi-wall carbon nano tube (MWCNT). The specimens were subjected to 45 and 90 days of freeze-thaw cycling. The results were interpreted in two ways, impedance spectra (magnitude and phase) and fitted parameters obtained from the equivalent circuit analysis. In addition to the raw data of impedance spectra, the resistive element (R_{po}) and the capacitive one (Cc) obtained from the equivalent circuit were studied versus a combination of carbon nano tube weight percent and aging time. It was observed the following:

- Raw data of impedance magnitude spectra decreases as the MWCNT wt percent increases.
- The percentage drop in impedance magnitude for the nylon 6,6 with 0, 1.25 and 10 wt percent of MWCNT over the low frequency range is linearly proportional to the amount of moisture absorbed due to the environmental aging. That is due to the fact

that at low frequencies, the current flow in the electrochemical cell is dominated by the movement of ions and different moisture levels affects the rate of ion transport.

- The impedance magnitude spectrum associated with10 wt percent behaves in a resistive manner over the low frequency range and capacitive over the mid to high frequency ranges. That was also observed from the phase spectra, and it is expected to have a more resistive impedance spectra mode when the MWCNT wt percent goes higher than 10 as for the case of 20 wt percent MWCNT.
- Measurements of the moisture absorption (wt percent) under both type of aging were linearly proportional to *Cc* parameter.

4.0 MOLECULAR DYNAMIC SIMULATIONS OF NANO COMPOSITES

4.1 Introduction

The emergence of nano-sciences during the last decade has drastically altered the landscape of scientific research and technology development. Nano reinforcement of engineering materials can impart dramatic structural (e.g. stiffness) and physical (e.g. reduced CTE) property benefits without adding significant weight [4.1-4.2]. For example, nanolayered reinforcement can impart greater thermal stability [4.3-4.4] with reduced permeability, making the polymer less flammable and improving barrier performance [4.5-4.7]. Ideally, the nano layer reinforcement distributes internal stresses more uniformly allowing greater dimensional latitude in forming and shaping processes compared to conventional macro scale reinforcement. The unparalleled characteristics of clay nanolayers to boost mechanical properties of an engineering polymer (Nylon-6) were first demonstrated by Toyota researchers [4.8]. With only 4.2 wt. percent of clay nanolayers, the modulus doubled and heat distortion temperature increased by 80°C compared to the pristine polymer, along with a reduction in water permeability and an increase in flame retardant properties. These dramatic improvements in properties made it possible to extend the use of low-cost polymers in under-the-hood applications. In order to fully utilize this type of mechanical property improvement for structural applications, the resulting nanoreinforced composite materials must have high modulus, high heat deflection temperature, low thermal expansion coefficient, high tensile strength and low permeation rates.

A critical issue for nanotechnology is the ability to understand, model and simulate the behavior of small structures and to make the connection between structure properties and functions. Most nanosystems are too small for direct measurements but too large to be described by current rigorous first principles in theoretical and computational methods. They exhibit too many statistical ensembles. This problem will be even more challenging in the case of nanocomposites where carbon nanotubes are dispersed randomly in a polymeric (i.e. polystyrene, epoxy etc.) matrix. The vital role of molecular modeling in this field is to enable engineering design at the component and systems level, and to set objectives that could guide laboratory efforts of the physical implications. An important component in molecular mechanics calculations of nanostructured materials is the description of the forces between individual atoms which are characterized by force fields.

The essence of nanotechnology is the ability to work at a scale of about 1 to 100 nanometers, in order to create, manipulate, and use materials, devices, and systems that have novel properties and functions. Nano-particle reinforced materials often have superior mechanical, thermal, electrical, magnetic, and electromagnetic properties. This is why nanotechnology finds its application in biomedical, biochemical, pharmaceutical, genetic engineering, material, polymer science, electronics, composites, and other engineering areas. It is anticipated for nanotechnology to become the primary driving force of the nation's economy within a decade or two. Carbon nano tubes (CNT) have become a primary focus in nanotechnology research due to their exceptionally high stiffness and strength.

4.2 Simulation of carbon nanotube composites using molecular dynamics approach

Many researchers have attempted to model the mechanical behavior of single wall carbon nanotube (SWCNT) taking input from molecular mechanics. Several new computational methods and their applications to nanostructures have been developed: equivalent continuum models [4.9-4.11], quasi-continuum models [4.12-4.18] using Tersoff and Brenner interatomic potential [4.19-4.20], and molecular dynamics simulations [4.21-4.22]. In this paper we focus on modeling and simulation of SWCNT composites using the molecular dynamics approach.

Molecular Modeling is a computational technique to model or mimic the behavior of the molecules. Force fields of computational chemistry and material science are applied for studying small chemical molecular systems and material assemblies. The common feature of molecular modeling techniques is the atomistic level systems; this is in contrast to quantum chemistry. The main benefit of molecular modeling is that it allows more atoms to be considered during the simulation, starting with a small number of molecules, and keep increasing the unit cell size, until we reach a periodic system, with represents the full scale material properties, it is recommended to simulate unit cells with 3000 atoms or more, to describe the behavior of any material in order to get the periodic unit cell which represents the infinite system.

4.2.1 The Born-Oppenheimer approximation

The Born-Oppenheimer approximation is the foundation of molecular dynamics [4.23]. Noting that the electrons are several thousands of times lighter than the nuclei and therefore move much faster, Born and Oppenheimer proposed that the motion of the electrons can be decoupled from that of the nuclei, giving two separate equations. The first of these equations describes the electronic motion where the energy is the function of coordinate of nucleus *E(R)* only and is termed as potential energy surface. The second part of the equation describes the motion of the nucleus on this potential energy surface. The solution of the nucleus motion is the basis of molecular dynamics. But prior to that, one needs to solve the equation pertaining to the motion of the electron for the expression of the *E(R; r)*. Solving the equation for electronic motion is not easy because the potential energy surface is not unique. Thus, an empirical fit to the potential energy surface, commonly called a force field (E_{total}), is usually used. Since the nuclei are relatively heavy objects, quantum mechanical effects are often insignificant and equation of motion for nuclei can be replaced by Newton's equation of motion given as:

$$-\frac{d\Theta}{dR} = m\frac{d^2R}{dt^2} \tag{4.1}$$

where, Θ is the force field, R describes the location of the nuclei in space, m is the mass of the nuclei and t is time. The solution of the above equation is the term $R\ (t)$ called the trajectory of the system.

4.2.2 The force field

A general definition for the force field in molecular mechanics or molecular dynamics can be found in many references. According to Wikipedia [4.24], a web based encyclopedia, a force field, in molecular mechanics and molecular dynamics, is the average description of the existing interactions among the various atoms in a molecule or a group of molecules in terms of functions and parameters sets. The electronic configuration around the atoms is not included into the description of these atomic interactions. Generally, the force field parameters are empirical, derived from the quantum modeling and sometimes, heuristic. According to Sun [4.25], the various force fields can be divided into following three categories.

(i) Force fields, which are very generic so that greater coverage can be achieved. Example: UFF (Universal force field) by Rappe et al [4.34].

(ii) Force fields that are designed to improve the accuracy in a focused area of application. Examples: Assisted Model Building and Energy Refinement (AMBER) for bio-molecules, Chemistry at HARvard Macromolecular Mechanics (CHARMM), Optimized Potential for Liquid Simulations (OPLS) etc.

(iii) Force fields that achieve high accuracy in predicting various molecular properties with a fairly broad coverage. In order to get the desired accuracy, these force fields either use complicated functional form including off-diagonal cross coupling terms and high order force constants or their parameters are derived from the high quality experimental data and/or quantum mechanics ab-initio data. Examples: MM3, MM4, MMFF, CFF93, PCFF etc.

Various kinds of interatomic potential are being used for MD simulations [4.35].

a) Lennard – Jones Potential

Lennard-Jones (12-6) potential function is the most widely used pair potential for molecular dynamics simulations and is given by:

$$\phi(r) = 4\varepsilon\left[\left(\frac{\sigma}{r}\right)^{12} - \left(\frac{\sigma}{r}\right)^{6}\right] \tag{4.2}$$

where, ε and σ are energy and length scales, respectively, and r is the intermolecular distance. This equation of motion can be made non-dimension by choosing σ and ε as length and energy scales, respectively. Generally, the Lennard-Jones potential has a cutoff at the intermolecular distance r_C = 2.5σ to 5.5σ. In order to reduce the discontinuity at the cut-off point, several smooth long tail functions have been proposed. However, for pressure or stress calculations, with modified potentials a contribution from far away molecules can produce erroneous data.

b) Effective pair potential for water

In this potential, a negative point charge is established on the oxygen atom with the OH bond length equal to 0.1 nm. The angle of H-O-H is the tetrahedral angle $\theta_t \approx 109.47^{\circ}$. The effective pair potential of molecules at R_1 and R_2 are expressed as the superposition of

Lennard-Jones functions of oxygen-oxygen interactions among neighboring molecules and the electrostatic potential by charges on oxygen and hydrogen.

$$\phi_{12} = 4\varepsilon_o\left[\left(\frac{\sigma_o}{r_{12}}\right)^{12} - \left(\frac{\sigma_o}{r_{12}}\right)^{16}\right] + \sum_i\sum_j \frac{q_i q_j e^2}{4\pi\varepsilon_0 r_{ij}} \tag{4.3}$$

where, r_{12} represents the distance of oxygen atoms, and σ_O and ε_O are Lennard-Jones parameters. The Coulombic interaction is the sum of nine pairs of point charges.

c) Potential for larger molecules in liquid phase (OPLS and AMBER)

The OPLS (optimized potential for liquid simulation) potential developed by Jorgensen is widely used for alcohols and other larger hydrocarbon molecules with hydroxyl groups. All bond lengths are rigidly constrained to their equilibrium values. Methyl and methylene groups are labeled C_1 through C_n from the tail group, i.e., methyl group, to the head group, i.e., hydroxyl group. The interaction potential E_{AB} between two molecules A and B is determined by the summation of Coulomb and Lennard-Jones interactions between all intermolecular pairs of sites as follows:

$$E_{AB} = \sum_i^A \sum_j^B \left[4\varepsilon_{ij}\left[\left(\frac{\sigma_{ij}}{r_{ij}}\right)^{12} - \left(\frac{\sigma_{ij}}{r_{ij}}\right)^{6}\right] + \frac{q_i q_j e^2}{4\pi\varepsilon_0 r_{ij}}\right] \tag{4.4}$$

where, q_i and q_j are the partial charges on united pseudo-atoms (methyl and methylene groups) i and j, r_{ij} is the distance between these atoms. Combination rule is used in order to obtain the Lennard-Jones potential parameters σ_{ij} and ε_{ij}.

$$\begin{aligned} \sigma_{ij} &= (\sigma_{ii} + \sigma_{jj})/2 \\ \varepsilon_{ij} &= \sqrt{\varepsilon_{ii}\varepsilon_{jj}} \end{aligned} \tag{4.5}$$

The force field parameters obtained from molecular mechanics and accurate ab-initio calculations are summarized as AMBER force field in order to describe the potential field for larger organic molecules and biological molecules.

$$\begin{aligned} E_{potential} = &\sum_{bonds} K_r(r - r_{eq})^2 + \sum_{angles} K_\theta(\theta - \theta_{eq})^2 + \frac{1}{2}V_n(1 + \cos(n\phi - \gamma)) + \\ &\sum_{vanderWaal}^{i<j}\left[\left(\frac{\sigma_{ij}}{R_{ij}}\right)^{12} - \left(\frac{\sigma_{ij}}{R_{ij}}\right)^{6}\right] + \sum_{electrostatic}^{i<j}\left(\frac{q_i q_j}{4\pi\varepsilon R_{ij}}\right) \end{aligned} \tag{4.6}$$

where, the energy associated with bonds and angles change is represented by a simple diagonal harmonic expression, the Vander Waals interaction is represented by Lennard-Jones (12-6) potential, electrostatic interactions are modeled by Coulombic interaction of atom-centered point charges, and dihedral energies are represented with a simple set of parameters. electrostatic and Vander Waals interactions are calculated between atoms in different molecules or for atoms in the same molecule only when they are separated by at least three bonds.

d) Tersoff – Brenner Potential

The Tersoff potential is used for simulations of solid silicon. Brenner modified the Tersoff potential for carbon and extended it for a hydrocarbon system. A simplified form of Brenner potential removing rather complicated 'conjugate terms' is widely used for studies of fullerene and carbon-nanotubes. Both the Tersoff potential and the simplified Brenner potential can be expressed in the form explained in the previous section dealing with quasi-continuum methods. Due to reactive short range bonded interactions in case of Tersoff – Brenner potential for carbon systems, chemical bonds may break or form during the simulation. Since this potential also considers the local environmental of each atom in the calculation, these are computationally expensive.

e) Pair potential and the Embedded Atom Method (EAM) for solid metals

For solid metal crystals, several physical properties can be used to fit to the pair potential functions such as Morse potential and Johnson potentials. The Morse potential is expressed as:

$$\phi(r) = D_e[\exp\{-2\beta(r - R_e)\} - 2\exp\{-\beta(r - R_e)\}] \tag{4.7}$$

where, D_e, R_e and β are dissociation energy, equilibrium bond length and a constant with dimensions of reciprocal distance, respectively.

The basic concept for EAM is that the potential energy can be calculated by embedding each atom to the electric field made of all other atoms. Later, 'Modified Embedded Atom Method' (MEAM) was also developed. In this case, the bond-angle was explicitly handled. Solid metals are always problematic for heat conduction problems due to the lack of the effective technique to handle free electrons in conjunction to molecular dynamics framework.

f) The force field used in the present study is called COMPASS which stands for Condensed-phase Optimized Molecular Potentials for Atomistic Simulation Studies. COMPASS was developed from 1990 to 1998, under the direction of the Polymer Consortium organized by Biosym/MSI (now a part of Accelrys Inc), which consisted of members from more than 50 industrial companies and government laboratories worldwide [4.25]. COMPASS is basically a hybrid approach consisting of both ab-initio and empirical methods to derive a general force field polymer consistent force field (PCFF). This force field is generally suitable for condensed phase applications with modified nonbonded interaction parameters and with modified valance terms incorporating the coupling between valance kind of interactions and nonbonded interactions.

The functional forms of various interactions, summed together in order to yield the COMPASS force field can be achieved from the introductory paper on COMPASS by Sun [4.25].

$$
\begin{aligned}
E_{Total} = & \sum_{b}[K_2(b-b_o)^2 + K_3(b-b_o)^3 + K_4(b-b_o)^4] + \sum_{\theta}[K_{2\theta}(\theta-\theta_o)^2 + K_{3\theta}(\theta-\theta_o)^3 + \\
& K_{4\theta}(\theta-\theta_o)^4] + \sum_{\phi}[K_{1\phi}(1-\cos\phi) + K_{2\phi}(1-\cos 2\phi) + K_{3\phi}(1-\cos 3\phi)] + \\
& \sum_{\chi} K_{2\chi}(\chi-\chi_o)^2 + \sum_{b,\theta} K_{b\theta}(b-b_o)(\theta-\theta_o) + \sum_{b,\phi}(b-b_o)[K_{1b}\cos\phi + K_{2b}\cos 2\phi + K_{3b}\cos 3\phi] + \\
& \sum_{\theta,\phi}(\theta-\theta_o)[K_{1\theta\phi}\cos\phi + K_{2\theta\phi}\cos 2\phi + K_{3\theta\phi}\cos 3\phi] + \sum_{b,\theta}(\theta'-\theta'_o)(\theta-\theta_o) + \\
& \sum_{\theta,\theta,\phi} K_{\theta\phi}(\theta'-\theta'_o)(\theta-\theta_o)\cos\phi + \sum_{i,j}\frac{q_i q_j e}{r_{ij}} + \sum_{i,j}\varepsilon_{ij}\left[2\left(\frac{r_{ij}^o}{r_{ij}}\right)^9 - 3\left(\frac{r_{ij}^o}{r_{ij}}\right)^6\right]
\end{aligned}
\tag{4.8}
$$

where, the LJ-9-6 parameters (ε and r^o) are given in any standard reference for like atom pairs. However, for unlike atom pairs, a 6th order combination law is used to calculate the off-diagonal parameters:

$$r_{ij}^o = \left(\frac{(r_i^o)^6 + (r_j^o)^6}{2}\right)^{1/6} \tag{4.9}$$

$$\varepsilon_{ij} = 2\sqrt{\varepsilon_i \varepsilon_j}\left(\frac{(r_i^o)^3.(r_j^o)^3}{(r_i^o)^6.(r_j^o)^6}\right) \tag{4.10}$$

The electrostatic interaction is represented using atomic partial charges. To make the charge parameters transferable, bond-increments δ_{ij}, which represent the charge separation between two valence-bonded atoms i and j, are used in the force field as parameters. For atom i, the partial charge is the sum of all charge bond increments δ_{ij}:

$$q_i = \sum_j \delta_{ij} \tag{4.11}$$

The valance terms are represented by internal coordinates of the bonds i.e. the bond length, bond angle, torsion angle and out of plane angle whereas the cross coupling terms include the combination of two or more internal coordinates. The cross coupling terms in this force field include the bond – bond, bond – angle and bond – torsion angle. The nonbonded interactions include Coulombic interaction terms for electrostatic interactions and LJ-9-6 (Lenard - Jones) function in order to formulate Van Der Waals interaction. The LJ-9-6 function is considered as a soft function in the repulsive region than the conventional LJ-12-6 function. According to Sun [4.25], the main effect of the representation of Van Der Waals interaction by LJ-9-6 potential may be observed in the torsional parameters but the changes in the torsion parameters have very little influence on the densities and cohesive energies of molecular liquids or crystals.

4.2.3 MD simulation using Materials Studio software

The commercially available Material Studio Software® [4.23] has been used for performing molecular dynamic simulations of single- and multi-wall carbon nanotube reinforced polymers to predict their mechanical properties. This was accomplished by using bulk amorphous polymer structures generated by constructing polymeric chains in a periodic cell, taking into account the bond torsion probabilities and bulk packing requirements. Models are then equilibrated by a series of energy minimization and molecular dynamic runs. Crystal structures for semi-crystalline and amorphous polymers are generated [4.26-4.28] and the simulated bulk structures subjected to three different methods for evaluating their mechanical behavior: the static method; the fluctuation method; and the dynamic method.

After molecular dynamics simulation has been performed, the resulting deformed molecular structure is analyzed for determining elastic constants. Elastic constants of the final atomic configuration are computed using the static approach suggested by Theodorou and Suter [4.29]. The elastic constants in this approach are defined as:

$$C_{lmnk} = \left.\frac{\partial \sigma_{lm}}{\partial \varepsilon_{nk}}\right|_{T,\varepsilon_{nk}} = \frac{1}{V_o}\left.\frac{\partial^2 A}{\partial \varepsilon_{lm}\partial \varepsilon_{nk}}\right|_{T,\varepsilon_{lm},\varepsilon_{nk}} \tag{4.12}$$

where, A denotes the Helmholtz free energy, ε is the strain component, σ is the stress component and V_o is the volume of the simulation cell in the undeformed configuration. It is assumed that contributions originating from changes in configurational entropy on deformation, and from the strain dependence of the vibrational frequencies are negligible for glassy polymers. Thus, it is possible to estimate the elastic stiffness coefficients from numerical estimates as:

$$d^2U/d\varepsilon_i \cdot d\varepsilon_i \left[= d\sigma_i/d\varepsilon_j\right] \tag{4.13}$$

where, U is the potential energy of the system.

For each configuration submitted for analysis of static elastic constants, the first step consists of energy minimization using conjugate gradients method. In this study, the target minimum derivative for the initial step is 0.1 kcal/Å. However, to reduce the time required for the calculation, a maximum of 1000 steps were performed in attempting to satisfy the convergence criterion. Following the initial stage, three tensile and three pure shear deformations of magnitude ±0.0005 were applied to the minimized system and the system was re-minimized following each deformation. The internal stress tensor was then obtained from the analytically calculated virial and used to obtain estimates of the 6 x 6 elastic stiffness coefficient matrices.

As a result of these simulations, the elastic stiffness coefficients could be obtained by estimating the second derivatives of the deformation energy with respect to strain using a finite difference formula (for diagonal components only), and by calculating $\Delta\sigma_i/\Delta\varepsilon_j$ for each of the applied strains, where σ_i represents, in vector notation, elements of the stress tensor obtained analytically using the following expression:

$$\sigma = -\frac{1}{V_o}\left[\left(\sum_{i=1}^{N} m_i\left(v_i v_i^T\right)\right) + \left(\sum_{i<j} r_{ij} f_{ij}^T\right)\right] \tag{4.14}$$

where, index i runs over all particles 1 through N; m_i, v_i and f_i denote the mass, velocity and force acting on particle i; and V_0 denotes the (undeformed) system volume. In an atomistic calculation, this expression for internal stress tensor is called virial expression.

Generally, it is assumed that the numerical estimation of second derivatives (of the energy) will be less precise than estimation of the first derivatives (of the stress). Therefore, the latter method has been used here for calculating the elastic constants. This approach creates the foundation of calculating elastic constants; however, the potential energy expression can alter depending upon the ensemble of thermodynamic variables of the simulation experiment.

In this project, we used COMPASS force field because it supports all the energy interaction terms, in the material simulated. Different ensembles were applied for the different dynamic thermostat or barostat steps, such as NVT, Constant-volume/constant-temperature dynamics, NPT, Constant-pressure/constant-temperature dynamics.

The equations of motion were solved with Anderson, for the NVT, and Berendsen for NPT, as velocity algorithms. The time step of integration was set to 1 fs in all cases that is chosen referring to the atoms are considered. The summation methods for van der Waals and Coulomb forces were all atom based (cutoff, spline width and buffer width was 9.5Å) unless it was set for an assigned value.

The Discover module within Materials Studio Software was used. Discover provides several methods for controlling temperature and pressure. Depending on which state variables (for example, the energy E, volume V, temperature T, pressure P, and number of particles N) are kept fixed, different statistical ensembles can be generated. A variety of structural, energetic, and dynamic properties can then be calculated from the averages or the fluctuations of these quantities over the ensemble generated.

4.2.4 Various forms of molecular dynamics simulations

There are several different forms of molecular dynamics, which may be used to calculate the elastic constants. These different forms of molecular dynamics are called as *ensembles*. The choice of any particular form in a simulation is governed by the nature of the experiment, experimental conditions and the physical state of participating components under experimental conditions. The four fundamental ensembles of molecular dynamics are given next page:

a) Microcanonical (*NVE*) ensemble, where the number of particles in the system, *N*, volume of the simulation unit cell, *V*, and the energy of the system, *E*, are held constant during MD simulation. This ensemble is considered to be the most fundamental form of the MD simulation. During the MD simulation, the Newtonian equations of motion of a set of *N* particles in volume *V* are solved numerically. The total energy, *E*, of the system is conserved as the system moves along its trajectory. The average of any property over the trajectory is an approximation to the measured value of that property for the thermodynamic state of the specified values of *N*, *V* and *E* [4.38]. A more strict case of this ensemble is *NhE* ensemble, where volume and shape of the simulation unit cell, both, are held constant during simulation. In this case, *h* is the matrix containing the vectors describing the sides of the unit cell; *a, b* and *c* [4.37, 4. 38].

b) Canonical (*NVT*) ensemble, where the number of particles in the system, *N*, volume of the simulation unit cell, *V*, and the temperature of the system, *T*, are held constant during MD simulation. In order to simulate such a system, one needs to introduce mechanisms for additional energy fluctuations. Here, the equations of motion of *N* particles in volume, *V*, are Hamiltonian equations with a supplementary stochastic collision term in the equation for each particle which changes the instantaneous momentum of the particle.

c) Isothermal – Isobaric (*NPT*) ensemble, where the number of particles in the system, *N*, pressure applied (hydrostatic or in the form of general stress tensor) on the simulation unit cell, *P*, and the temperature of the system, *T*, are held constant during MD simulation. Therefore, in constant pressure MD simulation, the volume of the unit cell containing *N* particles fluctuates. In order to bring this change into effect, the volume of the cell is made a dynamic variable rather than a fixed quantity. This task is completed by replacing the original coordinates of the atoms with a quantity called scaled coordinates, which is a function of the volume of simulation unit cell. When applied pressure is in the form of general stress tensor, in the formulation of problem, the general stress tensor is replaced by equivalent tensor of thermodynamic tension. This ensemble is distinguished from *NPT* ensemble by naming it as *NtT* ensemble where *t* is tensor of thermodynamic tension.

d) Isoenthalpic – Isobaric (*NPH* or *NtH*) ensemble, where the number of particles in the system, N, pressure applied on the simulation unit cell, P, and the enthalpy of the system, H, are held constant during MD simulation.

In latter two cases, the externally applied pressure could be described as hydrostatic pressure or general stress tensor. In these two ensembles, the imbalance between externally applied stress and the internally generated stresses makes the system to move along the trajectory [4.36]. Also, in new formulations, during computation, the applied pressure / stress is replaced by thermodynamic tension generated.

According to Ray et. al. [4.37], one can study equilibrium and transport properties of the system in solid → solid structural transformations using *NtH* (or *NPH*, in case of applied hydrostatic stresses), provided appropriate choices for dynamic characterization of unit cell are made in order to properly define the ensemble.

4.2.5 Molecular dynamics simulation of NPT ensemble (Constant number of particles, constant temperature, constant pressure) [4.25]

4.2.5.1 Constant pressure molecular dynamics

Consider a fluid containing N atoms, with coordinates $\boldsymbol{r}_1, \boldsymbol{r}_2 \ldots, \boldsymbol{r}_N$ in a cubic volume V with periodic boundary conditions. Each component of each atom is a number between 0 and $V^{1/3}$. Under the assumption of periodic boundary conditions, if there exists a particle i at position, $\boldsymbol{r}_i$, then there is an image particles at positions $\mathbf{r}_i + nV^{1/3}$, where n is a vector with integer component. The potential energy of the atom is

$$U(r^N) = \sum_{i<j} u(v_{ij}) \tag{4.15}$$

where, v_{ij} is the distance between $\boldsymbol{r}_i$ and either $\boldsymbol{r}_j$ or the nearest image of the particle j, whichever is closer. Thus,

$$v_{ij} = \left|r_{ij}\right| \equiv \min\left|r_i - r_j + nV^{1/3}\right| \tag{4.16}$$

This is the minimum image convention. In the all the summations over the particles, the lower and upper limits are 1 and N, respectively.

The Lagrangian for the fluid is given as:

$$L_1(r^N, \dot{r}^N) = \frac{m}{2}\sum_i \dot{r}^N . \dot{r}^N - \sum_{i<j} u(v_{ij}) \tag{4.17}$$

where, m is the mass of an atom. The momenta are defined as

$$p_i \equiv \frac{\partial L_1(r^N, \dot{r}^N)}{\partial(\dot{r}^N)} = m\dot{r}^N \tag{4.18}$$

The Hamiltonian equations of atomic motion are

$$\frac{d\dot{r}^N}{dt} = \frac{\partial H_1}{\partial p_i} = \frac{p_i}{m} \tag{4.19}$$

$$\frac{dp_i}{dt} = -\frac{\partial H_1}{\partial r_i} = -\sum_{j(\neq i)} \hat{r}_{ij} u'(v_{ij}) \tag{4.20}$$

where, **u'** denotes the derivative of **u** and $\hat{\boldsymbol{r}}_{ij}$ denotes the unit vector in the direction of $\boldsymbol{r}_i - \boldsymbol{r}_j$, using the minimum image convention.

Any measurable structural or thermodynamic property $\boldsymbol{F}$ of the system is associated with a function $\boldsymbol{F}(\boldsymbol{r}^N, \boldsymbol{p}^N, \boldsymbol{V})$ of the mechanical state of the system. The usual assumption of the statistical thermodynamics is that the measured value of $\boldsymbol{F}$ is equal to the ensemble average of the function $\boldsymbol{F}$ over a suitably chosen ensemble of states. The definition for the ensemble average of the property F can be found in [4.38].

In molecular dynamics, the Hamiltonian equations of motion are solved numerically and trajectory averages are calculated for thermodynamic property. Trajectory average of a property $\boldsymbol{F}$ is defined as

$$\overline{F} = \lim_{T\to\infty} T^{-1} \int_0^T F(r^N(t), p^N(t); V(t))dt \tag{4.21}$$

where, it is assumed that $\boldsymbol{r}^N(\boldsymbol{t})$, $\boldsymbol{p}^N(\boldsymbol{t})$ and $\boldsymbol{V(t)}$ are specified in some way at $t \geq 0$ and the limit in the above expression exists. It is also assumed that during the molecular dynamics simulation, the trajectory spends equal times in all equal volume with the same value of energy.

Under these conditions, trajectory average is equal to the ensemble average, where former can be calculated from the molecular dynamics simulation which defines the trajectory of the system.

For constant pressure molecular dynamics, the volume of the system fluctuates, i.e. in this case volume is a dynamical variable rather than a fixed quantity. For this, we replace the coordinates $\boldsymbol{r}_i$, $i = 1,2, \ldots, N$, of the atoms by scaled coordinates, $\boldsymbol{\rho}_i$, $i = 1,2, \ldots, N$, which is defined as follows:

$$\boldsymbol{\rho}_i = \boldsymbol{r}_i / \boldsymbol{V}^{1/3}, \; i = 1, 2, \ldots, N \tag{4.22}$$

Therefore, for each $\boldsymbol{r}_i$ in the box of volume V, there exist a dimensionless scaled coordinate $\boldsymbol{\rho}_i$ whose each component is between zero and one. This system is called as "scaled system" as compared to "the original system".

Consider the Lagrangian with a new variable $\boldsymbol{Q}$ given as:

$$L_2(\rho^N, \dot{\rho}^N, Q, \dot{Q}) = \frac{1}{2} m Q^{2/3} \sum_{i=1}^{N} \dot{\rho}_i . \dot{\rho}_i - \sum_{i<j=1}^{N} u(Q^{1/3} \rho_{ij}) + \frac{1}{2} M \dot{Q}^2 - \alpha Q \tag{4.23}$$

In the above expression, if we interpret $\boldsymbol{Q}$ as the volume $\boldsymbol{V}$, then the first two terms on the right hand side are the Lagrangian for the particle motion within the box expressed in terms of new scaled variable $\boldsymbol{\rho}$. The third term expresses the kinetic energy for the motion of $\boldsymbol{Q}$, and the fourth term represents the potential energy associated with $\boldsymbol{Q}$, where $\boldsymbol{\alpha}$ and $\boldsymbol{M}$ are constants.

The momentum conjugate to $\boldsymbol{\rho}_i$ (associated with particle motion) is defined as:

$$\pi_i = \frac{\partial L_2}{\partial \dot{\rho}_i} = m Q^{2/3} \dot{\rho}_i \tag{4.24}$$

and, the momentum conjugate to $\boldsymbol{Q}$ is defined as:

$$\Pi = \frac{\partial L_2}{\partial \dot{Q}} = M \dot{Q} \tag{4.25}$$

The Hamiltonian for the scaled system are given as:

$$\begin{aligned} H_2(\rho^N, \pi^N, Q, \Pi) &= \sum_{i=1}^{N} \dot{\rho}_i . \pi_i + \dot{Q}\Pi - L_2(\rho^N, \dot{\rho}^N, Q, \dot{Q}) \\ &= (2mQ^{2/3})^{-1} \sum_{i=1}^{N} \pi_i . \pi_i + \sum_{i<(j=1)}^{N} u(Q^{1/3} \rho_{ij}) + (2M)^{-1} \Pi^2 + \alpha \; Q \end{aligned} \tag{4.26}$$

The Hamiltonian equations of the motion are:

$$\frac{dp_i}{dt} = \frac{\partial H_2}{\partial \pi_i} = \frac{\pi}{m Q^{2/3}} \tag{4.27}$$

$$\frac{d\pi_i}{dt} = -\frac{\partial H_2}{\partial \rho_i} = -Q^{1/3} \sum_{j(\neq i)=1}^{N} \frac{\rho_{ij} u'(Q^{1/3}|\rho_{ij}|)}{|\rho_{ij}|} \tag{4.28}$$

$$\frac{dQ}{dt} = \frac{\partial H_2}{\partial \Pi} = \frac{\Pi}{M} \tag{4.29}$$

$$\frac{d\Pi}{dt} = -\frac{\partial H_2}{\partial Q} = -(3Q)^{-1}\left(-2(2mQ^{2/3})^{-1} \sum_{i=1}^{N} \pi_i . \pi_i + Q^{1/3} \sum_{i<j} \rho_{ij} u'(Q^{1/3}\rho_{ij}) + 3\alpha Q \right) \tag{4.30}$$

These equations of the motion for the scaled system can be solved numerically to give the coordinates and momenta as a function of time yielding the trajectory for the scaled system: $\boldsymbol{\rho}^N(t), \boldsymbol{\pi}^N(t), \boldsymbol{Q}^N(t)$ and $\boldsymbol{\Pi}(t)$.

The trajectory average of any function, $\boldsymbol{G}(\boldsymbol{\rho}^N, \boldsymbol{\pi}^N, \boldsymbol{Q}, \boldsymbol{\Pi})$, of the coordinates and momenta of scaled system can be given as:

$$\overline{G} = \lim_{T\to\infty} T^{-1} \int_0^T G(\rho^N(t), \pi^N(t), Q(t), \Pi(t))dt \tag{4.31}$$

The correspondence between the scaled system and original system can be defined as:

$$\begin{aligned} V &= Q \\ r_i &= Q^{1/3} \rho_i \\ p_i &= \pi_i / Q^{1/3} \end{aligned} \tag{4.32}$$

Each state of the scaled system corresponds to a unique value of $\boldsymbol{V}$ and a unique point in the phase space of the original system of volume $\boldsymbol{V}$. Using this correspondence, the calculated trajectory for the scaled system can be used to generate a trajectory for the original system. Therefore, along the new trajectory,

$$\begin{aligned} V(t) &= Q(t) \\ r_i(t) &= Q(t)^{1/3} \rho_i(t) \\ p_i(t) &= \pi_i(t) / Q(t)^{1/3} \end{aligned} \tag{4.33}$$

The equations of the motion after transformation can be given as:

$$\frac{dr_i}{dt} = \frac{p_i}{m} + \frac{1}{3} r_i \frac{d \ln V}{dt} \tag{4.34}$$

$$\frac{dp_i}{dt} = -\sum_{j(\neq i)=1}^{N} \hat{v} \quad u'(r_{ij}) - \frac{1}{3} p_i \frac{d \ln V}{dt} \tag{4.35}$$

$$\frac{Md^2V}{dt^2} = -\alpha + \left(\frac{2}{3} \sum_{i=1}^{N} \frac{p_i \cdot p_i}{2m} - \frac{1}{3} \sum_{i<(j=1)}^{N} v_{ij} \quad u'(v_{ij}) \right) \Big/ V \tag{4.36}$$

Because of the presence of parameter M, these equations, even after transformation, are not for the original system. However, in the limit, when the parameter M becomes infinitely large and $dV/dt = 0$, these equations become equivalent to the dynamical equations for the original system. The last equation of the above set describes the fluctuation of the volume of the simulation cell. The right hand side of the same equation consists of two parts. The first part is $-\alpha$ which is the negative of the externally applied pressure. The second part corresponds to the internal pressure of the fluid. An imbalance between the two forces causes the volume fluctuation in the system because the internal pressure of the system would fluctuate due to the motion of the atoms inside the system. In the presence of periodic boundary conditions where a small sample of fluid is embedded in a much larger sample of fluid, the volume of the small sample will fluctuate in response to an imbalance between external and internal pressure. Time average of any thermodynamic or structural property calculated from this trajectory is equal to the ensemble average of F for an isoenthalpic – isobaric ensemble in which external pressure is a given quantity (for proof of this statement, please refer to [4.38]).

4.2.5.2 Constant temperature molecular dynamics

In case of constant temperature molecular dynamics, the energy of the system fluctuates. In constant temperature molecular dynamics method, the equations of motion of N particles in volume V are the Hamiltonian equation of motion given as:

$$\frac{d\dot{r}^N}{dt} = \frac{\partial H_1}{\partial p_i} = \frac{p_i}{m} \tag{4.37}$$

$$\frac{dp_i}{dt} = -\frac{\partial H_1}{\partial r_i} = -\sum_{j(\neq i)} \hat{r}_{ij} u'(v_{ij}) + S \tag{4.38}$$

where, S is a stochastic collision term for atoms. Each stochastic collision is an instantaneous event that affects the momentum of the particle.

These collisions between atoms take place according to the Poisson process and the time instants at which different particles collide are statistically un-correlated. It is between these collisions, the state of the system evolves. In order to perform this kind of simulations, one needs to choose the desired temperature of the sample, T, and the mean rate, γ, at which each particle suffers stochastic collisions. The probability that a particle experiences a stochastic collision in any small time interval Δt is $\gamma \Delta t$.

The time instants at which any particle experiences a collision can be decided by using random numbers, which represents the time intervals between successive collisions. Another way to perform this task could be the use of random numbers to decide which particles are to suffer collision in any small time interval.

To start the simulation, needs to pick the initial positions and momenta for all the particles, and integrate the Hamiltonian equations of motion for the system until the first stochastic collision. The value of the momentum of the particle after the collision can be chosen from the Maxwell – Boltzmann distribution at temperature T. This change in momentum for the particle is instantaneous. The momentum of the other particles remains unaffected by the collision. Then, Hamiltonian equations of motion for the entire system are integrated until the time of next stochastic collision. This process is repeated for the desired length of the simulation time.

The result of this simulation is time dependent trajectory of the system. This trajectory can be used to calculate the time average of any thermodynamic or structural property. Under certain conditions (for details please refer to [4.38]), the time average of any thermodynamic or structural property, F, of the system is equal to the ensemble average of F for the canonical ensemble in which the temperature is constant, (T).

For large enough system, the stochastic collision frequency is much smaller than the intermolecular collision frequency. Therefore, for most of the time, most of the molecules are moving according to the Hamiltonian equations of motion for a closed system. The stochastic interruptions are infrequent but they cause the energy of the system to relax to a value appropriate to the temperature of the system. These interruptions also cause the energy to fluctuate about its equilibrium value with the value appropriate to a canonical ensemble.

4.2.5.3 Molecular dynamics at constant temperature and pressure

In case of molecular dynamics simulation at constant temperature and pressure, the energy and enthalpy of the system fluctuates. This is done by introducing stochastic collisions into the constant pressure molecular dynamics method. The resultant of this addition is a trajectory of the system in which the time average of any function $\boldsymbol{F}$ is equal to the *NPT* ensemble average of the quantity [4.38].

Perrinello and Rehman [4.39] extended this approach to the anisotropic system. They generalized the theory to system subjected to the arbitrary external stress. For this, they proposed a fluctuation formula for the stiffness tensor in terms of strain fluctuation in the simulation cell.

4.2.5.4 Constant stress molecular dynamics

According to Ray [4.37], one can study equilibrium and transport properties of the system in solid → solid structural transformations using *NtH* (or *NPH*, in case of applied hydrostatic stresses), provided appropriate choices for dynamic characterization of unit cell are made in order to properly define the ensemble. The formulation of *NtH* ensemble can be described as following:

Consider a system described by Hamiltonian, H:

$$\mathsf{H} = \sum_{a=1} p_a^2 \Big/ (2m_a) + \sum_{a<b} U(r_{ab}) \tag{4.39}$$

In order to account for dynamic nature of the volume and shape of the unit cell, one needs to carry out canonical transformation and therefore henceforth, the original coordinates of the atoms are replaced by scaled coordinates as follows:

$$\begin{aligned} s_{ai} &= \sum_{j=1}^{3} h_{ij}^{-1} x_{aj} \\ \pi_{ai} &= \sum_{j=1}^{3} h_{ij}^{-1} p_{aj} \end{aligned} \tag{4.40}$$

where, x and p are the two coordinates of Hamiltonian mechanics representing position and momentum and h_{ij} are elements of h matrix introduced above.

The distance r_{ab} is related to scaled distances, s_{ab}, by the metric tensor, G, as:

$$r_{ab}^2 = s_{ab}^{'} G s_{ab} \tag{4.41}$$

where, G, the matrix tensor is given by $h\,h'$, and prime indicates matrix transpose. After the proper transformation, the Hamiltonian, H, is given by:

$$\mathsf{H}(s, \pi, h) = \sum_{a=1} \pi_a' G^{-1} \pi_a \Big/ (2m_a) + \sum_{a<b} U(r_{ab}) \tag{4.42}$$

Since h is a dynamic variable, this new degree of freedom, h, will have kinetic energy, K_{cell}, and a potential energy, U_{cell}. The latter may be seen as associated with the stored energy in the system. The new Hamiltonian will be given as:

$$\mathsf{H}_1(s, \pi, h, \Pi) = \mathsf{H}(s, \pi, h) + K_{cell}(h, \Pi) + U_{cell}(h) \tag{4.43}$$

where, Π is the momentum conjugate of h and,

$$K_{cell} = (1/2)\, Tr\, \Pi'\, \Pi / W, \tag{4.44}$$

$$U_{cell} = \begin{cases} P(V - V_0) \\ V_0 Tr \sigma \varepsilon \end{cases} \tag{4.45}$$

In U_{cell}, the first case refers to isotropic systems whereas latter case describes anisotropic systems. The same equation in combined form can be written as:

$$U_{cell} = P(V - V_0) + V_0 Tr(\sigma - P)\varepsilon \tag{4.46}$$

where, it has been assumed that in isotropic case $\sigma = P$ and for anisotropic systems P can be taken as zero.

The strain tensor can be written in terms of h_0 and G matrix as:

$$\varepsilon = \tfrac{1}{2}\left(h_0'^{-1} G h_0^{-1} - 1 \right) \tag{4.47}$$

where, h_0 is the initial value of h.

Thus, the equation of motion for h can be given as:

$$W \ddot{h} = (\Phi_{ij} - P)A - h\Sigma \tag{4.48}$$

where, A is the area tensor and is given as $A = Vh'^{-1}$.

Microscopic stress tensor, Φ_{ij}, and $\sum$ are given as:

$$\Phi_{ij} = V^{-1}\left(\sum_a p_{ai} p_{aj} / m_a - \sum_{a<b} \chi_{ab} r_{abi} r_{abj} / r_{ab} \right) \tag{4.49}$$

$$\Sigma = V_0 h_0^{-1} (\sigma - P) h_0'^{-1} \tag{4.50}$$

According to Ray [4.40], in classical statistical mechanics, equilibrium properties of the system are independent of the particle masses and therefore in equilibrium we may neglect the contribution of K_{cell} to the total kinetic energy of the system.

Thus, for a system in equilibrium, we obtain the constant of the motion as [4.19]:

$$\mathsf{H}_1 = \mathsf{H} + U_{cell}(h) \tag{4.51}$$

In case of anisotropic systems,

$$\mathsf{H}_1 = \mathsf{H} + V_0 Tr\, \varepsilon\sigma \tag{4.52}$$

To define ε, h_0 should be taken as the average of h during a molecular dynamics calculation.

In thermodynamics, in order to construct the enthalpy of finite elasticity one introduces the tensor of thermodynamic tension, t_{ij}, which is related to externally applied stress, σ, by:

$$t = V_0 h^{-1} \sigma h^{'-1} h_0^{'} / V_0 \tag{4.53}$$

where, h_0 is the value of h when zero stress is applied to the system i.e. the stored energy in the system is zero. This could be an excellent criterion for choosing appropriate value of h_0 as in the expression of elastic energy, the proper choice of h_0 could be a governing issue.

The thermodynamic tension has the property of being the quantity appearing in the fundamental thermodynamics laws as:

$$TdS = dE + V_0 Tr\, t\, d\varepsilon \tag{4.54}$$

The thermodynamic enthalpy also contains the tension in the following form:

$$H = E + V_0 Tr\, t\varepsilon \tag{4.55}$$

Therefore, in the above formulation, (V_0 Tr $t\varepsilon$) is chosen to represent the U_{cell} with t as a given constant tensor as this appears to be more appropriate for large strains with respect to state of zero stress. The ensemble generated using the new choice of the U_{cell} is isoenthalpic - isotension of NtH ensemble. Thus, when such a system is equilibrium we obtain the constant of the motion as:

$$\mathsf{H}_1 = \mathsf{H} + V_0 Tr\, t\varepsilon \tag{4.56}$$

However, in case of an isotropic hydrostatic pressure the enthalpy of the system does not equal the enthalpy of ordinary thermodynamics as given in above expression. In such cases, $U_{cell} = PV$, and then the constant of motion for *NPH* systems is given as:

$$\mathsf{H}_1 = \mathsf{H} + PV \tag{4.57}$$

In the molecular dynamics of such form, the elastic constants are related to the fluctuation of the strain matrix ε. These constants are also called as *stiffness constants* or *elastic moduli*. The inverse of these elastic constant is called as compliance.

4.3 Research program

Two composites were studied using MD approach: Polyethylene-SWNT and Nylon 6,6 MWCNT composites.

4.3.1 Polyethylene-SWCNT composite

Elastic and engineering properties of nanoparticle enhanced composites and their constituents (matrix, reinforcement and interface) are calculated. The nanocomposites considered in this part of the study consist of a single-wall carbon nanotube (SWCNT) embedded in polyethylene matrix. Molecular dynamics simulations are used to estimate the elastic properties of SWCNT, interfacial bonding, polyethylene matrix and composites with aligned and randomly distributed SWCNTs. The elastic properties of bundles with 7, 9 and 19 SWCNTs are also compared using a similar approach. In all simulations, the average density of SWCNT-polymer nanocomposite was maintained in the vicinity of CNTs, to match the experimentally observed density of a similar nanocomposite. Results are found to be in good agreement with experimentally obtained values by other researchers. The interface is an important constituent of CNT-polymer composites, which has been modeled in the present research with reasonable success.

i- Molecular Dynamics Simulation of SWCNT

One of the primary aims of the present study is to determine the elastic and/or engineering constants of single-wall carbon nano tubes of different chirality. Molecular dynamics simulation runs of SWCNT with (7,0) chirality (Figure 4.1-a) and (5,5) chirality (Figure 4.1-b) were carried out under the NPT ensemble described above. These two chiralities were chosen because they have a similar radius of the CNT. The length of SWCNT was chosen as 105 Å so that an aspect ratio of 25:1 (length: diameter) could be maintained in order to capture the slender structure of SWCNTs. One SWCNT was then placed into a 105 Å x 8.7 Å x 8.7 Å simulation cell. The simulation parameters for NPT molecular dynamics of one SWCNT are given in Table 4.1.

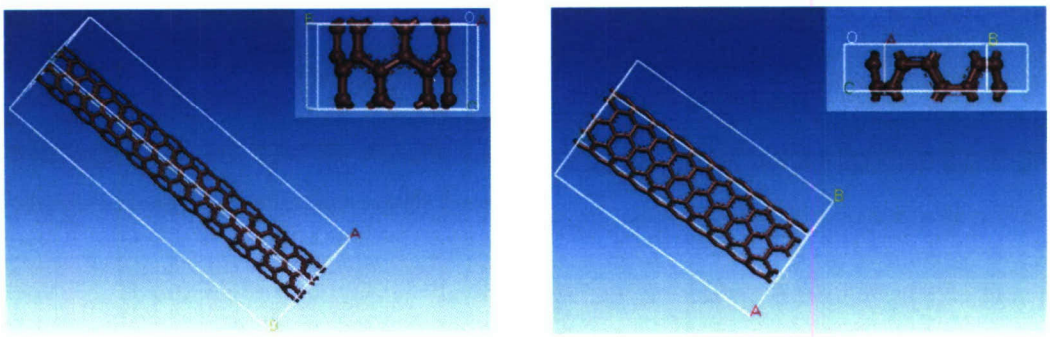

(a) (b)

Figure 4.1: Molecular Dynamic simulation of SWCNT with (a) 7,0 chirality, and (b) 5,5 chirality

Table 4.1: Molecular dynamics simulation parameters for one SWCNT

System	One (7,0) or (5,5) SWCNT, 105 Å length
MD ensemble	NPT
Temperature	293 K
Time step	1 femto second (*fs*)
Duration of simulation	100 pico second (*ps*)
Periodic boundary condition	ON

Depending upon load conditions, the simulation was divided into three parts: axial, transverse and shear loadings. The simulation cell was subjected to uniaxial tensile loading along the tube axis. The load was varied from 2.0265 x 10^{-2} MPa to 1.01325 x 10^{2} MPa during different simulation runs. In other simulation runs, the load was applied either in the transverse or shear direction with load varied between 2.0265 x 10^{-2} MPa to 1.01325 x 10^{2} MPa during different simulation runs. All of the runs gave similar results. Typical elastic constants obtained for the case of 7,0 SWCNT are:

$$C_{ij} = \begin{bmatrix} 1027 & 25.18 & 19.45 & 0 & 0 & 0 \\ 26.78 & 43.11 & 20.54 & 0 & 0 & 0 \\ 20.33 & 28.08 & 37.43 & 0 & 0 & 0 \\ 0 & 0 & 0 & 7.28 & 0 & 0 \\ 0 & 0 & 0 & 0 & 5.59 & 0 \\ 0 & 0 & 0 & 0 & 0 & 7.14 \end{bmatrix} GPa$$

And for the 5,5 SWCNT case are:

$$C_{ij} = \begin{bmatrix} 880.1 & 7.8 & 8.6 & 0 & 0 & 0 \\ 8.4 & 31.21 & 17 & 0 & 0 & 0 \\ 9.13 & 16.1 & 35.5 & 0 & 0 & 0 \\ 0 & 0 & 0 & .8 & 0 & 0 \\ 0 & 0 & 0 & 0 & 2.1 & 0 \\ 0 & 0 & 0 & 0 & 0 & 5.7 \end{bmatrix} GPa$$

where *i,j =1,2,3* with *1* representing the axial direction and 2, 3 representing plane of symmetry. Thus we have a transversely isotropic problem. For this case the five engineering constants may be calculated from elastic constants using the following relations [4.29]:

$$\begin{aligned} E_{11} &= C_{11} - \frac{2C_{12}^2}{C_{22} + C_{23}} \\ E_{33} &= E_{22} = C_{22} + \frac{C_{12}^2(-C_{22} + C_{23}) + C_{23}(-C_{11}C_{23} + C_{12}^2)}{C_{11}C_{22} - C_{12}^2} \\ \nu_{12} &= \nu_{13} = \frac{C_{12}}{C_{22} + C_{23}} \\ \mu_{23} &= \frac{1}{2}(C_{22} - C_{23}) \\ K_{23} &= \frac{1}{2}(C_{22} + C_{23}) \end{aligned} \tag{4.58}$$

ii- Molecular Dynamics Simulation of Clusters of SWCNT

Carbon nanotubes naturally tend to form crystals of hexagonally packed bundles or ropes that should exhibit transversely isotropic behavior. Determination of the effective mechanical properties of nanotube bundles is important so that their applicability as reinforcements in composite materials can be evaluated. Also, once the effective properties of the carbon nanotube bundles are determined, these values can be used as input parameters

for the next step in case of multi level modeling of SWCNT-polymer matrix composite. In these bundles, the inter-tube force interactions are due to primarily non-bonding Van der Waals interactions. These weak cohesive properties of nanotube bundles are important in the prediction of mechanical properties of nanotube composite materials and those of fibers of woven carbon nanotubes.

Three clusters of (7,0) SWCNTs were examined using molecular dynamics. The first cluster consists of 7 SWCNTs packed in hexagonal fashion in a simulation cell, the second cluster consists of 9, and third cluster consists of 19 SWCNTs packed in hexagonal fashion in a simulation cell as shown in Figures 4.2, 4.3 and 4.4, respectively. Constant temperature-constant pressure (NPT) molecular dynamics was performed. In order to simulate normal temperature and pressure conditions during the simulation experiment, the temperature of the system was maintained at 298 K and a hydrostatic pressure of 10 *atm* was applied on the simulation cell in all three experiments. The NPT MD simulation parameters are given in Table 4.2 and the results of MD simulation are reported in Table 4.3.

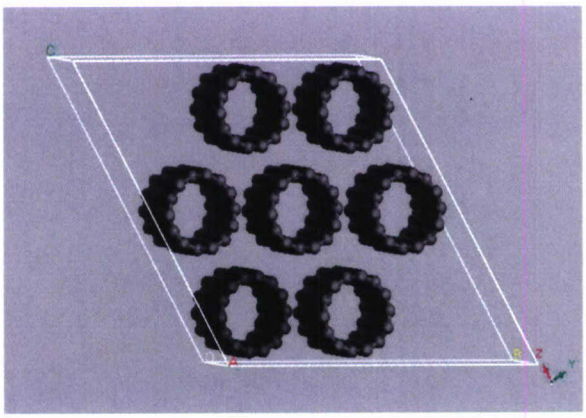

Figure 4.2: Cluster of 7 (7,0) SWCNTs inside the simulation cell

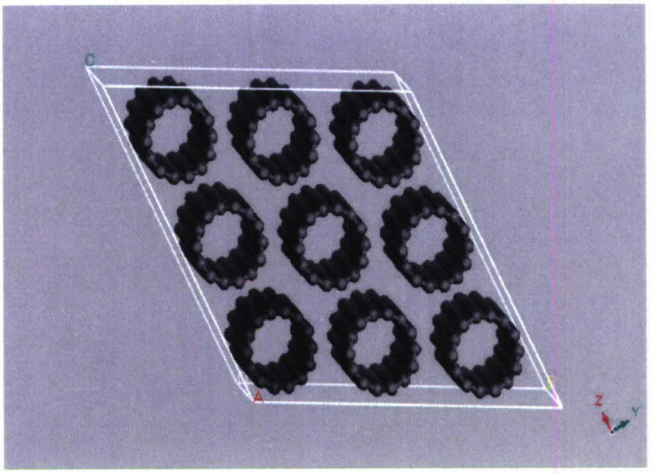

Figure 4.3: Cluster of 9 (7,0) SWCNTs inside the simulation cell

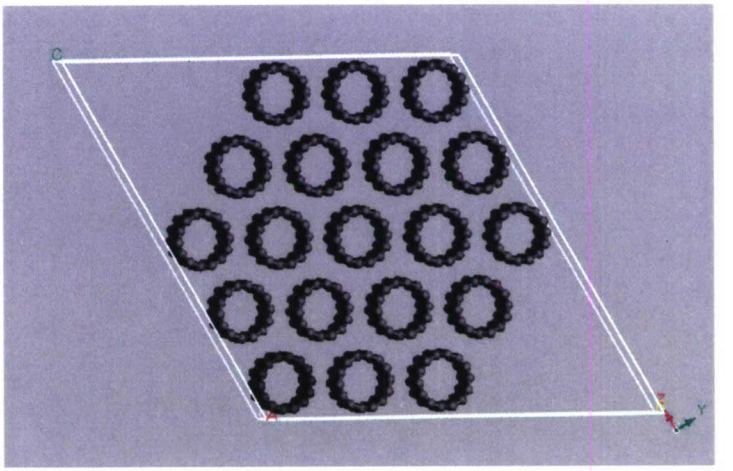

Figure 4.4: Cluster of 19 (7,0) SWCNTs inside the simulation cell

Table 4.2: Molecular dynamics simulation parameters for SWCNT bundles

System	**Cluster of (7,0) SWCNTs, 105 Å length**
MD ensemble	NPT
Temperature	298 K
Time step	1 femto second (*fs*)
Duration of simulation	100 pico second (*ps*)
Periodic boundary condition	ON

Table 4.3: Results of MD simulation of (7,0) SWCNT clusters

Simulation conditions	E_{11} (GPa)	E_{22} (GPa)	ν_{12}	μ_{23} (GPa)	K_{23} (GPa)
9 nanotubes, *NPT*, 1.0 *MPa* (hydrostatic), 293 *K*	1021.7	26.85	0.31	8.41	33.7
7 nano-tubes (displaced from their equilibrium positions), *NPT*, 1.0 *MPa* (hydrostatic), 293 *K*	1019.6	19.49	0.29	5.73	32.88
19 nanotubes, *NPT*, 1.0 *MPa* (hydrostatic), 293 *K*	931.3	14.96	0.29	4.44	23.9

iii- Molecular Dynamics Simulation of Matrix

Polyethylene, a thermoplastic, has been chosen as the matrix material for construction of the composite. Polyethylene [IUPAC name - polyethene (PE)] is a thermoplastic commodity polymer [4.31] created through polymerization of ethylene. Its name originates from the monomer ethene, also known as ethylene, used to create the polymer. The ethylene molecule, C_2H_4 is $CH_2{=}CH_2$, two CH_2 connected by a double bond. The polymerized structure of the polyethylene is shown in Figure 4.5.

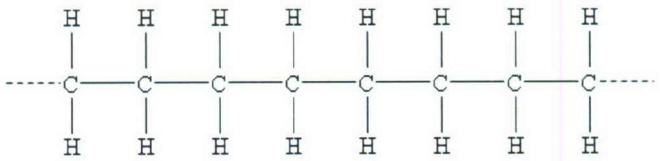

Figure 4.5: Polymerized structure of the polyethylene

Polyethylene is classified into several different categories based on its density and branching. Sometimes some of the carbons, instead of having hydrogen attached to them, will have long chains of polyethylene attached to them. This is called branched, or low-density polyethylene, or LDPE. When there is no branching, it is called linear polyethylene, or HDPE. Linear polyethylene is much stronger than branched polyethylene. The mechanical properties of PE depend significantly on variables such as the extent and type of branching, the crystal structure, and the molecular weight [4.31].

Simulation of the polymer consists of potential energy minimization followed by two steps of molecular dynamics. A single simulation cell of the polymer consists of 8 chains of monomer comprising of total 1216 atoms. This simulation cell was then subjected to periodic boundary conditions in order to simulate the behavior of the bulk polymer. Initially, during the actual chemical reaction the rate of the reaction is reported to be fast which gradually slows down as the chemical reaction proceeds. Therefore, in order to capture the complete trajectory of the polymer chains during molecular dynamics simulations, a two step molecular dynamics simulation was carried out. The first stage of dynamics was carried out for 20 pico second *(ps)* with a smaller time step of 0.2 femto second *(fs)*. This was followed by the second stage with a comparatively larger time step of 1.0 *fs* which lasted for 100 *ps*. The final density of the polymer matrix was maintained as 0.92 *gm/cc*. The temperature of the system was maintained at 298 K throughout the simulation and a hydrostatic pressure of 1 *atm* pressure was applied to the system during the dynamics. Figures 4.6 and 4.7 show the polymer chains used in this simulation, and Table 4.4 shows final engineering properties of the simulated polymer system.

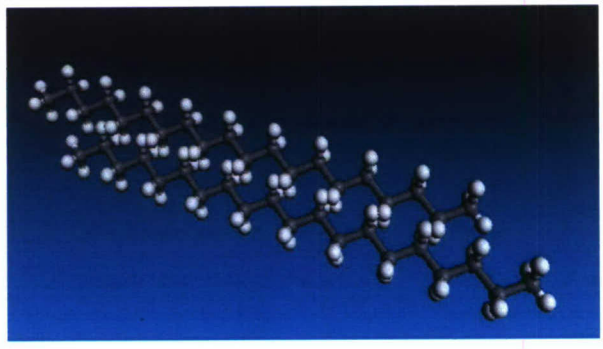

Figure 4.6: Simulated single polymer chain of polyethylene

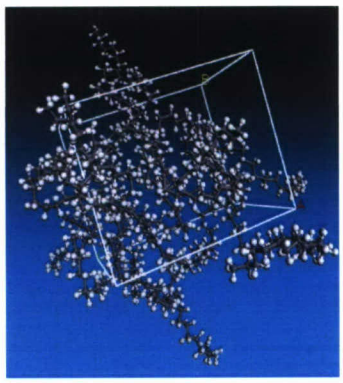

Figure 4.7: Simulated polymer chains of polyethylene

Table 4.4: Engineering constants of the simulated polyethylene

E (GPa)	ν_{12}
1.22	0.37

iv-Molecular Dynamics Simulation of the SWCNT-polymer Interfacial Bonding

In case of composites, the effective transfer of load from matrix to reinforcement occurs via the interface. The extent of this load transfer depends upon the degree of adhesion between the nanotube and matrix material. The adhesive strength between the nanotubes and the polymeric matrix can be evaluated by the interfacial bonding energy. In case of non-functionalized SWCNT-polymer composites, the nature of interfacial bonding energy comes from electrostatic and Van der Waals force in the composite system.

Molecular dynamics simulation of the interface for SWCNT-polymer composite was carried out by simulating the single fiber pull out test. Figure 4.8 shows the atomistic model used for interfacial binding simulations. The polymer composite model used in this study was 10,0 SWCNT-polyethylene composite. The model has a total of 1206 atoms and the final density of the composite was 1.3 gm/cc. Before the start of pull-out test, the periodic boundary conditions imposed on the system were removed. The total energy of the system increases as the SWCNT is pulled out of the composite. This increase in total energy can be attributed to an increase in the potential energy of the system due to the formation of new surfaces. Figure 4.9 shows the variation in total energy, essentially the potential energy, of

SWCNT-polyethylene resin composite as a function of the number of sub-units of SWCNT pulled out of the composite. Once, the whole SWCNT is pulled out of the matrix, the variation in total energy attains a plateau as the SWCNT is left far away from the matrix, because in such a situation the interaction between matrix and SWCNT is extremely weak.

According to Gou et al. [4.32], the pullout energy, $E_{pull\text{-}out}$, is defined as the energy difference between the fully embedded nanotube and the complete pull-out configuration. It can be related to the interfacial shear stress, τ_i, by the following relation:

$$E_{Pullout} = \int_0^L 2\pi a(l-x)\tau_i \; dx \;\; = \;\; \pi a \tau_i L^2 \tag{4.59}$$

$$\Rightarrow \;\; \tau_i \;\; = \;\; E_{Pullout} \Big/ \pi \;\; a \;\; L^2 \tag{4.60}$$

where, a and L are the radius and length of the nanotube, respectively, and x is the displacement of the nanotube.

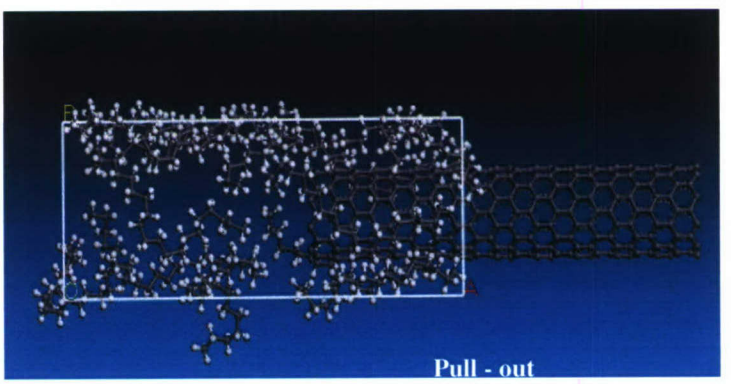

Figure 4.8: Atomistic model of the composite for interfacial binding energy analysis

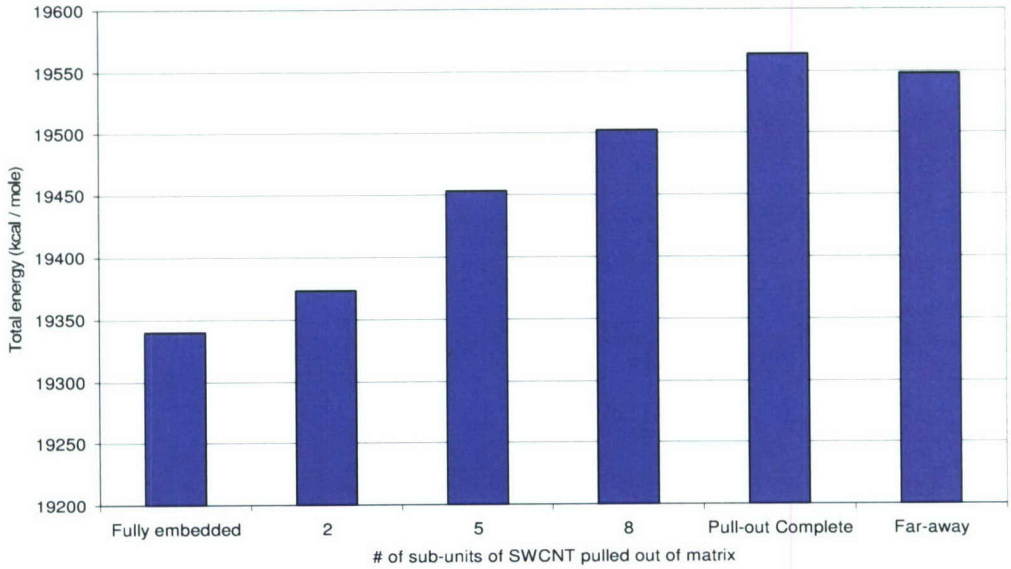

Figure 4.9: Potential energy variation for SWCNT pull-out test from polyethylene matrix in single SWCNT composite.

The $E_{pull\text{-}out}$ for the system comes out to be 224 k-cal/mole. The radius of the (10, 0) nanotube is 7.875Å and the length of the SWCNT in the present system was 42.26 Å. The interfacial shear strength for the system under consideration comes out to be 133 MPa. This value of interfacial strength is comparable to interfacial strength value of 150 MPa for nanotube-polystyrene system reported in literature [4.33].

In another set of simulations, the same system was subjected to periodic boundary conditions. But, because of periodic boundary conditions of the system, when a SWCNT is pulled out from one end, another SWCNT enters from the opposite end into the simulation cell from its neighboring image cell. Therefore, the total energy of the system remains almost unaffected. Therefore, effect of the SWCNT pulling on the total energy of the system could not be studied in such a scenario.

v- Molecular Dynamics Simulation of SWCNT-Polyethylene Composite

A key problem in the case of CNT polymer composites is the bonding between CNT and polymer matrix. On the one hand, the Van der Walls forces are too weak to provide strong connections between CNT and the matrix such that attacks on CNT by chemical agents may result in development of covalent bonds with carbon atoms, which will affect the

structure of CNT. On the other hand, due to spatial mismatch between the atomic structure of CNT and matrix material, there can exist (by analogy with epitaxial growth) significant residual stresses, which in turn may cause defects in the matrix and deformation of CNT. These factors can change key properties of the CNT such as electrical and thermal conductivity. Figure 4.10 illustrates the deformed shape of a CNT (departure from circularity of cross-section) when surrounded by polymer chains, as obtained from molecular dynamics simulation.

Molecular dynamics simulation was carried out for the SWCNT-polyethylene matrix composite. The simulation cell for the composite consists of single 7,0 SWCNT embedded in polyethylene matrix. The dimensions of the simulation cell were maintained as 100Å x 50 Å x 50 Å. The two step NPT molecular dynamics was applied to the present case as well. The temperature of the system was maintained at 298 K throughout the simulation and a hydrostatic pressure of 1 *atm* pressure was applied to the system. Figure 4.10 also shows the polymer chains used in this simulation and Table 4.5 shows final engineering constants of the simulated polymer system.

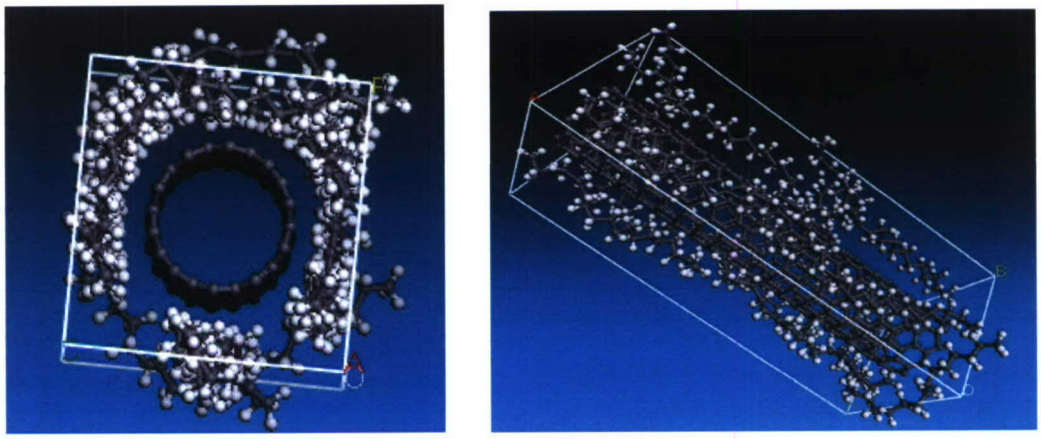

Figure 4.10: An arm chair CNT surrounded by ethylene molecules, before energy minimization.

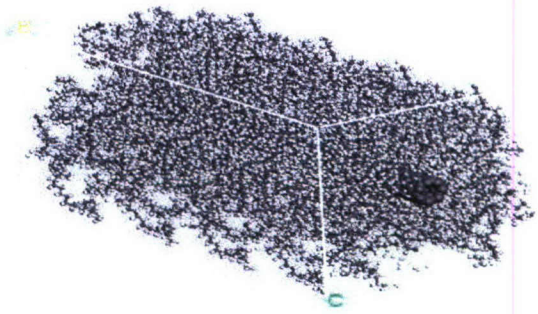

Figure 4.11: Molecular dynamics simulation cell for SWCNT- polyethylene matrix composite

Table 4.5: Mechanical properties for SWCNT-polyethylene composite from molecular dynamics simulation.

E_{11} (GPa)	E_{22} (GPa)	ν_{12}	μ_{23}(GPa)	K_{23} (GPa)
92.18	2.31	0.33	0.97	13.55

In order to account for random distribution of CNTs in the polymeric matrix, molecular dynamics simulation was carried out for the 3 SWCNTs embedded in polyethylene matrix as shown in Figure 4.12. The simulation cell for the composite consists of three single 7,0 SWCNTs embedded in the polyethylene matrix. The dimensions of the simulation cell were maintained as 100Å x 100 Å x 100 Å. Two step NPT molecular dynamics was applied. The temperature of the system was maintained at 298 K throughout the simulation and a hydrostatic pressure of 1 *atm* pressure was applied to the system. The same volume fraction used in the case of single CNT embedded in polyethylene matrix was maintained with a total of 13414 atoms used in the simulation. The engineering constants obtained as a result of this simulation are summarized in Table 4.6.

Table 4.6: Engineering constants of simulated composite with three 7,0 SWCNTs randomly embedded in polyethylene matrix.

E (GPa)	ν_{12}
24.62	0.36

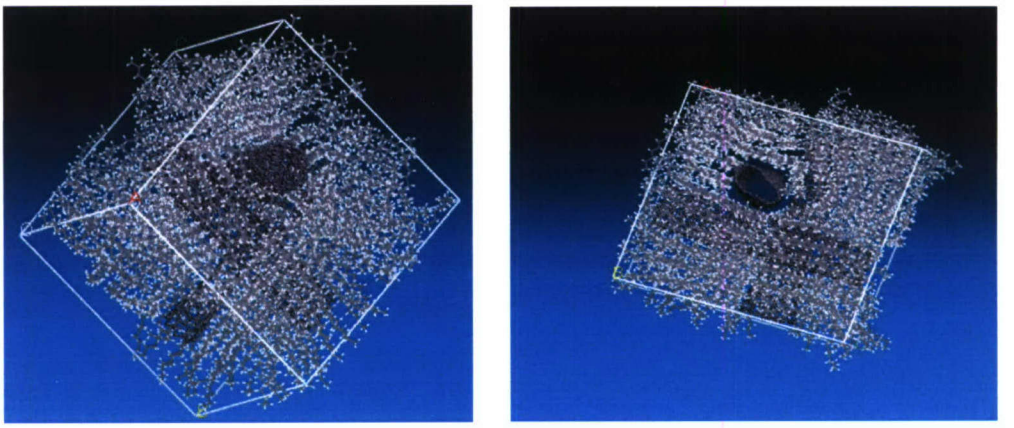

Figure 4.12: Molecular dynamics simulation cell for three 7,0 SWCNTs embedded in polyethylene matrix

4.3.2 Nylon 6,6 – Multi Wall Carbon Nanotube (MWCNT) Composites

In this part of the report, we focus of calculating mechanical properties of carbon nanotube reinforced nylon 6,6 nano composites and their constituents (e.g. matrices and reinforcements). Several weight fractions of reinforcements are evaluated.

i- Simulation of Multi Wall Carbon Nanotube.

In this project commercial software Materials Studio MS 4.1 was used [4.23]. Two ensembles were applied for the dynamics steps: NVT (Anderson thermostat) or NPT (Berendsen barostat and either Berendsen or Parrinello thermostat). Two vectors m and n were used to specify chirality and naming scheme of CNT (see Figure 4.13).

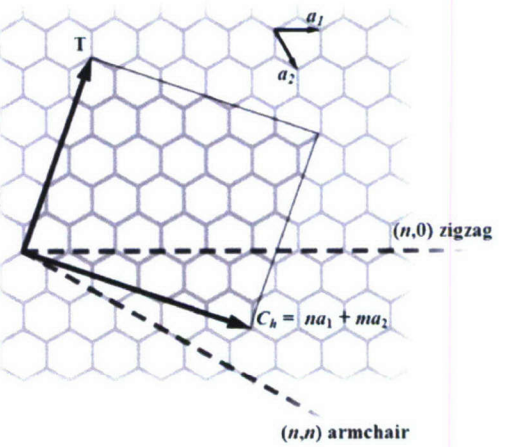

Figure 4.13: The (*n*,*m*) nanotube naming scheme.

To calculate the elastic constants, temperature was set to 298 K, raised to 400 K and then equilibrated back to room temperature. Different MWCNTs chiralities and different number of walls for both isobaric and isochoric ensembles were used. The MD trajectory was obtained by saving the coordinates and velocities of all atoms at each 100 fs. Static elastic properties were calculated by applying three tensile and three shear deformations of magnitudes ±0.0005 to the minimized equilibrated system. The system was reminimized after each deformation. The internal stress tensor was, then, obtained from the analytically calculated virial and was used to obtain estimates of elastic stiffness coefficients matrix.

When simulating MWCNTs, there are many variables that need to be considered which include the effect of: effective length aspect ratio (L/d), simulation temperature, number of carbon nanotube walls, chirality, and thermodynamic ensemble (thermostat and barostat) algorithm used. Various runs were carried out to study the effect of these variable on calculated engineering constants.

a. Effect of Aspect Ratio

The unit cell is regarded as the basic "building block" of a crystal. It is a human construction used to represent the size, location, and number of objects contained within the crystal. In other words, it is a parallel piped that has lengths and angles known as the lattice parameters. That are the same as the characteristic angles and magnified distances within the crystal. Theoretically we should be able to construct a super cell which is a repeated unit block in any of the symmetry axes. The CNT unit cell block is a triclinic unit cell with $\gamma = \beta = 90°, \alpha = 120°$ (see Figure 4.14). the length parameters B, C depend on the chirality of constructed vector which, also, defines the diameter of the CNT. The length parameter, A, defines the dimension of cell that represents the length required for the simulated molecular crystal.

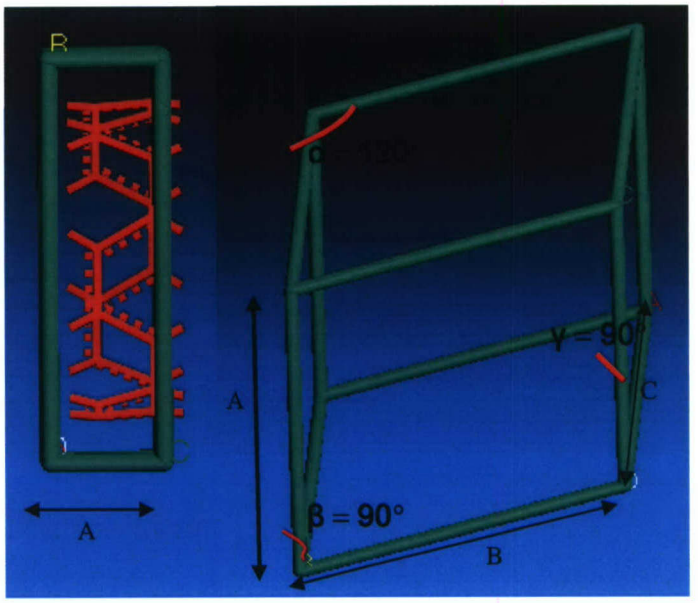

Figure 4.14: Schematic triclinic unit cell showing lattice parameters

In molecular modeling, it is important to optimize the unit cell size. This maybe can be achieved by minimizing the number of atoms to be simulated, to mimic the behavior and properties at structural scale. The limitations of molecular modeling include not only the size of the unit cell, but also the time required to equilibrate the unit cell for energy interaction calculations between atoms.

Aspect ratio of CNT affects the covalent bonding of carbon atoms to polymer matrices in CNT polymer composites. Several aspect ratios were considered to study the effect of CNT length on engineering constants as shown in Table 4.7 and Figure 4.15. The simulations were performed under NPT ensemble (barostat: Berrendsen, Thermostat: Perrinellio) where the boundaries of the unit cell were set to be free to allow for volumetric change during dynamic loading. The unit cell temperature was raised from 298K to 400K and, then, cooled back to room temperature. Same procedure was applied for all the cases shown in Table 4.7. Different dynamic time was used for equilibrating the system at a rate of 1 *fs* per dynamic step. The total dynamic time is proportional to the total number of atoms (length of CNT) considered.

Two stiffness matrices for eight and twenty units cell MWCNT, are shown below.

- Eight units super cell:

$$C_{ij} = \begin{bmatrix} 606.5 & 31.1 & 29.6 & 0 & 0 & 0 \\ 31 & 68 & 50.2 & 0 & 0 & 0 \\ 29.6 & 50.2 & 67.4 & 0 & 0 & 0 \\ 0 & 0 & 0 & .8 & 0 & 0 \\ 0 & 0 & 0 & 0 & .7 & 0 \\ 0 & 0 & 0 & 0 & 0 & 9.2 \end{bmatrix} GPa$$

- Twenty units super cell:

$$C_{ij} = \begin{bmatrix} 698.1 & 25 & 25 & 0 & 0 & 0 \\ 25 & 66.2 & 49 & 0 & 0 & 0 \\ 25 & 49 & 66.4 & 0 & 0 & 0 \\ 0 & 0 & 0 & .8 & 0 & 0 \\ 0 & 0 & 0 & 0 & .6 & 0 \\ 0 & 0 & 0 & 0 & 0 & 8.6 \end{bmatrix} GPa$$

Figure 4.16 shows the effect of CNT length on engineering constants E_{11}, E_{22}, v_{12}, M_{23}, K_{23}.

From Table 4.7 and Figure 4.16 it is fair to assume that, for this case of study 20 Å CNT is an optimum length because all engineering properties tend to be almost constants after that length.

Table 4.7: Engineering constants versus aspect ratio of a MWCNT

Three Wall	Length Å	L/d Ratio Inner tube	L/d Ratio Outer tube	E11	E22	v12	M23	K23
2 units	4.92	0.72	0.25	439	36	0.20	11	47.3
4 units	9.84	1.5	0.5	493	36	0.26	7.7	47.15
8 units	20	3.63	1.2	590	31.1	0.26	9	59.2
20 units	49.2	7.3	2.4	687	30	0.26	8.6	57.6
30 units	73.8	11	3.6	690	27.5	.33	7.9	52.6
40 unit	98.4	14.4	4.8	720	28.6	.33	8.3	54.9

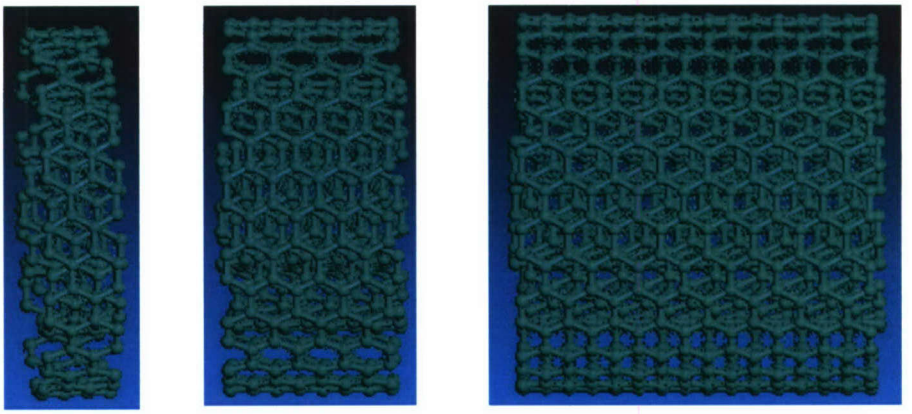

(a) (b) (c)

Figure 4.15: Typical MWCNT simulated for the case of (a) two, (b) four, and (c) eight. unit cells with assigned chirality vector (5_5, 10_10, & 15_15).

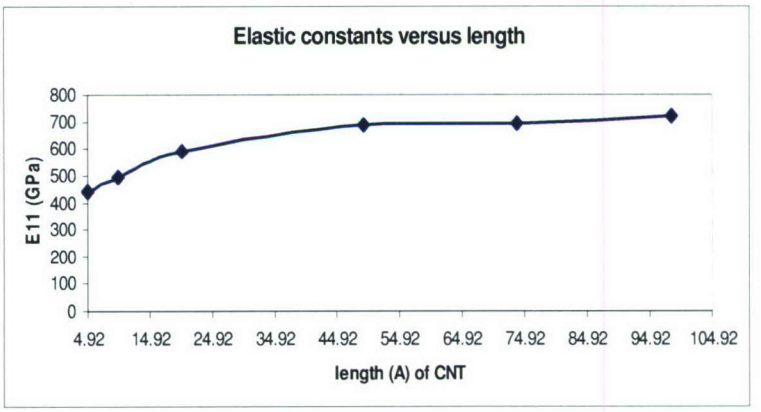

(a)

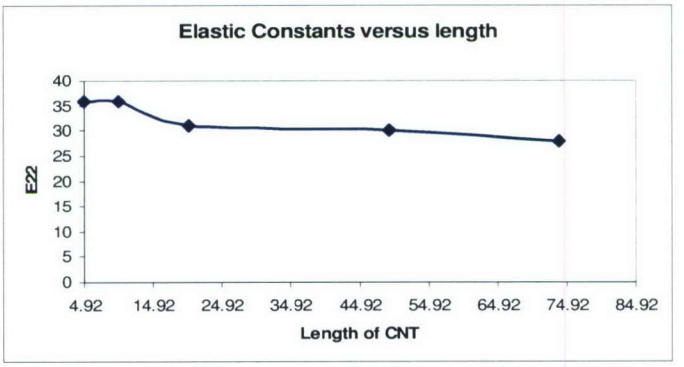

(b)

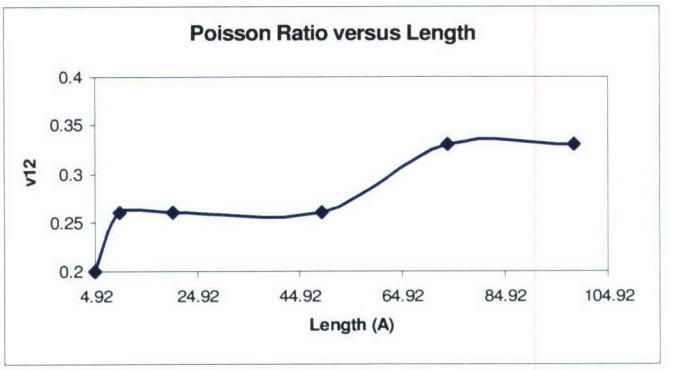

(c)

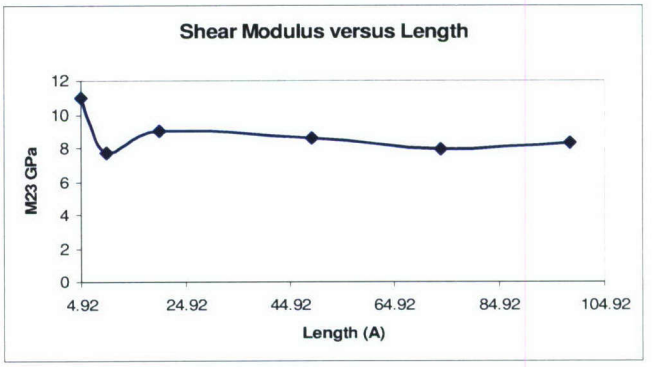

(d)

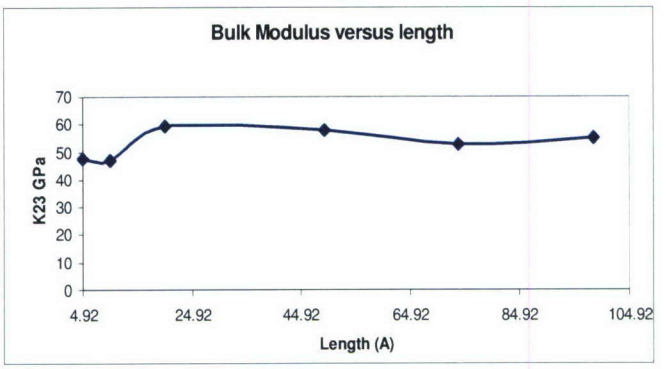

(e)

Figure 4.16: Engineering constants versus CNT length for (a)E_{11}, (b) E_{22}, (c) ν_{12}, (d) M_{23}, and (e) K_{23}

b. Heat Effect

Since CNT are produced at high temperatures (1100K), a three wall MWCNT was exposed to target temperatures of 400, 600, 800, 1000, and 1200 K. Two cases were considered. In the first case, the temperature of MWCNT was raised from room temperature to target temperature and then cooling back to room temperature at which elastic constants

were calculated (see Figure 4.17a). In the second case, the temperature was raised to target temperature at which elastic constants were calculated (see Figure 14.7b).

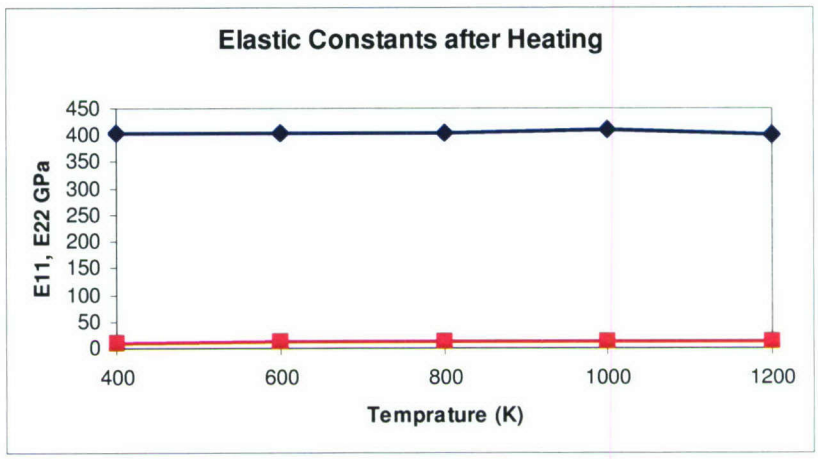

(a)

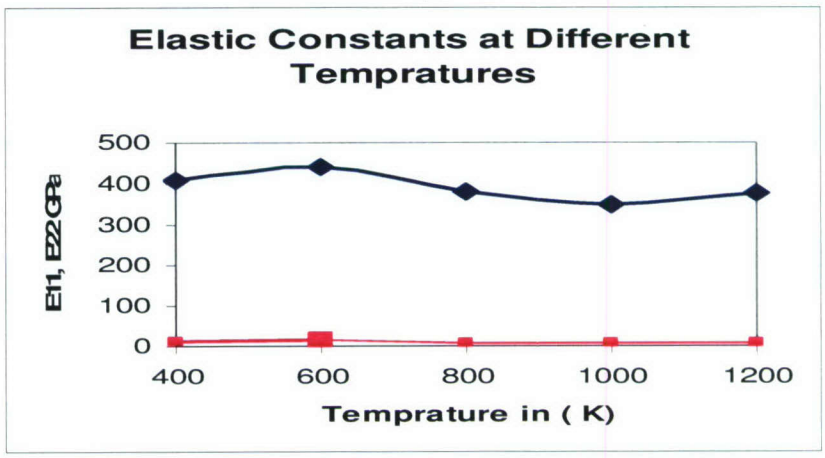

(b)

Figure 4.17: Elastic constants E_{11} & E_{22} of three walls CNT for the case of (a) heated to different target temperatures and then cooled back to room temperature, and (b) heated to different target temperatures.

Figures 4.17a, and 4.17b shows that the elastic properties of MWCNTs are not affected by temperature scheme.

c. Effect of Number of Layers

According to MWCNT manufactures, number of layers in a MWCNT can go from a single layer, up to ten layers. Figure 4.18 shows MWCNTs for multiple layers 1, 2, 3, 4, and 5. Optimum unit cells size and number of atoms are one of the main limitations in molecular modeling. For accurate energy interaction calculations at a global minimum of a structure, it

is required to have a minimum number of atoms. However, due to software limitations of maximum number of atoms that can be simulated, it is important to optimize number of layers used in the model. Figure 4.19 shows longitudinal stiffness versus number of layers for NPT ensemble. It can be observed that the SWCNT has the highest elastic longitudinal constant E_{11}. Increasing the number of layers drops the properties, but they tend to have a constant value after three layers. Therefore, three layers was chosen as an optimum number of layers for simulation purposes in this study.

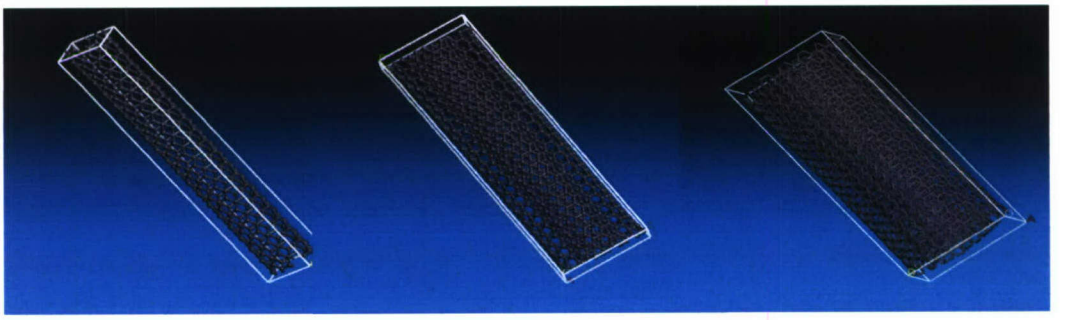

Single Wall Carbon Nano Tube
(5, 5)
Total length of 49.2 A
Total number of atoms

Double Wall Carbon Nano Tube
(5,5),(10,10)
Total length of 49.2 A
Total number of atoms 1200

Three Wall Carbon Nano Tube
(5,5),(10,10),(15,15)
Total length of 49.2 A
Total number of atoms 2400

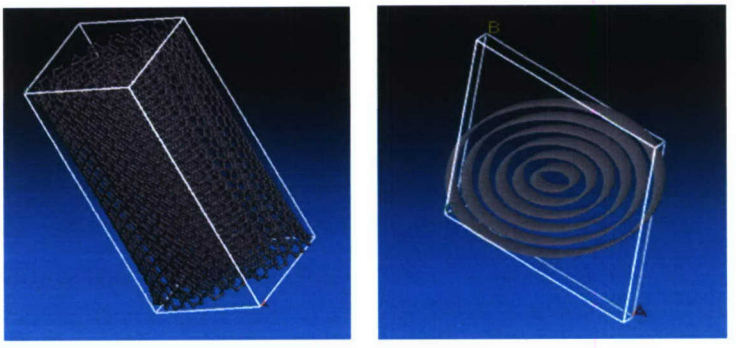

Four (5,5),(10,10),
(15,15),(20,20)
Total length of 49.2 A
Total number of atoms 4000

Five (5,5),(10,10),
(15,15),(20,20),(25,25)
Total length of 49.2 A
Total number of atoms 6000

Figure 4.18: MWCNT versus Number of Layers.

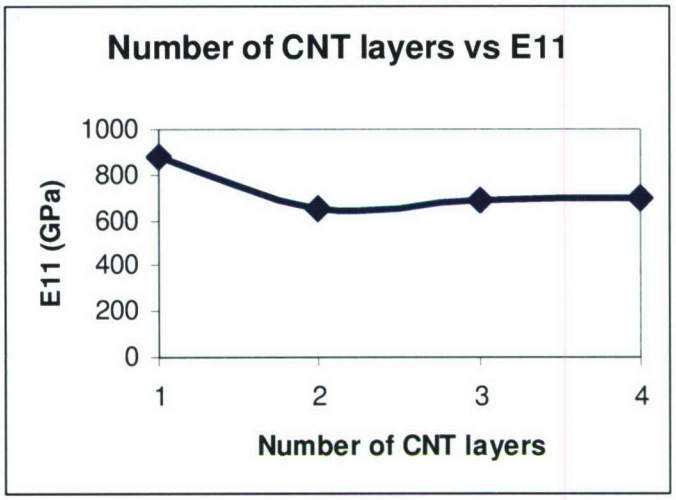

Figure 4.19: Longitudinal stiffness versus number of layers.

d. Effect of MWCNT Building Setup

Two build setups for MWCNT's were used: sequential and individual. In the sequential simulation, the number of walls, chirality of inner tube and the minimum separation distance between carbon nanotube walls were specified. This was assigned without specifying the chirality of the rest of the walls. Instead, the program automatically calculates chirality of subsequent layers by fixing the *m* vector and increasing *n* vector. In the individual simulation, the chirality of each wall of the MWCNT was specified with a restriction of a minimum separation distance to avoid over lapping. The distance was set to the thickness of a graphene sheet (3.347 Å). Typical stiffness matrices for MWCNT using NPT thermodynamic ensemble and Berendsen (thermostat, barostat) are shown below for the case of three walls:

$$C_{ij} = \begin{bmatrix} 202 & 21.6 & 11.2 & 0 & 0 & 0 \\ 15.9 & 45.5 & 11.9 & 0 & 0 & 0 \\ 21.7 & 36.9 & 23.7 & 0 & 0 & 0 \\ 0 & 0 & 0 & 3.2 & 0 & 0 \\ 0 & 0 & 0 & 0 & 10.41 & 0 \\ 0 & 0 & 0 & 0 & 0 & 1 \end{bmatrix} GPa \quad C_{ij} = \begin{bmatrix} 280 & 36.1 & 44.77 & 0 & 0 & 0 \\ 18.5 & 67.1 & 66.6 & 0 & 0 & 0 \\ 50.42 & 49.1 & 47.4 & 0 & 0 & 0 \\ 0 & 0 & 0 & 3 & 0 & 0 \\ 0 & 0 & 0 & 0 & 7.4 & 0 \\ 0 & 0 & 0 & 0 & 0 & 5.5 \end{bmatrix} GPa$$

Sequential Simulation *Individual Simulation*

By examining the above matrices, one can conclude that the MWCNT is transversely isotropic. This assumption was used in calculating engineering constants of MWCNT.

Figure 4.20 shows a plot of MWCNTs longitudinal elastic constant for both setups, sequential and individual, for an NPT thermodynamic ensemble, which shows that building ensemble has minor effect on the calculated elastic constants.

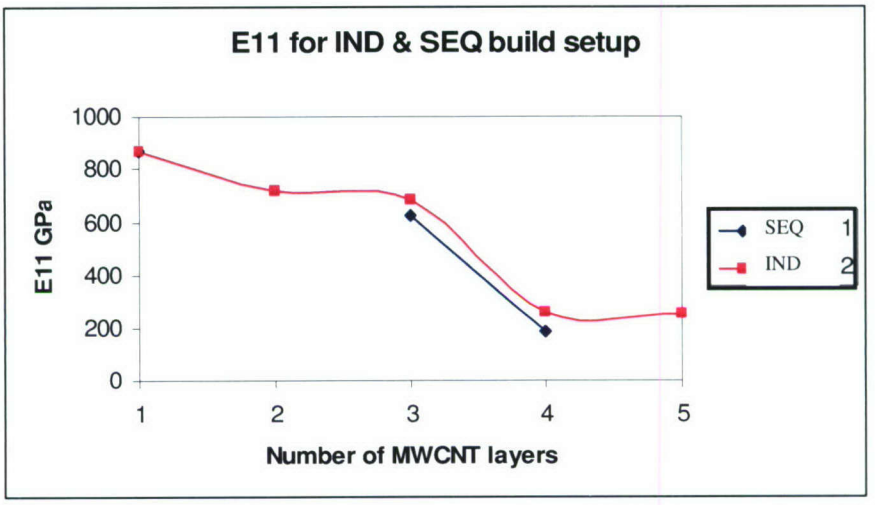

Figure 4.20: Longitudinal modulus, E_{11}, versus number of CNT layers using NPT ensemble for both sequential (SEQ) and individual (IND) setups.

e. Thermodynamics Ensemble Effect

The thermodynamic ensembles used in this project are:

a. Isothermal - Isobaric

This ensemble represents constant Number of atoms, constant Pressure, and constant Temperature (NPT). Therefore, NPT ensemble allows control of both temperature and pressure with no new atoms generated due to chemical reactions. Free surface unit vector are allowed to change, and the pressure is adjusted by adjusting the volume. This ensemble is equivalent to displacement control loading.

b. Isochoric

This ensemble represents constant Number of atoms, constant Volume, and constant Temperature (NVT). This ensemble is also referred to as the canonical ensemble. It is the default ensemble provided in Discover module [4.23].The ensemble is obtained by controlling the temperature through direct temperature scaling during the initialization stage and by temperature bath coupling during the data collection phase. The volume was kept constant through the run. This is the appropriate choice when conformational searches of molecules are carried out in a vacuum without periodic boundary defined. Even if periodic

boundary conditions are used, and if pressure is not a significant factor, the constant temperature constant volume provides the advantage of less perturbation of the trajectory due to the absence of coupling to a pressure bath.

Figure 4.21 shows the longitudinal elastic constant versus number of layers for fixed super cells length. The drop in properties in cases of four walls and the five walls, is due to the use of a periodic cell of limited size, this result is different than the one shown in Figure 4.19 for a larger unit cell. The Figure 4.19 shows that the effect for the thermodynamic ensembles is relatively small.

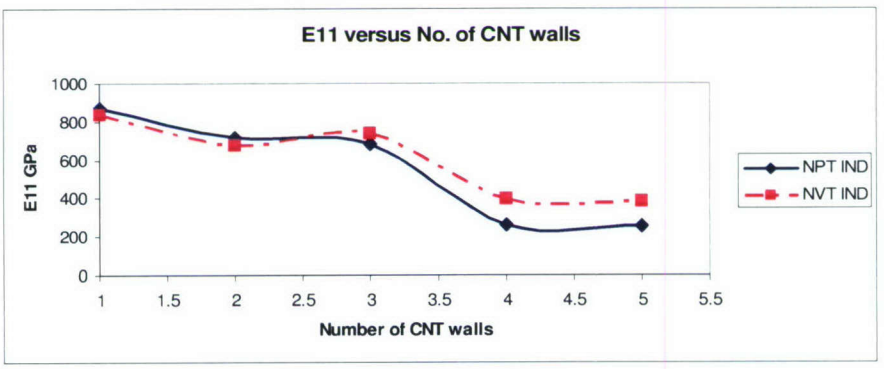

Figure 4.21: E11 versus number of layers, for NPT, NVT ensembles for a twenty super cells.

e. Thermostat and Barostat Algorithms Effect

The following algorithms were used:

1. *Berendsen algorithm*:

This algorithm is used as a thermostat and a barostat dynamic control. In this case the instantaneous temperature is pushed towards desired temperature by scaling velocities at each step. The momenta is dragged up or down towards the correct T. So, the Berendsen thermostat is not to be considered as a canonical or a stochastic algorithm. Any small variation in the energy standard deviation will vary the elastic calculated constants.

2. *Andersen algorithm:*

This thermostat algorithm is a stochastic collision method. The velocity of a particle are randomly chosen from a Maxwell-Boltzmann distribution at the desired T is replaced. The replacement represents a stochastic collision with the heat bath. This is equivalent to the system being in contact with a heat bath that randomly emits thermal particles that collide with the particles in the system and change their velocity. Between each collision, the system is simulated a constant energy. Thus, the overall effect is equivalent to a series of

microcanonical simulations, each performed at a slightly different energy. The distribution of energies of these "mini-microcanonical" simulations should be a Gaussian function.

3. *Parrinello algorithm*:

This is a barostat algorithm the induced dipoles are treated as additional dynamical variables that are included in a the extended Lagrangian function. Where mass is associated with the motion of dipoles. Given the starting configuration, the algorithm solves for the minimum energy of the electrons and evaluates the forces through energy derivatives with respect to nuclear positions. At the same time it perform a nuclear step at the same time. Figure 4.22 demonstrates the effect of using different thermostat and barostat algorithms clearly, for some of the cases the difference is considerable, for example for the case of DWCNT simulated under NVT ensemble the longitudinal modulus about 200 GPa, for Berendsen barostat, thermostat, compared to about 750 when Berendsen thermostat, and Parrinello thermostat is used.

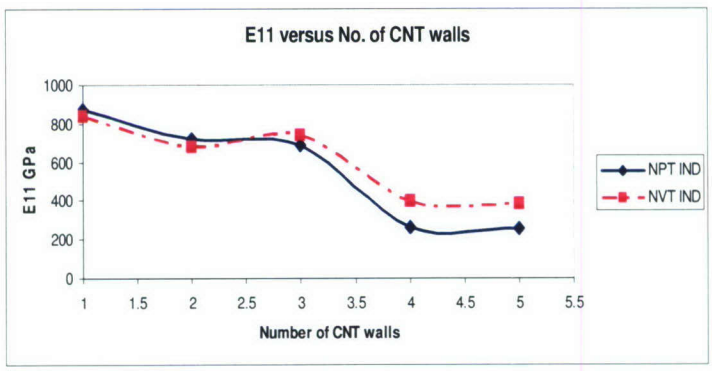

(a)

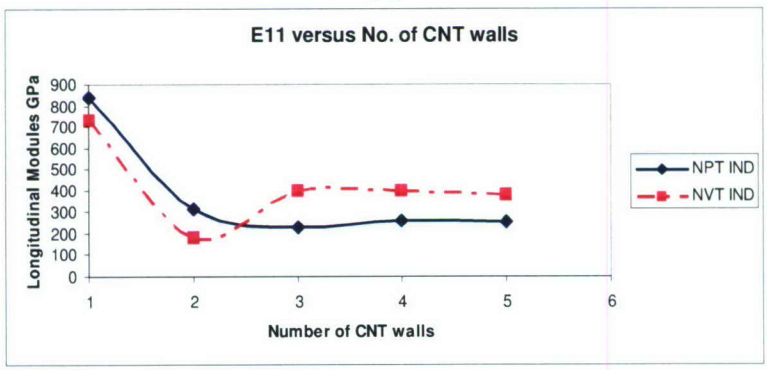

(b)

Figure 4.22: E11 versus MWCNT layers.
(a). Berrendsen Thermostat, and Parrneillo Barostat.
(b) Berrendsen Thermostat, and Berrendsen Barostat.

Examples of stiffness matrices using different ensembles, barostat, and thermostat
Stiffness matrices for both Individual and sequential setups under isochoric, and isobaric dynamic loadings are summarized below:

NPT, Individual:

Table 4.8: Molecular dynamics simulation parameters for MWCNT

System setup	Individual, 49.2 Å length
MD ensemble	NPT
Temperature	400 K
Thermostat	Berendsen
Barostat	Parrinello
Time step	1 femto second (fs)
Periodic boundary condition	ON
Energy Deviation	100 kcal/mol

- Single Wall armchair (5_5) Elastic Constants

$$C_{ij} = \begin{bmatrix} 880.1 & 7.8 & 8.6 & 0 & 0 & 0 \\ 8.4 & 31.21 & 17 & 0 & 0 & 0 \\ 9.13 & 16.1 & 35.5 & 0 & 0 & 0 \\ 0 & 0 & 0 & .8 & 0 & 0 \\ 0 & 0 & 0 & 0 & 2.1 & 0 \\ 0 & 0 & 0 & 0 & 0 & 5.7 \end{bmatrix} GPa$$

- Double Wall armchair (5_5,10_10) Elastic Constants

$$C_{ij} = \begin{bmatrix} 674.4 & 39.9 & 62.4 & 96.9 & 0 & 0 \\ 38.1 & 67.4 & 48.2 & 0 & 0 & 0 \\ 62.5 & 50.7 & 65.7 & 0 & 0 & 0 \\ 93.7 & 0 & 0 & 16.4 & 0 & 0 \\ 0 & 0 & 0 & 0 & 41.9 & 0 \\ 0 & 0 & 0 & 0 & 0 & 9.4 \end{bmatrix} GPa$$

- Triple Wall armchair (5_5, 10_10, 15_15) Elastic Constants

$$C_{ij} = \begin{bmatrix} 698.1 & 25 & 25 & 0 & 0 & 0 \\ 25 & 66.2 & 49 & 0 & 0 & 0 \\ 25 & 49 & 66.4 & 0 & 0 & 0 \\ 0 & 0 & 0 & .8 & 0 & 0 \\ 0 & 0 & 0 & 0 & .6 & 0 \\ 0 & 0 & 0 & 0 & 0 & 8.6 \end{bmatrix} GPa$$

- Four Wall armchair (5_5, 10_10, 15_15, 20_20) Elastic Constants

$$C_{ij} = \begin{bmatrix} 280 & 36.1 & 44.77 & 0 & 0 & 0 \\ 18.5 & 67.1 & 66.6 & 0 & 0 & 0 \\ 50.42 & 49.1 & 47.4 & 0 & 0 & 0 \\ 0 & 0 & 0 & 3 & 0 & 0 \\ 0 & 0 & 0 & 0 & 7.4 & 0 \\ 0 & 0 & 0 & 0 & 0 & 5.5 \end{bmatrix} GPa \qquad C_{ij} = \begin{bmatrix} 710 & 21 & 20.7 & 0 & 0 & 0 \\ 21.5 & 57.6 & 43 & 0 & 0 & 0 \\ 20 & 42.7 & 56.7 & 0 & 0 & 0 \\ 0 & 0 & 0 & 1.1 & 0 & 0 \\ 0 & 0 & 0 & 0 & 3.3 & 0 \\ 0 & 0 & 0 & 0 & 0 & 7.1 \end{bmatrix} GPa$$

Twenty unit super cells *Thirty unit super cells*

- Five Wall armchair (5_5, 10_10, 15_15, 20_20, 25_25) Elastic Constants

$$C_{ij} = \begin{bmatrix} 271 & 21 & 16.47 & 0 & 0 & 0 \\ 20.5 & 37.41 & 19.71 & 0 & 0 & 0 \\ 16.7 & 19.9 & 28.5 & 0 & 0 & 0 \\ 0 & 0 & 0 & 5.5 & 0 & 0 \\ 0 & 0 & 0 & 0 & 1.25 & 0 \\ 0 & 0 & 0 & 0 & 0 & 2.4 \end{bmatrix} GPa$$

NPT, Sequential:

Table 4.9: Molecular dynamics simulation parameters for MWCNT

System setup	Sequential , 49.2 Å length
MD ensemble	NPT
Temperature	400 K
Thermostat	Berendsen
Barostat	Parrinello
Time step	1 femto second (fs)
Periodic boundary condition	ON
Energy Deviation	100 kcal/mol

- Two CNT Elastic Constants:

$$C_{ij} = \begin{bmatrix} 391.6 & 136.3 & 63.4 & 0 & 0 & 63.7 \\ 132.9 & 62.5 & 38.4 & 0 & 0 & 17.8 \\ 62.2 & 40.7 & 37.5 & 0 & 0 & 5.4 \\ 0 & 0 & 0 & 112.6 & 66 & 0 \\ 0 & 0 & 0 & 67.8 & 39.6 & 0 \\ 64.7 & 17.6 & 6.8 & 0 & 0 & 12.5 \end{bmatrix} GPa$$

- Three CNT Elastic Constants:

$$C_{ij} = \begin{bmatrix} 732.2 & 55.5 & 46.6 & 164.2 & 0 & 0 \\ 55.6 & 30.3 & 27.1 & 6 & 0 & 0 \\ 46.1 & 27.1 & 28.8 & 4.3 & 0 & 0 \\ 164.2 & 6 & 4.3 & 38.3 & 0 & 0 \\ 0 & 0 & 0 & 0 & 29.5 & 6.5 \\ 0 & 0 & 0 & 0 & 6.5 & 2.6 \end{bmatrix} GPa$$

- Four CNT Elastic Constants:

$$C_{ij} = \begin{bmatrix} 202 & 21.6 & 11.2 & 5.4 & -9.3 & 4. \\ 15.9 & 45.5 & 11.9 & 2.7 & 16.4 & -4 \\ 21.7 & 36.9 & 23.7 & 5.3 & -5.3 & -5.4 \\ 0 & 3.71 & -4.4 & 3.2 & 0 & 0 \\ -3.9 & 0 & -12.7 & 5.9 & -10.4 & -2.1 \\ 0 & 0 & 7.1 & 0 & 0 & 1.0 \end{bmatrix} GPa$$

NVT, Individual:

Table 4.10: Molecular dynamics simulation parameters for MWCNT

System setup	Individual, 49.2 Å length
MD ensemble	NVT
Temperature	400 K
Thermostat	Berendsen
Barostat	Parrinello
Time step	1 femto second (fs)
Periodic boundary condition	ON
Energy Deviation	100 kcal/mol

- Single Wall armchair (5_5) Elastic Constants

$$C_{ij} = \begin{bmatrix} 878.9 & 17.3 & 19.1 & 0 & 0 & 0 \\ 19 & 59.2 & 40.5 & 0 & 0 & 0 \\ 19.1 & 42.8 & 61.9 & 0 & 0 & 0 \\ 0 & 0 & 0 & 2.6 & 0 & 0 \\ 0 & 0 & 0 & 0 & 1.7 & 0 \\ 0 & 0 & 0 & 0 & 0 & 9.4 \end{bmatrix} GPa$$

- Double Wall armchair (5_5,10_10) Elastic Constants

$$C_{ij} = \begin{bmatrix} 780.4 & 27 & 26.3 & 0 & 0 & 0 \\ 26.6 & 69 & 60.7 & 0 & 0 & 0 \\ 26.4 & 58 & 63.7 & 0 & 0 & 0 \\ 0 & 0 & 0 & .5 & 0 & 0 \\ 0 & 0 & 0 & 0 & -1.4 & 0 \\ 0 & 0 & 0 & 0 & 0 & 9.5 \end{bmatrix} GPa$$

- Triple Wall armchair (5_5, 10_10, 15_15) Elastic Constants

$$C_{ij} = \begin{bmatrix} 638.5 & 63.8 & 26.5 & 0 & 0 & 5.7 \\ 63.0 & 64.0 & 47.3 & 0 & 0 & 0 \\ 25.8 & 47.2 & 64.9 & 6.0 & 0 & 0 \\ 0 & 0 & 0 & 39.5 & 6.4 & 0 \\ 0 & 0 & 0 & 6.4 & 1.05 & 1.3 \\ 5.6 & 0 & 0 & 0 & 1.5 & 8.4 \end{bmatrix} Pa$$

- Four Wall armchair (5_5, 10_10, 15_15, 20_20) Elastic Constants

$$C_{ij} = \begin{bmatrix} 378 & 6.8 & 4.8 & 0 & 0 & 0 \\ 7.2 & 4 & 1.4 & 0 & 0 & 0 \\ 7.4 & 1.1 & 1.8 & 0 & 0 & 0 \\ 0 & 0 & 0 & 3.6 & 0 & 0 \\ 0 & 0 & 0 & 0 & 3.5 & 0 \\ 0 & 0 & 0 & 0 & 0 & .7 \end{bmatrix} GPa$$

- Five Wall armchair (5_5, 10_10, 15_15, 20_20, 25_25) Elastic Constants

$$C_{ij} = \begin{bmatrix} 378 & 6.8 & 4.8 & 0 & 0 & 0 \\ 7.2 & 4 & 1.4 & 0 & 0 & 0 \\ 7.4 & 1.1 & 1.8 & 0 & 0 & 0 \\ 0 & 0 & 0 & 3.6 & 0 & 0 \\ 0 & 0 & 0 & 0 & 3.5 & 0 \\ 0 & 0 & 0 & 0 & 0 & .7 \end{bmatrix} GPa$$

NVT, Sequential:

Table 4.11: Molecular dynamics simulation parameters for MWCNT

System setup	Sequential, 49.2 Å length
MD ensemble	NVT
Temperature	400 K
Thermostat	Berendsen
Barostat	Parrinello
Time step	1 femto second (fs)
Periodic boundary condition	ON
Energy Deviation	100 kcal/mol

- Double MWCNT:

$$C_{ij} = \begin{bmatrix} 890.5 & 4.3 & 4.2 & 0 & 0 & 0 \\ 4.3 & 7.3 & 4.5 & 0 & 0 & 0 \\ 4.2 & 4.5 & 7.7 & 0 & 0 & 0 \\ 0 & 0 & 0 & 10 & 0 & 0 \\ 0 & 0 & 0 & 0 & 9.5 & 0 \\ 0 & 0 & 0 & 0 & 0 & 1.3 \end{bmatrix} GPa$$

- Three MWCNT:

$$C_{ij} = \begin{bmatrix} 856.5 & 4 & 3 & 0 & 0 & 0 \\ 4 & 5.3 & 2.5 & 0 & 0 & 0 \\ 2.6 & 2.5 & 4.0 & 0 & 0 & 0 \\ 0 & 0 & 0 & 3.7 & 0 & 0 \\ 0 & 0 & 0 & 0 & 3.4 & 0 \\ 0 & 0 & 0 & 0 & 0 & 1.2 \end{bmatrix} GPa$$

ii- Simulation of Nylon6,6 Using Molecular dynamics approach:

Nylon-6,6 (PA66) is a semi crystalline polyamide that is commonly used as an engineering material in many fabric applications due to its good abrasion resistance and self-lubricating properties. The nylon 6,6, got its name because each repeated unit of the polymer chain has two stretches of carbon atoms, each being six carbon atoms long (see Figure 4.23). Other nylons can have different numbers of carbon atoms in these stretches.

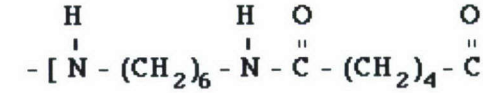

Figure 4.23: Chemical chain for Nylon6,6

Two basic reactions are used to synthesize polyamide engineering polymers (1) polycondensation of a dibasic acid and a diamine or (2) polymerization of an amino acid or lactam.

Generally, the polyamide analogs exhibit good chemical resistance and low moisture absorption at the expense of heat resistance, impact properties in wet environments, and stiffness. Water acts as a plasticizer in polyamides, reducing most mechanical and electrical properties while improving toughness and elongation. This problem, perhaps the major shortcoming of the nylons, is a function of the concentration of the amide groups. Water actually replaces the amide-amide hydrogen bonds with an amide-water hydrogen bond. It also provides very good mechanical and thermal properties in their dry-as-molded state. But, they are most susceptible to deterioration due to moisture absorption. They also provide many desirable properties to fulfill end-use requirements and account for the major share of the polyamide resins.

Glass transition (T_g), is the temperature at which the amorphous polymer is converted between rubbery and glassy states, it is considered the most important mechanical property for all polymers, that's because some physical properties undergo a drastic change under different glass transition temperature, such as hardness, Young's module, and volume. For simulation considerations, it was considered to be 348K.

Total energy of a molecular structure is calculated, using an analytical function which is the sum of a number of individual energy terms. At its simplest level this function includes, bond stretching, torsion, angle bending, and nonbonding interaction terms, which

determine the energetic penalty of the structure based upon deviations from the idealized equilibrium geometry. Since, terms of nonbonded energy interactions is a function of a distance which considers the energy between several atoms, according to equation 4.4, this will produce an mechanical properties effect on simulated systems. Choices of 9.5 Å and 6.5 Å were considered for both isochoric and isobaric ensembles.

Molecular dynamics simulations were used to predict the mechanical properties of nylon6,6 matrix. A single chain of twenty monomers connected repeatedly was built (Figure 4.24a). The total number of atoms for each chain was 382 with molecular weight of 2265 gram/mole. The chain was minimized using the conjugate gradient method. An amorphous periodic cubic lattice with lattice parameters a=b=c=33.3Å and $\alpha = \beta = 90°, \gamma = 90°$ (see Figure 4.14). Ten polymer chains with total number of 3820 atoms and final target density of 1.07 gm/cc (Figure 4.24.b) were constructed. A minimum potential position confirmation was adopted by conjugate gradient method. Each simulated amorphous cell was subjected to periodic boundary conditions in order to simulate the behavior bulk polymer.

Initially, minimized periodic cell was equilibrated after 100 pico seconds using either isochoric or isobaric thermodynamic controls at a rate of 1fs per time step. The system was heated to 400K which is beyond the glass transition of nylon6,6. This was followed by another thermodynamic step to cool each system back to room temperature at the same reaction rate.

Several systems were simulated in this research to study the joint effect of thermodynamic ensembles, heating, and nonbonded potential energy interaction cutoff point on obtained elastic constants.

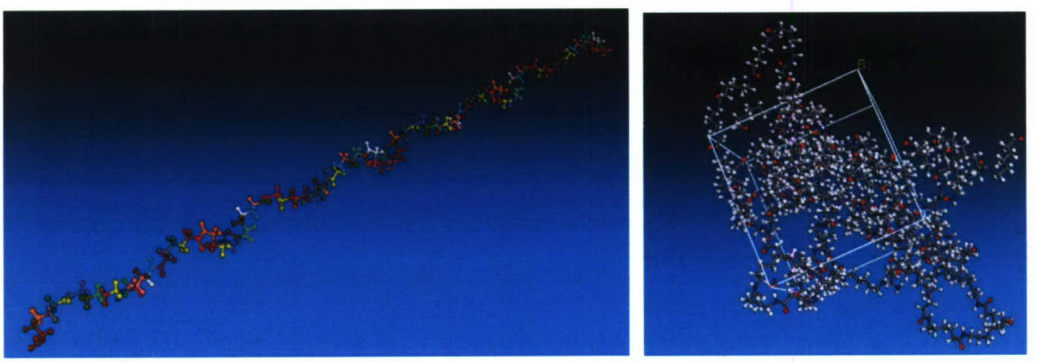

(a) (b)

Figure 4.24: MD simulation of (a) single, and (b) ten chains of nylon-6,6 polymer

Van der Waals interaction potential is relatively short range and dies out at a separation distance of 8-10 Å. Choosing how to treat long-range nonbond interactions is an important factor in determining the accuracy of energy evaluation. Our initial simulations resulted in higher mechanical properties compare to experimental ones. However, by adjusting the cutoff point more realistic values were obtained.

Default setup of cutoff points is 9.5 Å, so a 6.5 Å system was constructed to study the effect of nonbonded energy effect on mechanical properties table 4.12.

- NPT ensemble, 9.5 Å Elastic Constants

$$C_{ij} = \begin{bmatrix} 4.1 & 1.9 & 2.2 & 0 & 0 & 0 \\ 2.1 & 4.82 & 2.1 & 0 & 0 & 0 \\ 3 & 2.6 & 4.8 & 0 & 0 & 0 \\ 0 & 0 & 0 & 1 & 0 & 0 \\ 0 & 0 & 0 & 0 & 1.3 & 0 \\ 0 & 0 & 0 & 0 & 0 & 1.2 \end{bmatrix} GPa$$

- NPT ensemble, 6.5 Å Elastic Constants

$$C_{ij} = \begin{bmatrix} 3.6 & 1.5 & 1.6 & 0 & 0 & 0 \\ 1.5 & 3.8 & 1.6 & 0 & 0 & 0 \\ 1.4 & 1.6 & 3.5 & 0 & 0 & 0 \\ 0 & 0 & 0 & 0 & 1.1 & 0 \\ 0 & 0 & 0 & 0 & 1.1 & 0 \\ 0 & 0 & 0 & 0 & 0 & 1 \end{bmatrix} GPa$$

- NVT ensemble, 6.5 Å Elastic Constants

$$C_{ij} = \begin{bmatrix} 5.3 & 2.7 & 2.8 & 0 & 0 & 0 \\ 2.7 & 5.2 & 2. & 0 & 0 & 0 \\ 2.8 & 2.1 & 4.8 & 0 & 0 & 0 \\ 0 & 0 & 0 & 1.3 & 0 & 0 \\ 0 & 0 & 0 & 0 & 1.2 & 0 \\ 0 & 0 & 0 & 0 & 0 & 1.1 \end{bmatrix} GPa$$

Table 4.12 shows calculated Engineering Constants for the different simulation systems conditions considered.

Table 4.12: Nylon6,6 Engineering Constants.

Polymer Engineering Constants	NPT 9.5 Å	NPT 6.5 Å	NVT 6.5 Å
E_{11} (GPa)	**4.0**	**2.8**	**3.4**
Poisson ratio	**.24**	**.28**	**.37**
M_{23} (GPa)	**3.9**	**2.7**	**3.6**
K_{23} (GPa)	**1.25**	**1.1**	**1.6**

iii- Simulation of Multi Wall Carbon Nano tube Nylon 6,6 Composites Using Molecular dynamics approach:

Nylon 6,6 reinforced with different weight fractions of MWCNT (2.5%, 5%, 10%, and 20%) were simulated. Molecular modeling limitations such as time scale, dynamic time, number of atoms that can be simulated, and periodic unit cell size prevented predicting the effective weight fractions of nylon6,6 reinforced with MWCNT's for small weight fractions.

An infinite crystal of the MWCNT reinforced nylon-6,6 containing a given mass/volume fraction of the nanotube reinforcements was constructed using a cubic periodic unit cell of corresponding dimensions (see Table 4.13). A three wall CNT with individual setup chirality of (5_5, 10_10, and 15_15) was immersed in 20 monomers nylon6,6 chains of 382 atoms each. Unit cell lattices parameters *a, b* and *c* were aligned with the three coordinate axes *x, y* and *z* respectively with the nanotube longitudinal axis aligned with the z-axis (Figure 4.25). The atomic configuration of the cell corresponding to the cross-linked molecules of the nylon matrix and the MWCNT were generated using the following procedure:

a. A single molecule of the nylon was first constructed using the Visualizer [4.23] program from Accelrys, Figure 4.24.a
b. Next, the molecule generated in (a) was duplicated several times depending on the weight fraction of interest, Figure 4.24.b.
c. The nylon-6,6 molecules generated in (b) were used as fragments within the Amorphous Cell program from Accelrys [4.23] to generate a cubic computational cell

of a given size containing the nylon6,6 polymer chains of a specified density according to equation(4.9).

d. The atomic configuration corresponding to the MWCNT was then constructed using the procedure described earlier;

e. Segments of the molecules generated in (c) were, next, translated and rotated in order to create an amorphous cell with different configurations to insert the MWCNT at the center of plane xy as shown in Figure 4.25.

f. The atomic configuration obtained in (e) was subjected to a series of energy minimization and dynamic relaxations under NPT condition starting with a dynamic time of 20 pico second at a rate of 1 femto second per time step. The temperature was raised from room temperature to *400K* (beyond the glass transition temperature of nylon 6,6) then cooled down to room temperature.

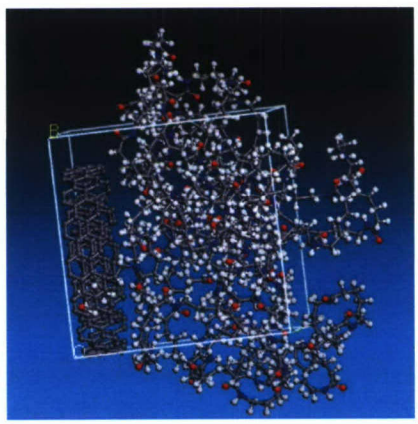

Figure. 4.25: MD simulation of nylon 6,6 reinforced with MWCNT.

Table 4.13: Composite Simulated Unit Cell

Weight Fractions	Unit Cell size $(Å)^3$	Number of Nylon6,6 chains	Number of Nylon6,6 atoms	Number of composite atoms
2.5%	$(38)^3$	14	5348	5468
5%	$(38)^3$	14	5348	5588
10%	$(33.5)^3$	10	3820	4060
20%	$(32)^3$	8	3056	3536

The unit cell volume was calculated according to the required weight percent of reinforcement according to the following relations.

$$w\ \% = \frac{w_r}{w_c}$$

$$w_t = w_r + w_m \tag{4.61}$$

$$w_r = \rho_r * v_r$$

$$w_m = \rho_m * v_m$$

where w is the weight, ρ is the density, v is the volume and *r refers to* reinforcement , *c* refers to composite and *m* refers to matrix.

Plot of nylon6,6 cubic unit cell volume versus number of chains, density,1.0 g/cm^3 Fig 4.26.

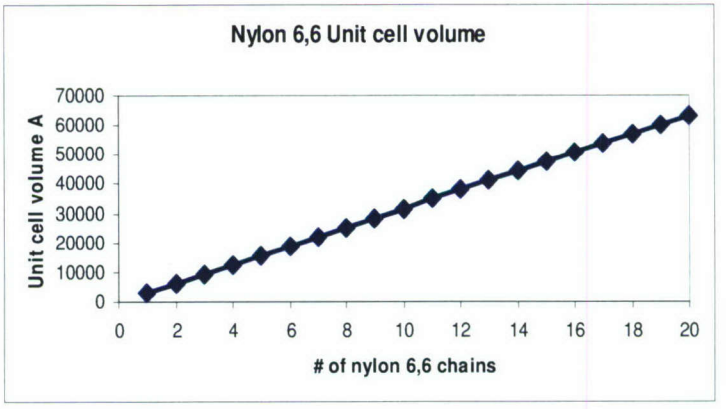

Figure 4.26: Number of polymer chains versus unit cell volume in Å^3.

Modeling MWCNT composites is dependent of the local load transfer along the longitudinal direction of the CNT. Since the minimum unit cell size for a three MWCNT of (5_5, 10_10, 15_15) chirality is 20 Å super cells, a large number of chains required to construct the periodic composite unit cell. The required unit cells for accurate calculations of elastic constants are summarized in Table 4.14.

Table 4.14: Recommended unit cell dimensions

Weight Fractions	Unit Cell size $(Å)^3$	Number of Nylon6,6 chains	Number of Nylon6,6 atoms	Number of composite atoms
1.25%	1122615	299	114218	114338
2.5%	554203	148	56536	56656
5%	269996	72	27504	27624
10%	127899	35	13370	13490
20%	56842	16	6112	6232

For the twenty percent weight fraction reinforcement, two unit cell sizes were considered for same thermodynamic and construction conditions. The first was constructed using 1768 atoms and a unit cell size of $(22.24)^3$ Å (Figure 4.27a). The second one was constructed using 3536 atoms and unit cell dimensions of Table 4.13. (Fig 4.27b).

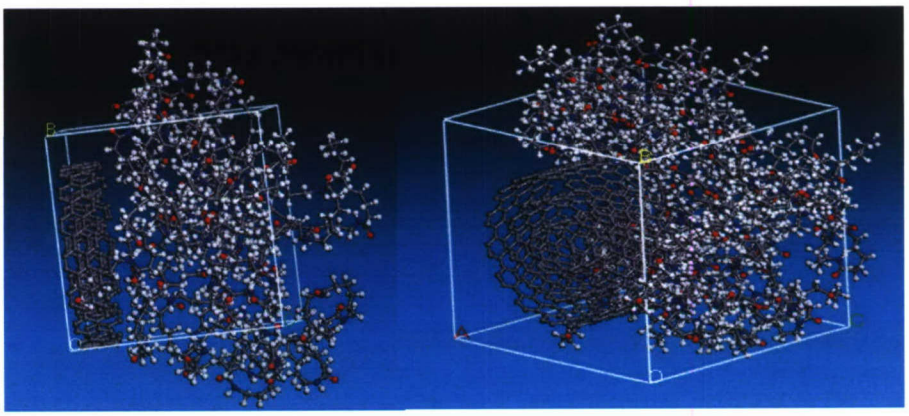

(a) (b)

Figure 4.27: Simulated 20% reinforced nanocomposite with (a) two super cell fiber and (b) four supercell fiber

The results of simulations for both unit cells are summarized in table 4.15. The large difference in engineering constants is due to the size of the simulated unit cell and the associated potential energy.

Figure 4.28 shows two images for a 20% unit cell with a total number of atoms 3565 after energy minimization. It is obvious that the MWCNT is being deformed, misaligned and pulled under the effect of the van der Waal forces. Also, the layers of the MWCNT are

misaligned. The simulated length is not enough to develop full load transfer between the CNT and its surrounding polymer chains.

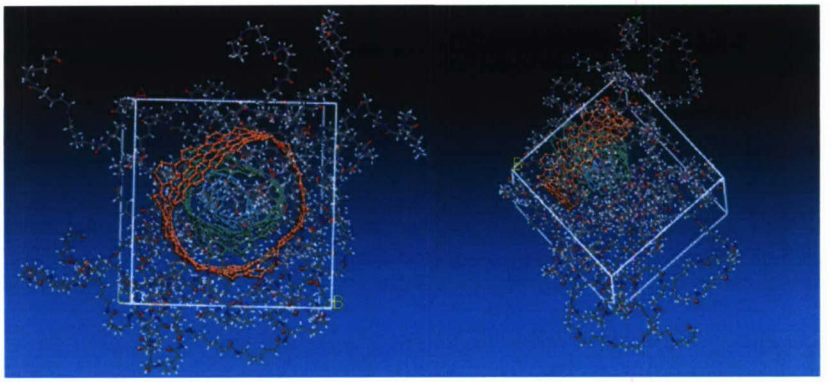

Figure 4.28: Unit cell of nylon 6,6 reinforced with 20% wt fraction MWCNT after energy minimization.

Table 4.15: Effect of Unit cell size on engineering constants of nylon 6,6 reinforced with 20% weight fraction of MWCNT.

Composite Engineering Constants	20% 1768 atoms/cell	20% 3536 atoms/cell
Tensile (GPa)	71.06	42.72
Poisson's Ratio	.58	.15
Bulk (GPa)	139.5	20.22
Shear (GPa)	22.42	18.6
Lame Const. Lamda	154.5	7.81
Lame Const. mu	22.42	18.6

Table 4.16 summarized the results obtained for engineering constants of nylon 6,6-MWCNT composites with different wt fractions using MD simulations.

Table 4.16: Nylon6,6 MWCNT composite Engineering Constants.

Composite Engineering Constants	2.5%	5%	10%	20%
E_{11} GPa	1.7	5.5	13.6	73.5
E_{22} GPa	.9	5.0	9.6	40.6
Possion ratio	.6	.32	.31	.5
Bulk Modulus GPa	1.4	5.3	10.5	18
Shear Modulus GPa	.33	1.8	6.3	8.6

For the case of 2.5 % wt fraction, the obtained results are surprisingly smaller than those of un-reinforced nylon 6,6. However, by examining Figure 4.29 which shows total deformation of the MWCNT through the unit cell for the case of nylon 6,6 reinforced with 2.5 wt fraction of MWCNT, one observes excessive deformation of the CNT. The large deformation is due to the van der Waal forces between the carbon atoms in the MWCNT and the carbon atoms in the polymer it self. Table 4.17 which shows the maximum van der Waal radius for carbon atoms to be 1.548 Å. Since the length of the MWCNT simulated is less than the van der Waal radius for carbon atoms, the obtained results in our MD simulations are smaller than experimental ones.

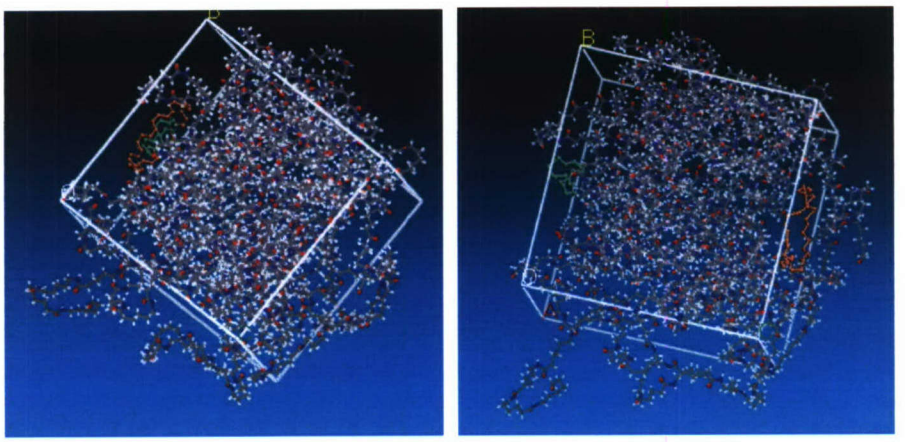

A) Before b) After

Figure 4.29: 2.5% composite a) Before minimization. b) After minimization.

Table 4.17: Van der Waal Radius

Atom	Van der Waals Radius (Å)
H	1.1
C	1.548
N	1.4
O	1.348

4.4 Conclusions:

- Mechanical properties of MWCNTs are sensitive to used cell size. Simulating a molecular cell smaller than the periodic super cell, will result in inaccurate mechanical properties. As demonstrated in Table 4.7.
- Temperature effect on MWCNT can be neglected. MD simulations show that temperature has negligible effect on MWCNT stiffness.
- Number of layers of a MWCNT is a big challenge. Increasing the number of layers increases the required minimum number of atoms simulated for each periodic unit cell. For example a periodic unit cell for a three wall carbon nanotube, requires an eight super unit cells with 960 atoms whereas for a four wall carbon nanotube, a periodic unit cell requires thirty super cells with 6000 atoms.
- From Figure 4.19. It is shown that longitudinal engineering constants tend to be constant after the three MWCNT.
- MWCNT build setup, either individual or sequential did not affect the elastic constants. Minimum separation distance was kept constant 3.347 Å for the sequential setup.
- MWCNT equilibrated periodic unit cells are not affected by thermodynamic ensemble used to control dynamic loading.
- Thermostat and Barostat algorithms are one of the critical coupling effects on obtained mechanical properties of MWCNT. It is very important to choose the right combined algorithms. NVT thermodynamic is recommended to be combined with an Anderson thermostat algorithm. And for NPT thermodynamic ensemble, it is recommended to use the Berendsen barostat, coupled with Parrinello thermostat.

- Results obtained from various types of loadings applied to SWCNT show that SWCNTs are transversely isotropic. Thus, SWCNT behaves as a linear elastic material.
- The simulation of various SWCNT clusters establishes the fact that hexagonal closed packing is the most favored packing scheme for a bunch of SWCNTs forming nano-ropes.
- SWCNTs and MWCNTs lose their circularity when a polymer chain is placed in their vicinity. This shows that their transverse properties are comparatively poor.
- The interface is an important constituent of CNT-polymer composites, which has been modeled in the present research with reasonable success.

5.0 ACOUSTIC IMPEDANCE OF NANOPARTICLE-ENHANCED PLASTICS AND ECO-CORE FOAMS

5.1 Objective

This report summarizes the application of Brüel & Kjær (B & K) Standing Wave Apparatus, Type 4002 for acoustic absorption coefficient of nano-reinforced and structural foam samples. Measurements were preformed to investigate the effect on acoustic properties, by the addition of multi-wall carbon nanotube (MWCNT) particles to nylon 6,6 matrices. Measurements were also performed on various Eco-Core foams supplied by North Carolina A&T state university. Specifically, the variation of acoustic sound absorption coefficient and acoustic impedance was observed.

5.2 Overview of the single microphone impedance tube theory

When normal acoustic plane waves are incident upon a surface, a portion of the sound wave is reflected. The remaining wave is absorbed and thermally dissipated within the material or propagates through the material. The acoustic absorption coefficient, α, is a dimensionless quantitive measure of a given material's ability to absorb acoustic energy and is defined by:

$$\alpha = 1 - r^2 = 1 - \left(\frac{B}{A}\right)^2$$

A = pressure amplitude of the incident sound wave

B = pressure amplitude of the reflected sound wave

Values of α range from 0 to 1; 1 being a perfect absorber, 0 being a perfect reflector and having no absorptive properties. Nominal published values for α range from 0.9 – 0.02.

The individual amplitudes cannot be measured directly, however another measurable quantity is useful in determining the constructive and destructive interference of the incident and reflected wave. This quantity is called the standing wave ratio, (SWR) or n, and is defined by [5.1]:

$$SWR = n = \frac{A + B}{A - B} = \frac{p_{\max}}{p_{\min}}$$

When the impedance tube is terminated at the open end by a material sample and the tube is excited by a sound source at a single frequency, a standing wave pattern develops within the tube. The maximum and minimum pressure amplitudes can be measured down the length of the impedance tube with a probe microphone that is placed in proximity of the tube diameter geometric center.

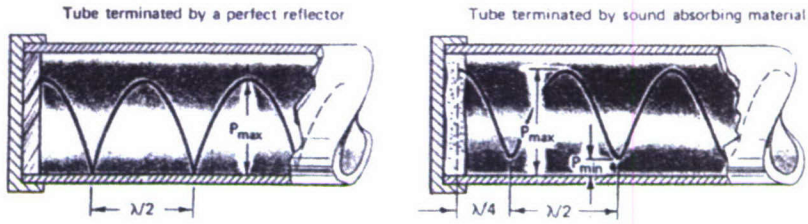

Figure 5.2.1: Representation of a standing wave in the impedance tube [5.1]

Figure 5.2.1 shows the pressure variation with a perfect reflector and an absorbing material. The distance between the maximum and minimum is a ¼ wavelength, $\lambda / 4$, where the wavelength

$$\lambda = c / f$$

c = speed of sound, m/s

f = frequency, Hz

The distance between maximum peaks is $\lambda / 2$, as is the distance between the minimum troughs.

To calculate the acoustic impedance, information about the phase angle between the incident and reflected plane wave is required. The phase angle can be determined by measuring the first and second pressure minimum from the sample, x_1 and x_2 respectively.

The phase angle, Δ is defined by:

$$\Delta = \left(\frac{2(x_1)}{x_2 - x_1} - 1 \right) \pi$$

x_1 = the first minimum pressure point from the sample

x_2 = the second minimum pressure point from the sample

The real and imaginary components of impedance, Re and Im, respectively are given by:

$$\mathrm{Re} = \left(\frac{1 - r^2}{1 + r^2 - 2r\cos\Delta} \right)$$

$$\mathrm{Im} = \left(\frac{2r\sin\Delta}{1 + r^2 - 2r\cos\Delta} \right)$$

So, impedance can be expressed as

$$Z = (\mathrm{Re} + i\mathrm{Im})\rho c$$

Where ρ, is the density of air and, c, is the speed of sound in air.

As previously stated, values of α range from 0 to 1. One being a perfect absorber and zero having no absorptive properties, i.e. a perfect reflector. Most common construction materials have values that range from 0.02-0.90. Acoustic absorption coefficient and impedance are used in calculating sound pressure attenuation when an incident wave is transmitted from one medium to another medium. Acoustic impedance is analogous to electrical impedance and is a function of frequency.

5.3 Assembling and testing the impedance tube

Prior to any testing being conducted with the impedance tube, it had to be assembled and verified that it operated properly. The B&K Type 4002 was supplied with two impedance tubes; a longer length, larger diameter tube for a measurement range of 90 – 1800 Hz and a shorter length, smaller diameter tube for a measurement range of 800 – 6500 Hz. It was not assembled, nor had it been used for several years. The last time it was used, there was mention of a significant amount of distortion present in the observed signals.

Once the unit was relocated to my lab, a swept sine tone was input to the speaker. It was obvious from the noise, that something was loose. The speaker enclosure was opened and all fasteners were tightened. Two of the speaker retaining screws were loose and the speaker was not securely held to the enclosure. The swept sine signal was run again into the speaker, and the rattling sound was not present.

Figure 5.3.1 is a plot of the frequency response of the apparatus speaker using a ½" B&K microphone approximately one inch from the speaker cone. Although it is not a very

"flat" response, the speaker was functioning. There was also not any visible damage and the speaker coil did not rub on the magnet.

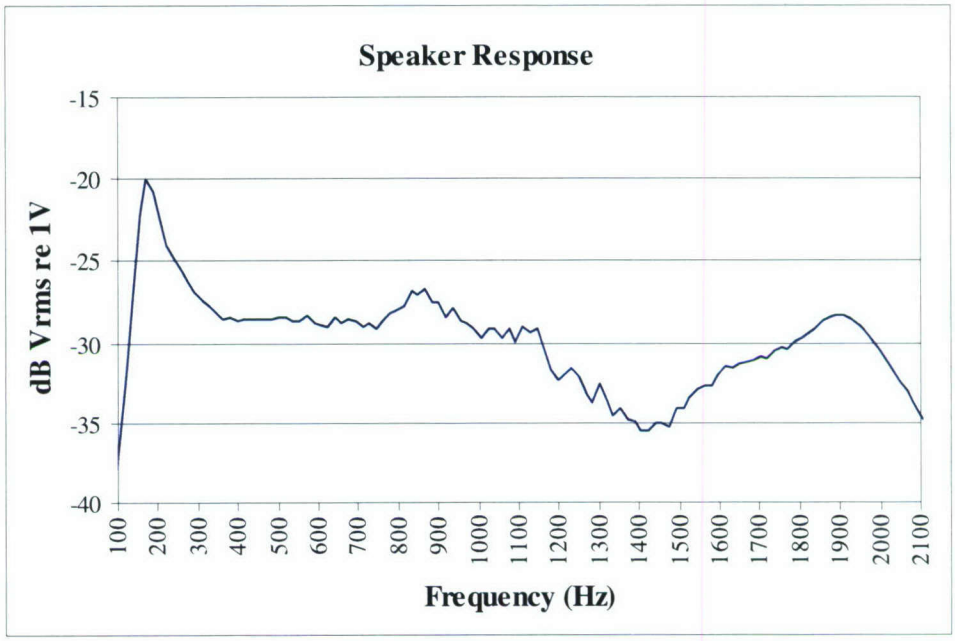

Figure 5.3.1: Frequency response of speaker.

Next, the frequency response of the probe microphone was measured using a B&K multi-function calibrator. This calibrator emits a variable frequency signal at a constant sound pressure level (SPL) of 94 dB. Figure 5.3.2 is a plot of the response of the microphone.

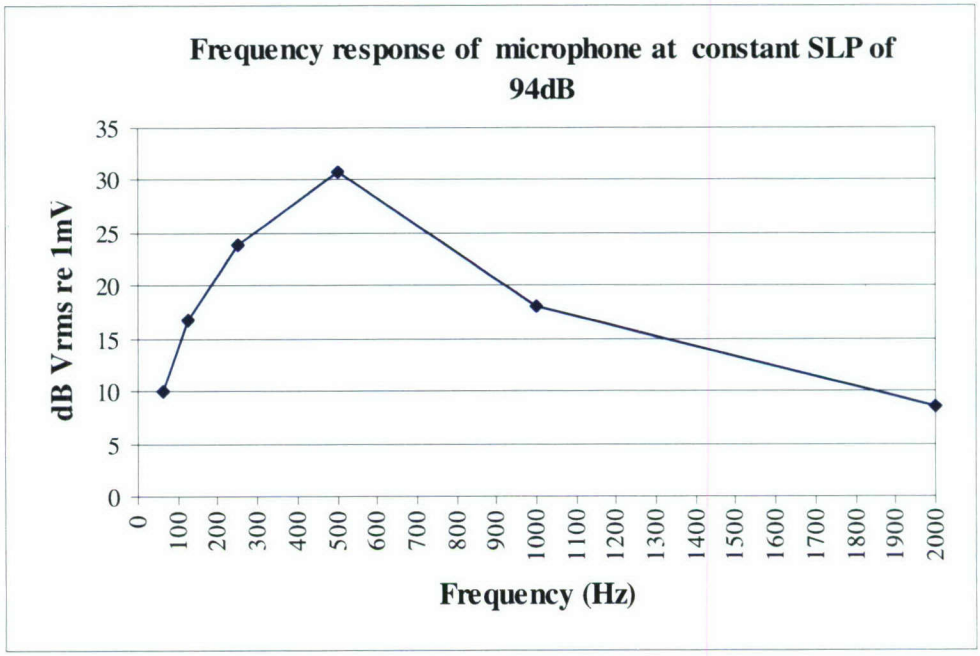

Figure 5.3.2: Frequency response of probe microphone.

The response of the microphone should be relatively flat for a laboratory instrument and the measured sensitivity was less than half of the rated sensitivity. So the microphone car was disassembled and was inspected to insure that all electrical and mechanical connections were good.

Despite the microphone sensitivity being approximately half of the value stated in the Type 4002 manual, the microphone was determined to be adequate for testing purposes. The measurements being made are relative to each other for a given frequency; therefore any variation in the output is due to the pressure amplitude fluctuation and not the frequency response of the microphone or speaker.

None of the original electronics and instruments for impedance tube measurements was with the unit, nor could they be found, so equipment was used that was more current. The original equipment was analog whereas the equipment used in this setup was digital based with the exception of the Tektronix oscilloscope.

5.4 Materials/Equipment

A list of the equipment used in setting up and taking measurements with the impedance tube is shown below.

Brüel & Kjær Standing Wave Apparatus, Type 4002
Stanford Research Systems Programmable Filter, SR650
Tektronix Oscilloscope, 2445A
Agilent Dynamic Signal Analyzer, 35670A
Brüel & Kjær Multi-Function Calibrator, Type 4226
Brüel & Kjær Calibrator, Type 4231
Stewart, World 600R Power Amplifier
Miscellaneous cables and connectors

Figure 5.4.1 shows a block diagram of the setup and Figure 5.4.2 is a picture of the assembled unit with some of the composite samples.

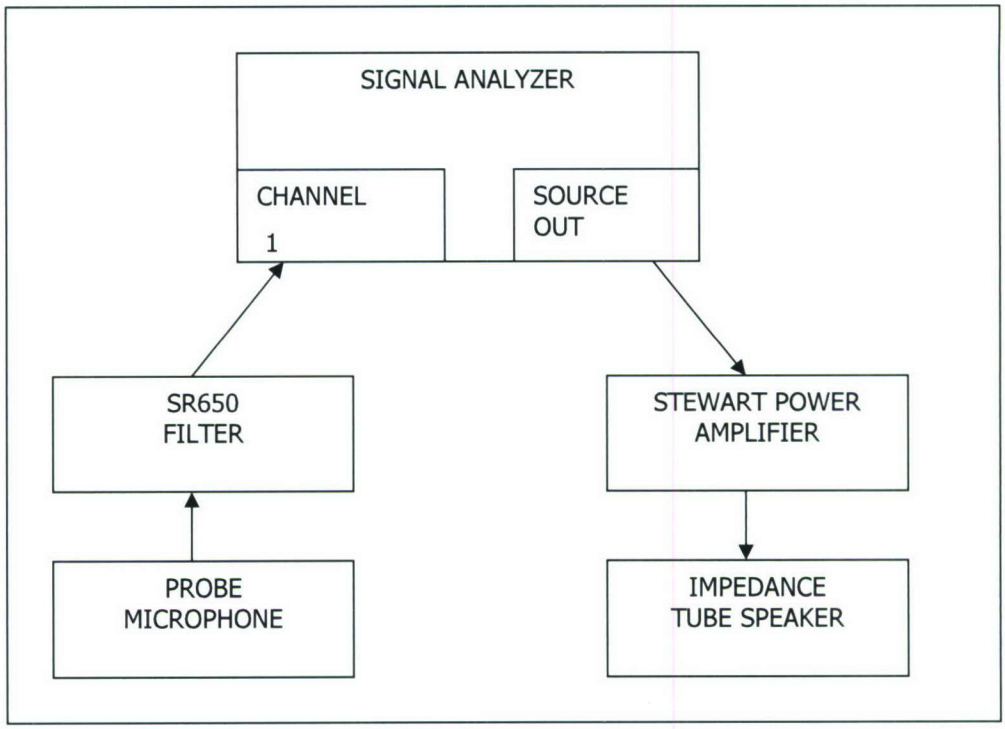

Figure 5.4.1: Block diagram of the impedance tube setup.

Figure 5.4.2: A picture of the impedance tube setup.

5.5 Sample preparation

Creating an air tight seal at the sample end of the impedance tube is critical. The presence of air gaps will erroneously influence the absorption values. For hard rigid materials or hard faced materials; metals, composites, wood, etc. it is crucial that the sample be machined to fit tightly in the sample holder in order to minimize air gaps between the sample and the sample holder. For porous materials such as fiberglass insulation, foam and acoustical ceiling tile, the fit was not as crucial, but still important to keep the sample rigidly secured in the holder. Porous material should be cut such that the sample outside diameter fits the inside diameter of the holder. Materials with a hard face should be cut such that the hard face fits the outside diameter of the holder and the backing fits the internal diameter of the holder. Figure 5.5.1(a) and (b), from the 4002 manual depicts how, depending on the material type, the sample should be placed and secured in the holder.

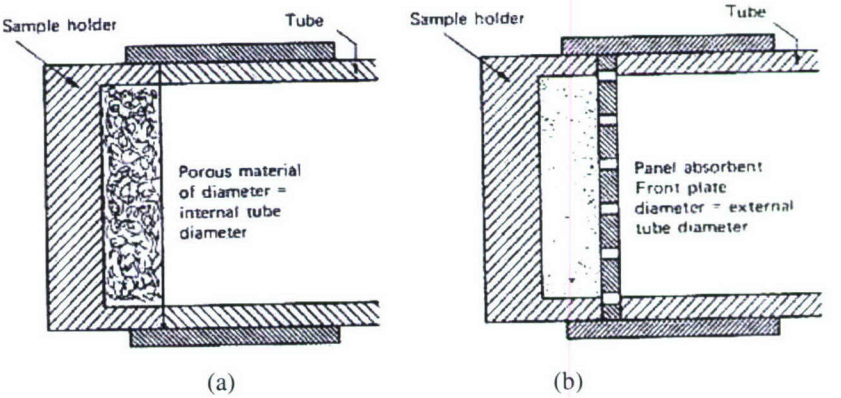

Figure 5.5.1: Mounting of material in the sample holder [5.1]
(a) Porous material
(b) Hard faced porous material

With these guidelines, it was decided that since the composite samples are hard faced, that they would be made to fit the outside diameter of the holder. Mounting the sample in this manner, it would be securely held between the end of the impedance tube and the sample holder once the clamping fixture was tightened. Machining tolerance of the sample's outside diameter could be relaxed, since the fit and seal no longer was dependent on the diameters of the sample and the impedance tube matching. Provided that the samples have a smooth surface finish, an airtight seal is obtained when sufficient axial force is applied with the clamping fixture.

Figure 5.5.2 is a plot comparing absorption coefficients between four samples that were prepared differently; filed to fit and machined to fit the inside and outside of the sample holder. Samples are 6061-T6 aluminum discs cut from a .313 inch thick plate on a band saw.

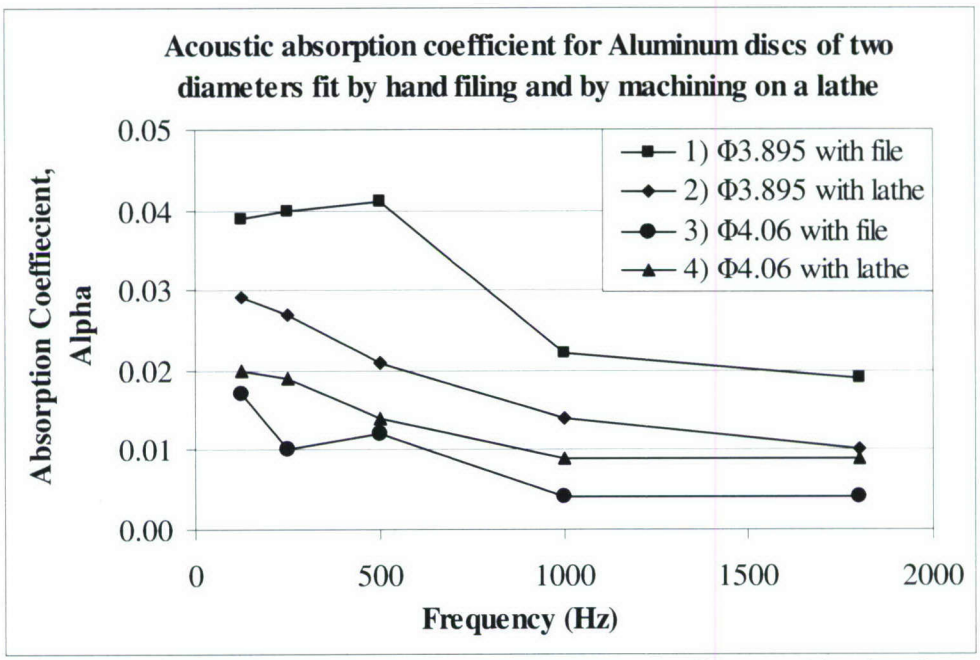

Figure 5.5.2: Absorption coefficients of aluminum discs machined to fit with a hand file and with a lathe.

Aluminum was primarily selected because it was readily available. A coarse file was used to remove material from Sample 1 until the specimen fit inside the sample holder. There were some air gaps between the sample and the holder, but very minimal. Sample 2 was machined down to size on a lathe for a slight press fit to the inside diameter of the sample holder. The diameters of Samples 3 and 4 were machined to match the outside diameter of the holder. Sample 3 was machined to fit by using a coarse hand file. Sample 4 was machined on a lathe to fit the outside diameter of the sample holder.

Tolerances required for machining to fit the outside diameter do not need to be as precise as samples machined to fit the inside of the sample holder. By observing Figure 7, samples that fit the outside diameter of the holder produced slightly smaller absorption coefficients than the samples that were mounted on the inside of the holder. These reduced values are due to the small but significant air gap between the sample and holder. It was

concluded from these results that the composite samples be machined to fit the outside diameter of the holder. When prepared in this manner, the sample thickness must not exceed 0.4 inch or the sample holder will not properly attach to the end of the impedance tube. Unless otherwise noted, all samples were machined to the following dimensions (inch): ϕ4.06 +0.0/–0.03, .375± .025 thick.

5.6 Acoustic absorption coefficient and impedance measurements procedure

In addition to the 4002 Instruction Manual [5.1], ASTM C384-04 Standard Test Method for Impedance and Absorption of Acoustic Materials by Impedance Tube Method [5.2] and ANSI S1.6 Preferred Frequencies and Band Numbers for Acoustical Measurements [5.3] was followed. One deviation from the ANSI standard was the frequency band. Standards and published data listed measurements at 125, 250, 500, 1000, 2000 and 4000 Hz. However, in this investigation absorption and impedance values were determined for 125, 250, 500, 1000 and 1800 Hz. Taking readings at 2000 and 4000 Hz would require the shorter, smaller impedance tube and the appropriate samples. Since there was not enough material for multiple samples, data for 4000 Hz was omitted and data at 1800 Hz was recorded instead of 2000 Hz.

After the sample was secured at the end of the tube, the microphone probe tube had to be adjusted to zero the vernier scale. This was done by placing an electrically conductive sample in the fixture and connecting a continuity meter to the probe tube and the sample holder. When the microphone car was rolled close to the speaker enclosure, the probe tube contacted the sample surface and continuity was measured. The probe tube was screwed in or out until the vernier scale on the microphone car was aligned with zero.

The signal analyzer's source output was connected to the Stewart's power amplifier and fed into the speaker [Figure 5.4.1]. For each frequency of interest, the standing wave maximum and minimum amplitude nearest the sample was measured with the probe microphone along the length of the impedance tube. The output was filtered, and then measured with the signal analyzer while simultaneously being observed with the oscilloscope. The oscilloscope was primarily used for visually detecting maximum and minimum amplitudes. Once a peak or trough was located, the distance was recorded and the signal analyzer took an average of three measurements then displayed the Vrms result.

To measure the absorption coefficient, data is needed only for p_{max} , p_{min}. To measure the impedance, p_{max}, p_{min}, x_1, and x_2 need to be recorded. Since the probe is in position x_1 when measuring p_{min}, it was only a matter of locating the second pressure minimum, x_2 and impedance could be calculated. So, data was recorded for impedance to be calculated if later desired.

5.7 Acoustic absorption coefficient results

Prior to testing the plastics and the nano-reinforced samples, considerable testing was conducted on materials that have known absorption values. This was done to ascertain that the impedance tube was operating properly and to become familiar with the theory and measurement with the impedance tube.

The preliminary measurements yielded results that were in agreement with published data [5.4]. It should be noted that the majority of published data for α was obtained with the reverberation room method and are designated by the Sabine coefficient. The Sabine Coefficient values are slightly higher than those of the impedance tube method. The impedance tube measures normal incident plane waves, whereas the reverberation room measures absorption over a random wide range of incidence angles. Values of absorption are compared with values from the Encyclopedia of Acoustics [5.4] & included in the Appendix.

The absorption of four materials that were tested are plotted in Figure 5.7.1.

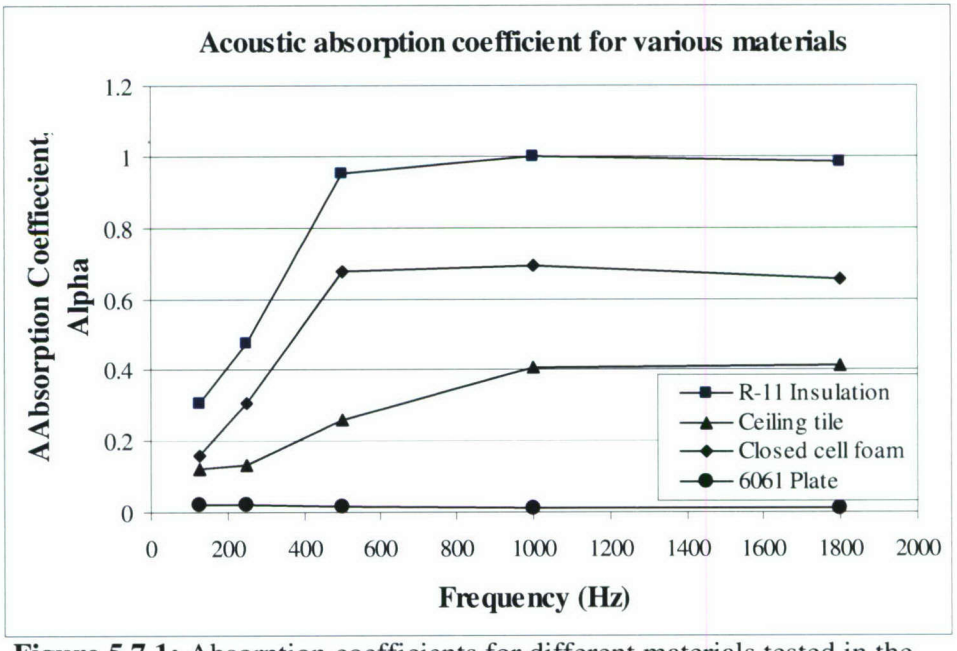

Figure 5.7.1: Absorption coefficients for different materials tested in the 4002 impedance tube.

These materials are: R-11 fiberglass insulation, Armstrong 755 acoustic ceiling tile, 2" thick closed cell foam and .313 inch thick 6061-T6 aluminum. Note that the aluminum sample has very low absorption values ranging from 0.01-0.02 depending on frequency. It will be subsequently compared to the values for the nano-composite material, as they appear to be similar.

5.7.1 Nylon 6,6 Test Results

The nylon 6,6 matrix material varied with the addition of MWCNT in the amounts of 0,1.25, 2.5, 5 and 10% by wt. Two samples were tested for each mixture, the results averaged, then plotted in Figure 5.7.2. By observing the plot, the variation of the absorption coefficient values was minimal and also produced values that approach those of the highly reflective aluminum. Absorption for the 2.5% samples did increase slightly, but this is likely caused by surface irregularities of the matrix sample itself rather than addition of the MWCNT. The irregularities consisted of parallel hair-line cracks whose length spanned the width of the sample and spaced approximately 3mm apart. The remaining samples in the nylon group did not possess these irregularities and produced absorption values that also approached those of the aluminum sample.

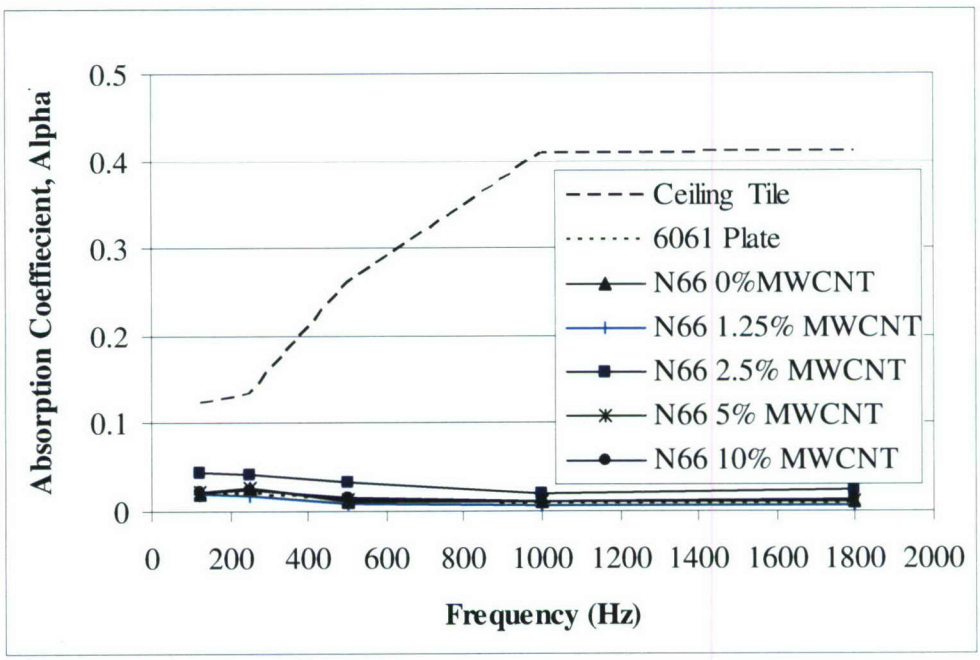

Figure 5.7.2: Absorption coefficients for nylon 6,6 with the addition of 0, 1.25, 2.5, 5 and 10% by wt of MWCNT.

5.7.2 Eco-Core Foam Test Results

The Center for Composite Materials Research (CCMR), North Carolina A&T State University provided Eco-Core Foam samples designated as OM7, OM8, OM11, OM12, OM16, OM18, OM19 and OM21 that were tested for acoustic absorption. These samples were prepared from flyash with phenolic resin but without any fibers added. To prepare the OM7 and OM8 samples for the sample holder, the thickness had to be machined in addition to machining the diameter to match the impedance tube. The plates from which the samples were machined were received in 1.96 cm thick blanks and cut to .953 cm thick samples by using slitting saw. When the sample was placed in the impedance tube for testing, the un-machined surface was oriented such that it was exposed to the incident pressure wave and not the machined surface. Figure 5.7.3a shows a plot of α for the OM7 & OM8 material. Although this material exhibits somewhat more absorption at the higher test frequencies, in general it is rather reflective.

The plates for OM11 & OM12 were manufactured to the nominal thickness, thus the samples were only machined to the nominal diameter. Another difference in this material was the presence of glazing on the material surfaces. The coating non-uniformly covered the surface, and excessive accumulation was observed on about 50% of the surface area on both sides of the sample. As expected, the glazing decreased the acoustic absorption, reducing the values nearly to those of the aluminum sample. Figure 5.7.3b shows a plot of α for OM11, 12, 16, 18, 19 and OM21 compared to ceiling tile and aluminum sheet.

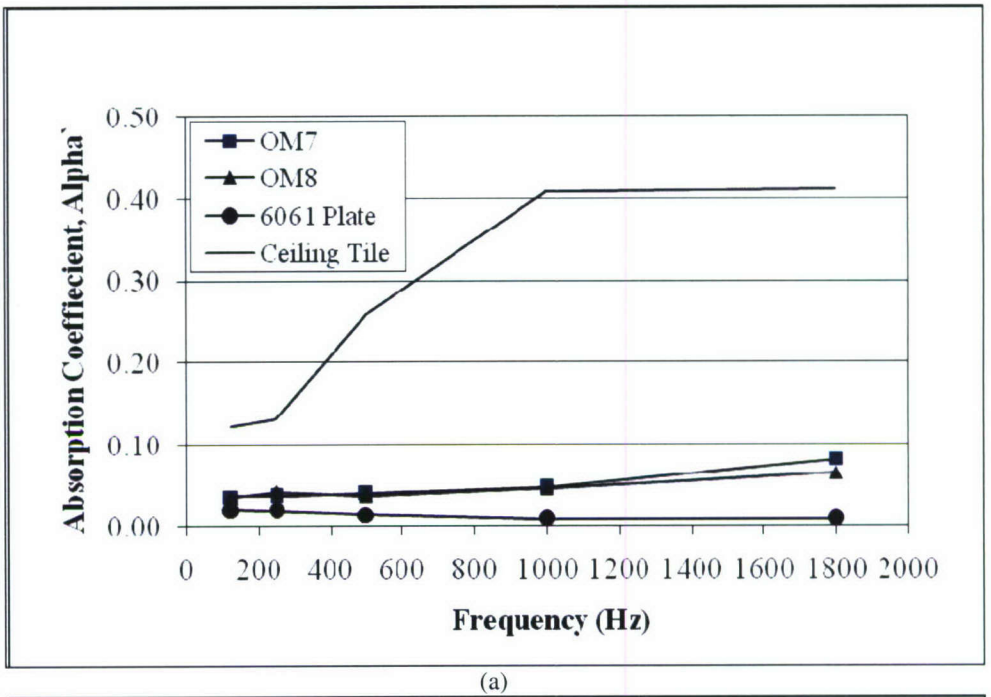

(a)

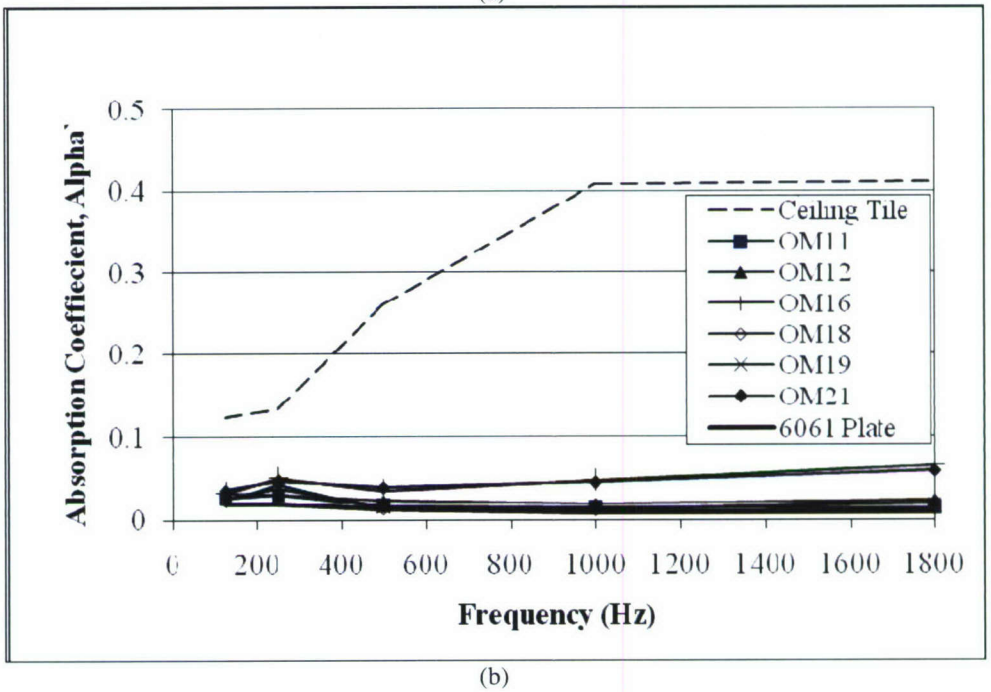

(b)

Figure 5.7.3: Absorption coefficients for Eco-Core Foam samples prepared from fly ash with phenolic resin.

5.8 Acoustic Impedance Results

At the onset of this project, only values of α were desired. As the project progressed, it was realized that information about acoustic impedance, Z, could be obtained with measurement of two more data points, x_1 and x_2. Values of acoustic impedance for materials are listed and compared in Fundamentals of Acoustics [5.5]. One of the materials listed is aluminum and since aluminum samples had already been used in the initial setup for absorption measurements, these samples were again used for measuring acoustic impedance.

Just as the impedance tube has limitations on measuring absorption coefficients, it also has limitations on measuring acoustic impedance. It was determined that materials that are highly reflective (poor absorbers) are well out of range for the impedance tube. Published values for $Z_{ALUMINUM} = 13x10^6$ kg/m^2 s. However measured values are near $10x10^4$ kg/m^2 s, off by two orders of magnitude. Initially it was believed to be a measurement error. So it was measured several more times with similar results. After much deliberation, it was concluded that the error is due to the large contrast between $Z_{ALUMINUM}$ and Z_{AIR}, $13x10^6$ kg/m^2 s and 415 kg/m^2 s respectively. To measure Z for materials that have a high impedance, essentially the speed of sound in the material is measured and multiplied by its density, $Z = \rho c$. Measurement of ρc in this manner is beyond the scope of this project.

5.9 Conclusions

Thus far, it is concluded that the, nylon 6,6 and Eco-Core foam samples tested can be considered poor acoustic absorbers and high acoustic reflectors. Variation of the MWCNTs to the nylon 6/6 had little effect and approached absorption coefficients to those of the aluminum samples. In general, the nanotubes do not significantly increase the porosity of the tested materials which in turn would effect the acoustic absorption.

6.0 HIGH STRAIN RATE COMPRESSION TESTING (Tested by Dr. David Hui, University of New Orleans)

6.1 Abstract

This paper discusses the experimental stress-strain characteristics, failure strength, and energy absorption in the dynamic impact of eight nanocomposite samples fabricated at the University of Mississippi, University, MS using various percentages of multiwalled carbon nanotubes (MWCNT). The effects of the percentage of MWCNT on the strength, stiffness, and energy absorption are discussed.

6.2 Introduction

Multi-walled carbon nanotube (MWCNT) in a polymer is believed to modify the energy absorbing characteristics of the resulting polymer composite. This paper discusses the stress-strain behavior, failure strength, and energy absorption in the dynamic impact of eight nanocomposite samples fabricated by Prof. R. Mantena of the University of Mississippi, University, MS., using various percentages of MWCNT in various formulations. The composites were fabricated as plates and later cut and supplied for tests as 5" x 0.45" x 0.39" bar pieces for high strain rate testing.

6.3 Test description

The nanocomposite samples that were used in the high strain rate testing are given in Table 6.3.1. Each sample was further cut to an approximate length of 0.5 in, edges polished and then used for Hopkinson bar tests. Three specimens were made from each bar sample, and in all 24 Hopkinson bar tests were performed.

The setup used in the current study consists of striker, incident, transmission bars, and the incident tube made of 1045 maraging steel. The diameter of striker, incident and transmission bars is 38 mm. The length of striker bar is 22.86 cm (9"), while that of incident and transmission bars is each 1.524 m (60"). The Specimen was sandwiched between the incident bar and the transmission bar. Petroleum jelly is applied at surfaces of the specimen in contact with the bars to reduce the effect of friction. A pressure setting of 30 psi was used through the testing. In using the Split Hopkinson Pressure Bar, strain gage transducers

mounted on the incident and the transmission bars at a distance of 76.2 cm (30") from the specimen are used as signal monitors.

Table 6.3.1: MWCNT composites used in tests

Sample code No.	Percentage of MWCNT	Remarks
DNM00AH	0.00	Pure Nylon 6
DNM00CH	0.00	
DNM25AH	2.5	
DNM25CH	2.5	
DNM50AH	5.0	
DNM50CH	5.0	
DNM10AH	10.0	
DNM10CH	10.0	

6.4 Data Analysis

The transient strain history is recorded from the strain gages mounted on the incident and the transmission bars. Two gages are mounted diametrically opposite to each other on each bar to record any bending strains. The data is acquired using a high-speed data acquisition card with Gagescope V2.92 software at a sampling rate of 2MHz. The stress-strain relation is developed based on one dimensional elastic bar-wave theory for a pulse propagating in a uniform bar, which is initially unstrained and at rest before the pulse arrives. The dynamic stress-strain is calculated as follows:

If ε_i, ε_r, ε_t, are respectively the incident, reflected and transmitted pulses and subscript 1 and 2 are the two ends of the specimen, the displacements at the ends of the specimen are given by

$$u_1 = \int_0^t C_0 \varepsilon_1 dt \tag{6.1}$$

$$u_2 = \int_0^t C_0 \varepsilon_2 dt \tag{6.2}$$

Where, C_0 is the wave velocity in the Hopkinson bars. In terms of the incident, reflected and transmitted pulses,

$$u_1 = C_0 \int_0^t (\varepsilon_i - \varepsilon_r) dt \tag{6.3}$$

$$u_2 = C_0 \int_0^t \varepsilon_t dt \tag{6.4}$$

Where, stresses and strains are assumed positive in compression. The average strain in the specimen is

$$\varepsilon_s = \frac{u_1 - u_2}{L} \tag{6.5}$$

Or in terms of the strain pulses

$$\varepsilon_s = \frac{C_0}{L} \int_0^t (\varepsilon_i - \varepsilon_r - \varepsilon_t) dt \tag{6.6}$$

Where, L is the length of the specimen. The forces at the ends of the specimen are obtained from

$$P_1 = EA(\varepsilon_i + \varepsilon_r) \tag{6.7}$$

$$P2 = EA\varepsilon_t \tag{6.8}$$

Where, E and A are Young's modulus and the cross-sectional area of the Hopkinson bars. The average force is calculated from

$$P_{av} = \frac{EA}{2}(\varepsilon_i + \varepsilon_r + \varepsilon_t) \tag{6.9}$$

If it is assumed that $P_1=P_2$, that is forces are equal at both the ends of the specimen, then from (7) and (8)

$$(\varepsilon_i + \varepsilon_r) = \varepsilon_t$$

or $$\varepsilon_i = \varepsilon_t - \varepsilon_r \tag{6.10}$$

substituting (10) in (6) and (9)

$$\varepsilon_s = \frac{C_0}{L} \int_0^t (\varepsilon_t - \varepsilon_r - \varepsilon_r - \varepsilon_t) dt$$

or $$\varepsilon_s = \frac{-2C_0}{L} \int_0^t \varepsilon_r dt \tag{6.11}$$

$$P_{av} = EA\varepsilon_t \tag{6.12}$$

For the specimen of cross-sectional area A_s, the stress and the strain rate in the specimen become

$$\sigma_s = E\frac{A}{A_s}\varepsilon_t = K_1\varepsilon_t \tag{6.13}$$

$$\dot{\varepsilon}_s = \frac{-2C_0}{L}\varepsilon_r = K_2\varepsilon_r \tag{6.14}$$

K_1 and K_2 are the stress and the strain rate multiplying factors for a given specimen and the setup. Hence, only the transient strain data is required to be recorded. Utilizing this data and using equations 13 and 14, the transient stress and strain rate can be calculated. Strain rate data is then integrated to get the strain versus time data. On superimposing with the stress versus time data, the transient stress-strain data is obtained. For this data analysis, VuPoint signal analysis software was used. To calculate the absorbed energy density (energy/unit volume), the following equation was used.

$$U_a(t) = \frac{1}{2}\int_0^t \sigma_{(t)}\varepsilon_{(t)}dt \tag{6.15}$$

The absorbed energy is then calculated by multiplying the above with the volume of the sample.

Typical incident, transmitted and reflected signals are shown in Figure 6.4.1. Table 6.4.1 gives the specimen dimensions after the Hopkinson bar tests. It would be noticed that the dimensions did not change much, as under the applied impact load internal fracturing and permanent deformations have just set in, and more energy would have needed to continue the fracturing process. At this threshold level, it would be more interesting to see the micrographs of the damage development, and determine the modes of failure.

The strain rate at which the tests were done was around 950, the minimum average being 910, and maximum 962.

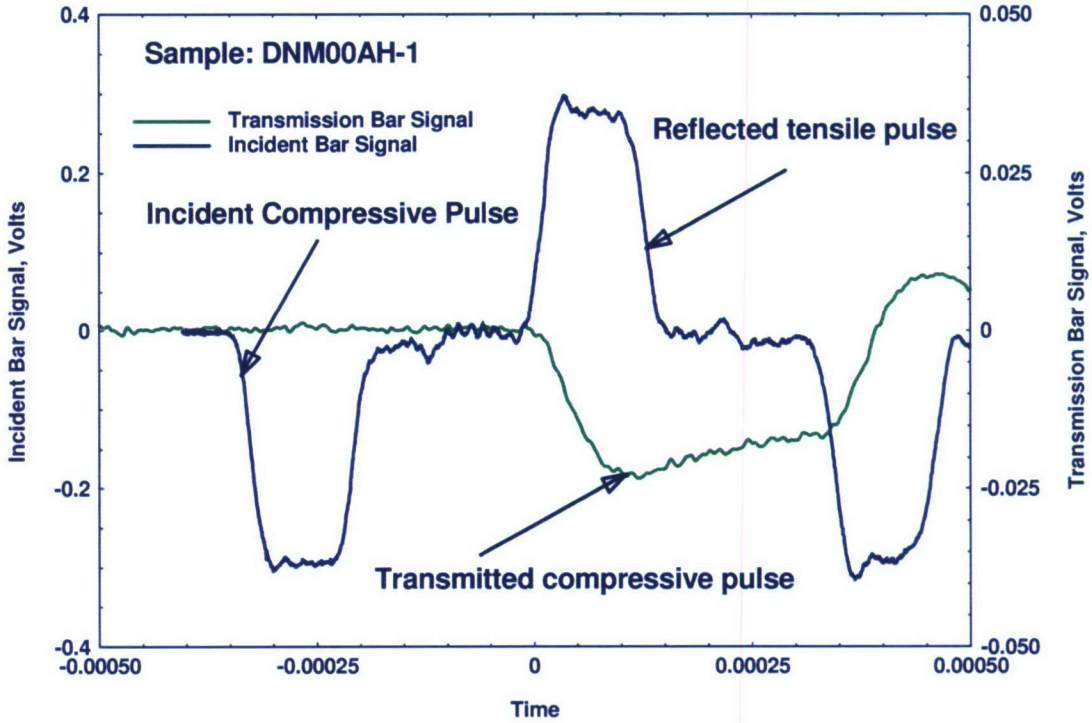

Figure 6.4.1: Typical signals from the Hopkinson's Bar Setup

Table 6.4.1: Change of sample dimensions after tests

Dimensions of HSR Samples						
Sample No	**before test length (l) m**	**after test length (l) m**	**before test width (w) m**	**after test Width (w) m**	**before test Thickness (t) m**	**after test Thickness(t) m**
DNM00AH-1	0.01128	0.01123	0.01245	0.01247	0.01006	0.01013
DNM00AH-2	0.01171	0.01163	0.01143	0.01146	0.01006	0.01011
DNM00AH-4	0.01156	0.01143	0.01130	0.01138	0.01006	0.01013
DNM00CH-1	0.01158	0.01151	0.01153	0.01156	0.01013	0.01013
DNM00CH-3	0.01146	0.01130	0.01143	0.01148	0.00991	0.00998
DNM00CH-4	0.01163	0.01148	0.01163	0.01166	0.01006	0.01011
DNM00AH-1	0.01120	0.01110	0.01151	0.01101	0.00986	0.00989
DNM00AH-2	0.01153	0.01148	0.01143	0.01147	0.00986	0.00986
DNM00AH-4	0.01166	0.01156	0.01143	0.01146	0.00991	0.00993
DNM10CH-1	0.01153	0.01144	0.01156	0.01160	0.00991	0.00993
DNM10CH-2	0.01146	0.01138	0.01130	0.01133	0.00996	0.00996
DNM10CH-3	0.01146	0.01119	0.01146	0.01152	0.00991	0.00994
DNM25AH-1	0.01130	0.01125	0.01140	0.01148	0.00986	0.00991
DNM25AH-2	0.01143	0.01138	0.01143	0.01146	0.00968	0.00972
DNM25AH-4	0.01148	0.01138	0.01158	0.01161	0.00980	0.00980
DNM25CH-2	0.01166	0.01163	0.01171	0.01173	0.01006	0.01006
DNM25CH-3	0.01158	0.01154	0.01168	0.01173	0.01003	0.01005
DNM25CH-4	0.01158	0.01153	0.01156	0.01162	0.01001	0.01002
DNM50AH-1	0.01120	0.01115	0.01120	0.01130	0.00996	0.01003
DNM50AH-2	0.01153	0.01147	0.01148	0.01151	0.00991	0.00993
DNM50AH-3	0.01153	0.01140	0.01143	0.01148	0.00980	0.00982
DNM50CH-2	0.01151	0.01146	0.01148	0.01151	0.00991	0.00993
DNM50CH-3	0.01151	0.01143	0.01156	0.01161	0.00993	0.00994
DNM50CH-4	0.01146	0.01143	0.01138	0.01140	0.00991	0.00993

The effects of higher percentage of MWCNT is clearly observed in the higher peak stress in DNM10AH and DNM10CH samples compared to other samples as seen in Table 6.4.2. The order of peak stress, from highest to lowest, are:

DNM10CH	170.03 Mpa	10.0% MWCNT
DNM50CH	166.06 Mpa	5.0% MWCNT
DNM10AH	162.32 Mpa	10.0% MWCNT
DNM25CH	157.91 Mpa	2.5% MWCNT
DNM50AH	156.68 Mpa	5.0% MWCNT
DNM25AH	154.65 Mpa	2.5% MWCNT
DNM00AH	136.85 Mpa	0.0% MWCNT
DNM00CH	127.05 Mpa	0.0% MWCNT

Above results, when plotted graphically, as shown in Figure 6.4.2 and Figure 6.4.3

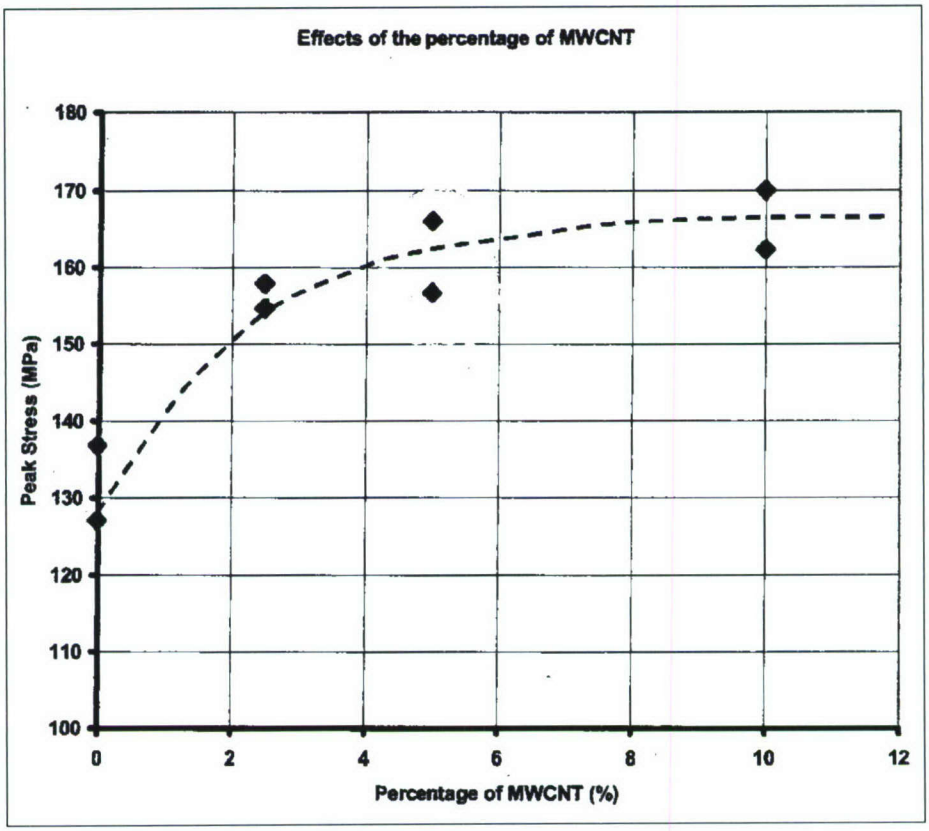

Figure 6.4.2: Effect of MWCNT on peak stress

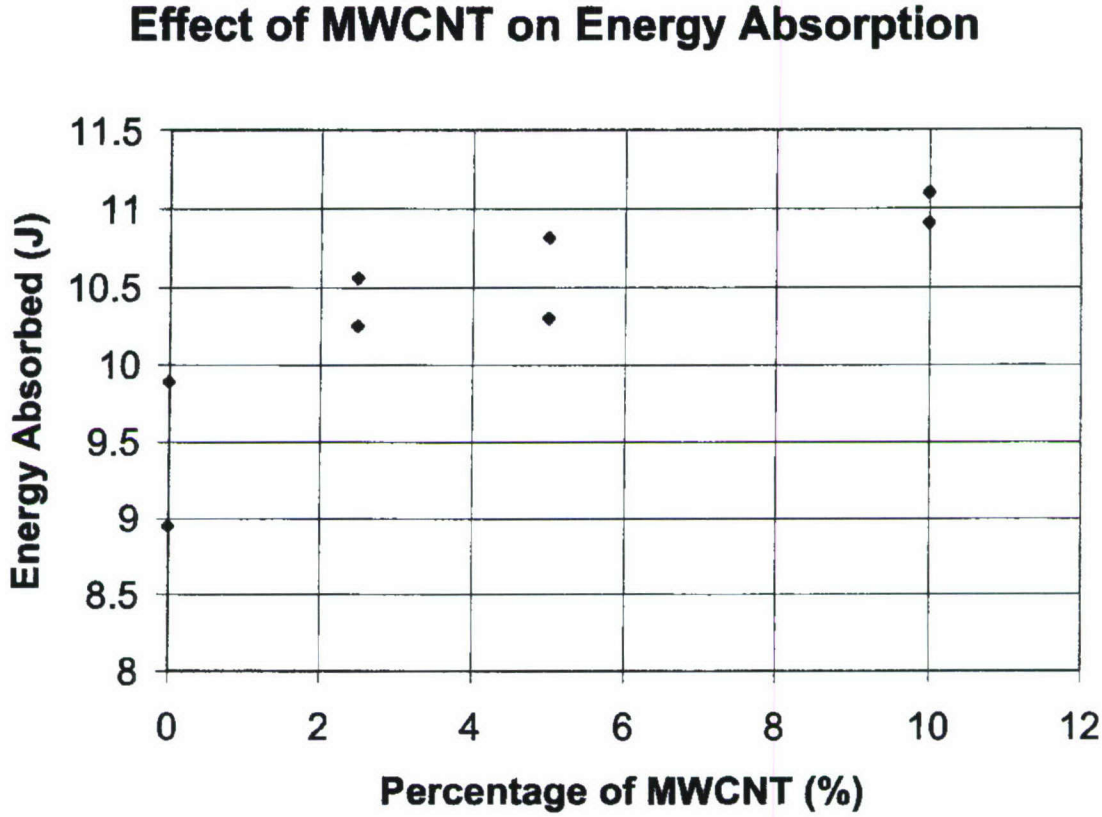

Figure 6.4.2: Effect of MWCNT on energy Absorption

The energy absorbed by the specimens are also given in Table 6.4.2. It follows the same trend as peak stress. Energy absorption increase with percentage of MWCNT. However, in both cases rate rises faster initially, the effect tapers down with higher percentage.

Table 6.4.2: High strain rate test – peak stress and energy absorption

HSR Results				
Sample No	**Strain Rate/s**	**Peak Stress, MPa**	**Energy Density, 10^6 J/m^3**	**Energy, J**
DNM00AH-1	958	134.42	6.96	9.83
DNM00AH-2	976	133.36	7.34	9.88
DNM00AH-4	952	142.77	7.59	9.97
AVERAGE	**962**	**136.85**	**7.30**	**9.89**
Standard Deviation	**12**	**5.16**	**0.32**	**0.07**
DNM00CH-1	893	134.45	6.54	8.85
DNM00CH-3	970	133.73	7.41	9.60
DNM00CH-4	944	112.96	6.16	8.39
AVERAGE	**936**	**127.05**	**6.70**	**8.95**
Standard Deviation	**39**	**12.21**	**0.64**	**0.61**
DNM10AH-1	975	160.83	8.60	10.91
DNM10AH-2	908	161.54	8.19	10.54
DNM10AH-4	940	164.59	8.54	11.28
AVERAGE	**941**	**162.32**	**8.44**	**10.91**
Standard Deviation	**34**	**2.00**	**0.22**	**0.37**
DNM10CH-1	960	170.66	8.64	11.41
DNM10CH-2	953	167.85	8.46	10.90
DNM10CH-3	927	171.57	8.46	10.99
AVERAGE	**947**	**170.03**	**8.52**	**11.10**
Standard Deviation	**17**	**1.94**	**0.10**	**0.27**
DNM25AH-1	944	161.97	8.04	10.22
DNM25AH-2	967	153.16	8.19	10.35
DNM25AH-4	947	148.83	7.80	10.17
AVERAGE	**953**	**154.65**	**8.01**	**10.25**
Standard Deviation	**13**	**6.70**	**0.19**	**0.09**
DNM25CH-2	918	160.29	8.04	10.76
DNM25CH-3	884	158.30	7.66	10.40
DNM25CH-4	928	155.13	7.86	10.53
AVERAGE	**910**	**157.91**	**7.86**	**10.56**
Standard Deviation	**23**	**2.60**	**0.19**	**0.18**
DNM50AH-1	921	161.61	8.37	10.45
DNM50AH-2	938	156.90	7.84	10.28
DNM50AH-3	975	151.55	7.86	10.16
AVERAGE	**945**	**156.68**	**8.03**	**10.30**
Standard Deviation	**28**	**5.03**	**0.30**	**0.14**
DNM50CH-2	933	166.29	8.34	10.91
DNM50CH-3	938	159.60	8.11	10.72
DNM50CH-4	936	172.29	8.40	10.84
AVERAGE	**936**	**166.06**	**8.28**	**10.82**
Standard Deviation	**3**	**6.35**	**0.15**	**0.10**

6.5 Conclusions

The multi-walled carbon nanotube (MWCNT) composites are extremely tough, and in high impact force of the Hopkinson Bar none of the specimens were fragmented, but suffered some permanent deformations, which should be examined by high magnification micrography to determine the fracture initiation and propagation.

Quantity of MWCNT modified the strength and stiffness. An addition of a small percentage significantly improved the strength, and energy absorption characteristics. However, additional of larger percentage does not proportionately improves the strength of the energy absorption.

6.6 Acknowledgement

The author is indebted to Prof Raju Mantena of the University of Mississippi for supplying the nanocomposite samples. Dr. Piyush Dutta of Dutta Technologies Inc., Florida, obtained the Hopkinson Bar Test results.

REFERENCES:

[1.1] Nori C., Mantena P. R. and McCarty T. A. (1996) "Experimental and finite element analysis of pultruded glass-graphite/epoxy hybrids in axial and flexural modes of vibration". Journal of Composite Materials, Vol. 30, No. 18, pp. 1996-2018.

[1.2] Suarez S. A. and R. F. Gibson (1987) "Improved Impulse-Frequency Response Techniques for Measurement of Dynamic Mechanical Properties of Composite Materials" Journal of Testing and Evaluation v.15, pp. 114-121.

[1.3] Mantena P.R., R Vangipuram and J. G. Vaughan (1994) "Dynamic Flexural Properties of Pultruded Glass/Graphite Hybrid Composites" 39th International SAMPE Symposium Proceedings, 32:231-244.

[1.4] Blevins Robert D (1979) "Formulas for natural frequency and mode shapes" Van Nostrand Reinhold Ltd. pp. 260-265.

[1.5] Gibson, Ronald F. (2007) "Principles of Composite Material Mechanics" McGraw Hill Companies, Inc.

[2.1] ASTM International, "D6110-06 Standard Test Method for Determining the Charpy Impact Resistance of Notched Specimens of Plastics", 2006

[3.1] Al-Ostaz, A., Mantena, R., Anakapalli, M., and Hwang, S. (2007). "Evaluation of high-performance pressure-sensitive adhesive and VHB acrylic foam tapes bonded aluminum joints subjected to environmental aging." J. Adhesion Sci.Technol, 339-361.

[3.2] Hong, S. (2003). "Electrochemical impedance spectroscopy based sensors for NDE of CFRB /concrete bond in beams." Ms thesis, Dept of Civil and Environmental Engineering, Michigan State University, East Lansing.

[3.3] Davis, G. D., Dacres, C. M., and Krebs, L. A. (1999). "In-situ sensor to detect moisture intrusion and degradation of coatings, composites, and adhesive bonds." Proc., Tri-Services Conf. on Corrosion.

[3.4] Davis,G.D., Krebs, L. A., Drzal, L. T., Rich, M.J., and Askeland, P.(2000). "Electrochemical sensors for nondestructive evaluation of adhesive bonds." J. Adhesion, 72, 335-358.

[3.5] Davis, G.D., Rich, M. J., Harichandran, R. S., Drzal, L. T., Mase, T., and Al-Ostaz, A. (2003). "Development of an electrochemical impedance sensor to monitor delamination and moisture uptake in CFRP- reinforced concrete structures." Proc., 81 st Annual Meeting (CD-ROM), Transportation Research Board, Washington, D.C., Paper No. 03-2392.

[3.6] Harichandran, R. S., Hong, S., Al-Ostaz, A., and Davis, G. D. (2003)."NDE of bond integrity in concrete structures strengthened with carbon FRP using EIS." Proc., 1st Int. Conf. on Structural Health Monitoring and Intelligent Infrastructure, Ibaraki University, Tokyo, 1183-1190.

[3.7] Gamry Instruments. (2003). "Equivalent circuit modeling using the Gamry EIS300 electrochemical impedance spectroscopy software." http://www.gamry.com.

[4.1] Deng C F, Wang D Z, Zhang X X and Li A B, Processing and properties of carbon nanotubes reinforced aluminum composites, *Materials Science and Engineering: A*, 444, 2007, pp 138 – 145

[4.2] Yoon P J, Fornes T D and Paul D R, Thermal expansion behavior of nylon 6 nanocomposites, *Polymer*, 43, 2002, pp 6727-6741

[4.3] Mishra S, Sonawane S and Chitodkar V, Comparative Study on Improvement in Mechanical and Flame Retarding Properties of Epoxy-$CaCO_3$ Nano and Commercial Composites, *Polymer-Plastics Technology and Engineering*, 44, 2005 , pp 463 – 473

[4.4] Gilman J W, Jackson C L, Morgan A B and Harris R, Jr., Flammability Properties of Polymer-Layered-Silicate Nanocomposites. Polypropylene and Polystyrene Nanocomposites, *Chemistry of Materials*, 12, 2000, pp 1866-1873

[4.5] Strawhecker K E and Manias E, Structure and Properties of Poly(vinyl alcohol)/Na^+ Montmorillonite Nanocomposites, *Chemistry of Materials*, 12, 2000, pp 2943–2949

[4.6] Krishnamoorti R, Vaia R A and Giannelis E P, Structure and Dynamics of Polymer-Layered Silicate Nanocomposites, *Chemistry of Materials*, 8, 1996 pp 1728 - 1734

[4.7] Xu R, Manias E, Snyder A J and Runt J, New Biomedical Poly(urethane urea)-Layered Silicate Nanocomposites, *Macromolecules*, 34, 2001, pp 337 – 339

[4.8] Kojima Y, Usuki A, Kawasumi M, Okada A, Fukushima Y, Kurauchi T and Kamigaito O, Mechanical properties of nylon 6 – clay hybrid, *Journal of Material Research*, 8. 1993, pp 1185 – 1189

[4.9] Odegard G M, Gates T S, Nicholson L M and Wise C, Equivalent continuum modeling with application to carbon nanotubes, *NASA ICASE report* NASA/TM-2002-211454, March 2002

[4.10] Odegard G M, Gates T S, Nicholson L M and Wise C, Equivalent continuum modeling of nano-structured materials, *NASA ICASE report* NASA/TM-2001-210863, May 2001

[4.11] Li C and Chou T, A structural mechanics approach for the analysis of carbon nanotubes, *International Journal of Solids and Structures*, 40, 2003, pp 2487 – 2499

[4.12] Zhang P, Huang Y, Geubelle P H, Klein P A and Hwang K, The elastic modulus of single-wall carbon nanotubes: a continuum analysis incorporating interatomic potentials, *International Journal of Solids and Structures,* 39, 2002, pp 3893 – 3906

[4.13] Zhang P, Huang Y, Gao H and Hwang K, Fracture nucleation in single-wall carbon nanotubes under tension: : a continuum analysis incorporating interatomic potentials, *Transactions of the ASME*, 69, 2002, pp 454 – 458

[4.14] Arroyo M and Belytschko T, Finite crystal elasticity of carbon nanotubes based on the exponential Cauchy – Born rule, *Physical Review B*, 69, 2004, pp 115415.1-115415.11

[4.15] Zhang P, Jiang H, Huang Y, Geubelle P H and Hwang K C, An atomistic-based continuum theory for carbon nanotubes: analysis of fracture nucleation, *Journal of Mechanics and Physics of Solids*, 52, 2004, pp 977 – 998

[4.16] Jiang H, Zhang P, Liu B, Huang Y, Geubelle P H, Gao H and Hwang K C, The effect of nanotube radius on the constitutive model for carbon nanotubes, *Computational Materials Science*, 28, 2003, pp 429 – 442

[4.17] Jiang H, Feng X Q, Huang Y, Hwang K C and Wu P D, Defect nucleation in carbon nanotubes under tension and torsion: Stone – Wales transformation, *Computer methods in Applied Mechanics and Engineering*, 193, 2004, pp 3419 – 3429

[4.18] Arroyo M and Belytschko T, Nonlinear mechanical response and rippling of thick multiwalled carbon nanotubes, *Physical Review Letters*, 91(21), 2003, pp 215505.1 – 215505.4

[4.19] Tersoff J, New empirical approach for the structure and energy of covalent systems, *Physical Review B*, 37, 1988, pp 6991 – 7000

[4.20] Brenner D W, Empirical potential for hydrocarbons for use in simulating chemical vapor deposition of diamond films, *Physical Review B*, 42, pp 9458 – 9471

[4.21] Yakobson B I, Cambell M P, Brabec C J, Bernholc J, High strain rate fracture and C-chain unrevealing in the carbon nanotubes, *Computational Materials Science*, 8, 1997, pp 341 – 348

[4.22] Belytschko T, Xiao S P, Schatz G C and Ruoff R S, Atomistic simulations of carbon nanotube fracture, *Physical Review B*, 65(23), 2002, pp 235430.1 – 235430.7

[4.23] MS Modeling 4.0 Online Help Manual, Accelrys Inc., 2005

[4.24] www.wikipedia.org, the free web based encyclopedia, accessed on 05-01-2006.

[4.25] Sun H, COMPASS: An ab initio force-field optimized for condensed-phase applications - Overview with details on alkane and benzene compounds, *Journal of Physical Chemistry B*, 102, 1998, pp 7338 – 7364

[4.26] Pal G., Al-Ostaz A., Mantena P.R., Cheng A. and Song C. "Molecular dynamic simulations of SWCNT-polymer nanocomposite and its constituents". *Proceedings of the 21st Annual Technical Conference of the American Society for Composites, Dearborn, MI,* Paper #136 on CD ROM, 2006.

[4.27] Ahmed Al-Ostaz, Ghanshyam Pal, P. Raju Mantena and Alex Cheng, " Molecular Dynamics Simulation of SWCNT - Polymer Nanocomposite and Its Constituents." *Journal of Materials Science*. (Accepted).

[4.28] Theodorou, D. N., U. W. Suter. 1986. "Atomistic Modeling of Mechanical Properties of Polymeric Glasses", *Macromolecules*, 19: 139 – 154.

[4.29] Christensen R. Mechanics of Composite Materials, Krieger Publishing Company, Malbar Fl, 1991, pp74-78.

[4.30] Chou T. W, Thostenson E. T. and Ren Z. F. Advances in the Science and Technology of Carbon Nanotubes and Their Composites: A Review, *Composites Science and Technology,* 61, 2001, 1899-1909.

[4.31] http://pslc.ws/macrog/pe.htm, Polymer science learning center, The University of Southern Mississippi.

[4.32] Gou J, Jiang S, Minaie B, Liang Z, Chuck Z and Wang B, Nanoscale modeling and simulation interfacial bonding of single walled nanotube reinforced composites, *IMECE'03 – 41138, Proceedings of IMECE'03 International Engineering Congress and Exposition*, Washington, D.C., November 16-21, 2003, pp 1 -5

[4.33] Liao K and Li S, Interfacial characteristics of a carbon nanotube – polystyrene composite system, *Applied Physics Letters*, 79 (25), 2001, pp 4225 – 4227

[4.34] Rappe´ A K, Casewit C J, Colwell K S, Goddard W A and Skiff W M, UFF, a full periodic table force field for molecular mechanics and molecular dynamics simulations, Journal of the American Chemical Society, 114, 1992, pp 10024 - 10035

[4.35] Maruyama S, Chapter 21, Molecular Dynamics Method for Micro/Nano Systems, *Handbook of Numerical Heat Transfer*, (2005), in press (available on world wide web)

[4.36] Parrinello M and Rahman A, Polymorphic transitions in single crystals: A new molecular dynamics method, *Journal of applied Physics*, 52(12), 1981, pp 7182 – 7190

[4.37] Ray J R and Rahman A, Statistical ensemble and molecular dynamics studies of anisotropic solids, *Journal of Chemical Physics*, 80(9), 1984, pp 4423 – 4428

[4.38] Anderson H C, Molecular dynamics simulations at constant pressure and/or temperature, *Journal of chemical physics*, 72 (4), 1980, 2384 – 2393

[4.39] Parrinello M and Rahman A, Strain fluctuations and elastic constants, *Journal of chemical physics*, 76 (5), 1982, 2662 – 2665

[4.40] Ray J R, Elastic constants and statistical ensembles in molecular dynamics, *Computer Physics Reports*, 8, 1988, pp 109 – 152

[5.1] "Instruction Manual for Standing Wave Apparatus Type 4002", Brüel & Kjær

[5.2] ASTM International, "C384-04 Standard Test Method for Impedance and Absorption of Acoustical Materials by Impedance Tube Method", 2005, pp 103-108

[5.3] ANSI S1.6 "Preferred Frequencies and Band Numbers for Acoustical Measurements"

[5.4] Crocker, Malcolm, "Encyclopedia of Acoustics", John Wiley and Sons, 1997

[5.5] Kinsler, Frey, Coppens and Sanders, "Fundamentals of Acoustics", Third Edition, John Wiley and Sons, 1982

[6.1] Dutta, P.K., D.Hui, and M.R.Altamirano, (1991), "Energy Absorption of Graphite/Epoxy Plates Using Hopkinson Bar Impact, US Corps of Engineers, Cold Regions Research and Engineering Laboratory, CRREL Report 91-20, Hanover, New Hampshire.

[6.2] Dutta, P.K., and D.Hui, (1992), "Stress Wave Propagation Through the Thickness of Graphite/Epoxy Laminated Plates using PVDF Sensors", Proceedings of the sixth Japan-U.S. Conference on Composite Materials, June 22-24, Orlando, Florida, Technomic Publishing, pp 845-854

[6.3] Dutta, P.K., and D.Hui, (1993), "High Strain-rate Behavior of Gr/Ep Laminate under Transverse Impact", Presented at the U.S.Army Research Office Workshop on Dynamic Response of Composite Structures, University of New Orleans, New Orleans, LA, August 30-September 1, 1993

[6.4] Dutta, P.K., K.J.L.Faran, and D.Hui, (1993), "Influence of LowTemperature on Energy Absorption in Laminated Composites", Proc.of the Ninth International Conference on Composite Materials (ICCM/9), Madrid, Ed. A. Miravete, Univ. of Zaragoza, Woodhead Publ. Ltd. pp 311-320

[6.5] Dutta, P.K., and D.Hui, (1994), "Low-Temperature High Strain Rate Behavior of Gr/Ep Laminate under Transverse Impact", In Advanced Structural Fiber Composites, Editor:P. Vincenzini, Techna Srl, Florence, Italy, 1995, pp 455-468.

[6.6] Dutta, P.K., D.Hui, and Patil, A. (2001), "High-strain Rate Fracture Energy of Unidirectional Composites", Eighth Annual International Conference on Composites Engineering, Ed. D. Hui, Aug 5-11, 2001, Tenerife, Canary Islands, Spain. Pp 1043-1045